Engineered Synthetic Materials for Stem Cell Biomanufacturing

By

Angela W. Xie

A dissertation submitted in partial fulfillment of

the requirements for the degree of

Doctor of Philosophy

(Biomedical Engineering)

at the

University of Wisconsin-Madison

2019

Date of final oral examination: February 7th, 2019

This dissertation is approved by the following members of the final oral committee:

William L. Murphy, Professor, Biomedical Engineering
Peiman Hematti, Professor, Medicine
Timothy J. Kamp, Professor, Medicine
Wan-Ju Li, Associate Professor, Biomedical Engineering
Sean P. Palecek, Professor, Chemical & Biological Engineering

ABSTRACT

Stem cell therapies are under development to treat a wide range of debilitating diseases, but their widespread translation depends on the ability to manufacture clinically effective cell products through bioprocesses that are controllable, scalable, and economical. Synthetic biomaterials may be uniquely enabling in the production of stem cell therapies, as they can be designed to precisely control soluble and insoluble components of the *in vitro* stem cell microenvironment. In this thesis, we describe the development of synthetic biomaterial-based approaches to 1) Improve the efficiency of stem cell expansion and 2) Understand and manipulate culture parameters that influence stem cell phenotype and therapeutic function. In the first portion of this work, we describe a biomaterial strategy for stabilizing and delivering thermally labile growth factors for efficient, cost-effective expansion of human pluripotent stem cells (hPSCs). Specifically, we developed mineral-coated microparticles (MCMs) for sustained release of basic fibroblast growth factor (bFGF), a soluble factor critical for hPSC survival, proliferation, and pluripotency. We found that MCMs protected bFGF activity at physiological temperatures, resulting in four-fold higher retention in biological activity compared to free soluble bFGF. Optimizing the process for generating bFGF-MCMs and the dosing of bFGF-MCMs enabled long-term expansion of hPSCs (over 25 passages) in a pluripotent state while reducing the amount of bFGF required by greater than 80% compared to conventional culture strategies. For the second portion of this work, we developed a novel approach based on engineered labile culture substrates that enabled control over spatial and temporal dynamics of cell aggregation. We then applied this platform to understand how the method and kinetics of aggregation influenced the three-dimensional microenvironment within hPSC and mesenchymal stem/stromal cell (MSC) aggregates. We found that the kinetics of aggregation affected structural features including cell

packing density, extracellular matrix deposition, and porosity within aggregates, which in turn had implications for the lineage-specific differentiation of hPSCs and the therapeutic function of MSCs. In summary, this thesis describes two synthetic biomaterial-based approaches to control soluble and insoluble aspects of the microenvironment during stem cell biomanufacturing. These studies highlight opportunities for biomaterials to facilitate translation of cell therapies by improving biomanufacturing processes and underscore the importance of understanding variables introduced by specific bioprocesses that may influence the ultimate potency of a cell therapy product.

To my family.

ACKNOWLEDGMENTS

I'd like to start by thanking my advisor, Dr. William Murphy, for his support and guidance throughout my PhD and for always being an advocate for my professional success. Bill's focus on near-term clinical translation gave me a new perspective for how I think about developing technologies in the lab, which I will carry with me far beyond my graduate work. Bill was also a constant source of encouragement for me to pursue leadership and professional opportunities. Among these were research collaborations with clinicians and industry, and my involvement with the Wisconsin Stem Cell Roundtable (WiSCR), all of which were instrumental to my growth as a scientist. I'd also like to thank my committee members: Drs. Tim Kamp, Peiman Hematti, Wan-Ju Li, and Sean Palecek, who have all been incredibly supportive and always willing to provide feedback and advice on my work. Each of them has brought a unique perspective that has helped to guide my thesis directions.

The Murphy lab has been a fantastic environment in which I've met some incredibly talented scientists and all-around wonderful people whose influence cannot be easily put into words. Many thanks to all Murphy lab members, past and present, for great scientific discussions, lab and life advice, comic relief, and words of encouragement when I needed it: Buffy Aisenbrey, Hamisha Ardalani, Kate Barteau, Dave Belair, Connie Chamberlain, Anna Clements, Bill Daly, Gianluca Fontana, Tori Harms, Gaurav Kaushik, John Krutty, Nhi Le, Jae-Sung Lee, "Uncle Jim" Molenda, Ulrika Müller, Eric Nguyen, Matt Parlato, Samantha Schmitt, Mike Schwartz, Liz Torr, Xiaohua Yu, and Junsu Yun. Beko Binder taught me to ask "Why tho?" and offered many enrichments to my life outside lab, including inspiring me to take up racquetball and making steaks so good that I had to buy a cast iron skillet and learn to cook them for myself. I am also incredibly grateful for the friendship of Andrew Khalil, who was with me from day one of this journey and promised to be there until the end (even if it meant sending encouragement from 1,000 miles away) – I couldn't ask for a better friend and colleague.

I also had the privilege of working with some very talented undergraduates throughout the course of graduate school. Hunter Johnson was instrumental in pushing the FGF delivery project forward (even while working on a hundred other things in the lab) and his positive energy in the lab was infectious. I am confident he will be successful at Berkeley and whatever he chooses to pursue in the future. Nick Zacharias slogged through much of the MSC aggregate work with me and improved tremendously as a scientist along the way. I wish him the very best and hope that he can use some of the lab and life lessons from the past few years in medical school and beyond.

I am truly indebted to so many people outside of the lab for their support as well. Dr. Joyce Wong opened up so many opportunities for me as an undergraduate researcher at Boston University, and without her guidance I would not be where I am today. Dr. Connie Lebakken, who took me on as an intern at Stem Pharm, has also been an incredible role model and I am appreciative for her continuing mentorship. I am also lucky to have had constant encouragement from many wonderful friends. Kim Powell, Kayla Schwalbe, Danielle Walker, Morgan Counts, Sarah Sprangers, and Jim, Vreni, Bjorn, and Tanya Paulson are close friends from home – they remind me of my roots and I am so grateful for their unwavering support over the years. Katy Rothenberg and Imaly Nanayakkara were in the trenches of a BME PhD with me – even from halfway across the country, they were always willing to lend a kind ear or serve as a welcome distraction, to celebrate and commiserate during the rollercoaster ride of graduate school.

Most importantly, I am so thankful for the support of my family: my parents and my brother Justin, who have been with me through the highest highs and the lowest lows, yet have never wavered in their love, encouragement, and understanding. Their support during this process came through in many ways – from dropping off homemade meals to helping me with car trouble, from joining me on walks along the lakeshore to giving me pep talks during difficult times. They have been my biggest cheerleaders and have sacrificed everything to provide me with the best education and the best life possible, and for that I am eternally grateful.

TABLE OF CONTENTS

List of Figures

List of Tables

CHAPTER 1. INTRODUCTION

1.1 BACKGROUND AND SIGNIFICANCE

Cell therapies, in which living cells are used as therapeutic agents, are under development as potentially transformative treatments for diseases including cancer, Parkinson's disease, spinal cord injury, heart failure, macular degeneration, and diabetes[1,2]. Cell therapies are considered to be the next generation of therapeutics – rather than addressing a single molecular target, these "living drugs" have the capacity to recapitulate the complex functions of cells lost to disease, can respond dynamically to cues from their environment, and can be engineered with new functionalities to address unmet clinical need. Even as cell therapies accelerate toward clinical use, however, there remain obstacles to ensuring their widespread adoption, many of which are associated with the large-scale manufacturing of these complex cell products, as current treatments are expected to require millions to billions of cells per dose[3,4]. While stem cells are recognized as a plentiful source of starting material for cell therapies due to their immense proliferative and differentiation capabilities, the development of controllable, efficient, and economical stem cell biomanufacturing processes relies on a deep understanding of the soluble and insoluble cell microenvironment as well as methods to manipulate the microenvironment in scalable culture formats such as three-dimensional (3D) cell aggregates.

The soluble microenvironment is composed of oxygen, ions, nutrients and metabolites (e.g., glucose, amino acids, lactate, fatty acids), and diffusible protein components such as growth factors and cytokines. Among these, growth factors are potent regulators of behaviors such as survival, proliferation, self-renewal, and differentiation, and conventional strategies for stem cell expansion and directed differentiation rely on exogenously providing recombinant forms of these

proteins in the bulk media[5]. This mode of delivery often requires high concentrations of the growth factor, as many growth factors display poor stability under these conditions and a large fraction of the provided dose is not readily accessible to target receptors on cells. In cell aggregates, a common format for scalable suspension culture of stem cells, additional barriers to growth factor accessibility can arise due to limited mass transport into the interior of these large, cell-dense structures[6,7]. In addition to serving as simple barriers to diffusion, structural features of the insoluble 3D aggregate microenvironment – including cell-cell adhesions and cell-secreted extracellular matrix – can themselves dictate stem cell fate and function through biochemical and cellular mechanosensing pathways[8]. However, the scarcity of methods to reliably control structural properties of cell aggregates has impeded efforts to optimize these aggregates for cell therapy applications.

Synthetic biomaterials can serve as powerful tools for deconstructing microenvironmental influences on stem cell fate and advances in materials science and bioengineering have led to new approaches for spatial and temporal control over the soluble and insoluble signals that direct stem cell behavior *in vitro*. This thesis describes the development of two synthetic biomaterial technologies for stem cell biomanufacturing applications – the first to control the delivery and extend the biological activity of soluble growth factors in stem cell culture, and the second to regulate spatiotemporal dynamics of 3D cell aggregation and the resultant morphometric and structural properties of stem cell aggregates. We show that these biomaterial-based strategies – in combination with statistical optimization approaches such as Design of Experiments – can be used to improve the efficiency of stem cell expansion and to understand and manipulate culture parameters that influence stem cell phenotype and therapeutic function.

1.2 SUMMARY OF THE WORK

Chapter 2 of this thesis provides a brief overview of progress and challenges in stem cell biomanufacturing and addresses areas in which synthetic biomaterials-based approaches may be particularly enabling. One area of focus is the use of biomaterials to potentiate exogenous growth factor signaling or to sequester or mimic endogenous growth factors, with the goal of reducing the quantities of costly recombinant growth factors currently required in stem cell biomanufacturing. A second avenue of opportunity centers around biomaterial strategies to tailor the properties of 3D stem cell aggregates. Specifically, we discuss the evolution of mainstream methods for forming cell aggregates including advantages and limitations of these approaches, and highlight emerging strategies for regulating the cell aggregation process and for engineering the aggregate microenvironment.

In Chapter 3, we describe the development of mineral-coated microparticles (MCMs) for sustained delivery of basic fibroblast growth factor (bFGF) in human pluripotent stem cell (hPSC) culture. We show that MCM-mediated stabilization and local release of bFGF enables a significant reduction in the growth factor dose required to support long-term pluripotency maintenance in two-dimensional culture, and provide evidence that bFGF delivery from MCMs in hPSC aggregates may overcome diffusion limitations to improve pluripotency in 3D culture. Chapter 4 focuses on the development and characterization of a biomaterial strategy to exert spatiotemporal control over formation of the 3D cell microenvironment via controlled cell aggregation from labile culture substrates. We demonstrate that micropatterning of labile chemical linkages can be used to manipulate the spatial and temporal presentation of Arg-Gly-Asp (RGD) cell adhesion ligands on synthetic culture substrates, with cleavage of labile linkages resulting in controllable self-assembly

of cell aggregates through mechanisms distinct from those described for existing aggregation methods.

Chapter 5 then applies the labile substrate technology from Chapter 4 to understand the effects of aggregation method and kinetics on stem cell phenotype in differentiating hPSC aggregates, or embryoid bodies (EBs). We show that slower aggregation kinetics results in lower cell packing densities, increased EB porosity, and elevated growth factor signaling in the EB interior, which is correlated with delayed loss of pluripotency and lineage bias toward mesendoderm fates. In Chapter 6, we demonstrate that aggregation method and kinetics similarly influence aggregate structure in human mesenchymal stem/stromal cells (MSCs), a promising cell type for treating immune- and inflammatory-related diseases. We then use a Design of Experiments approach to identify optimal aggregate sizes and aggregation kinetics for enhancing MSC immunomodulatory function. Finally, in Chapter 7, we summarize our findings, address limitations of our studies, and suggest avenues to pursue in future extensions of this work. Collectively, this thesis describes novel applications of synthetic biomaterials to control the *in vitro* microenvironment for two types of stem cells central to cell therapy, and highlights how spatiotemporal control over soluble and insoluble cues can be exploited for improved efficiency and functionality in stem cell biomanufacturing.

1.3 REFERENCES

1. Trounson, A. & McDonald, C. Stem Cell Therapies in Clinical Trials: Progress and Challenges. *Cell Stem Cell* **17,** 11–22 (2015).
2. Piscopo, N. J. *et al.* Bioengineering Solutions for Manufacturing Challenges in CAR T Cells. *Biotechnol. J.* **13,** 1–10 (2018).
3. Serra, M., Brito, C., Correia, C. & Alves, P. M. Process engineering of human pluripotent stem cells for clinical application. *Trends Biotechnol.* **30,** 350–359 (2012).
4. Rowley, J., Abraham, E., Campbell, A., Brandwein, H. & Oh, S. Meeting lot-size

challenges of manufacturing adherent cells for therapy. *Bioprocess Int.* **10,** 16–22 (2012).

5. Dalby, M. J., García, A. J. & Salmeron-Sanchez, M. Receptor control in mesenchymal stem cell engineering. *Nat. Rev. Mater.* **3,** (2018).

6. Van Winkle, A. P., Gates, I. D. & Kallos, M. S. Mass transfer limitations in embryoid bodies during human embryonic stem cell differentiation. *Cells Tissues Organs* **196,** 34–47 (2012).

7. Wu, J., Rostami, M. R., Cadavid Olaya, D. P. & Tzanakakis, E. S. Oxygen transport and stem cell aggregation in stirred-suspension bioreactor cultures. *PLoS One* **9,** 1–12 (2014).

8. Kinney, M. A., Hookway, T. A., Wang, Y. & McDevitt, T. C. Engineering three-dimensional stem cell morphogenesis for the development of tissue models and scalable regenerative therapeutics. *Ann. Biomed. Eng.* **42,** 352–367 (2014).

CHAPTER 2. STEM CELL BIOMANUFACTURING: PROGRESS AND CHALLENGES

Elements of this chapter have been published as:

Angela W. Xie and William L. Murphy (2019). Engineered biomaterials to mitigate growth factor cost in cell biomanufacturing. *Current Opinion in Biomedical Engineering*.
doi: 10.1016/j.cobme.2018.12.004

2.1 CURRENT PROGRESS AND CHALLENGES IN STEM CELL BIOMANUFACTURING

Stem cells are defined by two minimal criteria: i) the ability to self-renew to produce undifferentiated clones of themselves and ii) the capacity to differentiate into one or more specialized cell types. These features of stem cells have led them to become transformative tools in diverse areas spanning basic research, drug discovery, and regenerative medicine. Since the early successes in transplanting minimally manipulated hematopoietic stem cells from bone marrow to treat patients suffering from leukemia and other hematologic malignancies[1], innovations in techniques and technologies to isolate, grow, and maintain stem cells have opened the door for researchers to propagate these cells *in vitro*, induce and purify populations of desired phenotype or potency, and introduce targeted enhancements to cells of interest. Today, even as advances in basic stem cell science continue to be made in the laboratory, increasing focus is being placed on overcoming the barriers to widespread clinical translation of these transformative stem cell technologies and therapies. Among the major challenges faced by stem cell scientists and cell

therapy manufacturers today is generating cells that are clinically effective ("potent") through bioprocesses that are robust, reproducible, scalable, and economical[2].

Advancements in cell culture technologies and an increasingly detailed understanding of relevant developmental signaling pathways have enabled the *in vitro* generation of diverse stem cell-derived therapeutic cell types spanning ectoderm (e.g., neurons), mesoderm (cardiomyocytes), and endoderm (hepatocytes) lineages[3]. However, for the purposes of clinical translation, the current estimated cell doses required for long-term therapeutic effect are significant, and expansion of sufficient numbers of functionally "potent" cells presents a major bottleneck in cell therapy. For example, an estimated 10^9-10^{10} stem cell-derived cardiomyocytes[1] or hepatocytes[5] are needed to treat a single patient for myocardial infarction (MI) or liver failure, respectively, while MSCs have typically been delivered in clinical trials at doses of 1-2 x 10^6 cells/kg in adult patients[6]. Potential reasons for these elevated cell dose requirements include poor survival and local engraftment in the injury site, insufficient "potency" of the transplanted cell type *in vivo*, the need to replace massive loss of the cell type of interest in certain indications (e.g., cardiomyocytes after MI), or any combination of these factors[4,7–10]. Given the large patient populations for many proposed therapeutic applications of stem cells (for example, 7.9 million patients with MI[11] and 4.9 million with liver failure[12] in the U.S. alone), there is a pressing need to advance biomanufacturing capabilities to clinically and commercially meaningful scales while doing so at a price that healthcare payers can afford.

New technologies and approaches to advance cell therapy biomanufacturing may focus on i) Directly reducing cost-of-goods in the cell manufacturing process (Section 2.3), ii) Improving the yield and consistency of stem cell expansion (Section 2.4), iii) Generating cells with improved therapeutic "potency" to lower the effective cell dose required for clinical benefit, and iv)

Delivering cells in ways that improve their survival and sustain their function *in vivo*. At the nexus of these goals lies the central requirement that biomanufacturing strategies ensure control over the quality attributes of cells and result in therapies that are safe, clinically efficacious, and reproducible. Biomaterials approaches offer potential solutions that can simultaneously meet these criteria while addressing current bottlenecks in stem cell biomanufacturing, particularly as advances in engineered natural and synthetic materials can now be leveraged to define the *in vitro* cell microenvironment and control cell state with unprecedented precision[13]. In the following sections, we first summarize the environmental inputs that instruct stem cell fate and then discuss the design of biomaterial-based approaches to modify or control the stem cell microenvironment *in vitro*.

2.2 ENVIRONMENTAL FACTORS CONTROLLING STEM CELL FATE AND FUNCTION

The fate and function of stem cells *in vivo* are governed by a multitude of microenvironmental factors including soluble signals, extracellular matrices, and coordinated cell-cell interactions that comprise a biochemical and biophysical stem cell niche[14] (Fig. 2.1). Soluble cues such as growth factors, hormones, and cytokines are provided from exogenous sources or produced endogenously to regulate stem cell behavior through signal transduction pathways that are typically initiated by binding of the soluble ligand to cell-surface or nuclear receptors. These pathways, in turn, affect stem cell decisions including self-renewal, differentiation, proliferation, quiescence, and apoptosis. The ECM, which comprises structural proteins and carbohydrates secreted into the extracellular space, can also bind and control the delivery of these soluble cues to enable precise spatiotemporal regulation of stem cell fate[15].

Additionally, stem cells can directly interact with ECM glycoproteins and proteoglycans, largely through specific transmembrane receptors such as integrins, to receive and interpret information about the insoluble biochemical and mechanical characteristics of their surroundings[16]. Cell-matrix adhesion-mediated chemical signals are primarily sensed via cell type-specific expression of an ensemble of different integrin subtypes, where binding affinity for various ECM motifs is dictated by the integrin alpha and beta subunit dimer pairs[17]. For example, expression of $\alpha_6\beta_1$ and $\alpha_v\beta_5$ integrins in human embryonic stem cells facilitates their attachment and self-renewal on purified laminin[18] and vitronectin[19], respectively. In addition to recognition of specific motifs presented by protein and non-protein components of the ECM, integrins also comprise part of a bi-directional mechanosensing apparatus featuring components that link the ECM to the actin cytoskeleton[16]. This apparatus enables stem cells to use intracellular contractile forces generated by the cytoskeleton to actively probe their surroundings, thus transducing morphological features such as shape[20,21] and spreading as well as features of the external environment (ECM ligand density[22,23], nanotopography[24,25], substrate stiffness[26]) into phenotypic changes or stem cell fate decisions. Similarly, cadherins and other molecules involved in cell-cell interactions not only serve as physical connections between individual cells but are also linked to major signaling networks by way of proteins recruited to adherens junctions, which in turn can modulate cytoskeletal contractility[27,28] for mechanosensing or serve as components of soluble factor-driven pathways such as Wnt[29,30]. Finally, acellular aspects of the microenvironment, such as pH and oxygen tension, can influence stem cell fate by regulating metabolism and stress-response pathways to affect cell survival, senescence, proliferation, and differentiation (reviewed in [31–33]).

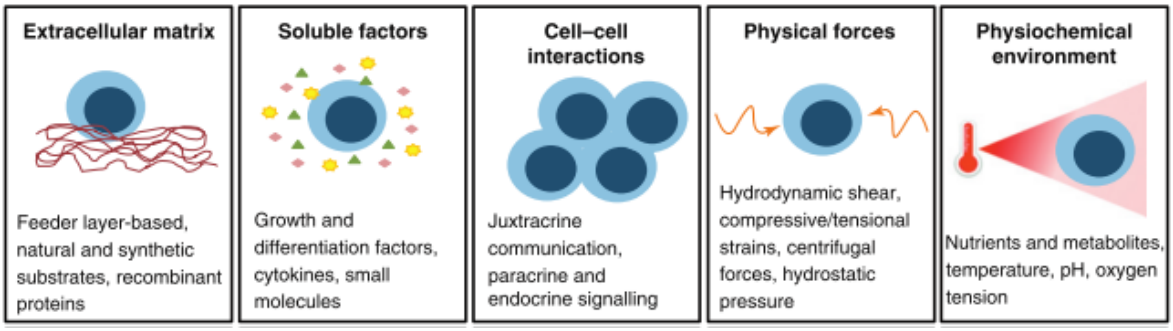

Figure 2.1 Environmental factors that influence stem cell fate. Stem cells integrate a multitude of soluble and insoluble cues to make decisions as to whether to self-renew, differentiate, proliferate, quiesce/senesce, and apoptose. [Adapted from Serra et al.[5]]

Based on the multitude of soluble and insoluble cues that direct stem cell behavior and fate, biomaterial technologies that can control biochemical and biophysical aspects of the *in vitro* stem cell microenvironment can serve as powerful tools during bioprocess development and stem cell manufacturing. Many general reviews exist on the topic of engineered biomaterials as well-defined systems for studying fundamental cell behaviors *in vitro* or for guiding tissue regeneration *in vivo*[14,34–36]. In the following sections, we focus primarily on the application of synthetic biomaterials as ancillary materials in the production of stem cell therapeutics. Special attention is given to biomaterial-based strategies for soluble growth factor regulation in the stem cell microenvironment and three-dimensional cell aggregate-based approaches that converge with existing paradigms in scalable biomanufacturing, such as expansion in suspension bioreactors.

2.3 ENGINEERED BIOMATERIALS TO MITIGATE GROWTH FACTOR COST IN STEM CELL BIOMANUFACTURING

Protocols to expand and differentiate stem cells into their therapeutically relevant derivatives require prolonged culture and often rely on administration of recombinant proteins such as growth factors (GFs) and cytokines in an effort to recapitulate developmental signaling

pathways that govern stem cell behavior *in vivo*[37–39]. GFs are major regulators of cell behavior, and their interactions with cognate cell-surface receptors initiate signal transduction processes that guide cell survival, proliferation, lineage commitment, and function. Media containing recombinant GFs constitute a primary cost driver in stem cell biomanufacturing, as GFs are expensive to produce and have limited stability in cell culture[2,40]. Cost-effective scale-up of cell biomanufacturing is a prerequisite to commercializing cell therapies[40], so strategies that reduce GF usage are of particular importance.

GF signaling can now be influenced by a variety of tools, which can be deployed to aid in cost-effective scale-up of cell biomanufacturing. Bioinspired materials, in particular, have the potential to reduce GF usage in stem cell biomanufacturing. Often these materials take inspiration from the native extracellular matrix (ECM), the collection of structural proteins, proteoglycans (PGs), glycosaminoglycans (GAGs), and biominerals that regulate multiple facets of GF signaling *in vivo*. In particular, in addition to supporting cell adhesion and tissue structure, the ECM serves to sequester and release GFs, preserve GF activity, and spatiotemporally control GF presentation to cells[15,41]. While GF-regulating biomaterials have historically been applied toward *in vitro* mechanistic studies or as therapeutic delivery vehicles[42,43], their potential utility as ancillary materials to enable cost-effective cell therapy biomanufacturing has received comparatively little attention. This portion of the review highlights recent development of biomaterials for cell therapy biomanufacturing, with a specific emphasis on synthetic biomaterials and associated strategies to achieve efficient GF usage in cell culture. We first address biomaterials-based strategies to potentiate the biological effects of exogenous (supplemented) GFs in culture. We then describe ways in which biomaterials can be engineered to activate or augment endogenous GF signaling. The intent of this section of the review is to provide an overview of exciting recent developments

in biomaterial-based GF regulation that have the potential to address challenges in the biomanufacturing of stem cell therapies.

2.3.1 Biomaterials to potentiate exogenous GF signaling

GFs *in vivo* are highly regulated by the ECM, which can present GFs to cells at low dose and with spatiotemporal precision. In contrast, supplementation of GFs in conventional stem cell culture results in their homogeneous dispersion throughout the cell culture media volume. Thus, soluble GFs are added at supraphysiological doses, as only a fraction of the administered GF is present in close enough proximity to interact with cell-surface GF receptors (GFRs) (Fig. 2.2). Biomaterials can be designed to mimic ECM functions by localizing delivery of exogenous GFs, and by controlling the mode and spatial distribution of GF presentation. The following subsections highlight examples in which GF-regulating biomaterials induced comparable cellular responses at lower GF doses compared to conventional GF supplementation. These biomaterials strategies offer potential to improve the efficiency of GF utilization in stem cell biomanufacturing.

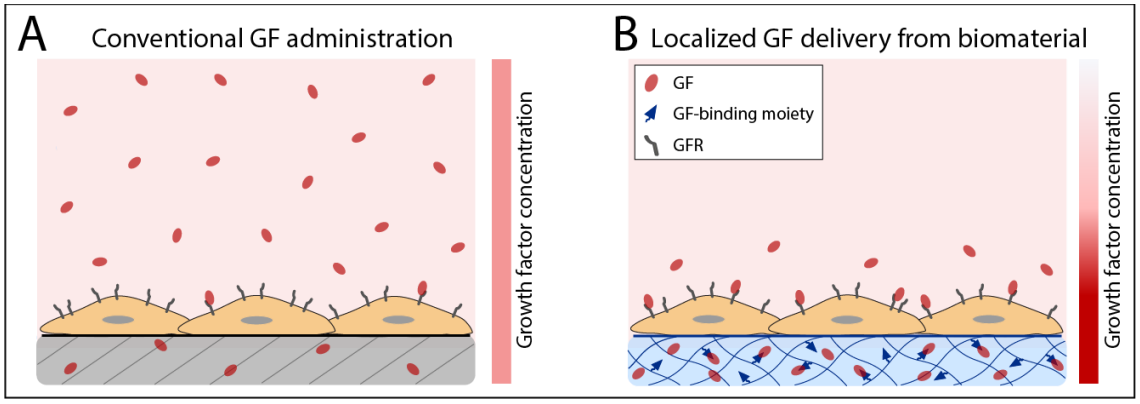

Figure 2.2. Spatial distribution of GFs in conventional cell culture vs. localized GF delivery from biomaterials. (A) Conventional GF administration leads to homogeneous GF distribution throughout the media, with a large fraction of the GF that is not accessible to GFRs due to slow diffusion from the bulk media to the cell surface. (B) Biomaterials can locally deliver GFs and/or present GF-binding moieties that increase effective GF concentrations in proximity to GFRs.

Local sustained delivery of exogenous GFs

Ideally, biomaterials for local delivery of GFs should induce the desired biological effect at physiologically relevant doses, and with controlled release kinetics over prolonged durations. Exogenous GF delivery from biomaterials has been achieved by two main strategies: by physical entrapment of GFs within porous and/or degradable materials, or by affinity-based GF binding and release from materials. In either strategy, localization of the GF signal can be accomplished by i) formulating the GF-loaded material into "reservoirs" to be placed in proximity to the cell surface; or ii) modifying the material (e.g., with cell-adhesive peptides such as Arg-Gly-Asp [RGD]) to allow cell attachment to - or encapsulation within - the GF-releasing material (Fig. 2.3). Typical materials used for physical entrapment of GFs include synthetic polymers such as thermoplastics (e.g., poly(α-hydroxy acids), poly(orthoesters)) and hydrogels[44]; GF release in these systems is achieved via a combination of material degradation and GF transport through the material. In contrast, affinity-based GF binding and delivery relies on electrostatic interactions, hydrophobic interactions, hydrogen bonding, and van der Waals forces between the GFs of interest and chemical functionalities inherent to or introduced into the biomaterial.

Several studies have shown advantages of biomaterials for local sustained delivery in cell culture. For example, Lotz et al. demonstrated that levels of basic fibroblast growth factor (bFGF) fluctuated dramatically over the course of 24 hours between media exchanges in conventional human pluripotent stem cell (hPSC) culture, whereas delivery of bFGF from poly(lactic-co-glycolic acid) microspheres in hPSC culture achieved sustained levels of bFGF that mitigated spontaneous differentiation and reduced the frequency of media changes needed to maintain hPSCs[45]. Similarly, controlled release of dextrin-conjugated GFs led to prolonged *in vitro*

proliferation of neural stem cells in both monolayer and neurosphere cultures, compared to unbound epidermal growth factor (EGF)/bFGF controls[46].

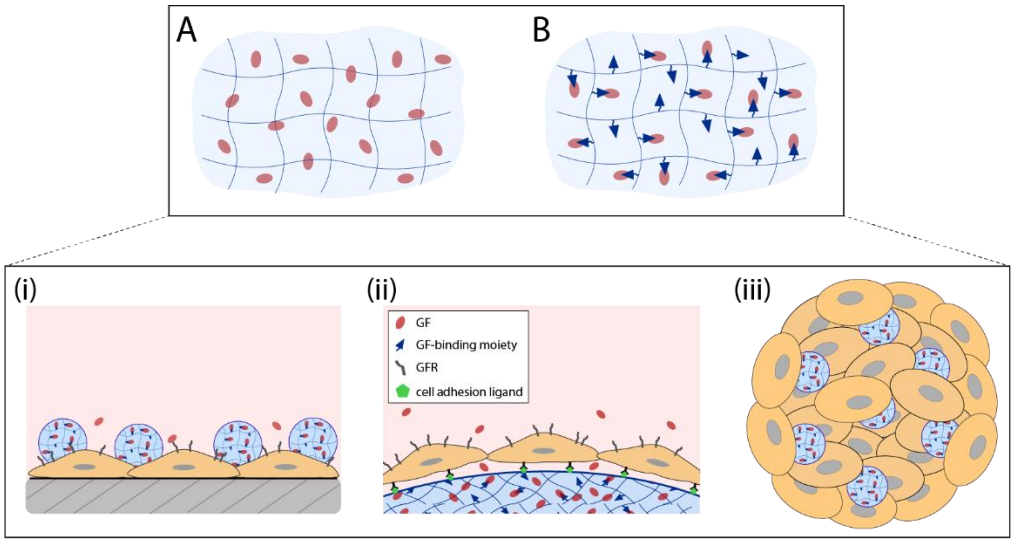

Figure 2.3 Biomaterial formats for localized GF delivery in 2D and 3D cell culture. GFs can be (A) physically entrapped within porous biomaterials or (B) loaded into biomaterials modified with GF-binding moieties. To achieve local GF delivery, these biomaterials can be (i) formulated into micro- or nano-scale carriers and physically localized in proximity to cells, (ii) modified with adhesion ligands to promote cell attachment near GF depots, or (iii) incorporated into 3D cell aggregates.

Biomaterials that release GFs can also be incorporated into three-dimensional (3D) cell culture formats, which may be particularly enabling for large-scale cell production in suspension bioreactors. For example, sustained delivery of bone morphogenetic protein-4 (BMP-4) from gelatin microparticles incorporated into embryoid bodies (EBs) generated Brachyury+ mesoderm at comparable efficiencies to soluble BMP-4 administration, despite using 12-fold lower BMP-4 dose[47]. In another example, Heidariyan et al. incorporated polymeric microparticles releasing hepatocyte growth factor (HGF) and FGF-4 into hPSC aggregates and reported similar differentiation efficiency toward albumin-expressing hepatocytes while using only 10% of the total GF when compared to soluble GF administration. This reduction in GF need was attributed to the

ability of embedded microparticles to overcome diffusion barriers that typically limit soluble GF penetration into cell aggregates[48]. Thus, strategies for controlled GF delivery improved the efficiency of GF-dependent processes in cell biomanufacturing, likely by enabling localized GF administration, reducing fluctuations in GF levels during culture, and addressing diffusion limitations to soluble GF delivery in 3D culture. While the prior efforts in this area are promising, future studies are needed to understand the detailed relationships between GF signaling kinetics and the emergence of desired cell phenotypes, and to build more sophisticated strategies for controlled release of multiple GF signals.

Controlling GF presentation

In nature, many GFs in the native ECM are presented to cells in both soluble and matrix-bound forms that possess distinct signaling functions[49,50]. Biomaterials inspired by this concept can control GF presentation (e.g., soluble vs. matrix-bound presentation, multivalency) to instruct specific biological responses while lowering the threshold of GF dose required in cell culture. Matrix-bound GFs can be mimicked by covalently immobilizing ("tethering") GFs to synthetic biomaterials via aqueous bioconjugation reactions[51], enzyme-based coupling approaches[52], or via site-specific azide-alkyne cycloaddition using GFs engineered with non-canonical amino acids[53]. Compared to soluble administration, covalent immobilization can prolong or enhance GF activity to support more efficient stem cell differentiation[54], self-renewal[55], or proliferation[56]. For example, while soluble EGF induced strong but transient EGFR activation in human mesenchymal stem/stromal cells (hMSCs), EGF tethered to poly(methyl methacrylate)-graft-poly(ethylene oxide) comb polymers inhibited receptor internalization, sustained low-level EGFR activation, and enhanced hMSC osteogenic differentiation[54]. In another study, Zandstra and coworkers

immobilized leukemia inhibitory factor to poly(octadecene-maleic-anhydride) copolymer thin films and maintained mouse embryonic stem cell pluripotency for at least 2 weeks without needing to supplement cultures with soluble GF[55]. Worrallo et al. generated magnetic particles presenting immobilized granulocyte-macrophage colony-stimulating factor (iGM-CSF) to expand hematopoietic-lineage cells in a stirred tank bioreactor[56]. At specific doses, controlled via either the number of GF molecules per particle or the number of particles per media volume, iGM-CSF sustained biological activity for eight days, with a >100-fold increase in GF potency relative to soluble GM-CSF. Although the mechanisms underpinning unique cellular responses to tethered GFs remain to be fully elucidated, these studies indicated that immobilized GFs can sustain signaling without continuous GF supplementation or generate cell phenotypes otherwise inaccessible by soluble GF administration[57].

Multivalent interactions, in which multiple ligands on one entity are concurrently engaged with multiple receptors on another, are prevalent throughout biology. In GF signaling, lateral mobility in the cell membrane enables GFR multimerization that is often necessary for strong signal transduction (e.g., for FGF[58], transforming growth factor-β[59] (TGF-β), vascular endothelial growth factor[60] (VEGF)). Therefore, biomaterials that support high-density, multivalent presentation of exogenous GFs[61], GF-binding moieties, or GFR-binding moieties have potentiated signaling by promoting GFR clustering (Fig. 2.4). Toepke et al. showed that a VEGF receptor 2 (VEGFR2)-derived peptide sequence, when synthesized as a branched divalent ligand, enhanced sequestering of VEGF into polyethylene glycol (PEG) microspheres when compared to the monomeric peptide[62]. Lin et al. used a similar approach to synthesize a branched version of a FGF-mimetic peptide linked to a heparin-binding sequence, which served as a stronger agonist of FGFR1-dependent ERK1/2 phosphorylation and endothelial cell proliferation when compared to

the monomeric sequence[63]. Kiessling and coworkers used synthetic substrates presenting TGF-β receptor-binding peptides to "pre-organize" GFRs; this strategy induced epithelial-to-mesenchymal transition at subpicomolar doses of TGF-β, as increasing GFR clustering alone effectively sensitized cells to the GF[64]. Together, these studies demonstrated the importance of multivalent presentation in potentiating cell responses to GFs and highlight the capacity for biomaterials to augment GF signaling by engaging multiple sites on a cognate GFR (Fig. 2.4). Emerging strategies to recapitulate the inter-ligand spacing of natural ligand-receptor interactions[65] and identify optimal clustering of signaling molecules[66] could accelerate development of engineered biomaterials that present signaling molecules with nano-scale precision, enabling more efficient receptor activation during the production of cell therapies.

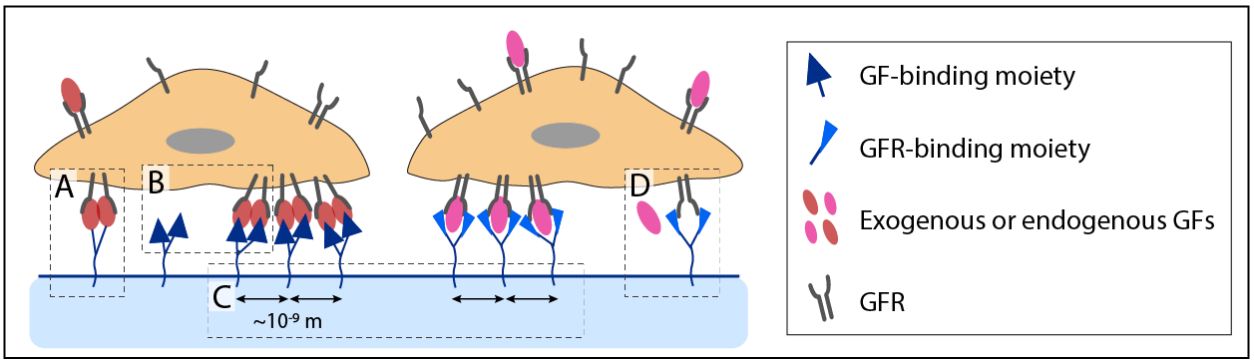

Figure 2.4 Biomaterial-mediated control over multivalent GF interactions. (A) Biomaterials can present divalent forms of (A) tethered GFs or (B) GF-binding moieties to promote GFR dimerization, and (C) biomaterials that control nanometer-scale spacing between GF-regulating moieties can additionally promote clustering of GFR complexes. (D) Biomaterials that present GFR-binding ligands can "pre-organize" GFRs or GFR complexes to potentiate GF signaling.

Improving stability of exogenous GFs in biomanufacturing

Materials strategies can also address the poor stability of many GFs in cell culture, which is a critical limiting factor for economical scale-up of stem cell biomanufacturing. The trend toward manufacturing of cGMP-grade cell products under xeno-free and chemically defined

conditions[67–70] presents particular challenges for maintaining active GFs, as many additives used to preserve GF activity in culture media (e.g., heparin) are either of xenogeneic origin[71] or are sourced from complex biological fluids such as serum, and thus pose supply chain and batch variability issues. *In vivo*, GFs are often stabilized by extracellular and cell-surface GAGs/PGs, which can protect GFs from proteolytic degradation[72], mitigate inherent molecular instability[73], and present GFs in appropriate orientations to potentiate GFR activation[74]. Binding of GFs occurs largely via interactions between the sulfate and carboxylic acid groups of heparin sulfate PGs and GAGs, and the positively charged amino acids of GFs[75].

Biomaterials can mimic natural GF-stabilizing interactions by binding GFs to oligosaccharides, peptides, or polymers modified with polyanionic functional groups such as sulfates and sulfonates. Maynard and Hubbell designed a library of >6000 sulfated tetrapeptides as potential heparin mimics, and identified a sulfated, tyrosine-rich sequence, SY(SO_3)DY(SO_3), as the strongest binder for $VEGF_{165}$[76]. Comparison of sequence identities among other candidate peptides determined that the sulfate group itself was important for VEGF binding, and also identified both the spacing between sulfated peptides and the presence of an intervening carboxylate-containing residue as important features that conferred VEGF affinity. Hendrikse et al. synthesized variants of the aforementioned tetrapeptide and showed that a more stable sulfonated variant bound and significantly enhanced the stability of TGF-β1 and BMP-4. Co-assembly of the sulfonated peptide with ureidopyrimidinone-based supramolecular polymers further extended TGF-β1 half-life and offered a stronger stabilizing effect than heparin, as measured by the response of TGF-β1-sensitive reporter cells to samples pre-incubated at 37°C[77]. Thus, biomaterials have been designed as excipients that stabilized GFs via specific non-covalent interactions.

Alternatively, inherently unstable GFs have been covalently derivatized with anionic polymeric groups to generate GF conjugates with improved *in vitro* and *in vivo* stability and sustained biological function. For example, Nguyen et al. achieved stabilization of bFGF by covalently conjugating it to a copolymer consisting of polysulfonated styrenes and methyl methacrylates bearing PEG side chains[78]. Unlike the native bFGF, bFGF-copolymer conjugates retained the capacity to stimulate fibroblast proliferation following exposure to heat, acid, or proteases. Stabilization depended on the presence of styrene sulfonate groups, as the control conjugate alone offered no significant protection of bFGF activity.

Additional biologically inspired materials have been reported to bind and stabilize GFs. A recent study used a biomimetic mineralization process to form nanostructured calcium phosphate mineral coatings capable of stabilizing bFGF against protease-mediated degradation[79]. Altering the size of nanostructural features of the mineral coatings influenced their capacity to protect bFGF and other proteins against chemical and proteolytic insult, suggesting that nano-scale features of GF-binding materials can be designed for improved GF stability during formulation, storage, and delivery. Additional work conducted by our group has directly shown the utility of bFGF stabilization by mineral coatings in reducing GF requirements for expansion of hPSCs, for which bFGF is crucial for pluripotency maintenance and proliferation. The mineral coatings stabilized bFGF against activity loss at 37°C and provided localized and sustained delivery of the active bFGF in culture, enabling >80% reduction in the amount of bFGF required for long-term hPSC expansion (unpublished). Interestingly, this approach to stabilize sensitive proteins bears similarities to the mechanisms by which biomacromolecules are preserved in fossils, and may be broadly applicable in biomanufacturing applications.

2.3.2 Biomaterials to sequester endogenous GFs, mimic GF functions, and exploit synergistic signaling pathways

Specific sequestering of endogenous GFs

Biomaterials that stabilize and/or deliver exogenous GFs provide a level of external control over "initial conditions" in culture. However, stem cells modify their microenvironment over time, including by secreting endogenous GFs that further instruct their self-renewal, proliferation, and differentiation[80–86]. For example, in response to FGF signaling, hPSCs secrete Activin that promotes pluripotency gene expression and induces FGF production in an autocrine manner[84,85,87–89]. Thus, strategies to amplify "autocatalytic" drivers of stem cell phenotype may reduce reliance on expensive recombinant GFs. An emerging class of biomaterials uses non-covalent interactions to capture, localize, and amplify the effects of endogenous cell-secreted GFs (Fig. 2.5). In this sub-section of the review, we focus on sequestering strategies based on highly specific, non-covalent interactions with GFs (e.g., via aptamer-based approaches, GFR-mimetic sequences), which may be advantageous in amplifying specific autocrine signaling programs as opposed to non-specific approaches (e.g., ECM protein-[90] or GAG-based[91,92] strategies) that sequester a variety of different GFs promiscuously and may initiate a broad range of cellular responses.

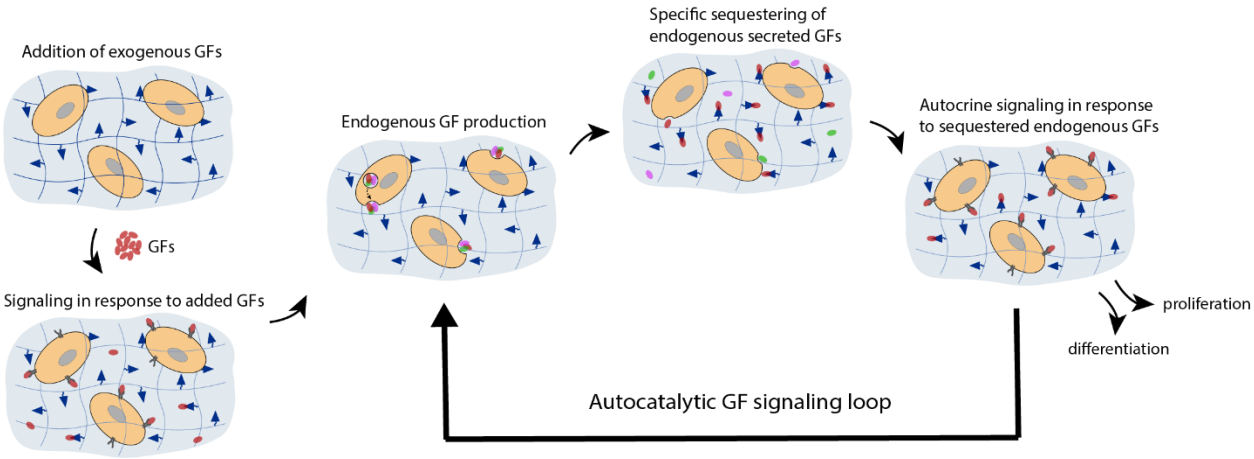

Figure 2.5 Using GF-sequestering biomaterials to harness endogenous GFs. Stem cells secrete endogenous GFs during their proliferation and differentiation. Biomaterials presenting GF-binding moieties can specifically sequester these inductive factors to initiate autocatalytic GF signaling processes that drive further proliferation or differentiation.

Recent studies highlight the potential for engineered biomaterials to sequester specific endogenous factors in biologically complex environments. Belair et al. used PEG microspheres presenting a VEGF-binding peptide sequence (VBP) derived from VEGFR2 to specifically regulate VEGF in platelet concentrates, a complex blood product obtained via platelet activation and lysis[93]. Multiplex ELISAs showed that VBP microspheres, but not blank microspheres or those presenting a scrambled version of the peptide, could specifically sequester VEGF from platelet concentrates amidst a background of several other platelet-derived factors including EGF, bFGF, and interleukin-8. In another study, Crispim et al. functionalized polycaprolactone films with a TGF-β1-binding peptide for use in tendon/ligament healing applications[94]. In addition to binding high levels of purified TGF-β1 *in vitro*, peptide-functionalized films retrieved at 7 days after subcutaneous implantation in a rat model showed enhanced sequestering of endogenous TGF-β1 and promoted robust fibroblast recruitment. Finally, Enam et al. demonstrated the ability of aptamer-based affinity ligands to sequester and concentrate fractalkine (FKN), a chemokine ligand for CX3CR1, *in vitro* and in a mouse model of excisional skin injury[95]. PEG-diacrylate hydrogels presenting a FKN-binding aptamer sequence concentrated mouse FKN by more than 60-fold compared to traditional soluble administration in cell culture, and could undergo multiple iterations of FKN sequestering and sustained release. *In vivo*, FKN-aptamer hydrogels demonstrated nearly four-fold enrichment of endogenous FKN compared to hydrogels presenting a random-sequence aptamer, and enhanced local recruitment of $CX3CR1^{hi}$ non-classical monocytes, supporting the *in vitro* finding that the sequestered FKN could be bound and released in a biologically active manner.

One can envision employing similar endogenous sequestering strategies to amplify autocrine signals produced in stem cell culture, which may reduce the exogenous GF dose needed to drive proliferation or lineage-specific differentiation. Alternatively, moieties with particularly high affinity for the target of interest can be presented on biomaterials to sequester GFs and prevent their interaction with cognate GFRs, a strategy that may remove a GF signal that is inhibitory to the desired stem cell phenotype.

Mimicking GF structure and function with synthetic materials

In parallel with strategies to regulate exogenous and endogenous GFs in cell culture, synthetic materials can be designed as GF mimetics. Progress to date in this area has focused on synthetic peptide- or nucleic acid-based GFR agonists, which can be readily engineered for enhanced stability[96] and are often more economical to produce at large scale compared to full-length GFs[97,98]. Short peptides that mimic the functions of VEGF[99–101], BMP-2[102,103], bFGF[63,104], and brain-derived neurotrophic factor[105] have been identified from fragments of native GFs[106] either by using computational or molecular docking simulations, screening of rationally designed peptide libraries, or phage display[42]. More recently, aptamers have gained interest as potential GFR agonists, as their programmable nature and high degree of 3D conformational flexibility enables GFR engagement with high affinity and specificity. Ramaswamy et al. showed that a divalent VEGF-mimetic aptamer assembly, created by linking two copies of a VEGFR2-binding aptamer via a hexaethylene glycol spacer, promoted VEGFR2 phosphorylation, endothelial nitric oxide synthase production, and HUVEC tubulogenesis comparable to that induced by soluble VEGF[107]. Other recent studies identified aptamer-based agonists that mimicked HGF[108] in stimulating HUVEC proliferation and OX40 ligand[109], a T cell co-stimulatory ligand, in promoting T cell

proliferation and interferon-γ secretion. Interestingly, for many peptide- and aptamer-based GFR agonists including those discussed here, the soluble or monomeric form of the agonist failed to strongly activate its target receptor. Thus, immobilizing GF mimetics on engineered biomaterial surfaces (e.g., peptide amphiphile nanofibers[105] or DNA scaffolds[109]) may often be necessary to achieve high-density multivalent presentation of the ligand to the target cell, and this dependency should be strongly considered in the design of novel synthetic GFR agonists.

Synergizing GF signaling with other signaling pathways

Finally, the variety of chemical and mechanical signals that cells integrate to instruct their behavior[110] offers new opportunities to engineer biomaterials with "multiplexed" activity. In particular, it may be possible to synergize GF signals with other biochemical and biophysical cues (e.g., cell-cell interactions, cell-matrix adhesion, substrate stiffness) to more efficiently derive target cell phenotypes. For example, signaling pathways associated with specific heterotypic or homotypic cell-cell interactions (e.g., Notch, cadherin, Eph/ephrin) often serve as instructive self-renewal or differentiation signals during tissue development, and may be manipulated *in vitro* by various biomaterials strategies[111]. For example, cadherin interactions were important in MSC secretion of therapeutic proteins and lineage commitment in a study that used hydrogels presenting short cadherin-mimicking peptides[112,27], as well as a study that used controlled hydrogel porosity[113] to manipulate the extent of N-cadherin interactions. Integrin receptors also have multi-faceted roles beyond simply mediating cell-matrix adhesion, including recruitment of adaptor proteins to regulate the signaling of GFRs and other receptor tyrosine kinases[114,115]. For example, Moulisova et al. developed poly(ethyl acrylate) materials that directed fibronectin organization into nano-networks in which the GF-binding and integrin-binding domains of fibronectin were

simultaneously accessible; these surfaces permitted synergy between VEGF and integrin signaling, and promoted HUVEC network formation and scaffold vascularization at reduced doses of exogenous VEGF[116]. In another example, surfaces presenting integrin-binding motifs alone versus in combination with motifs that bind cell-surface PGs shifted the balance between integrin-linked kinase/Akt and Smad2/3 signaling, and influenced hPSC decisions to self-renew or differentiate in the presence of soluble Activin[117]. Finally, cellular decision-making occurs in the context of the biophysical environment surrounding the cell, and thus biomaterial properties such as elastic modulus of the culture substrate can bias stem cell fate decisions by modifying the interpretation of soluble signals[118–121]. Further studies in these areas will aid understanding into how cross-talk between soluble and insoluble signals instructs stem cell behavior, and biomaterials-based approaches to exploit these synergies should yield more efficient systems for stem cell biomanufacturing.

While much progress has been made in using biomaterials to control the soluble growth factor microenvironment surrounding stem cells during *in vitro* propagation, increasing attention is being directed toward biomaterial strategies that offer control over the insoluble microenvironment. This aspect of the microenvironment depends in large part on the culture dimensionality (i.e., 2D surfaces vs. 3D scaffolds or scaffold-free cell aggregates), which determines the extent of cell-cell interactions, ECM deposition, and formation of oxygen and soluble factor gradients. Incidentally, beyond instructing stem cell phenotype, culture dimensionality is also a significant consideration during scale-up of cell manufacturing from a purely economical standpoint. In the following sections, we discuss the role of culture geometry in scalable stem cell biomanufacturing, summarize methods for generating cell aggregates, and introduce emerging biomaterial strategies to manipulate the cell aggregate microenvironment.

2.4 BIOMATERIALS FOR CONTROLLING THE INSOLUBLE STEM CELL MICROENVIRONMENT DURING BIOMANUFACTURING

2.4.1 Culture geometry in stem cell biomanufacturing: The advent of microcarrier- and cell aggregate-based approaches for stem cell expansion

Conventional two-dimensional (2D) adherent culture geometries (plates, dishes, T-flasks) have been a mainstay in bench-scale expansion of stem cells for basic research applications and pre-clinical studies, but the relatively low production yields of 2D platforms make them unsuitable for the scale of most clinical applications. For example, some reports estimate lot-size limitations in the realm of 10^{11} cells for existing multi-layer flask-based expansion processes, whereas suspension-based processes can achieve lot sizes several orders of magnitude higher[122–125] (Fig. 2.6). These limitations have spurred the development of stem cell culture technologies compatible with suspension bioreactors, which are better suited to mass production of cells by virtue of their more efficient utilization of physical space and raw materials (including media) and increased mass transport to accommodate higher cell densities per media volume[126,127].

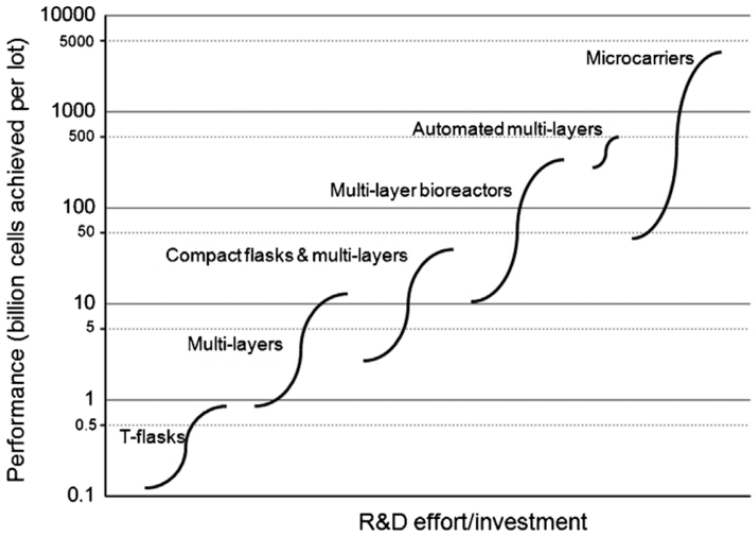

Figure 2.6 Conceptual illustration showing the evolution of cell expansion technologies for cell therapy manufacturing. The limits for each individual S-curve indicate the total number of cells achievable per lot (in billions) by the smallest and largest size of each technology. R&D effort/investment on the x-axis is a qualitative indication of the R&D effort required to transition from T-flasks to any of the respective technologies. [Figure from Simaria et al.[124]]

Historically, scalable expansion of mammalian cells in suspension bioreactors has been applied in the context of manufacturing biopharmaceuticals such as recombinant proteins and monoclonal antibodies), where the cells themselves are not part of the final product. While lessons from traditional biopharmaceutical manufacturing can inform commercial-scale production for cell therapies, tighter restrictions must be placed on the bioprocessing parameters. In particular, since stem cell biomanufacturing intends for the resulting cells to be used in the clinic as "living drugs", additional development is required with the materials used in the cell expansion process, as stem cells are notoriously sensitive to a multitude of environmental cues. Moreover, whereas common cell types used in biopharmaceutical manufacturing (e.g., Chinese hamster ovary, human embryonic kidney, murine myeloma cells) are readily grown in suspension[128,129], the limitation of anchorage-dependence for many human stem cells and their derivatives has largely prohibited the expansion of singularized cells in suspension bioreactors[5], as anchorage-dependent cells undergo anoikis in the absence of cell-ECM or cell-cell adhesion[130]. This restriction has prompted the

continued development of two main culture technologies – microcarriers and three-dimensional (3D) cell aggregates – that offer potential scalability and accommodate adhesion-dependent cell expansion in suspension culture (Fig. 2.7). Each of these technologies come with their own set of advantages and drawbacks that have bearing on their successful application to cell therapy manufacturing.

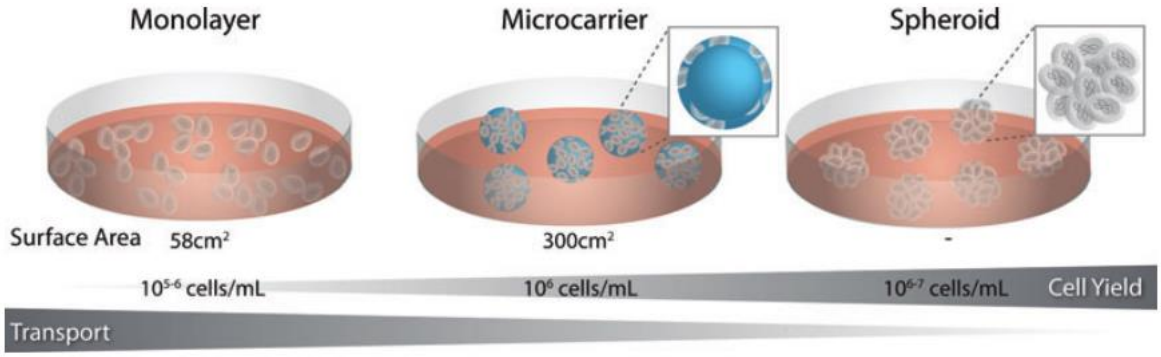

Figure 2.7 Formats for stem cell expansion. Stem cells can be cultured in monolayer or in suspension formats such as on adherent microcarriers or in 3D cell aggregates. Suspension cultures offer higher potential cell yields per volume of media and are typically preferred for large-scale cell manufacturing. Suspension cultures typically utilize various modes of convective flow to enhance transport of nutrients to all cells in the culture, but diffusion within 3D cell aggregates is often still limited, which may result in the formation of gradients of nutrients, metabolites, and oxygen throughout the aggregates. [Adapted from Kinney et al.[131]]

Microcarriers – typically spherical adherent support surfaces that present a high surface-to-volume ratio for the growth of anchorage-dependent cells – permit high expansion rates and are compatible with suspension bioreactor technology. Microcarriers have traditionally been manufactured from synthetic materials (polystyrene, glass) or natural polymers (dextran, cellulose) that can be coated with ECM proteins such as collagen or gelatin to provide additional sites for cell adhesion (reviewed in [132]). Immediate translation of these existing microcarrier materials to stem cell biomanufacturing has proven somewhat challenging based on the specific ECM cues required for stem cells to maintain/acquire a desired phenotype. For example, only a limited set of defined ECM proteins – including vitronectin[19] and laminins 511[18] and 521[133] – reliably maintain

long-term hPSC pluripotency and self-renewal whereas collagens, gelatin, and fibronectin cannot propagate hPSCs in an undifferentiated state. Alternatively, fully synthetic polymers or peptides supporting hPSC pluripotency were identified[134,135] and have been used to coat microcarriers. Cabral and coworkers showed that microcarriers coated with vitronectin or Synthemax (synthetic peptide) produced similar ~4.5-fold per passage expansion of hPSCs in 50 mL spinning flask-based stirred cultures[136]. More recently, the same group described the use of vitronectin-coated microcarriers to support 6.7-fold hPSC expansion over 6 days in a 500 mL vertical-wheel bioreactor.[137] Thus, materials that optimally propagate stem cells and their therapeutic derivatives are typically screened and identified in conventional 2D cultures but appear readily translatable to microcarriers in suspension bioreactors with some optimization of bioprocess parameters.

Despite the progress in using microcarriers for scalable stem cell expansion, enabling technologies in this area are still emerging. For example, existing microcarrier materials and coatings have limited versatility, as typically only the concentration and molecular weight of surface adhesion ligands can be tailored while other material properties such as microcarrier elastic modulus ("stiffness") are fixed. Approaches for forming tailorable hydrogel coatings on existing microcarrier materials[138] offer the potential for customizable microcarriers to explore the broader bioprocessing parameter space offered by synthetic cell culture substrates, which may identify substrates that improve the efficiency of stem cell propagation in scalable culture formats. Further technological advances will be needed to address remain lingering challenges with microcarriers, including uneven, low-efficiency seeding and long seeding times[136], agglomeration of carriers during culture leading to undesired differentiation, and difficulties in cell removal from the surface during passaging and harvest[139,140].

2.4.2 Historical approaches to generate 3D stem cell aggregates

3D scaffold-free aggregates are another well-established format for scalable stem cell culture in suspension culture (Fig. 2.8). In the context of cell expansion, this format is most suitable for cell types that are not subject to contact inhibition of cell growth – such as pluripotent stem cells – although the 3D aggregate microenvironment can also provide a favorable environment for encouraging differentiation and maturation of many cell types. Similar to microcarriers, cell aggregates offer a high surface area to volume ratio and are compatible with bioreactor technology[139]. However, cell aggregates obviate the need for a specialized growth surface, since requirements for anchorage dependence are fulfilled by the establishment of cell-cell adhesions. For example, it is now well-established that hPSCs can be expanded as scaffold-free aggregates under xeno-free and serum-free conditions in the absence of ECM supplementation[141,142]. The elimination of extraneous extracellular materials may be advantageous in cell therapy biomanufacturing; as previously mentioned, cell detachment from microcarrier surfaces during passaging/harvest and subsequent elimination of microcarrier material/particulates from the final cell product are not trivial steps.

Early methods for generating stem cell aggregates most commonly involved enzymatic detachment or mechanical scraping of adherent cells from their underlying culture substrates followed by transfer to low-adhesion surfaces, whereupon individual cells or cell clumps would spontaneously form cell-cell adhesions through random interactions with neighboring cells[143]. When Zandstra and coworkers examined this approach in the context of hPSCs, they observed the formation of EBs that were highly heterogenous in size and shape, leading to inconsistent organization of differentiated structures within the EBs[144]. This degree of intra- and inter-experimental variability hindered the use of EBs as a model system for studying embryonic

development and posed obvious challenges to the application of aggregates as a format for scalable stem cell expansion. Advancements in this area have used microcontact printing of ECM proteins to constrain cell adhesion to 2D micropatterned "islands" prior to mechanical or enzymatic detachment; this modification affords greater homogeneity in the sizes of aggregates formed[145].

Alternatively, hanging drop culture is a standard method for forming homogeneous aggregates with controllable size. With this approach, defined numbers of cells constrained within media droplets are suspended from the lid of a Petri dish and subjected to gravity-driven aggregation. The technique for forming hanging drops is conceptually simple and widely accessible (requiring no specialized equipment or materials), which has led to the persistence of this approach as a mainstay in many biology labs[146]. However, forming hanging drop cultures is impractically labor-intensive and not amenable to the scale required for implementation in cell-based therapies. To address the issue of scalability, several groups have employed photolithography or other microfabrication techniques to manufacture microwell arrays to serve as platforms for high-throughput generation of aggregates. Microwells can be modified with cell adhesion proteins/peptides[147] or fabricated from cell-repellent biomaterials[144,148,149], and aggregation in these systems is often encouraged by centrifugation of cells to promote immediate cell-cell interactions within the geometric constraints of the arrayed microwells. This paradigm is exemplified by AggreWells™, a commercialized product that has been applied toward scalable production of aggregates of hPSCs[150,151], MSCs[152,153], stem cell-derived hepatocytes[154,155], and other cell types.[156] While AggreWells™ and other similar platforms generate thousands of cell aggregates with narrow size distributions, functional equivalence in terms of cell expansion and final product potency across different methods of aggregation has not been well studied.

Finally, with increasing efforts to move stem cell aggregates toward scalable expansion in suspension bioreactors, many groups have investigated the use of hydrodynamic systems to encourage cell aggregation in various culture vessels ranging from bench-scale orbital shakers to industrial-scale stirred tank bioreactors. To date, most strategies for bioreactor-based aggregation rely on inoculating singularized cells directly into suspension. For hPSCs, this strategy has often resulted in poor initial survival (< 50%, even in the presence of ROCK inhibitor)[157], with further reduced viability likely due to agitation- or bubbling-related shear stresses in these systems[158]. Formation of aggregates of heterogeneous size and agglomeration of aggregates remain additional long-standing issues that are being addressed by emerging engineering approaches[140].

It is worth noting that most mainstream methods to generate cell aggregates are modifications of a scheme in which aggregation is driven by spontaneous cell-cell interactions. Bioprocess alterations can be introduced to change the likelihood of cell-cell contact (e.g., varying inoculation density, stir/spin speeds), but ultimately these methods offer minimal control over spatial and temporal aspects of cell aggregation or the resulting aggregate microenvironment. Thus, there is ample opportunity to develop biomaterial technologies that can be used to exert tighter control over the 3D microenvironment during scalable expansion of stem cell aggregates. We conclude with a discussion of emerging methods to engineer the cell aggregate microenvironment.

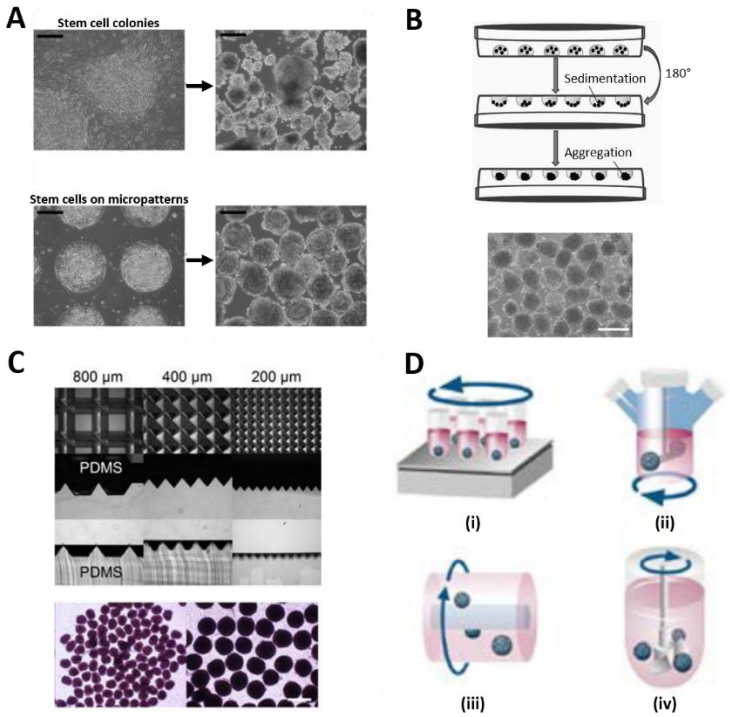

Figure 2.8 Common methodologies for cell aggregation. Historical methods for generating cell aggregates via static approaches include: (A) mechanical scraping or enzymatic dissociation of stem cells cultured as colonies or on protein micropatterns, followed by suspension culture, (B) formation of hanging drops, and (C) forced aggregation via centrifugation into high-throughput microwells. (D) Alternatively, systems employing hydrodynamic forces have been used to encourage aggregation through random collisions of cells in suspension. These formats include i) rotary orbital cultures, ii) spinner flasks, iii) rotating wall vessels, and iv) stirred tank reactors. [Images from Bauwens et al.[145], Penfornis et al.[159], Bai et al.[160], Ungrin et al.[144], Egger et al.[161]]

2.4.3 Approaches to engineer the cell aggregate microenvironment

The 3D microenvironment experienced by stem cells in cell aggregates is unquestionably dissimilar from the ones they experience in culture on 2D substrates or on microcarriers (Fig. 2.9). Distinct changes in diffusive mass transport, ECM deposition, and alterations in multicellular mechanics can dictate the phenotype and function of cell aggregates during a biomanufacturing process[139,140,162]. Thus, engineering strategies to manipulate biochemical and biophysical features of the 3D aggregate microenvironment may have immense utility for designing bioprocesses that can preserve or induce desired stem cell traits during scalable *in vitro* expansion. Many of the

technologies referenced here have yet to be translated to large-scale culture, but the initial proof-of-concept studies provide concrete examples of ways in which biomaterials can improve on conventional cell bioprocessing approaches regarding the formation, maintenance, and differentiation of 3D stem cell aggregates.

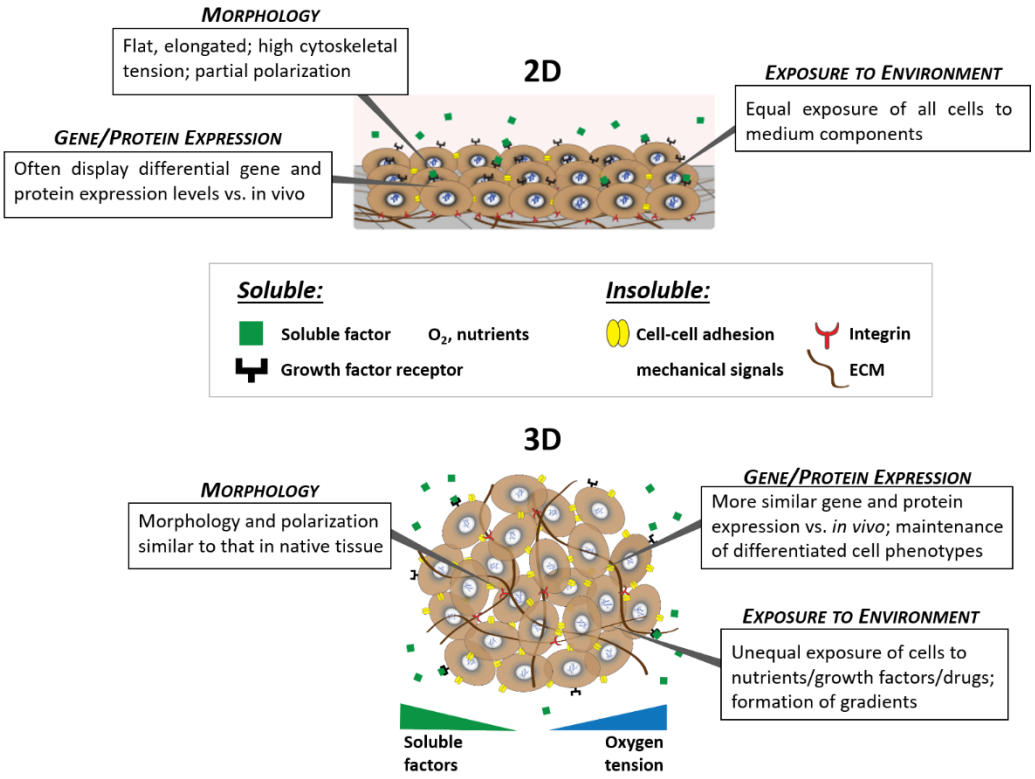

Figure 2.9 Features of the microenvironment in 2D and 3D cell culture. Cells in monolayer (2D) or cell aggregate (3D) culture experience differences in soluble factors, oxygen/nutrients, extent of cell-cell adhesions, interaction with the ECM, and passive and active mechanical signals. These differences contribute to their altered morphology, gene/protein expression, and response to environmental factors in 3D vs. 2D. [Adapted from Khalil, Xie, and Murphy[163]]

While gradients of cytokines/growth factors, oxygen, nutrients, and metabolites within 3D aggregates can be useful for modeling features of the *in vivo* context[164,165], in cell biomanufacturing these gradients are typically associated with undesirable phenotypic heterogeneities. These include spontaneous differentiation[140] or low purity of target differentiated cell types due to poor diffusion

of differentiation factors from the bulk media to the interior of stem cell aggregates[166]. These unfavorable outcomes have prompted the development of strategies to minimize heterogeneity in aggregates. One approach is simply to prevent expansion of aggregates to sizes at which mass transport into the interior becomes an issue[122,139,167]; however, this may not be practical for achieving efficient stem cell expansion because it necessitates more frequent passaging steps that are laborious and result in loss of cell yields[123,157,168,169]. As previously discussed (Section 2.3.1), various biomaterials (e.g., alginate, heparin, PLGA) can be used to bind/encapsulate signaling factors required for differentiation, formulated as microparticle carriers, and incorporated into aggregates formed in dynamic suspension culture or via forced aggregation[47]. Via this approach, delivery of proteins or small molecules from the interior of a cell aggregate can overcome limitations associated with their conventional administration in the bulk media, resulting in greater purity of a target cell type.

It is worth noting that even "blank" or "unloaded" biomaterials can instruct aggregate structure and stem cell phenotype in 3D. As an example, biomaterials with an intrinsic affinity for growth factors can sequester pro-differentiation molecules within aggregates to promote stemness. Rinker et al. incorporated heparin microparticles within spheroids of ATDC5 cells that routinely undergo endochondral ossification, and showed that high doses of heparin microparticles inhibited chondrocytic differentiation as seen by suppressed production of collagen II, aggrecan, and sulfated GAGs[170]. This effect was dependent on heparin sequestering of insulin-like growth factor binding proteins (IGFBPs), as chemical inhibition of IGFBPs recapitulated the effects of heparin microparticles whereas spheroids containing PEG microparticles (a low protein-binding control) displayed similar levels of differentiation compared to controls without microparticles. In addition to the sequestering capabilities of certain materials, material degradability is another property can

provide instructive signals to stem cells[36]. Degradation byproducts of PLGA and other polyesters alter the metabolism of multipotent neural progenitors[171], while release of calcium and other ions from inorganic minerals influences the differentiation of MSCs and their derivatives[172–174]. Recently, Nguyen et al. showed that incorporation of matrix metalloproteinase (MMP)-degradable microparticles within EBs stimulated increases in MMP activity, ECM remodeling, and gene expression profiles reminiscent of an epithelial-to-mesenchymal transition[175]. This example of using biomaterials to induce MMP activity may be particularly enabling for instructing ECM remodeling processes associated with stem cell differentiation, or for cell-activated degradation of endogenous ECMs that limit diffusion of exogenous growth factors and nutrients into cell aggregates[176].

Beyond the active introduction of materials to alter soluble signaling within aggregates, the kinetics of aggregation can be modulated to instruct the development of aggregate structural characteristics, thereby altering the biophysical microenvironment (e.g., cell packing density, ECM composition) created within aggregates[177,178] and phenotype of the cells within. For example, hPSC and MSC aggregates undergo dynamic transcriptomic changes that are temporally associated with distinct stages of aggregation. These changes involve not only cell adhesion-related genes such as E-cadherin[179,180] and N-cadherin,[181,182] but also genes associated with developmental[183] and cytokine[184] signaling that affect stem cell differentiation and therapeutic potency.

Published strategies for tailoring cell aggregation kinetics rely on modulating hydrodynamic forces, magnetically manipulating individual cells, and engineering cell surface adhesion molecules. Kinney et al. employed different rotary speeds to vary aggregation kinetics of embryonic stem cells; slow speeds encouraged accelerated aggregation kinetics that promoted

early Wnt/β-catenin signaling and cardiomyogenic differentiation of EBs[183]. However, the use of differential hydrodynamic forces with this approach introduces several confounding factors, as slower rotary speeds generated considerably larger aggregates than fast rotary speeds and fluid shear forces alone are known to affect stem cell viability and differentiation[185]. Modification of the cell surface via genetic approaches[186] or bioconjugation chemistries[187–189] offer control over aggregation without the need for mechanical or hydrodynamic forces. A concern associated with this approach is the possibility that the introduced modifications could compromise critical signaling pathways that depend on transmembrane binding events such as cadherin-cadherin or integrin-ECM interactions. Magnetic manipulation of individual cells could avoid these concerns while supporting precise spatiotemporal control over the aggregation process[190], but the cellular internalization of magnetic nanomaterials required for this approach may add complexity to the final cell product. These drawbacks should be considered in the development of new biomaterials capable of controlling spatiotemporal cell aggregation processes.

Just as mechanical signals can cue the self-renewal or differentiation of stem cells in 2D monolayer culture, recent engineering approaches have demonstrated that the microenvironment within 3D aggregates can also be biomechanically regulated. For example, Geuss et al. developed a method for using magnetic twisting cytometry in combination with RGD-functionalized paramagnetic beads incorporated homogeneously within EBs to mechanically stimulate the EBs toward cardiogenic differentiation[191]. In the presence of the differentiation factor BMP-4, short-term exposure to magnetically mediated strain activated protein Kinase A and ERK1/2 pathways and led to a higher percentage of sarcomeric α-actin-expressing cells compared to BMP-4 treatment alone. Interestingly, McDevitt and coworkers published a contemporaneous study showing that dynamic remodeling of the EB microenvironment and mesenchymal morphogenesis

in BMP-4 treated EBs correlated with differences in EB bulk mechanical properties[192]. Inhibitors of cytoskeletal contractility induced similar changes in EB mechanics and mesenchymal morphogenesis, and analysis of EB biomechanics was predictive of microtissue phenotypic profiles. Together, these reports suggest that the differentiated phenotypes induced by exogenous soluble factors may be due in part to alterations in multicellular mechanics that create a bi-directional signaling loop between the soluble and insoluble 3D microenvironment. Multicellular mechanics arise from a combination of cytoskeletal contractility, cell-cell adhesions, and ECM deposition[162,193], so engineering strategies that manipulate these elements in a spatially and temporally controlled fashion may reveal opportunities for scalable stem cell differentiation with minimal reliance on exogenous soluble factors.

2.5 PERSPECTIVE ON THE FUTURE OF ENGINEERED BIOMATERIALS IN STEM CELL BIOMANUFACTURING

Engineered biomaterials offer promise as tools to overcome the current barriers to scalable and cost-effective biomanufacturing of cell therapies. In particular, GF-regulating biomaterials may offer a more efficient means to deliver exogenous GFs or exploit endogenously secreted GFs to achieve elevated local concentrations relative to the bulk media. Such strategies have already shown promise in greatly reducing or eliminating expensive recombinant GFs during expansion and differentiation of therapeutic cell types in 2D and 3D culture. Using biomaterials to separate the mode of delivery for GFs vs. nutrients in basal media (amino acids, vitamins, lipids, etc.) should allow for more sophisticated bioprocessing feed strategies that ensure sufficient nutrient supply and waste removal while enabling independent control over GF signaling in cell culture.

Finally, the continuing adaptation of engineered biomaterials[138] to more universal formats for cell manufacturing *en masse* (i.e., microcarriers or cell aggregates in suspension bioreactors) should help advance current bioprocesses. In particular, established bioprocess engineering principles may be used to inform the design of new technologies for controlling the 3D cell aggregate microenvironment, which in turn should improve the reproducibility and efficiency of deriving and expanding target cell types in scalable suspension culture. The integration of knowledge from cell biology, chemistry, bioprocess engineering, and materials science should provide a framework for applying biomaterial technologies toward the robust, efficient, and economical production of stem cell therapies.

2.6 REFERENCES

1. Thomas, E. D. *et al.* Marrow transplantation for acute nonlymphoblastic leukemia in first remission. *N. Engl. J. Med.* **301,** 597–599 (1979).
2. Carmen, J., Brindley, D. A., Davie, N. L. & Smith, D. in *Stem Cells in Regenerative Medicine* 49–68 (John Wiley & Sons, Ltd, 2016). doi:10.1002/9781118846193.ch4
3. Irion, S., Nostro, M. C., Kattman, S. J. & Keller, G. M. Directed Differentiation of Pluripotent Stem Cells: From Developmental Biology to Therapeutic Applications. *Cold Spring Harb. Symp. Quant. Biol.* **73,** 101–110 (2008).
4. Laflamme, M. A. & Murry, C. E. Regenerating the heart. *Nat. Biotechnol.* **23,** 845–856 (2005).
5. Serra, M., Brito, C., Correia, C. & Alves, P. M. Process engineering of human pluripotent stem cells for clinical application. *Trends Biotechnol.* **30,** 350–359 (2012).
6. Galipeau, J. & Sensébé, L. Mesenchymal Stromal Cells: Clinical Challenges and Therapeutic Opportunities. *Cell Stem Cell* **22,** 824–833 (2018).
7. Don, C. W. & Murry, C. E. Improving survival and efficacy of pluripotent stem cell-derived cardiac grafts. *J. Cell. Mol. Med.* **17,** 1355–1362 (2013).
8. Potier, E. *et al.* Prolonged hypoxia concomitant with serum deprivation induces massive human mesenchymal stem cell death. *Tissue Eng.* **13,** 1325–1331 (2007).
9. Baldari, S. *et al.* Challenges and strategies for improving the regenerative effects of mesenchymal stromal cell-based therapies. *Int. J. Mol. Sci.* **18,** (2017).
10. Bravery, C. A. *et al.* Potency assay development for cellular therapy products: an ISCT review of the requirements and experiences in the industry. *Cytotherapy* **15,** 9–19 (2013).
11. Benjamin, E. J. *et al. Heart Disease and Stroke Statistics'2017 Update: A Report from the American Heart Association*. *Circulation* **135,** (2017).
12. National Center for Health Statistics. Selected diseases and conditions among adults aged 18 and over, by selected characteristics: United States, 2016. **8,** 1–9 (2016).
13. Madl, C. M., Heilshorn, S. C. & Blau, H. M. Bioengineering strategies to accelerate stem cell therapeutics. *Nature* **557,** 335–342 (2018).
14. Discher, D. E., Mooney, D. J. & Zandstra, P. W. Growth factors, matrices, and forces combine and control stem cells. *Science* **324,** 1673–7 (2009).
15. Rozario, T. & DeSimone, D. W. The extracellular matrix in development and morphogenesis: a dynamic view. *Dev. Biol.* **341,** 126–40 (2010).
16. Schwartz, M. A. Integrins and extracellular matrix in mechanotransduction. *Cold Spring Harb. Perspect. Biol.* **2,** a005066 (2010).
17. Hynes, R. O. Integrins : Bidirectional , Allosteric Signaling Machines In their roles as major adhesion receptors , integrins. **110,** 673–687 (2002).

18. Rodin, S. *et al.* Long-term self-renewal of human pluripotent stem cells on human recombinant laminin-511. *Nat. Biotechnol.* **28,** 611–615 (2010).

19. Braam, S. R. *et al.* Recombinant Vitronectin Is a Functionally Defined Substrate That Supports Human Embryonic Stem Cell Self-Renewal via αVβ5 Integrin. *Stem Cells* **26,** 2257–2265 (2008).

20. McBeath, R., Pirone, D. M., Nelson, C. M., Bhadriraju, K. & Chen, C. S. Cell shape, cytoskeletal tension, and RhoA regulate stem cell lineage commitment. *Dev. Cell* **6,** 483–95 (2004).

21. Lee, J., Abdeen, A. a, Zhang, D. & Kilian, K. a. Directing stem cell fate on hydrogel substrates by controlling cell geometry, matrix mechanics and adhesion ligand composition. *Biomaterials* **34,** 8140–8148 (2013).

22. Maheshwari, G., Brown, G., Lauffenburger, D. A., Wells, A. & Griffith, L. G. Cell adhesion and motility depend on nanoscale RGD clustering. *J. Cell Sci.* **113 (Pt 10),** 1677–1686 (2000).

23. Frith, J., Mills, R. & Cooper-White, J. Lateral spacing of adhesion peptides influences human mesenchymal stem cell behaviour. *J. Cell Sci.* 317–327 (2012).

24. Biggs, M. J. P., Richards, R. G. & Dalby, M. J. Nanotopographical modification: a regulator of cellular function through focal adhesions. *Nanomedicine Nanotechnology, Biol. Med.* **6,** 619–633 (2010).

25. Chen, W., Shao, Y., Li, X., Zhao, G. & Fu, J. Nanotopographical Surfaces for Stem Cell Fate Control: Engineering Mechanobiology from the Bottom. *Nano Today* **9,** 759–784 (2014).

26. Engler, A. J., Sen, S., Sweeney, H. L. & Discher, D. E. Matrix elasticity directs stem cell lineage specification. *Cell* **126,** 677–89 (2006).

27. Cosgrove, B. D. *et al.* N-cadherin adhesive interactions modulate matrix mechanosensing and fate commitment of mesenchymal stem cells. *Nat. Mater.* **1,** (2016).

28. Klezovitch, O. & Vasioukhin, V. Cadherin signaling: keeping cells in touch. *F1000Research* **4,** 550 (2015).

29. Mbalaviele, G., Chan, S. S. & Civitelli, R. Cell-cell adhesion and signaling through cadherins: Connecting bone cells in their microenvironment. *J. Bone Miner. Res.* **21,** 1821–1827 (2006).

30. Heuberger, J. & Birchmeier, W. Interplay of cadherin-mediated cell adhesion and canonical Wnt signaling. *Cold Spring Harb. Perspect. Biol.* **2,** 1–24 (2010).

31. Mohyeldin, A., Garzón-Muvdi, T. & Quiñones-Hinojosa, A. Oxygen in stem cell biology: A critical component of the stem cell niche. *Cell Stem Cell* **7,** 150–161 (2010).

32. Liu, Y. & Ma, T. Metabolic regulation of mesenchymal stem cell in expansion and therapeutic application. *Biotechnol. Prog.* **31,** 468–481 (2015).

33. Tatapudy, S., Aloisio, F., Barber, D. & Nystul, T. Cell fate decisions: emerging roles for

metabolic signals and cell morphology. *EMBO Rep.* **18,** e201744816 (2017).

34. Lutolf, M. P. & Hubbell, J. a. Synthetic biomaterials as instructive extracellular microenvironments for morphogenesis in tissue engineering. *Nat. Biotechnol.* **23,** 47–55 (2005).

35. Fisher, O. Z., Khademhosseini, A., Langer, R. & Peppas, N. A. Bioinspired Materials for Controlling Stem Cell Fate. *Acc. Chem. Res.* **43,** 419–428 (2010).

36. Murphy, W. L., McDevitt, T. C. & Engler, A. J. Materials as stem cell regulators. *Nat. Mater.* **13,** 547–557 (2014).

37. Terryn, J., Tricot, T., Gajjar, M. & Verfaillie, C. Recent advances in lineage differentiation from stem cells: hurdles and opportunities? *F1000Research* **7,** 220 (2018).

38. Rowe, R. G., Mandelbaum, J., Zon, L. I. & Daley, G. Q. Engineering Hematopoietic Stem Cells: Lessons from Development. *Cell Stem Cell* **18,** 707–720 (2016).

39. Maury, Y. *et al.* Combinatorial analysis of developmental cues efficiently converts human pluripotent stem cells into multiple neuronal subtypes. *Nat. Biotechnol.* **33,** 89–96 (2015).

40. Lipsitz, Y. Y. *et al.* A roadmap for cost-of-goods planning to guide economic production of cell therapy products. *Cytotherapy* **19,** 1383–1391 (2017).

41. Gattazzo, F., Urciuolo, A. & Bonaldo, P. Extracellular matrix: A dynamic microenvironment for stem cell niche. *Biochim. Biophys. Acta - Gen. Subj.* **1840,** 2506–2519 (2014).

42. Belair, D. G., Le, N. N. & Murphy, W. L. Design of growth factor sequestering biomaterials. *Chem. Commun.* **50,** 15651–15668 (2014).

43. Wang, Z. *et al.* Novel biomaterial strategies for controlled growth factor delivery for biomedical applications. *NPG Asia Mater.* **9,** e435-17 (2017).

44. Lee, K., Silva, E. A. & Mooney, D. J. Growth factor delivery-based tissue engineering: general approaches and a review of recent developments. *J. R. Soc. Interface* 153–170 (2010). doi:10.1098/rsif

45. Lotz, S. *et al.* Sustained Levels of FGF2 Maintain Undifferentiated Stem Cell Cultures with Biweekly Feeding. *PLoS One* **8,** 1–10 (2013).

46. Ferguson, E. L. *et al.* Controlled release of dextrin-conjugated growth factors to support growth and differentiation of neural stem cells. *Stem Cell Res.* **33,** 69–78 (2018).

47. Bratt-Leal, A. M., Nguyen, A. H., Hammersmith, K. A., Singh, A. & McDevitt, T. C. A microparticle approach to morphogen delivery within pluripotent stem cell aggregates. *Biomaterials* **34,** 7227–35 (2013).

48. Heidariyan, Z. *et al.* Efficient and cost-effective generation of hepatocyte-like cells through microparticle-mediated delivery of growth factors in a 3D culture of human pluripotent stem cells. *Biomaterials* **159,** 174–188 (2018).

49. Lee, S., Jilan, S. M., Nikolova, G. V., Carpizo, D. & Luisa Iruela-Arispe, M. Processing of

VEGF-A by matrix metalloproteinases regulates bioavailability and vascular patterning in tumors. *J. Cell Biol.* **169,** 681–691 (2005).

50. Müller, E., Pompe, T., Freudenberg, U. & Werner, C. Matrix Growth Factor and Surface Ligand Presentation. *Biol. Eng. Stem Cell Niches* 215–231 (2017). doi:10.1016/B978-0-12-802734-9.00014-7

51. Hermanson, G. T. in *Bioconjugate Techniques (Second Edition)* 1–168 (Academic Press, 2008). doi:https://doi.org/10.1016/B978-0-12-370501-3.00001-1

52. Ehrbar, M. *et al.* Cell-demanded liberation of VEGF121 from fibrin implants induces local and controlled blood vessel growth. *Circ. Res.* **94,** 1124–32 (2004).

53. Lühmann, T. *et al.* Bio-orthogonal Immobilization of Fibroblast Growth Factor 2 for Spatial Controlled Cell Proliferation. *ACS Biomater. Sci. Eng.* **1,** 740–746 (2015).

54. Platt, M. O., Roman, A. J., Wells, A., Lauffenburger, D. A. & Griffith, L. G. Sustained epidermal growth factor receptor levels and activation by tethered ligand binding enhances osteogenic differentiation of multi-potent marrow stromal cells. *J. Cell. Physiol.* **221,** 306–317 (2009).

55. Alberti, K. *et al.* Functional immobilization of signaling proteins enables control of stem cell fate. *Nat. Methods* **5,** 645–50 (2008).

56. Worrallo, M. J., Moore, R. L. L., Glen, K. E. & Thomas, R. J. Immobilized hematopoietic growth factors onto magnetic particles offer a scalable strategy for cell therapy manufacturing in suspension cultures. *Biotechnol. J.* **12,** (2017).

57. Yang, E. Y., Kronenfeld, J. P., Gattás-Asfura, K. M., Bayer, A. L. & Stabler, C. L. Engineering an 'infectious' Treg biomimetic through chemoselective tethering of TGF-β1 to PEG brush surfaces. *Biomaterials* **67,** 20–31 (2015).

58. Plotnikov, A. N., Schlessinger, J., Hubbard, S. R. & Mohammadi, M. Structural Basis for FGF Receptor Dimerization and Activation. *Cell* **98,** 641–650 (1999).

59. Wrana, J. L., Attisano, L., Wieser, R., Ventura, F. & Massagué, J. Mechanism of activation of the TGF-beta receptor. *Nature* **370,** 341–7 (1994).

60. Dosch, D. D. & Ballmer-Hofer, K. Transmembrane domain-mediated orientation of receptor monomers in active VEGFR-2 dimers. *FASEB J.* **24,** 32–8 (2010).

61. Wall, S. T. *et al.* Multivalency of sonic hedgehog conjugated to linear polymer chains modulates protein potency. *Bioconjug. Chem.* **19,** 806–812 (2008).

62. Toepke, M. W. *et al.* Regulating Specific Growth Factor Signaling Using Immobilized Branched Ligands. *Adv. Healthc. Mater.* **1,** 457–460 (2012).

63. Lin, X. *et al.* Synthetic peptide F2A4-K-NS mimics fibroblast growth factor-2 in vitro and is angiogenic in vivo. *Int. J. Mol. Med.* **17,** 833–9 (2006).

64. Li, L., Klim, J. R., Derda, R., Courtney, A. H. & Kiessling, L. L. Spatial control of cell fate using synthetic surfaces to potentiate TGF-β signaling. *Proc. Natl. Acad. Sci.* **108,** 11745–11750 (2011).

65. Rinker, S., Ke, Y., Liu, Y., Chhabra, R. & Yan, H. Self-assembled DNA nanostructures for distance-dependent multivalent ligand-protein binding. *Nat. Nanotechnol.* **3,** 418–422 (2008).

66. Kosmides, A. K., Necochea, K., Hickey, J. W. & Schneck, J. P. Separating T Cell Targeting Components onto Magnetically Clustered Nanoparticles Boosts Activation. *Nano Lett.* **18,** 1916–1924 (2018).

67. Campbell, A. *et al.* Concise Review: Process Development Considerations for Cell Therapy. *Stem Cells Transl. Med.* **4,** 1155–1163 (2015).

68. Lock, L., Dailey, K. & Rowley, J. A. Functional & economic comparability of Xeno-free stem cell bioprocess system. *Cytotherapy* **19,** S125 (2017).

69. Fan, Y., Wu, J., Ashok, P., Hsiung, M. & Tzanakakis, E. S. Production of Human Pluripotent Stem Cell Therapeutics under Defined Xeno-free Conditions: Progress and Challenges. *Stem Cell Rev. Reports* **11,** 96–109 (2015).

70. Chen, K. G., Mallon, B. S., McKay, R. D. G. & Robey, P. G. Human pluripotent stem cell culture: Considerations for maintenance, expansion, and therapeutics. *Cell Stem Cell* **14,** 13–26 (2014).

71. Oduah, E. I., Linhardt, R. J. & Sharfstein, S. T. Heparin: Past, present, and future. *Pharmaceuticals* **9,** 1–12 (2016).

72. Saksela, O., Moscatelli, D., Sommer, A. & Rifkin, D. B. Endothelial cell-derived heparan sulfate binds basic fibroblast growth factor and protects it from proteolytic degradation. *J. Cell Biol.* **107,** 743–751 (1988).

73. Buchtova, M. *et al.* Instability restricts signaling of multiple fibroblast growth factors. *Cell. Mol. Life Sci.* **72,** 2445–2459 (2015).

74. Yayon, A., Klagsbrun, M., Esko, J. D., Leder, P. & Ornitz, D. M. Cell surface, heparin-like molecules are required for binding of basic fibroblast growth factor to its high affinity receptor. *Cell* **64,** 841–8 (1991).

75. Xu, D. & Esko, J. D. Demystifying Heparan Sulfate–Protein Interactions. *Annu. Rev. Biochem.* **83,** 129–157 (2014).

76. Maynard, H. D. & Hubbell, J. A. Discovery of a sulfated tetrapeptide that binds to vascular endothelial growth factor. *Acta Biomater.* **1,** 451–459 (2005).

77. Hendrikse, S. I. S., Spaans, S., Meijer, E. W. & Dankers, P. Y. W. Supramolecular Platform Stabilizing Growth Factors. *Biomacromolecules* **19,** 2610–2617 (2018).

78. Nguyen, T. H. *et al.* A heparin-mimicking polymer conjugate stabilizes basic fibroblast growth factor. *Nat. Chem.* **5,** 221–227 (2013).

79. Yu, X. *et al.* Nanostructured Mineral Coatings Stabilize Proteins for Therapeutic Delivery. *Adv. Mater.* **29,** 1701255 (2017).

80. Gerber, H. P. *et al.* VEGF regulates haematopoietic stem cell survival by an internal autocrine loop mechanism. *Nature* **417,** 954–958 (2002).

81. Zaragosi, L.-E., Ailhaud, G. & Dani, C. Autocrine Fibroblast Growth Factor 2 Signaling Is Critical for Self-Renewal of Human Multipotent Adipose-Derived Stem Cells. *Stem Cells* **24,** 2412–2419 (2006).

82. Sheehan, S. M., Tatsumi, R., Temm-Grove, C. J. & Allen, R. E. HGF is an autocrine growth factor for skeletal muscle satellite cells in vitro. *Muscle Nerve* **23,** 239–45 (2000).

83. Dvorak, P. & Hampl, A. Basic fibroblast growth factor and its receptors in human embryonic stem cells. *Folia Histochem. Cytobiol.* **43,** 203–8 (2005).

84. Dvorak, P. *et al.* Expression and Potential Role of Fibroblast Growth Factor 2 and Its Receptors in Human Embryonic Stem Cells. *Stem Cells* **23,** 1200–1211 (2005).

85. Greber, B., Lehrach, H. & Adjaye, J. Fibroblast Growth Factor 2 Modulates Transforming Growth Factor β Signaling in Mouse Embryonic Fibroblasts and Human ESCs (hESCs) to Support hESC Self-Renewal. *Stem Cells* **25,** 455–464 (2007).

86. Montes, R. *et al.* Feeder-free maintenance of hESCs in mesenchymal stem cell-conditioned media: Distinct requirements for TGF-B and IGF-II. *Cell Res.* **19,** 698–709 (2009).

87. Lanner, F. & Rossant, J. The role of FGF/Erk signaling in pluripotent cells. *Development* **137,** 3351–3360 (2010).

88. Vallier, L. Activin/Nodal and FGF pathways cooperate to maintain pluripotency of human embryonic stem cells. *J. Cell Sci.* **118,** 4495–4509 (2005).

89. Xu, R. H. *et al.* NANOG Is a Direct Target of TGFβ/Activin-Mediated SMAD Signaling in Human ESCs. *Cell Stem Cell* **3,** 196–206 (2008).

90. Martino, M. M. & Hubbell, J. a. The 12th-14th type III repeats of fibronectin function as a highly promiscuous growth factor-binding domain. *FASEB J.* **24,** 4711–21 (2010).

91. Jha, A. K. *et al.* Enhanced survival and engraftment of transplanted stem cells using growth factor sequestering hydrogels. *Biomaterials* **47,** 1–12 (2015).

92. Lee, S. S. *et al.* Sulfated glycopeptide nanostructures for multipotent protein activation. *Nat. Nanotechnol.* **12,** 821–829 (2017).

93. Belair, D. G., Le, N. N. & Murphy, W. L. Regulating VEGF signaling in platelet concentrates via specific VEGF sequestering. *Biomater. Sci.* **4,** 819–825 (2016).

94. Crispim, J. *et al.* TGF-β1 activation in human hamstring cells through growth factor binding peptides on polycaprolactone surfaces. *Acta Biomater.* **53,** 165–178 (2017).

95. Enam, S. F. *et al.* Enrichment of endogenous fractalkine and anti-inflammatory cells via aptamer-functionalized hydrogels. *Biomaterials* **142,** 52–61 (2017).

96. Kong, H. Y. & Byun, J. Nucleic acid aptamers: New methods for selection, stabilization, and application in biomedical science. *Biomol. Ther.* **21,** 423–434 (2013).

97. Lax, R., Ph, D., Development, B., America, N. & Group, P. The Future of Peptide Development in the Pharmaceutical Industry. *PharManufacturing Int. Pept. Rev.* **4,** 10–15

(2010).

98. Zhou, J. & Rossi, J. Aptamers as targeted therapeutics: current potential and challenges. *Nat. Rev. Drug Discov.* **16,** 181–202 (2017).

99. Webber, M. J. *et al.* Supramolecular nanostructures that mimic VEGF as a strategy for ischemic tissue repair. *Proc. Natl. Acad. Sci.* **108,** 13438–13443 (2011).

100. Koepsel, J. T., Nguyen, E. H. & Murphy, W. L. Differential effects of a soluble or immobilized VEGFR-binding peptide. *Integr. Biol. (United Kingdom)* **4,** 914–924 (2012).

101. Kumar, V. A. *et al.* Highly angiogenic peptide nanofibers. *ACS Nano* **9,** 860–868 (2015).

102. Zouani, O. F., Chollet, C., Guillotin, B. & Durrieu, M. C. Differentiation of pre-osteoblast cells on poly(ethylene terephthalate) grafted with RGD and/or BMPs mimetic peptides. *Biomaterials* **31,** 8245–8253 (2010).

103. Bilem, I. *et al.* RGD and BMP-2 mimetic peptide crosstalk enhances osteogenic commitment of human bone marrow stem cells. *Acta Biomater.* **36,** 132–142 (2016).

104. Rubert Pérez, C. M., Álvarez, Z., Chen, F., Aytun, T. & Stupp, S. I. Mimicking the Bioactivity of Fibroblast Growth Factor-2 Using Supramolecular Nanoribbons. *ACS Biomater. Sci. Eng.* **3,** 2166–2175 (2017).

105. Edelbrock, A. N. *et al.* Supramolecular Nanostructure Activates TrkB Receptor Signaling of Neuronal Cells by Mimicking Brain-Derived Neurotrophic Factor. *Nano Lett.* acs.nanolett.8b02317 (2018). doi:10.1021/acs.nanolett.8b02317

106. Baird, A., Schubert, D., Ling, N. & Guillemin, R. Receptor- and heparin-binding domains of basic fibroblast growth factor. *Proc. Natl. Acad. Sci.* **85,** 2324–2328 (1988).

107. Ramaswamy, V. *et al.* DNA Aptamer Assembly as a Vascular Endothelial Growth Factor Receptor Agonist. *Nucleic Acid Ther.* **25,** 227–234 (2015).

108. Ueki, R., Ueki, A., Kanda, N. & Sando, S. Oligonucleotide-Based Mimetics of Hepatocyte Growth Factor. *Angew. Chemie - Int. Ed.* **55,** 579–582 (2016).

109. Dollins, C. M. *et al.* Assembling OX40 Aptamers on a Molecular Scaffold to Create a Receptor-Activating Aptamer. *Chem. Biol.* **15,** 675–682 (2008).

110. Kim, S. H., Turnbull, J. & Guimond, S. Extracellular matrix and cell signalling: The dynamic cooperation of integrin, proteoglycan and growth factor receptor. *J. Endocrinol.* **209,** 139–151 (2011).

111. Blagovic, K., Gong, E. S., Milano, D. F., Natividad, R. J. & Asthagiri, A. R. Engineering cell-cell signaling. *Curr. Opin. Biotechnol.* **24,** 940–947 (2013).

112. Bian, L., Guvendiren, M., Mauck, R. L. & Burdick, J. a. Hydrogels that mimic developmentally relevant matrix and N-cadherin interactions enhance MSC chondrogenesis. *Proc. Natl. Acad. Sci. U. S. A.* **110,** 10117–22 (2013).

113. Qazi, T. H., Mooney, D. J., Duda, G. N. & Geissler, S. Biomaterials that promote cell-cell interactions enhance the paracrine function of MSCs. *Biomaterials* **140,** 103–114 (2017).

114. Comoglio, P. M., Boccaccio, C. & Trusolino, L. Interactions between growth factor receptors and adhesion molecules: Breaking the rules. *Curr. Opin. Cell Biol.* **15,** 565–571 (2003).

115. Petreaca, M. & Martins-Green, M. Cell-ECM Interactions in Repair and Regeneration. *Princ. Regen. Med.* 19–65 (2011). doi:10.1016/B978-0-12-381422-7.10002-1

116. Moulisová, V. *et al.* Engineered microenvironments for synergistic VEGF – Integrin signalling during vascularization. *Biomaterials* **126,** 61–74 (2017).

117. Wrighton, P. J. *et al.* Signals from the surface modulate differentiation of human pluripotent stem cells through glycosaminoglycans and integrins. *Proc. Natl. Acad. Sci.* **111,** 18126–18131 (2014).

118. Banks, J. M., Mozdzen, L. C., Harley, B. A. C. & Bailey, R. C. The combined effects of matrix stiffness and growth factor immobilization on the bioactivity and differentiation capabilities of adipose-derived stem cells. *Biomaterials* **35,** 8951–8959 (2014).

119. Zouani, O. F., Kalisky, J., Ibarboure, E. & Durrieu, M. C. Effect of BMP-2 from matrices of different stiffnesses for the modulation of stem cell fate. *Biomaterials* **34,** 2157–2166 (2013).

120. Gilde, F. *et al.* Stiffness-dependent cellular internalization of matrix-bound BMP-2 and its relation to Smad and non-Smad signaling. *Acta Biomater.* **46,** 55–67 (2016).

121. Musah, S. *et al.* Glycosaminoglycan-Binding Hydrogels Enable Mechanical Control of Human Pluripotent Stem Cell Self-Renewal. *ACS Nano* **6,** 10168–10177 (2012).

122. Rowley, J., Abraham, E., Campbell, A., Brandwein, H. & Oh, S. Meeting lot-size challenges of manufacturing adherent cells for therapy. *Bioprocess Int.* **10,** 16–22 (2012).

123. Merten, O. W. Advances in cell culture: Anchorage dependence. *Philos. Trans. R. Soc. B Biol. Sci.* **370,** (2015).

124. Simaria, A. S. *et al.* Allogeneic cell therapy bioprocess economics and optimization: Single-use cell expansion technologies. *Biotechnol. Bioeng.* **111,** 69–83 (2014).

125. Ma, T., Tsai, A. C. & Liu, Y. Biomanufacturing of human mesenchymal stem cells in cell therapy: Influence of microenvironment on scalable expansion in bioreactors. *Biochem. Eng. J.* **108,** 44–50 (2016).

126. Chu, L. & Robinson, D. K. Industrial choices for protein production by large-scale cell culture. *Curr. Opin. Biotechnol.* **12,** 180–187 (2001).

127. Placzek, M. R. *et al.* Stem cell bioprocessing: fundamentals and principles. *J. R. Soc. Interface* **6,** 209–32 (2009).

128. Zhang, J. Mammalian Cell Culture for Biopharmaceutical Production. *Man. Ind. Microbiol. Biotechnol. Third Ed.* 157–178 (2014). doi:10.1128/9781555816827.ch12

129. Dumont, J., Euwart, D., Mei, B., Estes, S. & Kshirsagar, R. Human cell lines for biopharmaceutical manufacturing: history, status, and future perspectives. *Crit. Rev. Biotechnol.* **36,** 1110–1122 (2016).

130. Merten, O.-W. Advances in cell culture: anchorage dependence. *Philos. Trans. R. Soc. B Biol. Sci.* **370,** 20140040–20140040 (2014).

131. Kinney, M. A., Sargent, C. Y. & McDevitt, T. C. The multiparametric effects of hydrodynamic environments on stem cell culture. *Tissue Eng. Part B. Rev.* **17,** 249–262 (2011).

132. Li, B. *et al.* Past, present, and future of microcarrier-based tissue engineering. *J. Orthop. Transl.* **3,** 51–57 (2015).

133. Rodin, S. *et al.* Clonal culturing of human embryonic stem cells on laminin-521/E-cadherin matrix in defined and xeno-free environment. *Nat. Commun.* **5,** 1–13 (2014).

134. Villa-Diaz, L. G. *et al.* Synthetic polymer coatings for long-term growth of human embryonic stem cells. *Nat. Biotechnol.* **28,** 581–583 (2010).

135. Melkoumian, Z. *et al.* Synthetic peptide-acrylate surfaces for long-term self-renewal and cardiomyocyte differentiation of human embryonic stem cells. *Nat. Biotechnol.* **28,** 606–610 (2010).

136. Badenes, S. M. *et al.* Defined Essential 8^{TM} Medium and Vitronectin Efficiently Support Scalable Xeno-Free Expansion of Human Induced Pluripotent Stem Cells in Stirred Microcarrier Culture Systems. *PLoS One* **11,** e0151264 (2016).

137. Rodrigues, C. A. V. *et al.* Scalable culture of human induced pluripotent cells on microcarriers under xeno-free conditions using single-use vertical-wheel^{TM} bioreactors. *J. Chem. Technol. Biotechnol.* **93,** 3597–3606 (2018).

138. Dias, A. D., Elicson, J. M. & Murphy, W. L. Microcarriers with Synthetic Hydrogel Surfaces for Stem Cell Expansion. *Adv. Healthc. Mater.* **6,** 1–9 (2017).

139. Adil, M. M. & Schaffer, D. V. Expansion of human pluripotent stem cells. *Curr. Opin. Chem. Eng.* **15,** 24–35 (2017).

140. Lipsitz, Y. Y., Tonge, P. D. & Zandstra, P. W. Chemically controlled aggregation of pluripotent stem cells. *Biotechnol. Bioeng.* **115,** 2061–2066 (2018).

141. Abbasalizadeh, S., Larijani, M. R., Samadian, A. & Baharvand, H. Bioprocess Development for Mass Production of Size-Controlled Human Pluripotent Stem Cell Aggregates in Stirred Suspension Bioreactor. *Tissue Eng. Part C Methods* **18,** 831–851 (2012).

142. Wang, Y. *et al.* Scalable expansion of human induced pluripotent stem cells in the defined xeno-free E8 medium under adherent and suspension culture conditions. *Stem Cell Res.* **11,** 1103–1116 (2013).

143. Itskovitz-Eldor, J. *et al.* Differentiation of human embryonic stem cells into embryoid bodies compromising the three embryonic germ layers. *Mol. Med.* **6,** 88–95 (2000).

144. Ungrin, M. D., Joshi, C., Nica, A., Bauwens, C. & Zandstra, P. W. Reproducible, ultra high-throughput formation of multicellular organization from single cell suspension-derived human embryonic stem cell aggregates. *PLoS One* **3,** e1565 (2008).

145. Bauwens, C. L. *et al.* Control of human embryonic stem cell colony and aggregate size heterogeneity influences differentiation trajectories. *Stem Cells* **26,** 2300–10 (2008).

146. Froehlich, K. *et al.* Generation of Multicellular Breast Cancer Tumor Spheroids: Comparison of Different Protocols. *J. Mammary Gland Biol. Neoplasia* **21,** 89–98 (2016).

147. Mohr, J. C., de Pablo, J. J. & Palecek, S. P. 3-D microwell culture of human embryonic stem cells. *Biomaterials* **27,** 6032–6042 (2006).

148. Dahlmann, J. *et al.* The use of agarose microwells for scalable embryoid body formation and cardiac differentiation of human and murine pluripotent stem cells. *Biomaterials* **34,** 2463–71 (2013).

149. Pettinato, G., Wen, X. & Zhang, N. Formation of well-defined embryoid bodies from dissociated human induced pluripotent stem cells using microfabricated cell-repellent microwell arrays. *Sci. Rep.* **4,** 7402 (2014).

150. Antonchuk, J. in *Basic Cell Culture Protocols* (eds. Helgason, C. D. & Miller, C. L.) 523–533 (Humana Press, 2013). doi:10.1007/978-1-62703-128-8_32

151. Hookway, T. A., Butts, J. C., Lee, E., Tang, H. & McDevitt, T. C. Aggregate formation and suspension culture of human pluripotent stem cells and differentiated progeny. *Methods* (2015). doi:10.1016/j.ymeth.2015.11.027

152. Baraniak, P. R. & McDevitt, T. C. Scaffold-free culture of mesenchymal stem cell spheroids in suspension preserves multilineage potential. *Cell Tissue Res.* **347,** 701–11 (2012).

153. Zimmermann, J. A. & McDevitt, T. C. Pre-conditioning mesenchymal stromal cell spheroids for immunomodulatory paracrine factor secretion. *Cytotherapy* **16,** 331–45 (2014).

154. Stevens, K. R. *et al.* InVERT molding for scalable control of tissue microarchitecture. *Nat. Commun.* **4,** (2013).

155. Blackford, S. J. I. *et al.* Validation of Current Good Manufacturing Practice Compliant Human Pluripotent Stem Cell-Derived Hepatocytes for Cell-Based Therapy. *Stem Cells Transl. Med.* 1–14 (2018). doi:10.1002/sctm.18-0084

156. Razian, G., Yu, Y. & Ungrin, M. D. Production of large numbers of size-controlled tumor spheroids using microwell plates. *J. Vis. Exp.* e50665 (2013). doi:10.3791/50665

157. Singh, H., Mok, P., Balakrishnan, T., Rahmat, S. N. B. & Zweigerdt, R. Up-scaling single cell-inoculated suspension culture of human embryonic stem cells. *Stem Cell Res.* **4,** 165–179 (2010).

158. Kehoe, D. E., Jing, D., Lock, L. T., Tzanakakis, E. S. & Ph, D. Scalable Stirred-Suspension Bioreactor Culture. **16,** (2010).

159. Penfornis, P., C Vallabhaneni, K., Janorkar, A. & Pochampally, R. *Three dimensional tumor models for cancer studies*. *Frontiers in Bioscience - Elite* **9,** (2017).

160. Bai, H., Xie, Y.-L., Gao, Y.-X., Cheng, T. & Wang, Z. Z. The balance of positive and

negative effects of TGF-beta signaling regulates the development of hematopoietic and endothelial progenitors in human pluripotent stem cells. *Stem Cells Dev.* **22,** 2765–2776 (2013).

161. Egger, D., Tripisciano, C., Weber, V., Dominici, M. & Kasper, C. Dynamic Cultivation of Mesenchymal Stem Cell Aggregates. *Bioengineering* **5,** 48 (2018).

162. Kinney, M. A., Hookway, T. A., Wang, Y. & McDevitt, T. C. Engineering three-dimensional stem cell morphogenesis for the development of tissue models and scalable regenerative therapeutics. *Ann. Biomed. Eng.* **42,** 352–367 (2014).

163. Khalil, A. S., Xie, A. W. & Murphy, W. L. Context clues: the importance of stem cell-material interactions. *ACS Chem. Biol.* **9,** 45–56 (2014).

164. Laschke, M. W. & Menger, M. D. Life is 3D: Boosting Spheroid Function for Tissue Engineering. *Trends Biotechnol.* **35,** 133–144 (2017).

165. Knight, E. & Przyborski, S. Advances in 3D cell culture technologies enabling tissue-like structures to be created in vitro. *J. Anat.* **227,** 746–756 (2015).

166. Van Winkle, A. P., Gates, I. D. & Kallos, M. S. Mass transfer limitations in embryoid bodies during human embryonic stem cell differentiation. *Cells Tissues Organs* **196,** 34–47 (2012).

167. Kropp, C., Massai, D. & Zweigerdt, R. Progress and challenges in large-scale expansion of human pluripotent stem cells. *Process Biochem.* **59,** 244–254 (2017).

168. Ratcliffe, E., Thomas, R. J. & Williams, D. J. Current understanding and challenges in bioprocessing of stem cell-based therapies for regenerative medicine. *Br. Med. Bull.* **100,** 137–155 (2011).

169. Abecasis, B. *et al.* Expansion of 3D human induced pluripotent stem cell aggregates in bioreactors: Bioprocess intensification and scaling-up approaches. *J. Biotechnol.* **246,** 81–93 (2017).

170. Rinker, T. E. *et al.* Microparticle-mediated sequestration of cell-secreted proteins to modulate chondrocytic differentiation. *Acta Biomater.* **68,** 125–136 (2018).

171. Lampe, K. J., Namba, R. M., Silverman, T. R., Bjugstad, K. B. & Mahoney, M. J. Impact of lactic acid on cell proliferation and free radical-induced cell death in monolayer cultures of neural precursor cells. *Biotechnol. Bioeng.* **103,** 1214–1223 (2009).

172. Nakamura, S. *et al.* Effect of calcium ion concentrations on osteogenic differentiation and hematopoietic stem cell niche-related protein expression in osteoblasts. *Tissue Eng. Part A* **16,** 2467–2473 (2010).

173. Barradas, A. M. C. *et al.* A calcium-induced signaling cascade leading to osteogenic differentiation of human bone marrow-derived mesenchymal stromal cells. *Biomaterials* **33,** 3205–3215 (2012).

174. Viti, F. *et al.* Osteogenic differentiation of MSC through calcium signaling activation: Transcriptomics and functional analysis. *PLoS One* **11,** 1–21 (2016).

175. Nguyen, A. H., Wang, Y., White, D. E., Platt, M. O. & McDevitt, T. C. MMP-mediated mesenchymal morphogenesis of pluripotent stem cell aggregates stimulated by gelatin methacrylate microparticle incorporation. *Biomaterials* **76,** 66–75 (2016).

176. Sachlos, E. & Auguste, D. T. Embryoid body morphology influences diffusive transport of inductive biochemicals: A strategy for stem cell differentiation. *Biomaterials* **29,** 4471–4480 (2008).

177. Sart, S., Tsai, A.-C., Li, Y. & Ma, T. Three-dimensional aggregates of mesenchymal stem cells: cellular mechanisms, biological properties, and applications. *Tissue Eng. Part B, Rev.* **20,** 365–80 (2014).

178. Bratt-leal, M., Carpenedo, R. L. & Mcdevitt, T. C. Engineering the embryoid body microenvironment to direct embryonic stem cell differentiation. 43–51 (2009). doi:10.1021/bp.139

179. Azarin, S. M. *et al.* Modulation of Wnt/β-catenin signaling in human embryonic stem cells using a 3-D microwell array. *Biomaterials* **33,** 2041–9 (2012).

180. Sargent, C. Y. *et al.* Hydrodynamic modulation of embryonic stem cell differentiation by rotary orbital suspension culture. *Biotechnol. Bioeng.* **105,** 611–626 (2010).

181. Tuli, R. *et al.* Transforming growth factor-beta-mediated chondrogenesis of human mesenchymal progenitor cells involves N-cadherin and mitogen-activated protein kinase and Wnt signaling cross-talk. *J. Biol. Chem.* **278,** 41227–41236 (2003).

182. Hsu, S. & Huang, G.-S. Substrate-dependent Wnt signaling in MSC differentiation within biomaterial-derived 3D spheroids. *Biomaterials* **34,** 4725–4738 (2013).

183. Kinney, M. A., Sargent, C. Y. & McDevitt, T. C. Temporal modulation of β-catenin signaling by multicellular aggregation kinetics impacts embryonic stem cell cardiomyogenesis. *Stem Cells Dev.* **22,** 2665–77 (2013).

184. Bartosh, T. J., Ylöstalo, J. H., Bazhanov, N., Kuhlman, J. & Prockop, D. J. Dynamic compaction of human mesenchymal stem/precursor cells into spheres self-activates caspase-dependent il1 signaling to enhance secretion of modulators of inflammation and immunity (PGE2, TSG6, and STC1). *Stem Cells* **31,** 2443–2456 (2013).

185. Nsiah, B. A. *et al.* Fluid Shear Stress Pre-Conditioning Promotes Endothelial Morphogenesis of Embryonic Stem Cells Within Embryoid Bodies. *Tissue Eng. Part A* **20,** 954–965 (2014).

186. Libby, A. R. G. *et al.* Spatiotemporal mosaic self-patterning of pluripotent stem cells using CRISPR interference. *Elife* **7,** e36045 (2018).

187. Gothard, D., Roberts, S. J., Shakesheff, K. M. & Buttery, L. D. Controlled embryoid body formation via surface modification and avidin-biotin cross-linking. *Cytotechnology* **61,** 135–44 (2009).

188. Gartner, Z. J. & Bertozzi, C. R. Programmed assembly of 3-dimensional microtissues. **106,** (2009).

189. Amaral, A. J. R. & Pasparakis, G. Rapid Formation of Cell Aggregates and Spheroids Induced by a ‘Smart’ Boronic Acid Copolymer. *ACS Appl. Mater. Interfaces* **8,** 22930–22941 (2016).

190. Fayol, D. *et al.* Use of magnetic forces to promote stem cell aggregation during differentiation, and cartilage tissue modeling. *Adv. Mater.* **25,** 2611–2616 (2013).

191. Geuss, L. R., Wu, D. C., Ramamoorthy, D., Alford, C. D. & Suggs, L. J. Paramagnetic Beads and Magnetically Mediated Strain Enhance Cardiomyogenesis in Mouse Embryoid Bodies. *PLoS One* **9,** e113982 (2014).

192. Kinney, M. A., Saeed, R. & McDevitt, T. C. Mesenchymal morphogenesis of embryonic stem cells dynamically modulates the biophysical microtissue niche. *Sci. Rep.* **4,** (2014).

193. Sasai, Y., Eiraku, M. & Suga, H. In vitro organogenesis in three dimensions: self-organising stem cells. *Development* **139,** 4111–21 (2012).

CHAPTER 3. SUSTAINED RELEASE AND PROTEIN STABILIZATION REDUCE THE GROWTH FACTOR DOSAGE REQUIRED FOR HUMAN PLURIPOTENT STEM CELL EXPANSION

Elements of this chapter have been submitted for publication as:

Angela W. Xie*, Andrew S. Khalil*, Hunter J. Johnson*, and William L. Murphy. Sustained release and protein stabilization reduce the growth factor dosage required for human pluripotent stem cell expansion. *Equal contribution.

3.1 PREFACE

In Chapter 2, we provided a brief overview of the current state of the art in the design and development of synthetic biomaterials for growth factor regulation and delivery. While controlled growth factor release from biomaterials has a 40-year history of development for *in vivo* delivery applications, the deployment of these technologies as ancillary materials in *ex vivo* cell biomanufacturing has gained increasing interest, in parallel with recent advancements in cell therapies and the need for economical approaches toward producing these therapies. In this chapter, we describe a biomaterial strategy for stabilizing and delivering thermally labile growth factors for efficient expansion of human pluripotent stem cells (hPSCs). This work demonstrates the value of biomaterial-based delivery strategies to greatly reduce the need for costly growth factors in cell culture, and should aid in overcoming challenges in cost-effective cell biomanufacturing.

3.2 ABSTRACT

Translation of human pluripotent stem cell (hPSC)-derived therapies to the clinic demands scalable, cost-effective methods for cell expansion. Culture media currently used for hPSC expansion rely on high concentrations and frequent supplementation of recombinant growth factors due to their short half-life at physiological temperatures. Here, we developed a biomaterials strategy using mineral-coated microparticles (MCMs) to sustain delivery of basic fibroblast growth factor (bFGF), a thermolabile protein critical for hPSC pluripotency and proliferation. We show that the MCMs stabilize bFGF against thermally induced activity loss and provide more efficient sustained release of active growth factor compared to polymeric carriers commonly used for growth factor delivery. bFGF-loaded MCMs supported hPSC expansion over 25 passages without the need for additional bFGF supplementation to the media, resulting in greater than 80% reduction in bFGF usage compared to standard approaches. This materials-based strategy to stabilize and sustain delivery of a thermolabile growth factor has broad potential to reduce costs associated with recombinant protein supplements in scalable biomanufacturing of emerging cell therapies.

3.3 INTRODUCTION

Cell therapies are poised to significantly impact public health over the coming decades, as evidenced by over 350 clinical trials since 2016 (>70 currently active) using cell-based products to treat cardiovascular disease, diabetes, and cancer (http://www.clinicaltrials.gov). Stem cells provide a rich source from which to derive cellular therapies, due to their unlimited expansion capacity and ability to differentiate into a variety of clinically relevant cell types[1,2]. However, scaling up established stem cell culture methods for biomanufacturing cell therapies remains a significant challenge. For example, the number of cells needed for human pluripotent stem cell (hPSC)-derived therapies range from 10^5-10^{10} cells/patient[3], and recent reports project that

commercialization of these therapies will need to accommodate treatment of 10,000-100,000 patients per year (i.e., production of 10^{11}-10^{14} cells per year)[4,5].

Culture media constitute a significant portion of the costs of cell biomanufacturing, as cell expansion and differentiation protocols often rely on media containing high concentrations of costly recombinant growth factors and cytokines. In addition, culture media must be replenished frequently to offset limited stability of these components[6,7]. As a result, it has been estimated that growth factors and cytokines account for 25-58% of the costs of producing stem cell-based therapies at a commercial scale[4,8,9]. The need for basic fibroblast growth factor (bFGF) in hPSC culture provides an illustrative example, as a threshold level of bFGF signaling is critical for hPSC survival, proliferation, and self-renewal[10]. Due to the poor stability of bFGF[6,11], standard commercial media such as Essential 8 (E8) and TeSR[6,12] contain high concentrations of recombinant bFGF (100 ng/ml). Even with these high concentrations, daily media changes are required to provide sufficient active bFGF and prevent spontaneous differentiation events that can quickly compromise hPSC quality[7,10,13].

Here, we report the use of mineral-coated microparticles (MCMs) that stabilize bFGF and sustain its delivery in order to reduce the amount of the growth factor needed for long-term expansion of hPSCs. The use of MCMs reduced the total bFGF required for hPSC culture by more than 80%. In addition, bFGF-loaded MCMs (bFGF-MCMs) eliminated the need for supplemental addition of soluble bFGF during long-term, chemically defined expansion of hPSCs. Together, these findings demonstrate that a biomaterial that both stabilizes and sustains delivery of a thermolabile growth factor can aid in cost-effective biomanufacturing of stem cells, and the approach may be broadly applicable in chemically defined biomanufacturing of emerging cell therapies.

3.4 RESULTS

3.4.1 MCMs efficiently bound and released bFGF to maintain Oct4 and Nanog expression in hPSCs in a dose-dependent manner.

Incubation of hydroxyapatite powder in modified simulated body fluid produced microparticles with inorganic nanostructured, plate-like coatings capable of sustaining delivery of bFGF in hPSC culture (Supplementary Fig. S3.1A). These coatings demonstrated a high capacity for bFGF binding, with 80.1 ± 6.5% (0.97 μg bFGF/mg MCM) bound after incubation for one hour at room temperature (Fig. 3.1A, Supplementary Fig. S3.1B). The MCMs afforded sustained bFGF release by gradually dissolving at physiological pH, as indicated by sustained calcium dissolution in pH 7.4 Tris-buffered saline over 7 days (Fig. 3.1B, Supplementary Fig. S3.1C). In Transwell culture, MCMs released bFGF without directly contacting cells, and bFGF-MCM-containing Transwells were carried over for continued sustained release throughout the duration of culture. In the direct culture format, bFGF-MCMs were prepared fresh for each passage and added directly to wells containing hPSCs (Fig. 3.1C). The MCMs interacted closely with the cell membrane but were not internalized, as evidenced by the clear nanostructured features that remained observable by SEM after direct culture of MCMs with hPSCs (Fig. 3.1D).

Sustained bFGF release from MCMs maintained hPSC expression of pluripotency markers Oct4 and Nanog in a dose-dependent manner in chemically defined media devoid of bFGF (Essential 8 media minus bFGF, hereafter referred to as “E7”). Culture with bFGF-MCMs maintained hPSC colonies with epithelial-like morphologies, similar to those of cells in E8. The appearance of spontaneously differentiating mesenchymal-like cells was inversely correlated with bFGF-MCM dose (Fig. 3.2A). hPSCs cultured in E7 alone underwent spontaneous differentiation

by passage 2, as evidenced by the appearance of cells with mesenchymal-like morphology and concomitant loss of Oct4 and Nanog expression (21.2 ± 10.5% Oct4+/Nanog+ by passage 2; 14.0 ± 1.7% by passage 3) (Fig. 3.2A-B). Increasing amounts of bFGF-MCMs (mass of MCMs per well = 0.1 mg/"low", 0.5 mg/"med", or 1.0 mg/"high") resulted in 50.0 ± 1.4%, 76.1 ± 5.6%, and 88.8 ± 3.1% Oct4+/Nanog+ hPSCs at passage 3, respectively (Fig. 3.2B-C). Importantly, the presence of unloaded MCMs did not significantly affect pluripotency marker expression of hPSCs cultured in Transwell or direct culture formats over 10 passages (40 days) in E8 medium (Supplementary Fig. S3.2). In comparison to standard culture of hPSCs in E8 (which consistently maintained ~95% Oct4+/Nanog+ cells with 100 ng/mL bFGF per day), the high dose of bFGF-MCMs reduced bFGF consumption by 16.7% (Fig 3.2B, Supplementary Table S3.1), but was unable to maintain undifferentiated hPSCs beyond passage 3 (Supplementary Fig. S3.3).

3.4.2 A Design of Experiments (DOE)-based optimization of bFGF-MCM fabrication afforded maintenance of >95% Oct4+/Nanog+ hPSCs while minimizing the required bFGF dose.

We constructed a rotatable response surface design to determine the effects of MCM and bFGF concentrations in the MCM loading solution on hPSC pluripotency. The two-factor, five-level design generated nine unique MCM loading conditions that we tested in Transwell culture for their capacity to maintain pluripotency marker expression for three passages (Fig. 3.3A). These conditions maintained a range of 44.5 ± 5.6% to 98.1 ± 0.4% Oct4+/Nanog+ hPSCs. Four of the nine MCM loading conditions maintained >95% Oct4+/Nanog+ hPSCs with undifferentiated colony morphology at passage 3, comparable to control hPSCs maintained in E8 media (Fig. 3.3B-

C). Of these four conditions, only (--) reduced the amount of bFGF utilized in comparison to E8 by 16.7% (Supplementary Table S3.1).

Multivariate analysis of the experimental data resulted in a model with goodness of fit $F < 0.0001$ and statistically significant dependence ($P < 0.0001$) of %Oct4+/Nanog+ hPSCs on both MCM and bFGF concentration in the MCM loading solution (Fig. 3.3D, Supplementary Fig. S3.4). By defining desirability as "minimizing the amount of bFGF utilized while achieving 95% Oct4+/Nanog+ population," we used the model to determine an optimized MCM loading solution of 0.375 mg/mL MCMs and 0.456 µg/mL bFGF (Fig. 3.3D). We tested the model by comparing bFGF-MCMs fabricated using the optimized loading condition to non-optimized bFGF-MCMs, across a range of doses in which total bFGF utilization was matched between the two conditions (Supplementary Table S3.2). All optimized conditions outperformed non-optimized conditions over three passages in the Transwell culture format. Specifically, MCM doses of 0.6, 0.9, and 1.2 µg bFGF maintained >90% Oct4+/Nanog+ hPSCs using optimized MCMs, while corresponding doses of the non-optimized formulations maintained only 54-64% Oct4+/Nanog+ (Fig. 3.3E, Supplementary Table S3.2). In the direct culture format, all four tested doses of optimized MCMs (61-246 µg bFGF-MCMs per well) successfully maintained >97% Oct4+/Nanog+ hPSCs in E7 media over 3 passages, while corresponding doses of the non-optimized formulations maintained 83-93% Oct4+/Nanog+ (Fig. 3.3E, Supplementary Table S3.2). In addition, the optimized MCMs reduced total bFGF usage by 25.0% (Transwell) and 81.2% (direct) compared to standard hPSC culture in E8 medium with daily feeding (100 ng bFGF/mL per day) while maintaining >95% Oct4+/Nanog+ hPSCs (Table 3.1, Supplementary Table S3.2).

3.4.3 Long-term direct culture with optimized bFGF-MCMs maintained hPSC pluripotency while reducing bFGF by >80%.

Direct culture with optimized bFGF-MCMs maintained pluripotency of two hPSC lines (H1 hESCs and WTc11 hiPSCs) in E7 for 25 passages (>3 months), while reducing the amount of required bFGF by 81.2% compared to standard culture in E8 (Table 3.1). Throughout the course of 25 passages, direct culture bFGF-MCMs yielded colonies with typical undifferentiated morphology for both hPSC lines (Fig. 3.4A). In addition, hPSCs in direct culture were able to be transitioned back to standard culture conditions (E8 media/Matrigel) with no apparent MCM carryover after 2 passages (Fig. 3.4B), likely due to EDTA-mediated passaging resulting in dissolution and removal of the MCMs (Supplementary Fig. S3.5).

Long-term expansion with bFGF-MCMs maintained robust expression of pluripotency markers in both hPSC lines, as determined by immunofluorescence staining and flow cytometry (Fig. 3.4C, Table 3.2), and both lines displayed a normal karyotype (Fig. 3.4D). Following 25 passages in direct culture with bFGF-MCMs, hPSCs from both lines retained the ability to generate derivatives of ectoderm, mesoderm, and endoderm *in vitro* and in teratoma assays. Specifically, differentiated cells expressed βIII-tubulin (ectoderm), alpha smooth muscle actin (mesoderm), and alpha-fetoprotein (endoderm) in spontaneously differentiating embryoid bodies *in vitro* (Fig. 3.4E, Supplementary Fig. S3.6) and each of the hPSC lines generated teratomas containing neuroectoderm, cartilage, and liver tissue in nude mice (Fig. 3.4F, Supplementary Fig. S3.7). In addition, we transitioned hPSCs back to E8 after 25 passages in bFGF-MCM-E7, carried out directed differentiation toward neural, endothelial, and hepatic lineages, and observed generation of βIII-tubulin+ neurons, PECAM-1+ endothelial cells, and AFP+ hepatocyte-like cells, respectively (Supplementary Fig. S3.8). Taken together, these results demonstrate that direct

culture with bFGF-MCMs maintains hPSC pluripotency, while reducing the amount of bFGF needed by >80% when compared to standard hPSC media.

3.4.4 Local bFGF delivery correlated with higher growth factor activity at the culture surface and increased biological response.

bFGF-MCMs in direct culture significantly outperformed Transwell culture by maintaining Oct4/Nanog expression at >95% with lower quantities of input bFGF required (Fig. 3.3E, Table 3.1). Indeed, the amount of bFGF-MCMs sufficient for long-term hPSC maintenance in direct culture was unable to maintain Oct4/Nanog expression in the Transwell culture format, even when bFGF-MCMs were added fresh at every passage (Fig. 3.5A). As this suggested that localization of the growth factor in close proximity to cells may enhance the biological response, we utilized an enzyme-linked immunosorbent assay (ELISA) that detects only active bFGF (Supplementary Fig. S3.9 and S3.10) to assess why localized delivery of bFGF-MCMs improved pluripotency maintenance. In this cell-free assay, we observed a 9-fold increase in the amount of active bFGF detected in direct culture relative to Transwell culture when comparing equivalent amounts of input bFGF-MCMs (Fig. 3.5B). This indicated that direct culture with bFGF-MCMs resulted in a higher local bioavailability of active bFGF at the culture surface compared to Transwell culture.

3.4.5 MCMs stabilized bFGF against activity loss at physiological temperatures.

Experiments in which media were exchanged only at the time of cell passaging (i.e., every 4 days) showed that bFGF-MCMs better maintained Oct4/Nanog expression in hPSCs when compared to “bolus” conditions, in which a matched amount of soluble bFGF was spiked into E7

media. Under these conditions, bFGF-MCMs in direct culture maintained Oct4/Nanog expression in hPSCs for three passages (96.3 ± 0.1% Oct4+/Nanog+ at P3), while bolus incorporation of soluble bFGF failed to maintain Oct4/Nanog after just one passage (78.0 ± 0.9% Oct4+/Nanog+ at P2) (Fig. 3.6A). After 8 passages, bFGF-MCMs produced a substantially higher percentage of Oct4+/Nanog+ hPSCs (75.9 ± 0.5%) than the bolus soluble bFGF (41.2 ± 2.3%) (Fig. 3.6A). To quantify bFGF activity, we again used a bFGF ELISA assay that gave a linear response to active bFGF concentration (Supplementary Fig. S3.10A-B). Importantly, we demonstrated that the assay detected thermally induced loss of bFGF activity in E8 media. bFGF activity loss in media pre-incubated at 37°C and 65°C correlated with decreases in ERK phosphorylation in hPSCs treated with the pre-incubated media (Supplementary Fig. S3.10C-D). Using the bFGF ELISA, we observed that while only 5.37 ± 2.72% and 1.16 ± 0.31% of soluble bFGF remained active after 1 and 4 days of incubation at 37°C, respectively, bFGF-MCMs maintained 15.84 ± 3.33% and 5.36 ± 1.61% bFGF activity over these same periods (Fig. 3.6B).

MCMs released active bFGF over four days at 37°C more efficiently than commonly used and commercially available polymer microspheres designed for bFGF release in hPSC culture. Specifically, PLGA microspheres with encapsulated bFGF released significantly more total protein (1556 ± 188 ng/mL cumulative) over the course of four days compared to MCMs (597 ± 140 ng/mL) (Fig. 3.6C). However, MCMs released nearly 10-fold more active bFGF over four days (103.5 ± 15.8 ng/mL cumulative) compared to PLGA microspheres (10.8 ± 4.8 ng/mL), which only released detectable active bFGF at days 1 and 2 (Fig. 3.6D).

3.5 DISCUSSION

In the present study, we report the development of bFGF-loaded mineral-coated microparticles (bFGF-MCMs) that both stabilized and sustained release of bFGF to markedly reduce the amount of growth factor needed in stem cell culture. Sustained bFGF release from MCMs maintained long-term expansion of undifferentiated hPSCs in the absence of supplemental bFGF, while reducing the total amount of bFGF needed by >80% relative to contemporary culture methods. This is the first reported bFGF delivery approach that is synthetic, requires no supplemental bFGF beyond what is delivered from the material, and can be incorporated into existing workflows using chemically defined media for hPSC expansion and downstream directed differentiation. In addition, as protein binding and release from the mineral coatings is based on promiscuous charge-charge interactions[14] and has been used for release of myriad other proteins[15–21], this approach can be potentially extended to other costly proteins in stem cell culture.

We focused on bFGF due to its role in promoting the expansion, maintenance, and differentiation of numerous cell types, including hPSCs[22,23]. In hPSC culture, bFGF is a critical growth factor that promotes cell adhesion and proliferation, and works in concert with TGFβ/Activin signaling to regulate self-renewal[24–27]. Thus, inclusion of bFGF is a commonality across several commercial hPSC media used for chemically-defined, feeder-free culture[12,28–32]. We chose Essential 8 (E8) medium as a basis for comparison throughout our study, as it is minimally complex (eight supplemental components, of which two are growth factors), is chemically defined and xeno-free, and has already seen success in translating to scalable hPSC culture in bioreactors[33,34]. The short half-life of bFGF ($t_{½}$ ~ 7-10 hrs at 37°C[35–37]) necessitates high concentrations of the growth factor in cell culture and frequent media changes that contribute considerably to the cost of expanding hPSCs. Heparin, a natural stabilizer of bFGF, has been included in some hPSC media formulations to ameliorate this issue in research applications.

However, as sources of heparin are almost exclusively of xenogeneic origin[38,39], its introduction into cell culture poses issues of batch variability, risk of zoonotic contamination, and potential supply chain limitations. Thus, synthetic materials that improve protein stability in cell culture may be particularly attractive alternatives in large-scale biomanufacturing of clinical-grade stem cells and their derivatives.

Although the concept of sustained delivery of bFGF in stem cell culture is straightforward, identifying materials that do not intrinsically interfere with stem cell pluripotency in long-term culture is not trivial, as stem cells are known to be sensitive to their microenvironment[40–43]. Notably, MCMs alone – without bFGF – had no detrimental effects on pluripotency when implemented in either indirect (Transwell) or direct co-culture with hPSCs in E8 (Supplementary Fig. S3.2), and were compatible with enzyme-free passaging workflows[44] (Supplementary Figs. S3.2 and S3.5). Loading MCMs with bFGF afforded sustained release of the growth factor in hPSC culture via gradual dissolution of the mineral coating (Fig. 3.6C-D, Supplementary Fig. S3.1B), a mechanism described in our previous work wherein the rate of coating dissolution corresponded to protein release kinetics[19].

While it is known that bFGF is required for hPSC maintenance, the relationship between bFGF signaling kinetics and the pluripotent state is poorly understood, which precludes a rational design of dosage and release kinetics for a controlled bFGF release platform. Thus, following initial experiments demonstrating the capacity of sustained bFGF release from MCMs to maintain hPSC pluripotency in a dose-dependent manner (Fig. 3.2), we used Design of Experiments (DOE) methodology to optimize MCM-bFGF formulations that would improve maintenance of hPSCs. Our DOE experiment identified a non-intuitive relationship between MCM:bFGF ratio and their absolute concentrations, which significantly influenced maintenance of Oct4+/Nanog+ hPSCs by

bFGF-MCMs (Fig. 3.3D, Supplementary Fig. S3.4). It was unsurprising that MCM-bFGF loading formulations with a high ratio of bFGF to MCMs performed well in maintaining hPSC pluripotency (Supplementary Table S3.2), as we previously observed a positive correlation between protein concentration in the MCM binding solution (with constant MCM mass) and the amount of MCM-bound protein[15,45]. These results indicated that increasing the bFGF:MCM ratio would increase the total bFGF dose delivered from MCMs. However, there is a known tradeoff between the total mass of protein bound and the MCM-protein binding efficiency[45], so DOE was valuable in determining optimal binding formulations that simultaneously maintained pluripotency and reduced the amount of bFGF required. A two-factor, five-level factorial design was sufficient to develop bFGF-MCM formulations that significantly outperformed non-optimized bFGF-MCMs in both Transwell and direct culture (Fig. 3.3E) for at least 25 passages (>100 days), at which point the expanded cells retained both a normal karyotype and the capacity to spontaneously differentiate *in vitro* and form teratomas *in vivo* (Fig. 3.4).

In this study, we tested serial dilutions of DOE-optimized bFGF-MCMs in both Transwell and direct culture to determine the minimum amount of optimized bFGF-MCMs required for long-term hPSC expansion and identified a condition that reduced bFGF usage by >80% compared to standard culture in E8. Future studies could employ additional iterations of DOE optimization with factors such as bFGF-MCM dose and total media volume in culture to further reduce the amount of growth factor required to maintain hPSCs, as well as use MCMs to deliver each of the protein components of E8 in order to further reduce the costs of cell manufacturing. In addition, further mechanistic insight into why optimized bFGF-MCMs outperformed non-optimized may be of value. Such studies may elucidate optimal growth factor release and signaling kinetics for hPSC

pluripotency and exploit these relationships to drive process improvements in stem cell biomanufacturing.

MCMs offered advantages over existing biomaterials for controlled protein release, such as amenability to protein loading in gentle processing conditions devoid of organic solvents and detergents (Fig. 3.1A, Supplementary Fig. S3.1C). Importantly, we demonstrated here, and in a previous study[20], that MCMs can bind and release a wide range of proteins, and that nanostructured features of the mineral coatings can offer protection against protein instability in the face of stressors such as organic solvents, proteases, and thermal challenge (Fig. 3.6). This contrasts with traditional controlled protein release approaches based on biodegradable polymers, wherein loss of protein activity from formulation and processing conditions (e.g., high heat, agitation, exposure to detergents and non-aqueous solvents) is a common issue[20,46]. Loss of biological activity in cell culture is a particular concern for many FGF family members, including bFGF, due to an intrinsic instability at physiological temperatures[6,11]. In the current study, we showed that binding of bFGF to MCMs stabilized the protein against thermally induced activity loss at physiological temperatures. In cell-free assays, bFGF-MCMs demonstrated 3- to 4-fold higher preservation of bFGF biological activity during incubation at 37°C when compared to free soluble bFGF (Fig. 3.6B). This protein stabilization likely depends on a physical interaction of the protein with the nanostructured coating that confines bFGF to its native conformation. This proposed hypothesis is in line with previous studies from our group[20] and others[47–51] showing that stabilization of protein conformation structures at material interfaces can enhance protein bioactivity. Taken together, the unique advantages of MCMs' ease of protein loading and protein stabilization may be of critical value in the biomanufacturing of cell therapies.

MCMs sustained delivery of biologically active growth factor more efficiently than a commonly used and commercially available polymer-based approach developed for hPSC culture[7]. bFGF-MCMs demonstrated nearly linear kinetics of active protein release over 4 days (8.9 ng/mL/day) at 37°C, whereas PLGA microspheres with encapsulated bFGF failed to release detectable quantities of active bFGF beyond the first 2 days at 37°C. This result is remarkable, as the PLGA microspheres released more total protein than MCMs during the same time period (Fig. 3.6C-D). While this observed difference between MCMs and PLGA microspheres can be attributed in part to the stabilization of bFGF by MCMs, degradation of PLGA to create an acidic microclimate that promotes protein unfolding, aggregation, and peptide chain hydrolysis may have also contributed to the compromised bioactivity of bFGF released from PLGA microspheres[46,52]. Taken together, these results demonstrate that MCM-mediated bFGF delivery enabled more efficient sustained protein delivery in culture, with a higher fraction of the released protein remaining active and capable of stimulating downstream FGF receptor (FGFR) signaling, compared to PLGA-based delivery.

Localized delivery enhanced the cellular response to bFGF released from MCMs. Direct co-culture of hPSCs with bFGF-MCMs enabled a 4-fold reduction in the total bFGF needed to maintain hPSC pluripotency marker expression when compared to Transwell culture (Table 3.1). When comparing equivalent bFGF-MCM dosages, direct culture maintained >2.8-fold higher %Oct4+/Nanog+ hPSCs at passage 3 compared to Transwell culture (Fig. 3.5). This increase in apparent biological potency of a protein delivered in close proximity to cells has previously been demonstrated in several *in vitro* and *in vivo* studies (reviewed in [53–55]). In the current study, the stabilization of bFGF by MCMs likely further accentuated the effect of local growth factor delivery. In a cell culture model in which exogenously delivered bFGF exists in three spatial

domains - sequestered in the mineral coating, soluble in the media, and bound to FGF receptors - bFGF delivered to cells from a distant source takes longer to transport to the cell surface, during which the growth factor would be expected to undergo continuous activity loss in solution prior to reaching cell surface FGFRs. Local release of bFGF would be expected to decrease the time it spends in the soluble domain, where it is more subject to activity loss. Experiments in which we separated the soluble releasate from the remaining MCM-bound bFGF after 4 days of release support this hypothesis. After 4 days, the releasate showed no detectable levels of bFGF activity (Supplementary Fig. S3.11), indicating that the ability of bFGF to withstand long-term thermal challenge in our study depends on the protein remaining bound to the mineral coating.

Technologies that control protein release kinetics offer a potential avenue for tailoring soluble factor signaling and increasing the efficiency and yield of stem cell biomanufacturing. Here, we incorporated bFGF-MCMs into standard hPSC culture workflows, with minimal modification of cell culture or passaging protocols. This amenability to conventional workflows may represent a general advantage of this approach in cell biomanufacturing. One could envision a generalizable workflow, in which biomaterials provide sustained delivery of recombinant proteins from a solid matrix while remaining media components (e.g., amino acids, vitamins, lipids, carbohydrates) and metabolic waste products are exchanged by batch or perfusion feeding. This type of approach would allow cells to receive sufficient nutrients for cell survival and growth via frequent media changes, while conserving the proteins needed to maintain or establish cell state/function. As an example, we tested the effect of less frequent media exchanges on hPSCs in direct culture with bFGF-MCMs and observed a decrease in %Oct4+/Nanog+ cells when media were exchanged every 4 days, which could be rescued by either doubling the volume of E7 or increasing the frequency of E7 exchange (Supplementary Fig. S3.12). As the amount of bFGF was

the same in all conditions, these results suggest that bFGF depletion was not the only factor limiting hPSC maintenance and provide a proof-of-concept for how combining scalable factors like basal media volume with controlled release of expensive growth factors and signaling molecules may broadly facilitate cost reduction in cell biomanufacturing.

Finally, formation of mineral coatings on micro- and nano-scale carriers can enable their incorporation into three-dimensional (3D) hPSC aggregates, which may provide a means to overcome diffusion barriers encountered by soluble growth factor delivery from the bulk media. This is a particularly attractive feature for scalable cell biomanufacturing, as cell aggregates are increasingly being used for clinical and commercial-scale expansion of hPSCs and other adhesion-dependent cell types[56,57]. We demonstrated the utility of this approach in an experiment in which we incorporated varying amounts of bFGF-MCMs into the interior of large (~400 μm diameter) hPSC aggregates while keeping the total dose of bFGF (soluble + MCM-bound) the same between conditions (Supplementary Fig. S3.13). Aggregates cultured under standard conditions (bFGF provided in bulk E8 media) exhibited drastic loss of *NANOG* expression, in line with previous reports showing rapid pluripotency loss in large-diameter hPSC aggregates[58–60]. Notably, increasing the fraction of bFGF delivered from MCMs within the aggregates resulted in a dose-dependent increase in *NANOG*. Thus, sustained growth factor delivery from MCMs has potential broader utility for controlling stem cell expansion and differentiation in formats amenable to scalable suspension culture.

3.6 CONCLUSIONS

Advancing stem cell therapies is critically dependent on efficiently scaling up culture methods and reducing the costs of cell biomanufacturing. Here, we describe a scalable, materials-

based approach to reduce by >80% the amount of growth factor required for manufacturing human pluripotent stem cells. MCMs enabled this reduction by protecting bFGF from degradation while providing sustained, localized release of the active growth factor. Adoption of this mineral-based material, combined with statistically driven optimization methodologies such as DOE, has the potential to significantly improve scale-up and cost reduction in biomanufacturing of therapeutically relevant cell types.

3.7 MATERIALS AND METHODS

3.7.1 Fabrication and characterization of MCMs: Hydroxyapatite powder (Plasma Biotal Limited) was used as the microparticle core material. The core material was suspended at concentrations of 1 mg/mL in modified simulated body fluid (mSBF) formulated as follows: 141 mM NaCl, 4.0 mM KCl, 0.5 mM $MgSO_4$, 1.0 mM $MgCl_2$, 100 mM $NaHCO_3$, 20.0 mM HEPES, 5.0 mM $CaCl_2$, and 2.0 mM KH_2PO_4 with the pH was adjusted to 6.80. The suspension was rotated at 37°C for 24 hrs, at which point the microparticles were centrifuged at 2,000g for 2 min, and the supernatant decanted and replaced with freshly made mSBF. We repeated this process daily for 5 days, at which point the MCMs were washed three times with 50 mL deionized water, filtered through a cell strainer (40 µm pore size), suspended in 15 mL distilled water, flash frozen in liquid nitrogen, and lyophilized for 48 hrs. The lyophilized MCMs were then analyzed by SEM and calcium release assays as previously described[19,61]. MCMs were sputter-coated with gold and imaged on a LEO 1530 scanning electron microscope (Gemini) at 3kv. Ca^{2+} release was measured by incubating MCMs in 0.02 M Tris base buffer (pH 7.4) with gentle rotation, and centrifuging

MCMs, collecting supernatant, and replacing with fresh buffer daily. The supernatant Ca^{2+} concentration was measured by mixing 50 μL of supernatant with 150 μL of assay working solution containing 0.4 mM Arsenazo III (MP Biomedicals, Solon, OH). The absorbance of this solution was measured at 650 nm to determine Ca^{2+} concentration using a standard curve.

3.7.2 Generation of bFGF-loaded MCMs: MCMs were spread onto a flat surface and sterilized via UV irradiation for 30 min, then aliquotted into sterile tubes and stored until use. For MCM loading, sterilized MCMs were suspended in sterile PBS to make a 1 mg/mL stock solution, and appropriate volumes of recombinant human basic fibroblast growth factor (bFGF, carrier-free; R&D Systems) and MCM stock solutions were combined to achieve the desired final concentration of each in the loading solution (e.g., 1.0 μg/mL bFGF, 1.0 mg/mL MCMs for non-optimized loading; 0.456 μg/mL bFGF, 0.375 mg/mL MCMs for optimized loading). The MCM-bFGF solution was incubated at 37°C under constant rotation for 1 hr. The suspension was then centrifuged at 2000g for 3 min to pellet the MCMs. For cell culture experiments, the MCMs were resuspended in E7 media and used immediately unless otherwise stated. bFGF-loaded MCMs were prepared fresh every three passages for Transwell culture studies (unless otherwise specified) and prepared fresh at each passage in the direct culture studies. Protein binding efficiency was determined indirectly by Quantikine bFGF ELISA, by measuring the amount of bFGF in original loading solution and subtracting the amount of bFGF in the supernatant after MCM loading.

3.7.3 General culture of hPSCs: H1 human embryonic stem cells (WA01-DL-12, WiCell) or WTc11 human induced pluripotent stem cells (kindly provided by Dr. Bruce Conklin, Gladstone Institute of Cardiovascular Disease) were maintained in Essential 8 medium in 6-well plates coated

with Matrigel (8.7 μg/cm^2) at 37°C and 5% CO_2 in a humidified incubator. Media were exchanged daily, and cells were passaged onto new Matrigel-coated plates every 3 to 4 days by standard protocols[44] using Versene (Life Technologies). Media used in hPSC maintenance experiments were Essential 8 (E8, Life Technologies) and E7 (Essential 6 media (Life Technologies) supplemented with 1.76 ng/mL human transforming growth factor beta 1 (TGF-β1, carrier free; R&D Systems)).

3.7.4 Transwell culture method: MCMs or bFGF-MCMs were prepared as described above and added to polycarbonate Transwells (0.4 μm pore size) in 12-well culture plates (Corning). hPSCs were cultured on Matrigel as described above, in either E8 or E7 media as indicated in each figure. The Transwell inserts were removed while the cells were imaged via phase microscopy and the base media (i.e., without bFGF-MCMs) were exchanged daily. At each passage, the Transwell inserts were removed while the cells were passaged with Versene as described above. The cells were allowed to adhere to new Matrigel-coated plates for 30 min prior to adding Transwell inserts to the culture wells. Unless otherwise stated, the same Transwells (containing original bFGF-MCMs) were used throughout the entirety of an experiment and transferred to new wells at each passage.

3.7.5 Direct culture method: MCMs or bFGF-MCMs were prepared as described above and added directly to hPSCs cultured in 12-well culture plates on Matrigel, in either E8 or E7 media as indicated in each figure. The base media were exchanged daily (unless otherwise indicated) and the cells were imaged via phase microscopy. At each passage, the cells were passaged with Versene as described in the general hPSC culture method section. The cells were allowed to adhere

to new Matrigel-coated plates for 30 min prior to adding fresh bFGF-loaded MCMs directly into the new wells.

3.7.6 DOE design and modeling: We designed the surface-response design of experiments (DOE) using JMP software (SAS). The design was rotatable around a single center point with axial positions for two factors: bFGF concentration and MCM concentration during MCM loading. The factor levels were set at $\log_2$ steps (step sizes of -/+1 for the surface positions and -/+ 1.41 for the axial positions) away from the center point concentrations of 1 μg bFGF and 1 mg MCMs per mL, as specified by JMP. The DOE was carried out in triplicate and %$Oct4^+$/$Nanog^+$ at passage 3 was used as the response variable for all conditions. The model was generated with least squares fitting of linear and squared dependences for bFGF and MCM (bFGF, MCM, $bFGF^2$, and MCM^2) and crossed dependences for bFGF and MCM (bFGF*MCM) as factors for the $Oct4^+$/$Nanog^+$ response. The Factor Profiler in JMP was used to select the DOE-optimized MCM loading conditions using the desirability plot to identify concentrations of bFGF and MCMs that achieved 95% $Oct4^+$/$Nanog^+$ while minimizing total bFGF.

3.7.7 Quantification of Oct4+/Nanog+ populations by flow cytometry: Briefly, hPSCs were collected, washed with PBS, and incubated with 0.25% trypsin/EDTA for 8-10 min at 37°C followed by pipetting to dissociate. Trypsin activity was quenched by adding 2X volume of 20% FBS in RPMI supplemented with 5 μM Y-27632. Samples were centrifuged at 200g for 5 min and pelleted samples were fixed with 1% paraformaldehyde for 20 min at room temperature, permeabilized with ice-cold 90% methanol for 15 min at 4°C, and stored at -20°C until processing. Samples were washed twice with Flow Buffer 1 (0.5% BSA in PBS) to remove residual methanol,

incubated for 1 hr at room temperature with primary antibodies in Flow Buffer 2 (0.5% BSA + 0.1% Triton X-100 in PBS), washed with Flow Buffer 2, and incubated in the dark for 30 min at room temperature with secondary antibodies in Flow Buffer 2. Samples were washed twice with Flow Buffer 2, resuspended in Flow Buffer 1, and stored on ice prior to analysis. Data were collected on a MACSQUANT flow cytometer (Miltenyi Biotec) and analyzed using FlowJo software. Primary antibodies and dilutions used were mouse anti-human Oct3/4 (Santa Cruz Biotechnology, sc-5279, 1:400), rabbit anti-human Nanog (Cell Signaling Technology, 4903S, 1:200). Secondary antibodies and dilutions used were goat anti-mouse AlexaFluor 488 and goat anti-rabbit AlexaFluor 647 (Thermo Fisher Scientific, 1:1000 each).

3.7.8 Immunocytochemistry: Samples were fixed with 10% neutral buffered formalin for 15 min, permeabilized with 0.2% Triton X-100 in PBS for 5 min, blocked with 1% BSA in PBS for 30 min, and stained with primary antibodies (dilutions made in 1% BSA in PBS) for 1 hr at room temperature. Samples were washed three times with 0.05% Tween-20 in PBS and stained with secondary antibodies (dilutions made in PBS) for 1 hr at room temperature or overnight at 4°C. Nuclei were counterstained with DAPI. Primary antibodies and dilutions used: mouse anti-human Oct3/4 (Santa Cruz Biotechnology, sc-5279, 1:100), rabbit anti-human Nanog (Cell Signaling Technology, 4903S, 1:100), mouse IgG2a anti-βIII tubulin (R&D, MAB1195, 1:200), mouse IgG2b anti-alpha fetoprotein (R&D, MAB1369, 1:200), rabbit anti-alpha smooth muscle actin (Abcam, ab124964, 1:200), mouse IgG1 anti-PECAM-1 (EMD Millipore, MAB2184, 1:50). Secondary antibodies and dilutions used were goat anti-mouse AlexaFluor 488, goat anti-mouse IgG2a AlexaFluor 488, goat anti-rabbit or anti-mouse AlexaFluor 568, and goat anti-mouse IgG2b AlexaFluor 647 (Thermo Fisher Scientific, 1:1000 for all secondaries).

3.7.9 Spontaneous differentiation of embryoid bodies: To form spontaneous EBs, hPSCs in standard E8 culture (6-well format) were washed with PBS and incubated in pre-warmed Dispase (Gibco, 1 U/mL) for 3 min at 37°C. Dispase was removed by aspiration and 2 mL PBS was added per well. Cells were dislodged from the culture surface using a cell scraper and the cell suspension was added to a tube and centrifuged for 200g/5 min. The cell pellet from each individual well was resuspended in 2.5 mL of E8 supplemented with 5 μM Y-27632 and the cell suspension was added to a 6-well ultra-low adhesion culture plate (Corning). The time of initial seeding was designated as "day -3." EBs were subjected to spontaneous differentiation as previously described[60]. Briefly, EBs were transitioned from E8 to differentiation medium (DM) from day 0 to day 3; EBs were placed in 75:25 E8:DM at day 0, 50:50 E8:DM at day 1, 25:75 E8:DM at day 2, and 100% DM at day 3, and maintained in DM thereafter. DM consisted of 20% Knockout Serum Replacement in Knockout-DMEM with 0.1 mM β-mercaptoethanol, 1% non-essential amino acids, and 1% L-glutamine. At day 4, EBs were transferred to Matrigel-coated plates and allowed to form adherent outgrowths. Media was changed on adherent EBs every 2 days. Adherent EBs were fixed with 10% neutral buffered formalin at day 14 for analysis.

3.7.10 Directed differentiation toward ectoderm, mesoderm, and endoderm lineages: H1 hESCs and WTc11 hiPSCs were subjected to directed differentiation following established protocols. *Neural progenitor differentiation (adapted from* [62]*):* Starting from 60% confluency, hPSCs were passaged via Accutase and seeded in SB medium (DF3S containing 10 μg/mL transferrin, 5 μg/mL insulin, and 10 μM SB431542) supplemented with 100 ng/mL basic fibroblast growth factor (bFGF) and 10 μM Y-27632 at a density of $5x10^4$ cells/well in 12-well Matrigel-

coated plates. DF3S medium consisted of DMEM/F-12, L-ascorbic acid-2-phosphate magnesium (64 µg/mL), sodium selenium (14 ng/mL), and $NaHCO_3$ (543 µg/mL). The cells were transitioned to medium without Y-27632 the following day. The adherent cells were then transitioned to either SB medium for hindbrain specification or SBNog medium (SB medium containing 100 ng/mL Noggin) for forebrain specification and maintained in the respective media for 6 days with daily media exchange. On day 9, the cells were passaged with Accutase at a 1:6 ratio and seeded onto Matrigel-coated plates in Neural Expansion Medium (DF3S medium containing N-2 supplement, B-27 supplement, and 5 ng/mL bFGF). Neural Expansion Medium was changed every 2-3 days and the cells were passaged 1:6 with Accutase every 6-8 days. The cells were maintained in Neural Expansion Medium for a total of 24 days prior to fixing for immunocytochemistry.

Endothelial differentiation (adapted from [63]*):* hPSCs at 80% confluency were dissociated with Accutase (Invitrogen) and passaged 1:4 onto Matrigel-coated plates. hPSCs were differentiated into mesoderm by culturing for 2 days in E8BAC medium (Essential 8 with 5 ng/mL bone morphogenetic protein (BMP)-4, 25 ng/mL Activin A, and 1 µM CHIR-99021), with 10 µM Y-27632 included in the media on the first day to improve cell survival. Mesoderm was then cultured for 4 days in E7Vi medium (Essential 6 with 100 ng/mL bFGF, 50 ng/mL vascular endothelial growth factor (VEGF)-A165, and 5 µM SB431542) before fixing for immunocytochemistry.

Hepatocyte differentiation (adapted from [64]*):* One day before starting differentiation, hPSCs were dissociated with Accutase and seeded onto Matrigel-coated plates at 5 x 10^4 cells/cm^2 in E8 supplemented with 10 µM Y-27632. To initiate differentiation, media was changed to RPMI containing 1X B-27 minus insulin and 100 ng/mL Activin A on the day after seeding. Cells were maintained in this differentiation medium for a total of three days. Media was then changed to RPMI + B-27 minus insulin supplemented with 30 ng/mL FGF-4 and 20 ng/mL BMP-2 for five

days. Finally, cells were maintained in RPMI + B-27 minus insulin supplemented with 20 ng/mL hepatocyte growth factor (HGF) for an additional five days, prior to fixing for immunocytochemistry.

3.7.11 Karyotyping and teratoma assays: Samples were provided to WiCell (Madison, WI) for teratoma formation assays and G-banded karyotyping with analysis and interpretation by the Cytogenetics Lab at WiCell. Histology from teratoma assays was analyzed and interpreted by the Comparative Pathology Laboratory of the University of Wisconsin-Madison.

3.7.12 ELISAs: ELISAs for measuring bFGF (Quantikine basic FGF ELISA, R&D Systems, DFB50), phosphoERK and total ERK (Abcam, ab176660) were performed following the manufacturer's recommended protocol. MCMs were confirmed not to interfere with bFGF Quantikine ELISA readouts (Supplementary Fig. S3.9). For phosphoERK and total ERK assays, 10 µg total protein was loaded per well of the ELISA based on protein concentration of cell lysates as quantified by microBCA.

3.7.13 bFGF biological activity: For experiments correlating bFGF ELISA readout to ERK phosphorylation, hPSCs were starved of bFGF (in E7) for 24 hrs, followed by 2 hr restimulation with E7 containing different concentrations of fresh bFGF in solution (created by mixing E8 and E7 media at different ratios). For experiments correlating loss of bFGF bioactivity to ERK phosphorylation, E8 media was incubated for 1, 6, or 24 hr at 37°C or 65°C and allowed to cool before restimulating bFGF-starved hPSCs as described above. bFGF content in restimulation media was measured by Quantikine bFGF ELISA. Relative phosphoERK content in restimulated

hPSCs was determined by phosphoERK and total ERK ELISAs on cell lysates. Briefly, cells were washed with PBS and resuspended in ice-cold RIPA buffer containing 1X Halt Protease/Phosphatase Inhibitor Cocktail. Samples were agitated for 15 min at 4°C and spun at 12,000g for 15 min at 4°C. The supernatants from samples were collected and total protein in lysates was quantified by microBCA assay (Thermo Fisher Scientific). For experiments comparing thermal stability of free bFGF vs. MCM-bound bFGF, solutions containing 100 ng/mL bFGF in E7 or 62 µg/mL optimized bFGF-MCMs in E7 (to match usage in cell culture experiments) were stored at 4°C or incubated for different durations at 37°C prior to assessing active bFGF content via Quantikine bFGF ELISA.

3.7.14 Comparison of bFGF-MCMs and PLGA microspheres: bFGF-releasing PLGA microspheres (StemBeads® FGF2) were purchased from StemCultures. For all comparison studies, bFGF-MCMs and PLGA microspheres were resuspended to concentrations equivalent to those used in cell culture experiments (62 µg/mL for optimized bFGF-MCMs; 8 µL/mL for PLGA microspheres, following manufacturer's recommendations).

Active and total bFGF release. bFGF-MCMs and PLGA microspheres were suspended in DF3S medium (Thermo Fisher Scientific), as TGF-β1 in E7 was found to contribute substantial background to the total protein measurement. The resulting solutions were incubated and rotated at 37°C with daily collection of releasate over 4 days. To measure active bFGF release, a fraction of the homogeneous MCM and microsphere suspensions was first collected. To measure total bFGF release, the MCM or microsphere suspensions were then centrifuged at 22,000g/2 min and the supernatant was collected and fresh DF3S medium replaced. The amount of active and total bFGF released were determined by Quantikine bFGF ELISA (R&D Systems) and NanoOrange

Protein Quantitation kit (Thermo Fisher Scientific), respectively. Cumulative daily values of active bFGF release were extrapolated from bFGF content in releasates during the 2 hr sample incubation step of the bFGF Quantikine ELISA (Supplementary Fig. S3.9). Quantitation of total protein content by NanoOrange was performed after concentrating releasates with Amicon 3 kDa MWCO Centrifugal Filter Units (EMD Millipore).

3.7.15 Incorporation of bFGF-MCMs into 3D hPSC aggregates: hPSCs were singularized and optimized bFGF-MCMs were fabricated as described above. For each $bFGF_{sol}$:$bFGF_{MCM}$ condition, total bFGF quantity ($bFGF_{sol}$ + $bFGF_{MCM}$) and total media volume were held constant. Cell pellets were resuspended in $bFGF_{sol}$ fractions prepared by combining E8 (100 ng/mL bFGF) and E7 (0 ng/mL bFGF) in appropriate ratios to achieve the desired concentration of $bFGF_{sol}$, and varying quantities of bFGF-MCMs (resuspended in E7) were added to cell suspensions accordingly. Cell suspensions were dispensed into wells containing agarose microwells and hPSC aggregates containing ~17,500 cells each were formed by forced centrifugation as previously described[60]. Aggregates were collected at 72 hr following seeding and washed with PBS prior to isolation of total RNA using the RNeasy mini kit (Qiagen) according to manufacturer's instructions. RNA was reverse transcribed into cDNA using the QuantiTect Reverse Transcription Kit (Qiagen). cDNA (2.75 ng input RNA/10 μL reaction) was mixed with Qiagen SYBR Green Master Mix and QuantiTect *NANOG* primer (Qiagen, QT01025850), and run on a LightCycler 4800 system according to the manufacturer's protocol. *ACTB* (Qiagen, QT00095431) was used as a reference gene.

3.7.16 Figure generation and statistics: All schematic graphics were created by the authors using Adobe Illustrator and Photoshop except for the microparticle graphic, which was commissioned from professional graphic designer. The DOE graphs and models were generated in JMP while all other graphs were generated in GraphPad Prism. Statistics between $Oct4^+/Nanog^+$ population percentages were done in GraphPad Prism. The degree of significance for each comparison is denoted in each figure/caption.

3.8 ACKNOWLEDGMENTS AND AUTHOR CONTRIBUTIONS

WTc11 human induced pluripotent cells were kindly provided by Dr. Bruce Conklin (UCSF/Gladstone Institutes). The authors acknowledge support from staff and the use of equipment at the Materials Science Center (NSF DMR-1121288), the UW Carbone Cancer Center Flow Cytometry Laboratory (Support Grant P30 CA014520), and the UW Comparative Pathology Laboratory at UW-Madison. This work was supported by funding from the National Institutes of Health (R01HL093282 to W.L.M.; Biotechnology Training Program NIGMS 5 T32-GM08349 to A.W.X. and A.S.K.), the U.S. Environmental Protection Agency (STAR grant no. 83573701 to W.L.M.), and the National Science Foundation (DGE-1256259 to A.W.X. and A.S.K.; DMR-1306482 to W.L.M.)

A.W.X., A.S.K., and W.L.M. designed the study; A.W.X., A.S.K., and H.J.J. performed the experiments and analyzed data; A.W.X., A.S.K., and W.L.M. wrote the manuscript; and all authors reviewed and approved the manuscript.

3.9 REFERENCES

1. Fox, I. J. *et al.* Use of differentiated pluripotent stem cells in replacement therapy for treating disease. *Science (80-.).* **345,** 1247391–1247391 (2014).

2. Trounson, A. & DeWitt, N. D. Pluripotent stem cells progressing to the clinic. *Nat. Rev. Mol. Cell Biol.* **17,** 194–200 (2016).

3. Serra, M., Brito, C., Correia, C. & Alves, P. M. Process engineering of human pluripotent stem cells for clinical application. *Trends Biotechnol.* **30,** 350–359 (2012).

4. Carmen, J., Brindley, D. A., Davie, N. L. & Smith, D. in *Stem Cells in Regenerative Medicine* 49–68 (John Wiley & Sons, Ltd, 2016). doi:10.1002/9781118846193.ch4

5. Pigeau, G. M., Csaszar, E. & Dulgar-Tulloch, A. Commercial Scale Manufacturing of Allogeneic Cell Therapy. *Front. Med.* **5,** 1–8 (2018).

6. Chen, G., Gulbranson, D. R., Yu, P., Hou, Z. & Thomson, J. A. Thermal Stability of Fibroblast Growth Factor Protein Is a Determinant Factor in Regulating Self-Renewal, Differentiation, and Reprogramming in Human Pluripotent Stem Cells GUOKAI. *Stem Cells* **30,** 623–630 (2012).

7. Lotz, S. *et al.* Sustained Levels of FGF2 Maintain Undifferentiated Stem Cell Cultures with Biweekly Feeding. *PLoS One* **8,** 1–10 (2013).

8. Lopes, A. G., Sinclair, A. & Frohlich, B. Cost Analysis of Cell Therapy Manufacture: Autologous Cell Therapies, Part 1. *Bioprocess Int.* **16,** S3–S8 (2018).

9. Lipsitz, Y. Y. *et al.* A roadmap for cost-of-goods planning to guide economic production of cell therapy products. *Cytotherapy* **19,** 1383–1391 (2017).

10. Levenstein, M. E. *et al.* Basic Fibroblast Growth Factor Support of Human Embryonic Stem Cell Self-Renewal. *Stem Cells* **24,** 568–574 (2006).

11. Buchtova, M. *et al.* Instability restricts signaling of multiple fibroblast growth factors. *Cell. Mol. Life Sci.* **72,** 2445–2459 (2015).

12. Ludwig, T. E. *et al.* Derivation of human embryonic stem cells in defined conditions. *Nat. Biotechnol.* **24,** 185–187 (2006).

13. Horiguchi, I., Urabe, Y., Kimura, K. & Sakai, Y. Effects of glucose, lactate and basic FGF as limiting factors on the expansion of human induced pluripotent stem cells. *J. Biosci. Bioeng.* **125,** 111–115 (2017).

14. Jongpaiboonkit, L., Franklin-Ford, T. & Murphy, W. L. Mineral-coated polymer microspheres for controlled protein binding and release. *Adv. Mater.* **21,** 1960–1963 (2009).

15. Jongpaiboonkit, L., Franklin-Ford, T. & Murphy, W. L. Mineral-Coated Polymer Microspheres for Controlled Protein Binding and Release. *Adv. Mater.* **21,** 1960–1963 (2009).

16. Lee, J. S., Lu, Y., Baer, G. S., Markel, M. D. & Murphy, W. L. Controllable protein

delivery from coated surgical sutures. *J. Mater. Chem.* **20,** 8894–8903 (2010).

17. Lee, J. S., Suarez-Gonzalez, D. & Murphy, W. L. Mineral Coatings for Temporally Controlled Delivery of Multiple Proteins. *Adv. Mater.* **23,** 4279–4284 (2011).

18. Suárez-González, D. *et al.* Controllable mineral coatings on PCL scaffolds as carriers for growth factor release. *Biomaterials* **33,** 713–721 (2012).

19. Yu, X., Khalil, A., Dang, P. N., Alsberg, E. & Murphy, W. L. Multilayered inorganic microparticles for tunable dual growth factor delivery. *Adv. Funct. Mater.* **24,** 3082–3093 (2014).

20. Yu, X. *et al.* Nanostructured Mineral Coatings Stabilize Proteins for Therapeutic Delivery. *Adv. Mater.* **29,** 1701255 (2017).

21. Clements, A. E. B., Groves, E. R., Chamberlain, C. S., Vanderby, R. & Murphy, W. L. Microparticles Locally Deliver Active Interleukin-1 Receptor Antagonist In Vivo. *Adv. Healthc. Mater.* **7,** 1–8 (2018).

22. Bikfalvi, A., Klein, S., Pintucci, G. & Rifkin, D. B. Biological roles of fibroblast growth factor-2. *Endocr. Rev.* **18,** 26–45 (1997).

23. Xu, C. *et al.* Basic Fibroblast Growth Factor Supports Undifferentiated Human Embryonic Stem Cell Growth Without Conditioned Medium. *Stem Cells* **23,** 315–323 (2005).

24. Vallier, L. Activin/Nodal and FGF pathways cooperate to maintain pluripotency of human embryonic stem cells. *J. Cell Sci.* **118,** 4495–4509 (2005).

25. Xiao, L., Yuan, X. & Sharkis, S. J. Activin A Maintains Self-Renewal and Regulates Fibroblast Growth Factor, Wnt, and Bone Morphogenic Protein Pathways in Human Embryonic Stem Cells. *Stem Cells* **24,** 1476–1486 (2006).

26. Greber, B., Lehrach, H. & Adjaye, J. Fibroblast Growth Factor 2 Modulates Transforming Growth Factor β Signaling in Mouse Embryonic Fibroblasts and Human ESCs (hESCs) to Support hESC Self-Renewal. *Stem Cells* **25,** 455–464 (2007).

27. Singh, H. & Brivanlou, A. H. *The Molecular Circuitry Underlying Pluripotency in Embryonic Stem Cells and iPS Cells*. *Principles of Regenerative Medicine* **3,** (Elsevier Inc., 2011).

28. Greber, B., Lehrach, H. & Adjaye, J. Control of Early Fate Decisions in Human ES Cells by Distinct States of TGFβ Pathway Activity. *Stem Cells Dev.* **17,** 1065–1078 (2008).

29. Yao, S. *et al.* Long-term self-renewal and directed differentiation of human embryonic stem cells in chemically defined conditions. *Proc. Natl. Acad. Sci. U. S. A.* **103,** 6907–12 (2006).

30. Lu, J., Hou, R., Booth, C. J., Yang, S.-H. & Snyder, M. Defined culture conditions of human embryonic stem cells. *Proc. Natl. Acad. Sci. U. S. A.* **103,** 5688–5693 (2006).

31. Akopian, V. *et al.* Comparison of defined culture systems for feeder cell free propagation of human embryonic stem cells. *Vitr. Cell. Dev. Biol. - Anim.* **46,** 247–258 (2010).

32. Chen, G. *et al.* Chemically defined conditions for human iPS cell derivation and culture. *Nat. Methods* **8,** 424–429 (2011).

33. Wang, Y. *et al.* Scalable expansion of human induced pluripotent stem cells in the defined xeno-free E8 medium under adherent and suspension culture conditions. *Stem Cell Res.* **11,** 1103–1116 (2013).

34. Badenes, S. M. *et al.* Defined Essential 8^{TM} Medium and Vitronectin Efficiently Support Scalable Xeno-Free Expansion of Human Induced Pluripotent Stem Cells in Stirred Microcarrier Culture Systems. *PLoS One* **11,** e0151264 (2016).

35. Shiba, T. *et al.* Modulation of mitogenic activity of fibroblast growth factors by inorganic polyphosphate. *J. Biol. Chem.* **278,** 26788–26792 (2003).

36. Beenken, A. & Mohammadi, M. The FGF family: Biology, pathophysiology and therapy. *Nat. Rev. Drug Discov.* **8,** 235–253 (2009).

37. Dvorak, P. *et al.* Computer-assisted engineering of hyperstable fibroblast growth factor 2. *Biotechnol. Bioeng.* 1–13 (2018). doi:10.1002/bit.26531

38. Keire, D. *et al.* Diversifying the global heparin supply chain: Reintroduction of bovine heparin in the united states? *BioPharm Int.* **28,** 36–42 (2015).

39. Oduah, E. I., Linhardt, R. J. & Sharfstein, S. T. Heparin: Past, present, and future. *Pharmaceuticals* **9,** 1–12 (2016).

40. Derda, R. *et al.* High-Throughput Discovery of Synthetic Surfaces That Support Proliferation of Pluripotent Cells. **282,** 1289–1295 (2010).

41. Mei, Y. *et al.* Combinatorial development of biomaterials for clonal growth of human pluripotent stem cells. *Nat. Mater.* **9,** 768–78 (2010).

42. Brafman, D. a *et al.* Long-term human pluripotent stem cell self-renewal on synthetic polymer surfaces. *Biomaterials* **31,** 9135–44 (2010).

43. Villa-Diaz, L. G. *et al.* Synthetic polymer coatings for long-term growth of human embryonic stem cells. *Nat. Biotechnol.* **28,** 581–583 (2010).

44. Beers, J. *et al.* Passaging and colony expansion of human pluripotent stem cells by enzyme-free dissociation in chemically defined culture conditions. *Nat. Protoc.* **7,** 2029–2040 (2012).

45. Clements, A. E. B., Leiferman, E. M., Chamberlain, C. S., Vanderby, R. & Murphy, W. L. Addition of Mineral-Coated Microparticles to Soluble Interleukin-1 Receptor Antagonist Injected Subcutaneously Improves and Extends Systemic Interleukin-1 Inhibition. *Adv. Ther.* **1800048,** 1800048 (2018).

46. Fu, K., Klibanov, A. M. & Langer, R. Protein stability in controlled-release systems. *Nat. Biotechnol.* **18,** 24–25 (2000).

47. Mozhaev, V. V., Sergeeva, M. V., Belova, A. B. & Khmelnitsky, Y. L. Multipoint attachment to a support protects enzyme from inactivation by organic solvents: α-Chymotrypsin in aqueous solutions of alcohols and diols. *Biotechnol. Bioeng.* **35,** 653–

659 (1990).

48. Takahashi, H. *et al.* Catalytic activity in organic solvents and stability of immobilized enzymes depend on the pore size and surface characteristics of mesoporous silica. *Chem. Mater.* **12,** 3301–3305 (2000).

49. Kim, J. & Grate, J. W. Single-enzyme nanoparticles armored by a nanometer-scale organic/inorganic network. *Nano Lett.* **3,** 1219–1222 (2003).

50. Wang, P. Nanoscale biocatalyst systems. *Curr. Opin. Biotechnol.* **17,** 574–579 (2006).

51. Giri, J., Li, W. J., Tuan, R. S. & Cicerone, M. T. Stabilization of proteins by nanoencapsulation in sugar-glass for tissue engineering and drug delivery applications. *Adv. Mater.* **23,** 4861–4867 (2011).

52. Zhu, G., Mallery, S. R. & Schwendeman, S. P. Stabilization of proteins encapsulated in injectable poly (lactide-co- glycolide). *Nat. Biotechnol.* **18,** 52–57 (2000).

53. Chen, R. R. & Mooney, D. J. Polymeric growth factor delivery strategies for tissue engineering. *Pharm. Res.* **20,** 1103–1112 (2003).

54. Zisch, A. H., Lutolf, M. P. & Hubbell, J. A. Biopolymeric delivery matrices for angiogenic growth factors. *Cardiovasc. Pathol.* **12,** 295–310 (2003).

55. Ansorge, M. & Pompe, T. Systems for localized release to mimic paracrine cell communication in vitro. *J. Control. Release* **278,** 24–36 (2018).

56. Kempf, H. *et al.* Controlling expansion and cardiomyogenic differentiation of human pluripotent stem cells in scalable suspension culture. *Stem Cell Reports* **3,** 1132–1146 (2014).

57. Adil, M. M. & Schaffer, D. V. Expansion of human pluripotent stem cells. *Curr. Opin. Chem. Eng.* **15,** 24–35 (2017).

58. Sachlos, E. & Auguste, D. T. Embryoid body morphology influences diffusive transport of inductive biochemicals: A strategy for stem cell differentiation. *Biomaterials* **29,** 4471–4480 (2008).

59. Van Winkle, A. P., Gates, I. D. & Kallos, M. S. Mass transfer limitations in embryoid bodies during human embryonic stem cell differentiation. *Cells Tissues Organs* **196,** 34–47 (2012).

60. Xie, A. W. *et al.* Controlled Self-assembly of Stem Cell Aggregates Instructs Pluripotency and Lineage Bias. *Sci. Rep.* **7,** 1–15 (2017).

61. Choi, S., Yu, X., Jongpaiboonki, L., Hollister, S. J. & Murphy, W. L. Inorganic coatings for optimized non-viral transfection of stem cells. *Sci. Rep.* **3,** 1567–93 (2013).

62. Chambers, S. M. *et al.* Highly efficient neural conversion of human ES and iPS cells by dual inhibition of SMAD signaling. *Nat. Biotechnol.* **27,** 275–280 (2009).

63. Zhang, J. *et al.* A Genome-wide Analysis of Human Pluripotent Stem Cell-Derived Endothelial Cells in 2D or 3D Culture. *Stem Cell Reports* **8,** 907–918 (2017).

64. Sengupta, S. *et al.* Aggregate culture of human embryonic stem cell-derived hepatocytes in suspension are an improved in vitro model for drug metabolism and toxicity testing. *Toxicol. Sci.* **140,** 236–45 (2014).

3.10 FIGURES

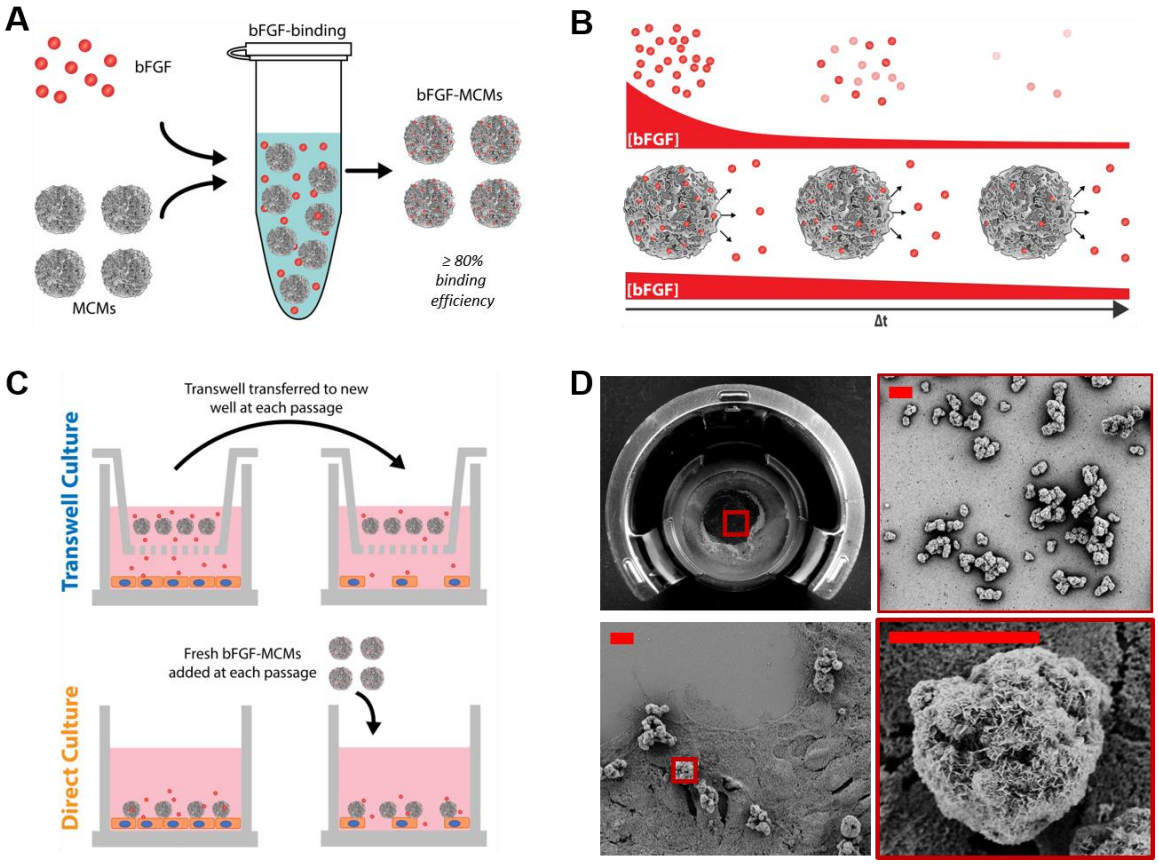

Figure 3.1 MCMs bind and release bFGF for sustained bFGF presentation in hPSC culture. (A) Schematic for binding of bFGF to mineral-coated microparticles (MCMs) in solution. (B) Proposed model for presentation and presence of bioactive bFGF over time in (top) conventional chemically-defined hPSC culture or (bottom) culture with bFGF-loaded MCMs (bFGF-MCMs). bFGF loses activity over time when delivered as soluble protein via daily media changes in culture, while MCMs stabilize and allow sustained release of bioactive bFGF. (C) Schematic representation of two culture formats employed in this study: Transwell culture, in which MCMs release bFGF from Transwells, and direct culture, in which MCMs releasing bFGF are added directly to cells. (D) Photographs and scanning electron micrographs of bFGF-MCMs in (top) 12-well Transwell format and (bottom) direct culture format with hPSCs. Scale bar = 10 μm.

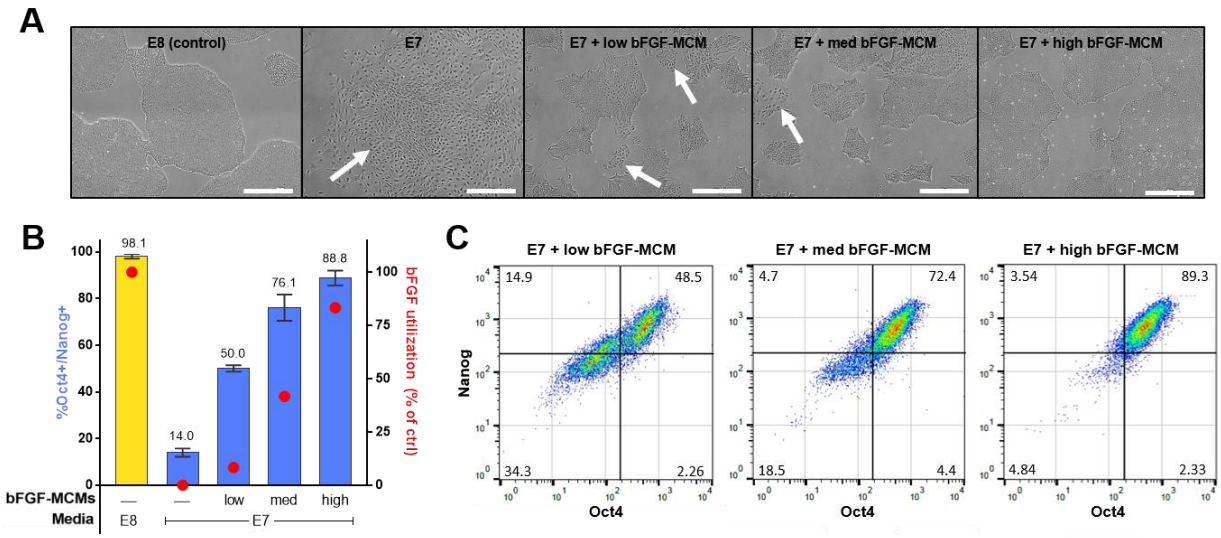

Figure 3.2 bFGF-loaded MCMs (bFGF-MCMs) in Transwell culture have a dose-dependent effect on the percentage of hPSCs expressing Oct4 and Nanog. (A) Representative images of H1 hPSCs at passage 3 (day 12) of culture in E8 (control) or E7 with varying doses of bFGF-MCMs (scale bar = 250 µm). Colonies with normal stem cell morphology were observed in the E8 control and E7 + high bFGF-MCM conditions, while varying degrees of spontaneous differentiation were seen in the E7, E7 + low bFGF-MCM, and E7 + med bFGF-MCM conditions (white arrows). (B) Quantification of Oct4/Nanog expression in hPSCs grown with or without bFGF-MCMs in Transwell culture for 3 passages (n = 3, error bars = s.d.), as assessed by flow cytometry. *n* = 3, error bars = s.d. (C) Representative flow cytometry plots of hPSCs after Transwell culture with E7 containing low, medium, or high doses of bFGF-MCMs for 3 passages. bFGF utilization as denoted on the right y-axis was calculated based on amount of bFGF used to maintain a single well of hPSCs in a 12-well plate format (1 mL media/well) for three passages, relative to E8 control (100%).

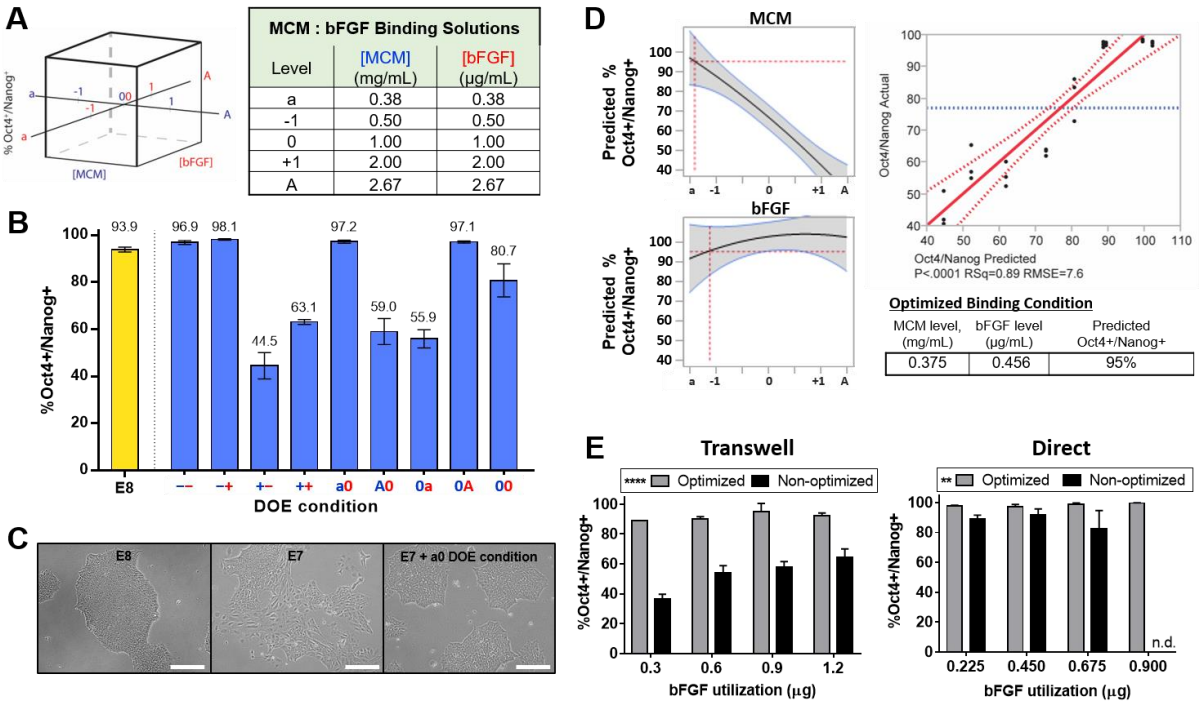

Figure 3.3 Design of Experiments (DOE) optimization of bFGF binding solution identifies MCM conditions that maintain hPSC pluripotency marker expression while minimizing bFGF usage. (A) Representation of DOE experimental space. The concentrations of bFGF and MCMs in the binding solution were varied while the total amount of bFGF-MCMs used in Transwell culture was held constant. %Oct4+/Nanog+ hPSCs at passage 3 was measured as the response variable. (B) Flow cytometry quantification of %Oct4+/Nanog+ hPSCs cultured with bFGF-MCMs from each DOE condition for 3 passages. $n = 3$, error bars = s.d. (C) Representative images of hPSCs in E8 medium, E7 medium, and the a0 DOE condition in E7. (D) Results of the DOE-generated model. The model allowed for identification of an optimized binding solution that minimizes bFGF utilization with a predicted 95% Oct4+/Nanog+ cell population at passage 3 of Transwell culture. (E) Comparison of the performance of DOE-optimized MCMs vs. non-optimized MCMs in maintaining hPSC pluripotency in Transwell (left) and direct (right) culture formats. For each culture format, four bFGF-MCM doses were tested, with total bFGF utilization matched between optimized and non-optimized MCMs for each respective dose. bFGF utilization as denoted on the x-axis was calculated based on amount of bFGF used to maintain a single well of hPSCs in a 12-well plate format (1 mL media/well) for three passages (see Supplementary Table S3.2). $n = 3$, error bars = s.d.; **** $p < 0.0001$, ** $p < 0.01$; two-way ANOVA. "n.d." denotes a condition for which P3 flow cytometry data were not collected due to inability of the hPSCs to be effectively passaged at the corresponding dose of non-optimized bFGF-MCMs.

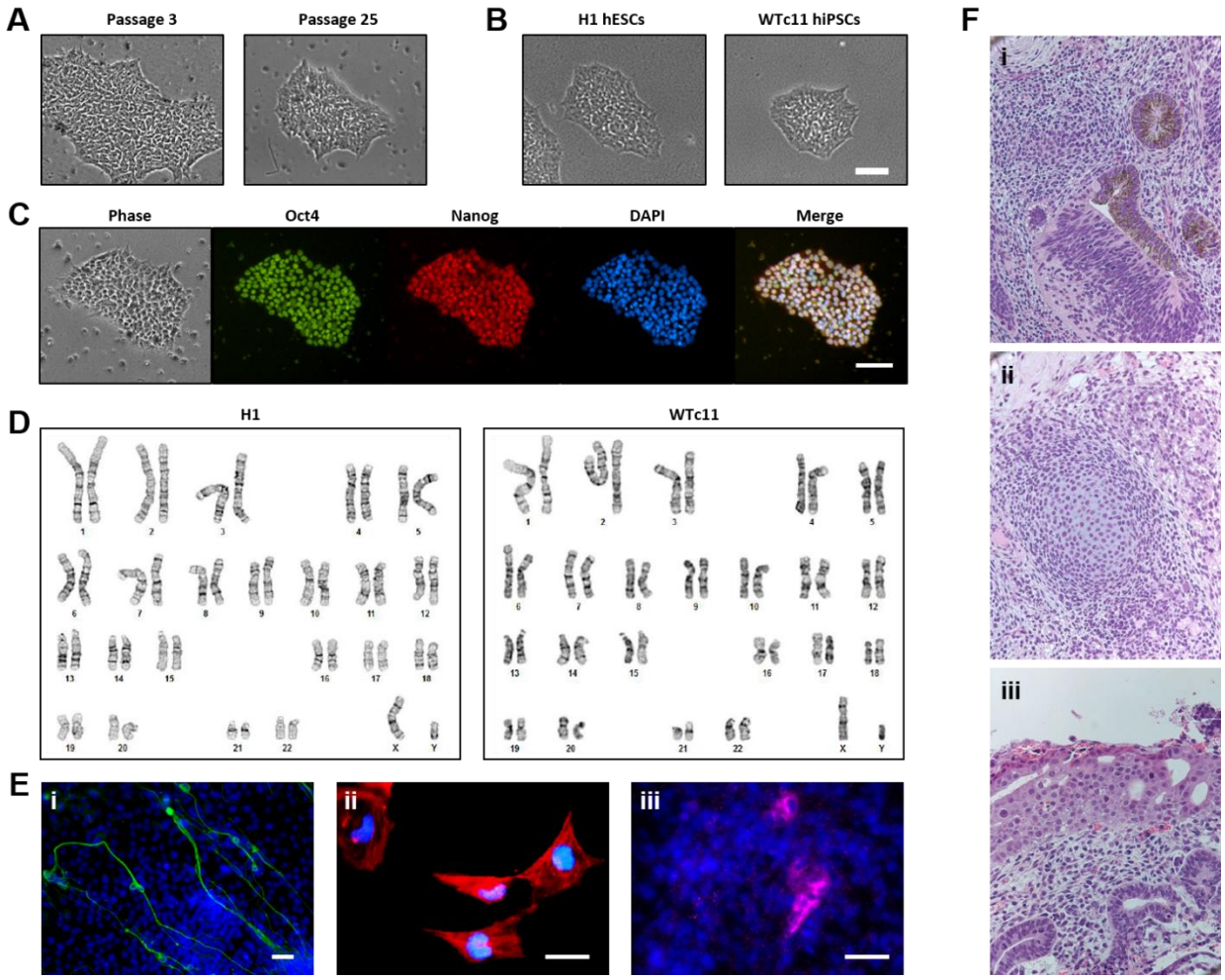

Figure 3.4 Direct culture with optimized bFGF-MCMs maintains hPSC pluripotency and normal karyotype during long-term culture. (A) Comparison of colony morphology in H1 hESCs at passages 3 and 25 with bFGF-MCMs. (B) hPSCs in direct culture with bFGF-MCMs can be transitioned back to E8/Matrigel with minimal MCM carryover within 2 passages, and display normal hPSC colony morphology. Scale bars = 100 µm. (C) hPSCs in direct culture with bFGF-MCMs for 25 passages maintain robust expression of pluripotency markers Oct4 and Nanog. Scale bar = 100 µm. (D) G-banded karyotyping of hPSCs maintained in direct culture with optimized bFGF-MCMs for 25 passages. (E) hPSCs in direct culture with bFGF-MCMs retain the potential to spontaneously differentiate into derivatives of the three primary germ layers. EBs were formed, allowed to spontaneously differentiate and adhere to Matrigel-coated dishes, and stained for markers of i) ectoderm (beta-III tubulin), ii) mesoderm (alpha smooth muscle actin), and iii) endoderm (alpha-fetoprotein) lineages. Scale bars = 50 µm. (F) Histological analysis of teratomas generated from hPSCs after long-term (25 passages) direct culture with bFGF-MCMs. Differentiation into all three germ layers is shown: (i) ectoderm (neuroepithelium, pigmented retinal tissue), (ii) mesoderm (cartilage) and endoderm (liver). Images shown in (E) and (F) are for H1 hESCs.

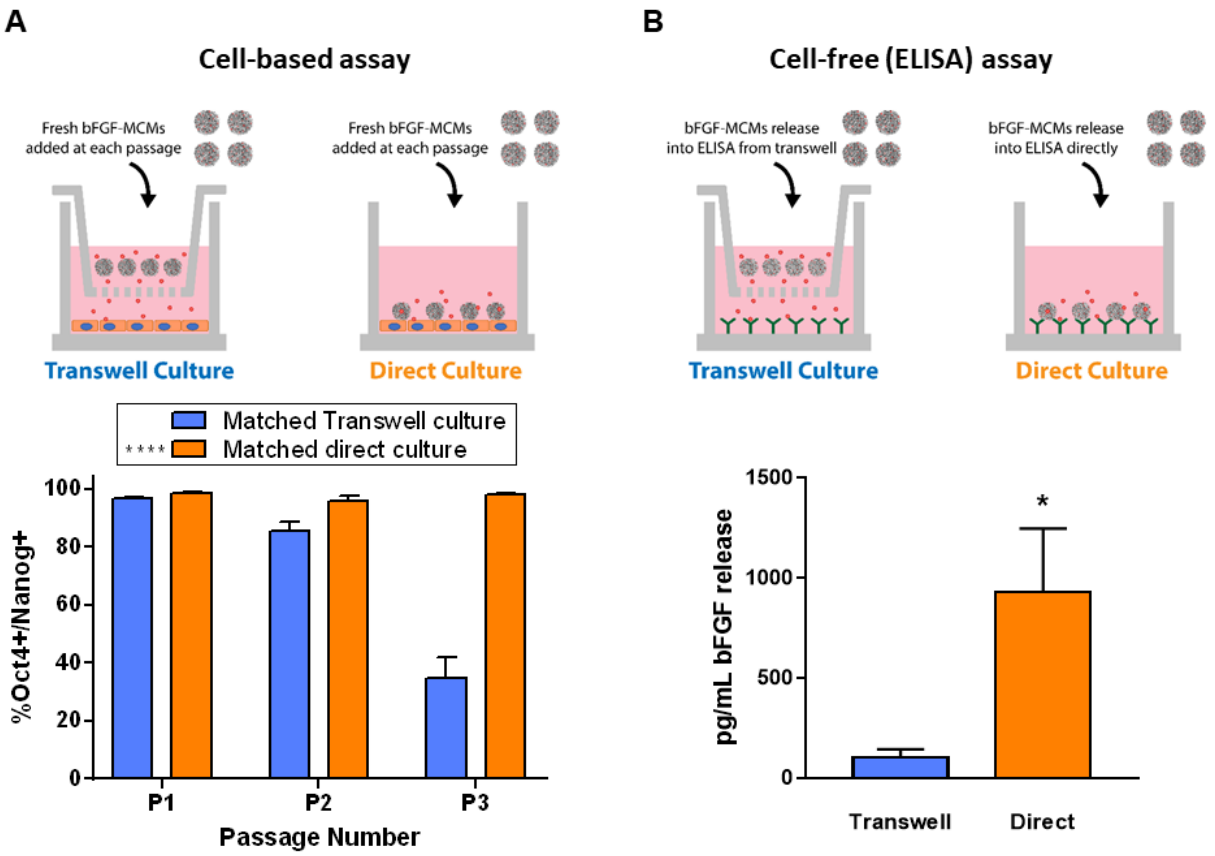

Figure 3.5 Local delivery increases growth factor biological potency. (A) %Oct4/Nanog expression of hPSCs cultured with the same amount of optimized bFGF-MCMs in either Transwell or direct culture. In this experiment, fresh MCMs were replaced at each passage (i.e., every 4 days) in both Transwell and direct culture formats. $n = 3$, error bars = s.d.; **** $p < 0.0001$, two-way ANOVA. (B) Local delivery (i.e., direct culture with bFGF-MCMs) amplifies growth factor activity at the culture surface, as measured in a cell-free bFGF bioactivity assay using the Quantikine bFGF ELISA kit. $n = 3$, error bars = s.d.; * $p < 0.05$, t-test.

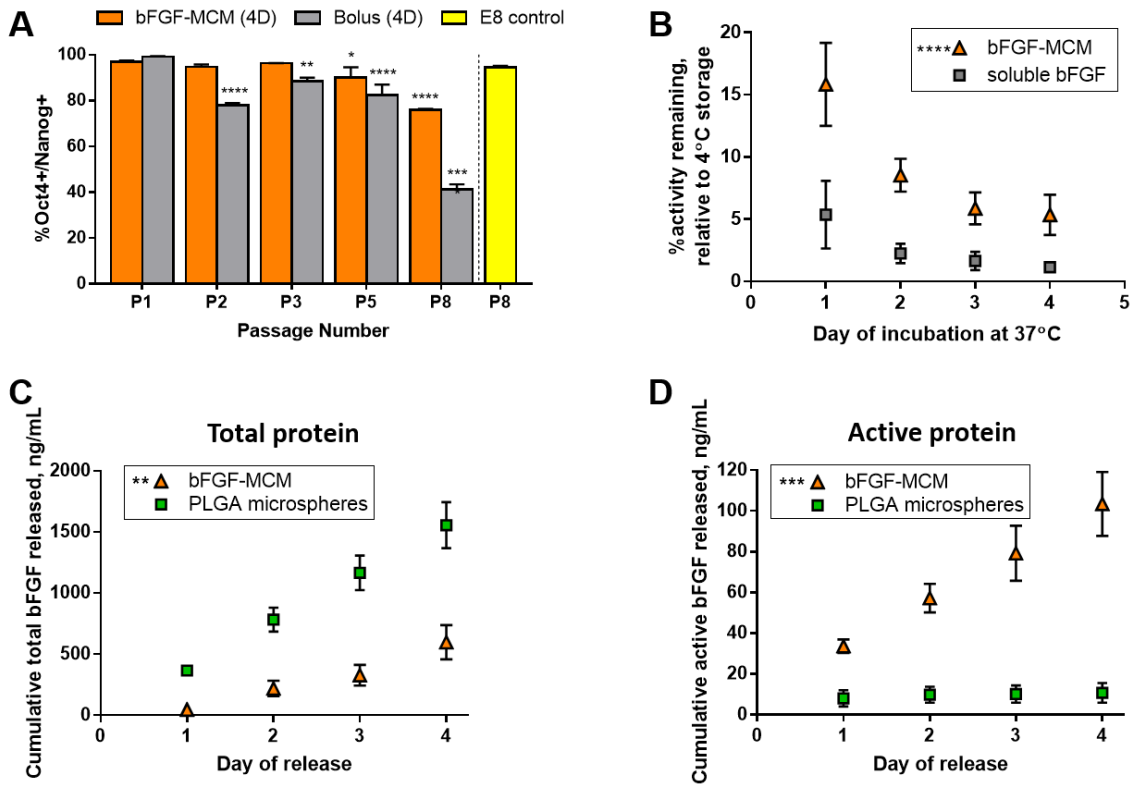

Figure 3.6 Binding to MCMs improves bFGF thermal stability. (A) bFGF bound to and released from MCMs maintains hPSC pluripotency marker expression more effectively than a matched amount of soluble bFGF ("Bolus"). "4D" denotes media changes every 4 days (i.e., only at the time of passaging). (B) bFGF bound to MCMs is stabilized against activity loss during incubation at physiological temperatures, as measured by Quantikine bFGF ELISA. "%activity remaining" is expressed relative to 4°C storage of each respective condition. (C) Comparison of total bFGF protein release from bFGF-MCMs vs. PLGA microspheres at 37°C. (D) Comparison of active bFGF protein release from bFGF-MCMs vs. PLGA microspheres. Values for cumulative daily release were extrapolated based on 2 hr release in the Quantikine bFGF ELISA for each time point assessed. Asterisks indicate statistically significant difference compared to (A) E8 control, (B) E7+soluble bFGF, (C-D) PLGA microspheres. $n = 3$, error bars = s.d.; $p < 0.05$ (*), 0.01 (**), 0.001 (**), or 0.0001 (****), two-way ANOVA.

Table 3.1 Summary of bFGF utilization vs. E8, for optimized Transwell and optimized direct culture bFGF-MCMs.

Culture Method	hPSC Maintenance	Use in Extended Culture	bFGF Reduction vs. E8
Transwell 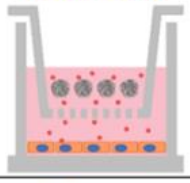	Passage 3 (Day 12) = 95.0% Oct4+/Nanog+	Add new bFGF-MCMs every 12 days	**25.0%**
Direct 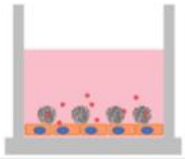	Passage 3 (Day 12) = 97.7% Oct4+/Nanog+	Add new bFGF-MCMs every passage	**81.2%**

Table 3.2 Percentage of Oct4+/Nanog+ hPSCs vs. passage number during long-term direct culture with bFGF-MCMs.

Passage #	P6	P10	P20	P25
H1 hESC	98.8%	95.6%	94.7%	95.0%
WTc11 hiPSC	96.8%	92.4%	93.1%	92.9%

3.11 SUPPLEMENTARY FIGURES & TABLES

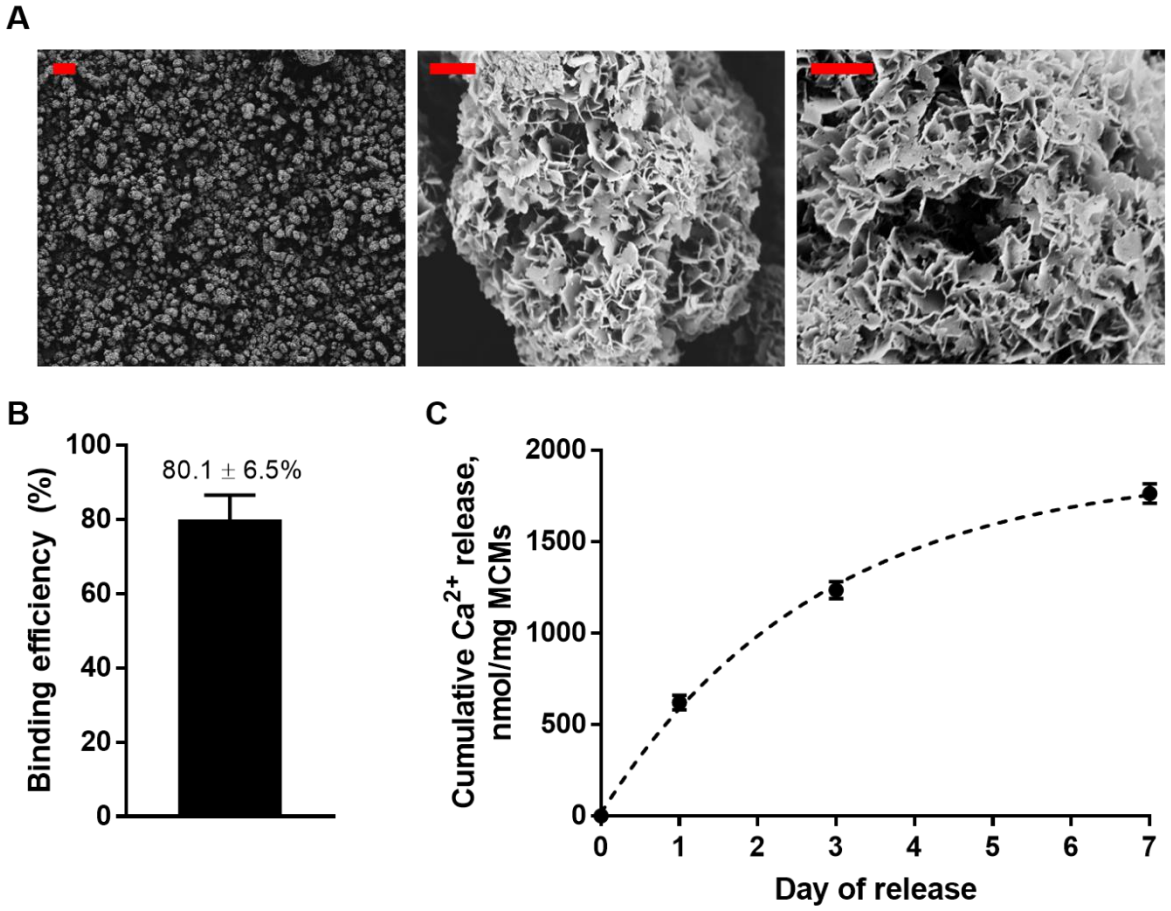

Supplementary Fig. S3.1 Characterization of MCMs for bFGF delivery. (A) Scanning electron microscopy of MCMs used for bFGF delivery. Scale bar = 10 µm (left) and 1 µm (middle and right). (B) Cumulative calcium release from MCMs based on dissolution of the mineral coating. (C) Efficiency of bFGF binding by MCMs, as measured by Quantikine bFGF ELISA.

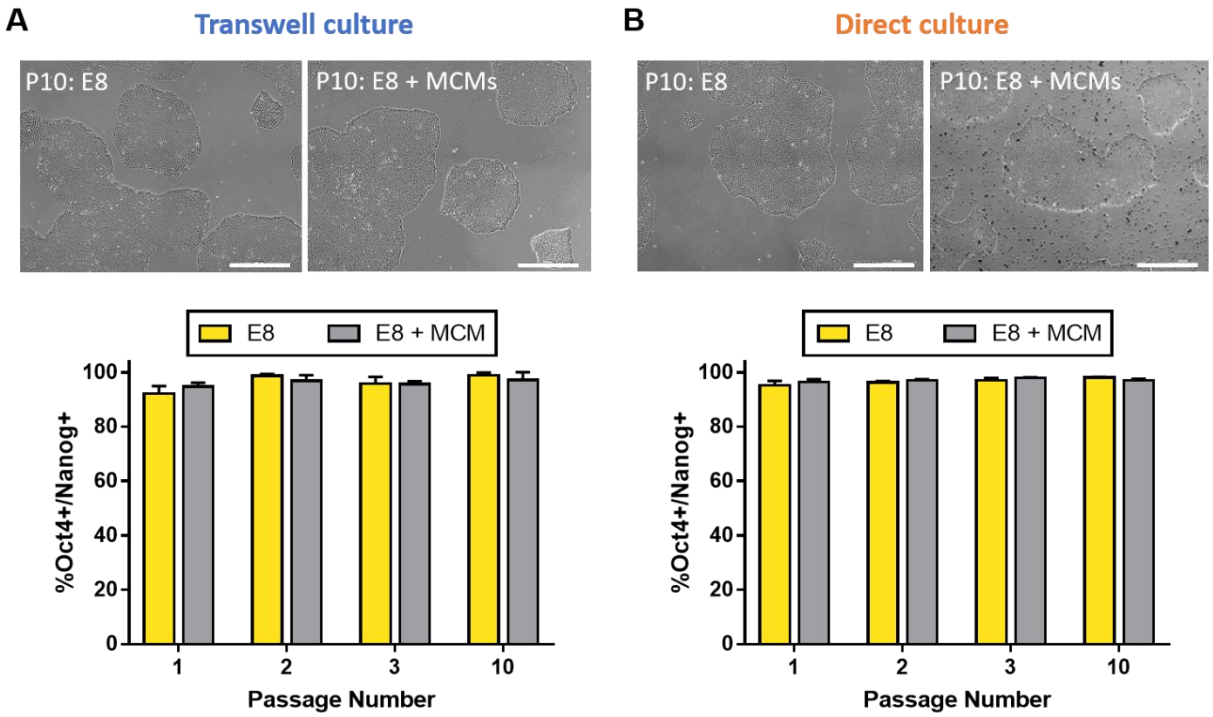

Supplementary Fig. S3.2 Blank (unloaded) MCMs do not significantly affect pluripotency marker expression. Representative phase contrast images (passage 10) and flow cytometry analysis for %Oct4+/Nanog+ hPSCs cultured in E8 media, in the presence or absence of unloaded MCMs in (A) Transwell culture or (B) direct culture over 10 passages. No statistically significant effect of MCMs on %Oct4+/Nanog+ hPSCs was found in Transwell ($p = 0.73$) or direct culture ($p = 0.21$, two-way ANOVA). Scale bars = 500 μm.

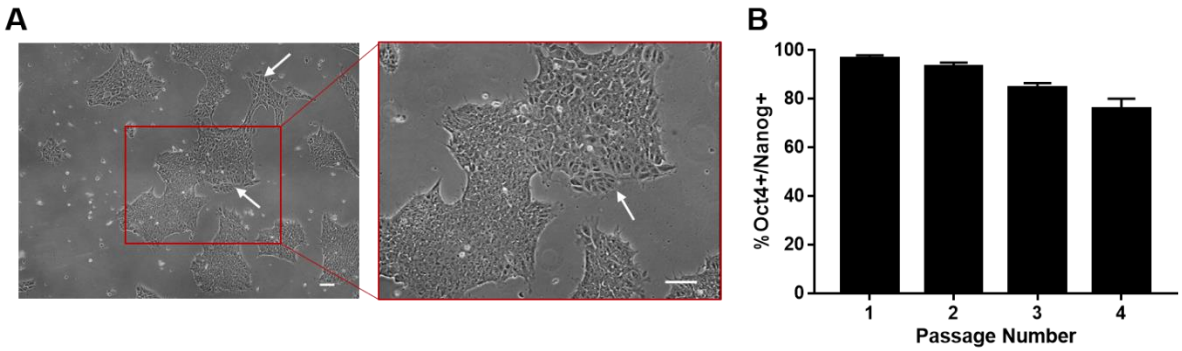

Supplementary Fig. S3.3 Non-optimized bFGF-MCMs are unable to maintain undifferentiated hPSCs beyond passage 3. (A) Areas of spontaneous differentiation (white arrows) were observed in H1 hESCs in Transwell culture with non-optimized bFGF-MCMs (1.0 mg/"high" dose) by passage 4. Scale bars = 100 μm. (B) High dose of non-optimized bFGF-MCMs is insufficient for maintaining >95% Oct4+/Nanog+ hPSCs beyond passage 2.

A

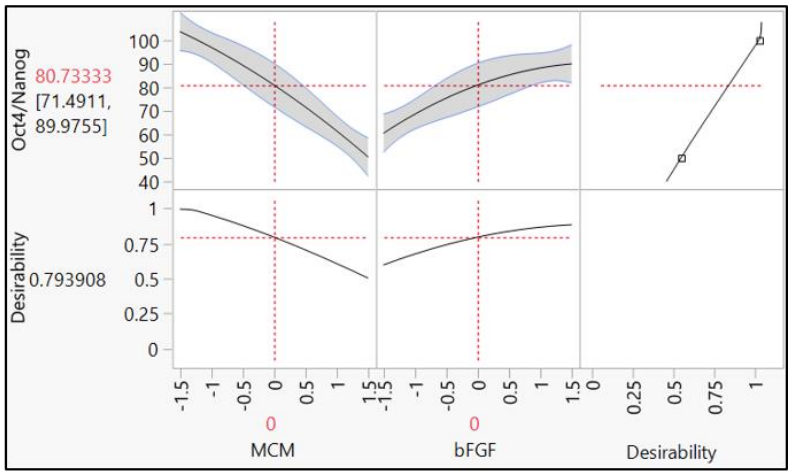

B

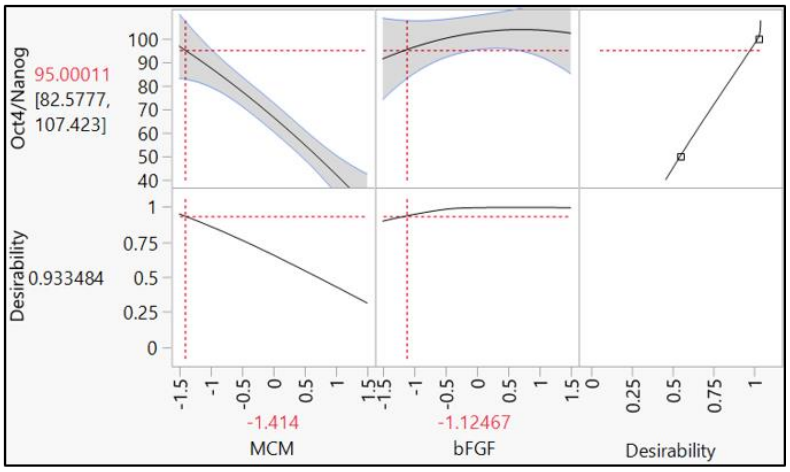

C

Source	Nparm	DF	Sum of Squares	F Ratio	Prob > F
MCM	1	1	7498.7055	126.5549	<.0001*
bFGF	1	1	2288.4351	38.6217	<.0001*
MCM*bFGF	1	1	226.2008	3.8176	0.0642
MCM*MCM	1	1	26.0319	0.4393	0.5147
bFGF*bFGF	1	1	55.7337	0.9406	0.3432

Supplementary Fig. S3.4 Results of DOE model for optimizing bFGF-MCM binding formulation. (A) Prediction profile for non-optimized bFGF-MCMs, showing model prediction for %Oct4/Nanog vs. MCM and bFGF concentration in binding solution. (B) Prediction profile for optimized bFGF-MCMs predicted to outperform non-optimized conditions, as indicated by the desirability function. X-axis for (A) and (B) is plotted on a log2 scale. (C) Summary table of effects tested in the DOE.

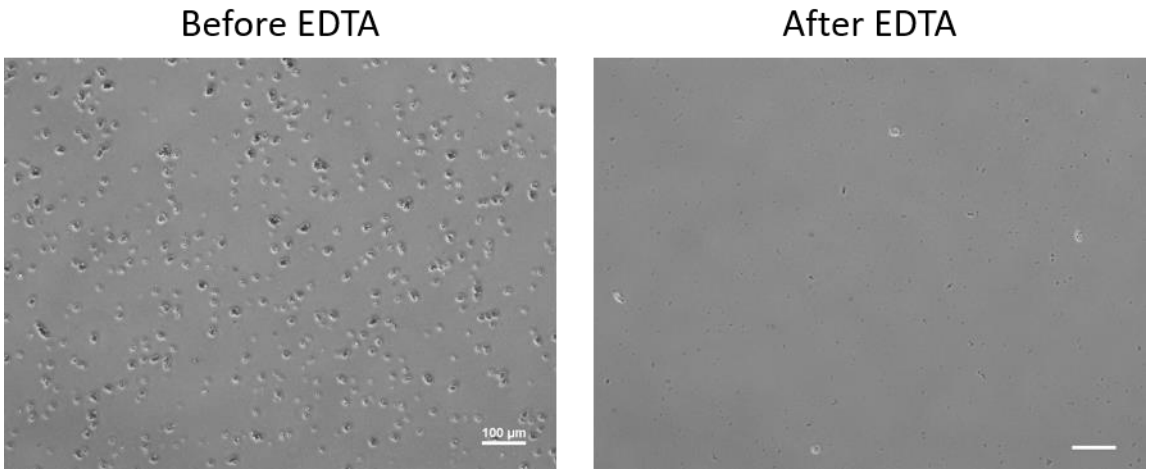

Supplementary Fig. S3.5 Mineral coatings dissolve upon cell passaging using EDTA. MCMs before and after incubation in Versene EDTA solution, a calcium chelator used in standard hPSC passaging.

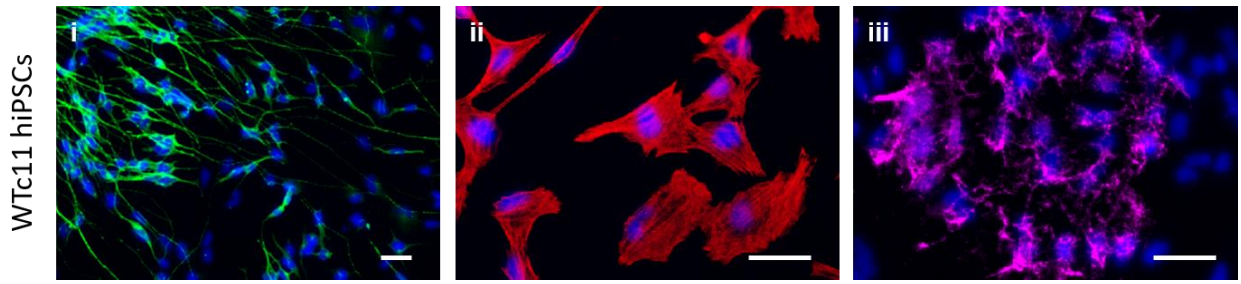

Supplementary Fig. S3.6 Tri-lineage spontaneous differentiation of hPSCs following direct culture with bFGF-MCMs for 25 passages. WTc11 hiPSCs were maintained in direct culture with bFGF-MCMs for 25 passages. EBs were formed, allowed to spontaneously differentiate and adhere to Matrigel-coated dishes for 14 days, and stained for markers of i) ectoderm (beta-III tubulin), ii) mesoderm (alpha smooth muscle actin), and iii) endoderm (alpha-fetoprotein) lineages. Scale bars = 50 μm.

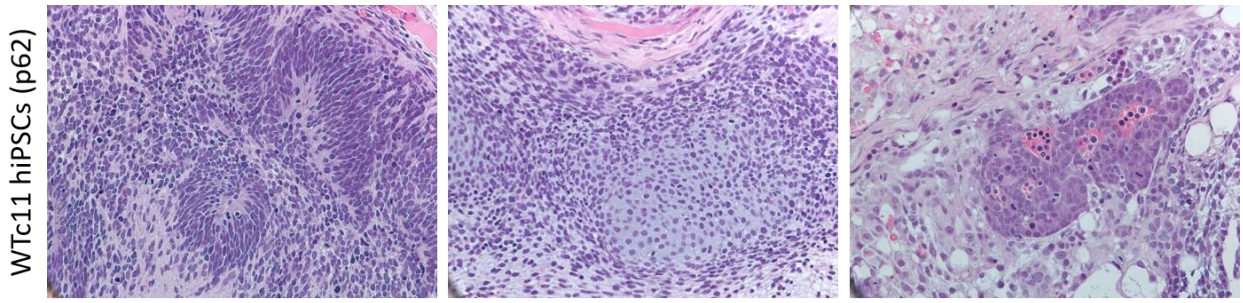

Supplementary Fig. S3.7 Histological analysis of teratomas generated from WTc11 hiPSCs after long-term (25 passages) direct culture with bFGF-MCMs. Differentiation into all three germ layers is shown: (i) ectoderm (neuroepithelium), (ii) mesoderm (cartilage) and endoderm (liver).

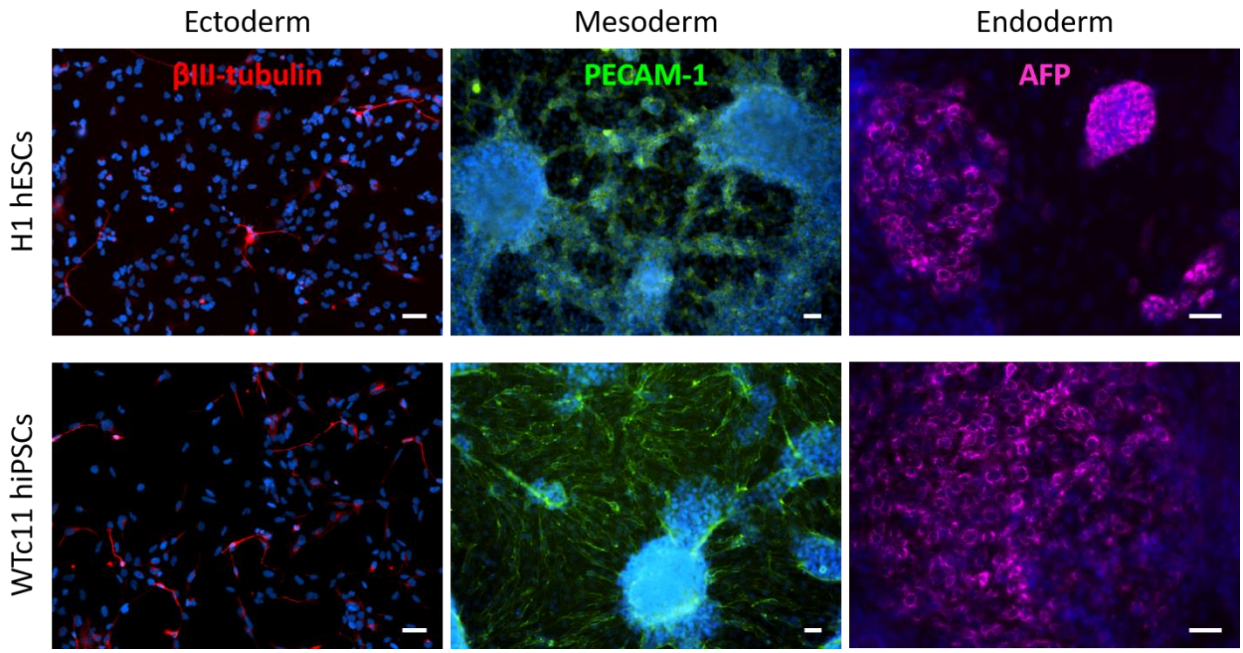

Supplementary Fig. S3.8 Directed differentiation of hPSCs following direct culture with bFGF-MCMs for 25 passages. H1 hESCs or WTc11 hiPSCs were maintained in direct culture with bFGF-MCMs for 25 passages, subjected to established directed differentiation protocols, and stained for markers of i) ectoderm (beta-III tubulin), ii) mesoderm (PECAM-1), and iii) endoderm (alpha-fetoprotein) lineages. Scale bars = 50 µm.

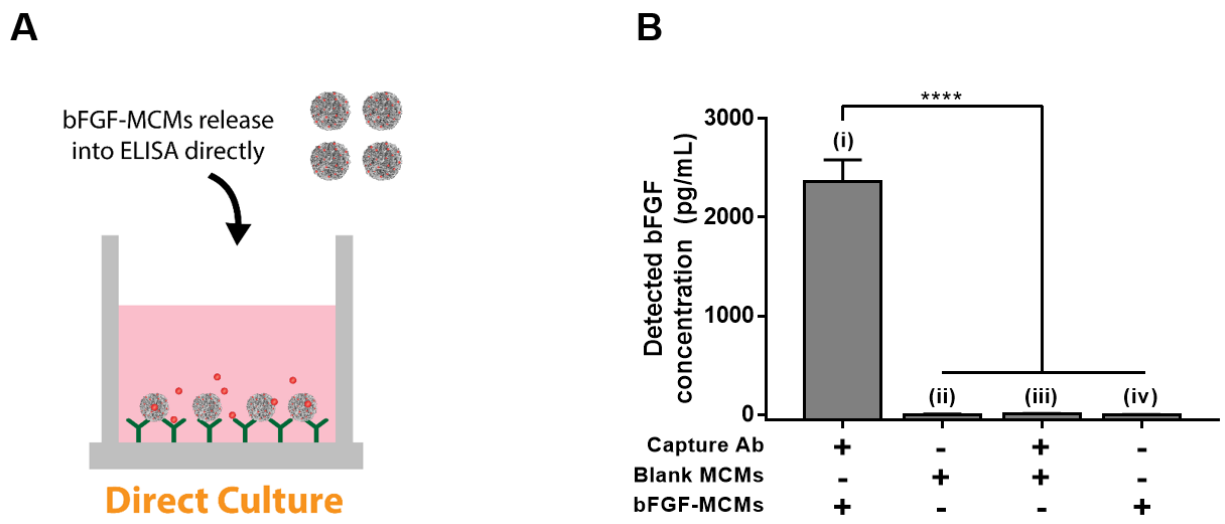

Supplementary Fig. S3.9 Development of bFGF bioactivity ELISA for MCMs. (A) Schematic of experimental setup for direct in-plate bFGF ELISA. To detect bioactivity of bFGF released from MCMs in real-time, solutions containing bFGF-MCMs were added to wells of a Quantikine bFGF ELISA assay shown to detect only bioactive bFGF (see Supplementary Fig. S3.9). All following steps of the ELISA (binding, washes, detection) were carried out following the manufacturer's protocol. (B) MCMs were confirmed not to interfere with bFGF Quantikine ELISA readouts. Assay controls demonstrated that signal produced in direct in-plate ELISA is due to i) released bFGF from MCMs, and not due to binding of detection antibody to blank MCMs in the ii) absence or iii) presence of capture antibody, or iv) insufficient removal of bFGF-MCMs during washes and binding of detection antibody to remaining bFGF-MCMs. **** $p < 0.0001$ (one-way ANOVA with Tukey's post-hoc)

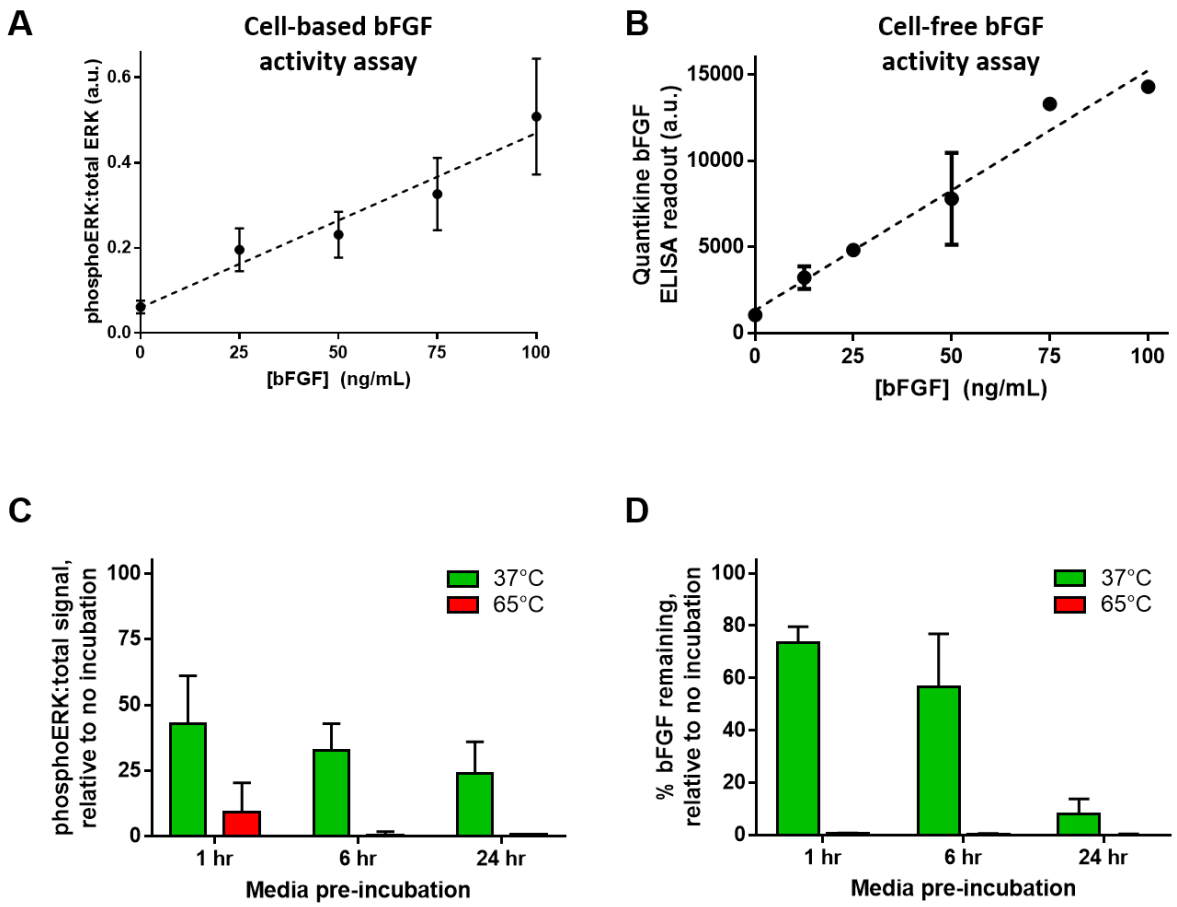

Supplementary Fig. S3.10 Quantikine bFGF ELISA readouts correlate with bFGF activation of MAPK pathway and reflect thermal instability of free bFGF. (A) ERK phosphorylation correlates with amount of bioactive bFGF. hPSCs were starved of bFGF (in E7) for 24 hrs, followed by 2 hr restimulation with E7 containing different concentrations of fresh bFGF in solution (created by mixing E8 and E7 media at different ratios). Soluble bFGF restimulated early ERK phosphorylation in a dose-dependent manner. Error bars = s.d., n = 3 independent biological replicates. (B) Quantikine bFGF ELISA correlates with amount of bioactive bFGF. E8 and E7 were combined at different ratios to produce media containing different concentrations of bFGF, and each media formulation was analyzed by Quantikine ELISA. Error bars = s.d., n = 2 independent biological replicates. (C) bFGF thermal instability is reflected by the decreased capacity of bFGF-containing E8 media to induce ERK phosphorylation after pre-incubation at 37°C and 65°C. Error bars = s.d., n = 2 independent biological replicates. (D) Loss of bFGF bioactivity after pre-incubation at 37°C and 65°C is recapitulated in Quantikine bFGF ELISA. Error bars = s.d., n = 2 independent biological replicates.

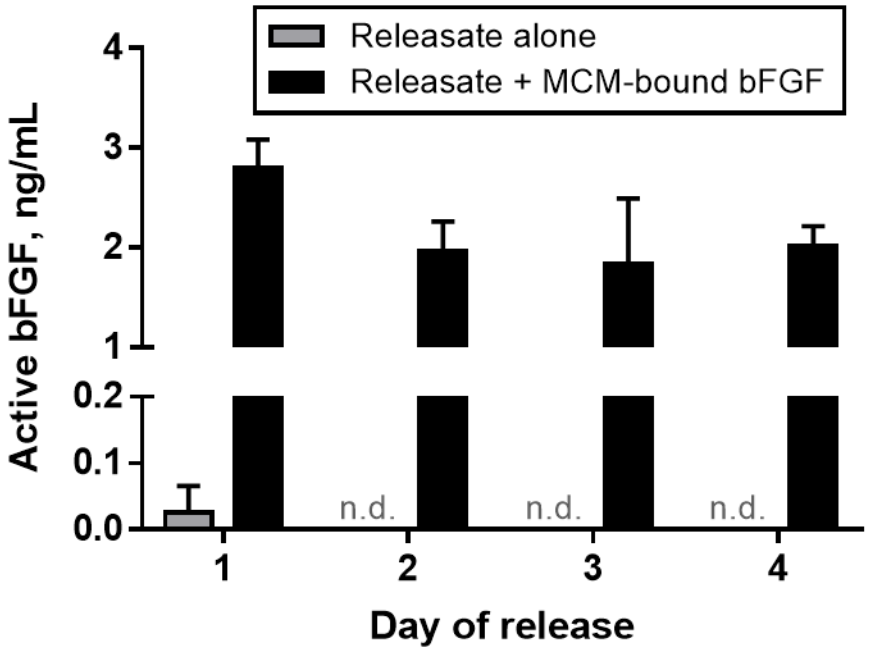

Supplementary Fig. S3.11 Preservation of bFGF activity ("stabilization") at 37°C depends on the growth factor remaining bound to MCMs. Quantification of active growth factor in soluble releasate alone or releasate plus actively releasing bFGF-MCMs, by Quantikine bFGF ELISA. "n.d." indicates not detectable by ELISA. Growth factor released from bFGF-MCMs is active and detectable immediately following release into media (black bars), but soluble bFGF in the releasate loses its activity quickly at 37°C and is largely undetectable by Quantikine ELISA (gray bars).

A

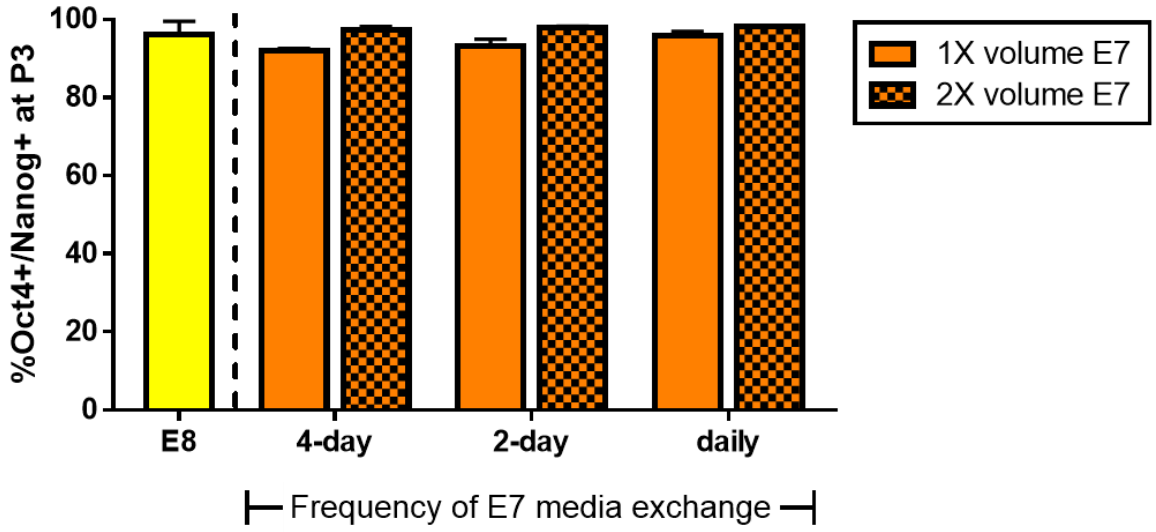

B

Condition	Media	Volume of media exchange	Frequency of media exchange	%Oct4+/Nanog+ at P3	
				Mean	*S.D.*
Control	E8	1X	daily	96.2	3.4
Direct culture bFGF-MCM	E7	1X	every 4 days	92.0	0.5
		1X	every 2 days	93.1	1.8
		1X	daily	95.8	1.1
		2X	every 4 days	97.4	0.8
		2X	every 2 days	98.0	0.3
		2X	daily	98.2	0.2

Supplementary Fig. S3.12 Volume and frequency of E7 media exchange influences hPSC maintenance in direct culture with optimized bFGF-MCMs. (A) Effect of volume and frequency of media exchange on %Oct4+/Nanog+ hPSCs at passage 3. H1 hESCs were maintained on Matrigel in 12-well plate format in direct culture with optimized bFGF-MCMs. E7 media at 1 mL/well ("1X volume") or 2 mL/well ("2X volume") were exchanged every 4 days, every 2 days, or daily. Cells grown in E8 (no MCMs, daily media exchange) were included as a control. (B) Table summarizing results from (A).

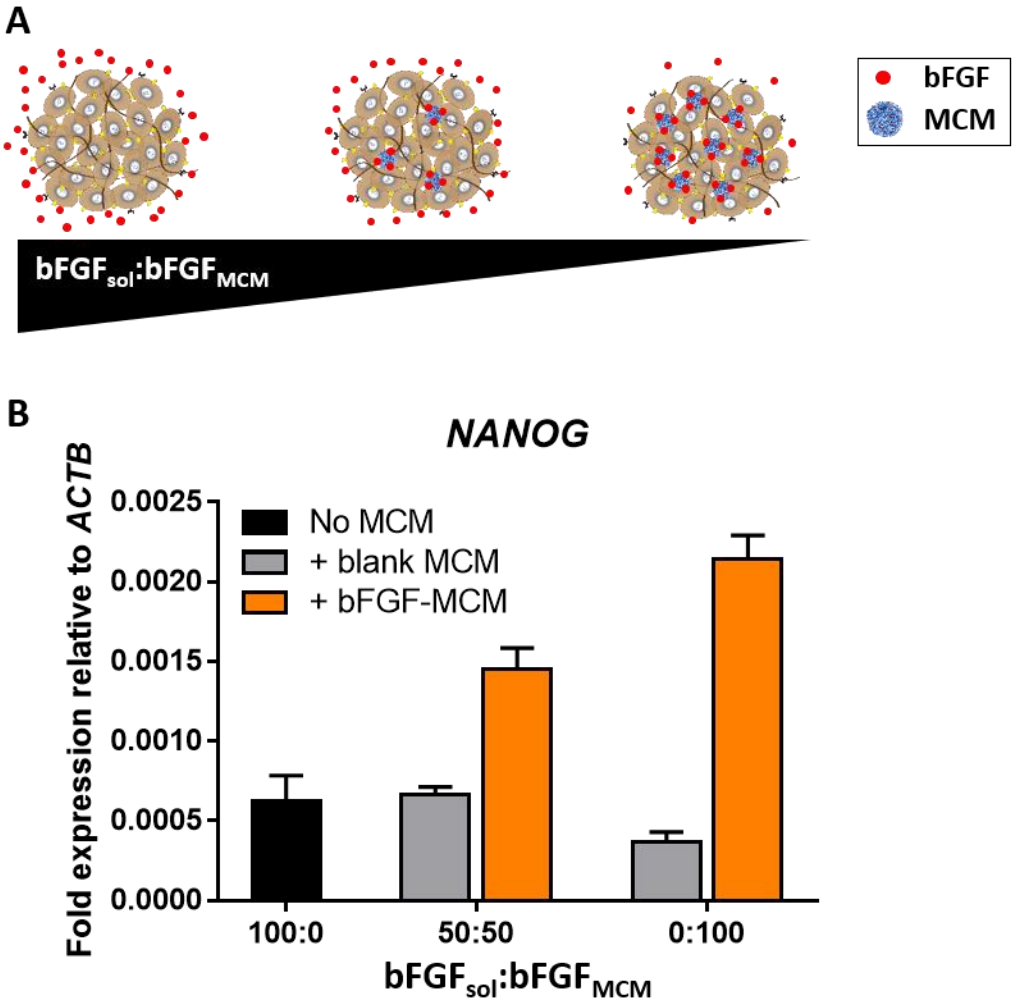

Supplementary Fig. S3.13 Growth factor delivery from MCMs mitigates pluripotency loss in 3D hPSC aggregates. (A) Schematic of experimental setup. Total bFGF in the system was kept constant while the fraction of soluble bFGF delivered via external media ("$bFGF_{sol}$") vs. delivered via MCMs ("$bFGF_{MCM}$") was varied. bFGF-MCMs were suspended uniformly within the cell suspension prior to formation of hPSC aggregates, resulting in their incorporation into the aggregate interior. (B) Expression of *NANOG* at 72 hrs in hPSC aggregates with varying fractions of $bFGF_{sol}$:$bFGF_{MCM}$. Blank MCM controls contained matched amounts of $bFGF_{sol}$ and unloaded MCMs, as compared to their corresponding bFGF-MCM conditions.

Supplementary Table S3.1 Total bFGF utilization over 3 passages for MCM binding conditions tested in DOE optimization experiment.

Culture format	TRANSWELL CULTURE									E8 CONTROL
Description	*fresh bFGF-MCMs made at initiation of culture and maintained through 3 passages*									
DOE condition	--	-+	+-	++	a0	A0	0a	0A	00	N/A
Loading formulation	0.5 mg/mL MCM, 0.5 µg/mL bFGF	0.5 mg/mL MCM, 2.0 µg/mL bFGF	2.0 mg/mL MCM, 0.5 µg/mL bFGF	2.0 mg/mL MCM, 2.0 µg/mL bFGF	0.38 mg/mL MCM, 1.0 µg/mL bFGF	2.67 mg/mL MCM, 1.0 µg/mL bFGF	1.0 mg/mL MCM, 0.38 µg/mL bFGF	1.0 mg/mL MCM, 2.67 µg/mL bFGF	1.0 mg/mL MCM, 1.0 µg/mL bFGF	N/A
Mass of bFGF-MCMs/well, 12w format (mg)	1.0	1.0	1.0	1.0	1.0	1.0	1.0	1.0	1.0	N/A
Total bFGF utilization for 3 passages (µg)	1.00	4.00	0.25	1.00	2.67	0.37	0.38	2.67	1.00	1.20
Total bFGF utilization, relative to E8 control (%)	83.3%	333.3%	20.8%	83.3%	222.2%	31.2%	31.3%	222.5%	83.3%	100.0%
Avg %Oct4+/Nanog+ at P3	96.9	98.1	44.5	63.1	97.2	59.0	55.9	97.1	80.7	93.87

Supplementary Table S3.2 Comparison of total bFGF utilization between non-optimized and optimized bFGF-MCM conditions in Transwell and direct culture formats (see Figure 3E), versus standard E8 culture. Bolded, italicized conditions are those referred to as "optimized Transwell" and "optimized direct" in the manuscript text, the results for which are summarized in Table 3.1. All calculations for bFGF utilization were made on a "per well" basis in 12-well plate format with 1.0 mL media volume per well.

Culture format	**TRANSWELL CULTURE**								**DIRECT CULTURE**							
Description	fresh bFGF-MCMs made at initiation of culture and maintained through 3 passages								fresh bFGF-MCMs made and added at each passage							
	Non-optimized				**Optimized**				**Non-optimized**				**Optimized**			
Loading formulation	1.0 mg/mL MCM, 1.0 µg/mL bFGF				0.375 mg/mL MCM, 0.456 µg/mL bFGF				1.0 mg/mL MCM, 1.0 µg/mL bFGF				0.375 mg/mL MCM, 0.456 µg/mL bFGF			
Mass of bFGF-MCMs/well, 12w format (mg)	0.300	0.600	0.900	1.200	0.250	0.500	***0.750***	1.000	0.075	0.150	0.225	0.300	***0.061***	0.123	0.185	0.246
bFGF utilization per passage (µg)	N/A				N/A				0.075	0.150	0.225	0.300	***0.075***	0.150	0.225	0.300
Total bFGF utilization for 3 passages (µg)	0.300	0.600	0.900	1.200	0.300	0.600	***0.900***	1.200	0.225	0.450	0.675	0.900	***0.225***	0.450	0.675	0.900
Total bFGF utilization, relative to E8 control (%)	25.0%	50.0%	75.0%	100.0%	25.0%	50.0%	***75.0%***	100.0%	18.8%	37.5%	56.3%	75.0%	***18.8%***	37.5%	56.3%	75.0%
Average %Oct4+/Nanog+ at P3	36.5	54.1	57.8	64.4	88.8	90.2	***95.0***	92.1	88.8	91.6	82.5	N/A	***97.7***	97.5	99.0	99.7

CHAPTER 4. LABILE CHEMISTRIES FOR THE SIMPLE AND ENHANCED-THROUGHPUT GENERATION OF CONTROLLABLE CELL AGGREGATES

Angela W. Xie, Maureen K. Bunger, Samantha K. Schmitt, and William L. Murphy. Labile chemistries for simple and enhanced-throughput generation of controllable cell aggregates. *In Preparation.*

4.3 PREFACE

In Chapter 3, we developed an approach using mineral-based biomaterials to provide localized and sustained release of growth factors, thereby exerting temporal control over the soluble biochemical environment of cells grown in conventional two-dimensional (2D) culture. In this chapter, we develop and characterize a biomaterial strategy designed to exert spatiotemporal control over formation of the 3D cell microenvironment via controlled cell aggregation from labile culture substrates. Our strategy uses patterning of labile chemical linkages to manipulate the spatial and temporal presentation of RGD cell adhesion ligands on otherwise bioinert substrates, with cleavage of labile bonds resulting in RGD release accompanied by cell aggregation over the course of 24-72 hours. We demonstrate that this method can be used to generate cell aggregates in a controllable and scalable manner, and furthermore show advantages of this approach over conventional aggregation methods. This chapter establishes mechanisms and describes processing advantages associated with our approach, while the ability of our platform to control aggregate formation kinetics and resulting structure – as well as their implications for cell phenotype and function – are detailed in Chapters 5 and 6. To the best of our knowledge, the application of labile chemistries toward generating cell aggregates is a novel concept not previously described in the

literature, and may find utility in areas spanning drug/toxicity screening, *in vitro* microtissue/organoid models, and regenerative medicine.

4.2 ABSTRACT

Three-dimensional cell aggregates are becoming widely regarded as valuable tools for bridging the gap between *in vitro* and *in vivo* cell biology. Numerous methods have been developed for generating cell aggregates, the most common of which rely on trypsinization and spontaneous or forced aggregation of singularized cells in suspension. While many of these suspension-based methods are conceptually simple, poor viability[1–3], inconsistent aggregation[4], and lack of control over aggregate properties[5] remain persistent issues for the aggregation of various primary and stem cell types. Here, we describe a method for the consistent production of viable cell aggregates from synthetic substrates presenting cell adhesion peptides via labile chemical linkages. In contrast to traditional mechanisms of *in vitro* aggregate formation, aggregation on these labile substrates occurs by initial establishment of integrin-mediated cell-matrix adhesions, followed by gradual loss of adhesion that accompanies peptide loss from the substrates over time in culture. This mechanism allows aggregation kinetics to be controlled by modulating substrate peptide density, or by manipulating cell adhesion or cytoskeletal contractility via chemical means. Patterning of labile substrates enables enhanced-throughput formation of size- and shape-controlled aggregates, including hPSC and hepatocyte aggregates with improved viability and consistency compared to those generated via a common suspension-based method. Finally, we demonstrate that hepatocyte aggregates from labile substrates display a more mature metabolic phenotype and extended viability compared to hepatocytes in a standard Matrigel overlay format, underscoring the broad utility of this approach for generating highly functional 3D microtissue models *in vitro*.

4.3 INTRODUCTION

Three-dimensional microtissue models are gaining increasing traction for *in vitro* disease modeling, drug and toxicity screening, and tissue engineering, due to their capacity to more faithfully recapitulate *in vivo*-like biology compared to cells in traditional 2D culture. Unlike in 2D culture, cells in 3D environments adopt morphologies and polarization similar to those found in native tissues[6,7] and often recapitulate *in vivo* gene expression, metabolism, and responses to chemical insult.[3,8,9] These advantageous features are attributed to aspects of the 3D culture environment that are not appropriately mimicked in 2D, including the increased extent of cell-cell interactions, cell interactions with extracellular matrix, and gradients of soluble signals and oxygen tension that affect cell viability and phenotype during tissue formation and homeostasis.[10–12] In addition to serving as more physiologically relevant tissue models in basic research, 3D cell cultures have considerable promise for applications in regenerative medicine including biomanufacturing[13–17] and cell therapy.[18,19]

Common methods for generating cell aggregates include spontaneous aggregation in low-adhesion plates or round-bottom plates, hanging drop (HD) cultures, and forced aggregation via centrifugation (FC) into cell-repellent microwell arrays (reviewed in [11]). Aggregates formed in hanging drops or round-bottom plates, in which defined numbers of cells within media droplets are subjected to gravity-driven aggregation, are the gold standard for forming size-controlled aggregates but are impractically labor intensive and present challenges to scale-up. To address these shortcomings, recent approaches have largely relied on the placement of defined numbers of dissociated cells into geometrically constrained microwells that are manufactured as high-throughput arrays. Formation of size-controlled aggregates in these systems is often encouraged

by forced aggregation[5,20,21], which involves centrifugation of cells into the arrayed wells to promote immediate cell-cell interactions. Although the aforementioned methods employ different types of external forces to encourage initial cell-cell contacts, they employ a common mechanism for aggregation that requires cadherin-based interactions between neighboring cells, in the absence of cell-matrix interactions, in order to promote formation of viable aggregates. On the whole, this reliance on spontaneous formation of stable cell-cell contacts precludes spatiotemporal control over the process of aggregation, which in turn limits control over aggregate properties that consequently define the cell microenvironment within. Moreover, the aforementioned aggregation technologies rely on the accumulation of cadherins and low-affinity *trans* interactions between cadherin molecules[22] on opposing cell surfaces, which can pose challenges for the aggregation of many adhesion-dependent cell types that depend on cell-cell and/or cell-matrix interactions to avoid anoikis. In particular, cell dissociation with trypsin or other enzymes – a routine step to acquire singularized cells prior to aggregation – can result in substantial enzymatic cleavage of cell-surface cadherins[23–25] that leads to anoikis if cell-cell or cell-matrix adhesions are not re-established quickly enough[26]. We posited that an approach utilizing the integrin ligand Arg-Gly-Asp (RGD) could provide improved consistency of viable cell aggregate formation, permitting singularized cells to establish immediate cell-matrix interactions to avoid anoikis while still allowing for eventual formation of cell-cell contacts. We further hypothesized that presenting RGD via labile bonds in geometrically controlled patterns would enable control over spatiotemporal aspects of aggregation, including aggregate size, shape, and formation kinetics.

This paper describes the development and characterization of labile synthetic substrates that can generate self-assembled (SA) aggregates from a diverse array of cell types including pluripotent stem cells and their derivatives, mesenchymal stem/stromal cells, and primary

hepatocytes. Patterning of labile substrates enabled control over the size and shape of SA aggregates, and aggregation itself was dependent on RGD peptide loss from the substrates. We found that aggregation could also be controlled by manipulating integrin-specific adhesion and cytoskeletal contractility, providing two additional ways to control aggregation kinetics. Finally, we investigated the effects of aggregation method on cell viability and downstream function, comparing aggregates formed via SA and conventional methods using two cell types previously shown to be sensitive to apoptosis following trypsinization, human pluripotent stem cells (hPSCs) and primary hepatocytes. Labile substrates facilitated the enhanced-throughput generation of SA hPSC aggregates and hepatocyte spheroids with improved viability and consistency, compared to FC in microwell arrays. Furthermore, SA hepatocyte spheroids displayed a more differentiated metabolic phenotype and extended viability over time in culture compared to hepatocytes in a standard Matrigel overlay format.

4.4 RESULTS AND DISCUSSION

4.4.1 Design and fabrication of labile substrates promoting cell aggregation.

We initially hypothesized that spatial patterning of chemically defined substrates employing labile chemistries would enable the generation of size-controlled cell aggregates in the absence of physical manipulation, through a process we termed “cell aggregate self-assembly”. We chose alkanethiol SAMs as an initial testbed for this concept, as SAMs are well established as chemically well-defined biointerfaces and present a highly ordered molecular layer that is amenable to common bioconjugation chemistries and allows for tight control over surface biomolecule density and orientation[27]. SAMs also offer advantages for spatial patterning in biological environments. Whereas intentionally presented moieties such as RGD can be rapidly

masked by non-specific adsorption of cell-secreted and serum-derived proteins to traditional cell culture surfaces, alkanethiols featuring oligo(ethylene glycol) groups are readily available for generating bioinert SAMs[28]. Here, we employed a mixed self-assembled monolayer (SAM) system to fabricate patterned arrays of alkanethiols with tunable peptide density in each array spot. In this system, a hydroxyl-terminated "bioinert" alkanethiol ("EG_3OH") served to prevent non-specific protein adsorption, while a carboxylate-terminated alkanethiol ("EG_6COOH") provided a functional group for reaction via carbodiimide chemistry. Individual conditions within the array were isolated by patterning alkanethiols using an elastomeric stencil, and peptide density in each pattern was controlled by the percentage of reactive carboxylic acid groups (i.e., $\%EG_6COOH$) available for reaction.

Figure 4.1A shows the steps for patterning SAM-based culture substrates. Mixed solutions of EG_3OH and EG_6COOH alkanethiols at different molar ratios were pipetted into the wells formed by microfabricated stencils to generate patterned SAMs presenting varying $\%EG_6COOH$. After activation of –COOH groups and functionalization with RGD cell adhesion peptides, the PDMS stencil was removed to "backfill" with –OH-terminated alkanethiols to prevent non-specific cell adhesion outside of patterned regions. We introduced substrate lability via the specific RGD variant chosen to react with –COOH groups[29–31]. Specifically, we expected a reaction with peptides containing a free amine (e.g., cycRGDfK, NH_2-CRGDS) to form amide bonds enabling stable long-term presentation of the peptide, whereas peptides containing free thiols with no free amines (e.g., cycRGDfC, ac-CRGDS) were hypothesized to form labile thioester bonds leading to loss of peptide from the substrate over time in aqueous media (Fig. 4.1B; Supplementary Fig. S4.1). Indeed, following a 7-day incubation in aqueous media, the percentage of peptide remaining on substrates reacted with cycRGDfC or ac-CRGDS was significantly lower than that on substrates

reacted with cycRGDfK or NH_2-CRGDS, respectively (Fig. 4.1C, Supplementary Fig. S4.1). The reduced ability of cells to adhere to cycRGDfC but not cycRGDfK substrates that had been pre-incubated in PBS or cell culture media prior to seeding (Fig. 4.1D) further supported our hypothesis that loss of thioester-linked peptides in aqueous media would promote cell aggregation on labile substrates.

SAMs patterned with RGD via a labile thioester bond promoted the formation of self-assembled cell aggregates, typically within 72 hours after seeding, whereas RGD presentation via comparatively stable bonds (e.g., amide, thioether) prevented aggregate formation (Fig. 4.2). Specifically, 5% EG_6COOH SAMs functionalized with a Cys-containing cyclic RGD ("5% cycRGDfC"; Fig. 4.2A, Scheme 1) supported formation of a confluent monolayer of hPSCs followed by contraction and self-assembly of the intact layer within 36-60 hours to form a compact 3D aggregate (Fig. 4.2B, Panel 1). On 5% cycRGDfK SAMs (Fig. 4.2A, Scheme 2), hPSC growth was largely restricted to the 2D substrate and no aggregate formation was observed within 104 hours (Fig. 4.2B, Panel 2). Reaction efficiency with the SAM was not significantly different between cycRGDfC and cycRGDfK (Supplementary Fig. 4.2), and we observed no differences in the potency of the two peptides in an integrin-blocking competition assay (Supplementary Fig. S4.3), suggesting that cell aggregate self-assembly was due to lability of the chemical linkage between RGD and the SAM, rather than differences in peptide density or affinity for cell-surface integrins.

4.4.2 Mechanisms of peptide loss and cell aggregate self-assembly from labile substrates.

To confirm that the mechanism of controllable aggregate self-assembly from RGD-presenting SAMs depended on bond lability, we reacted *N*-(2-aminoethyl-maleimide), a short

heterobifunctional crosslinker, with EG_6COOH prior to cycRGDfC conjugation to form stable amide and thioether bonds between cycRGDfC and SAMs (Fig. 4.2A, Scheme 3). Unmodified and maleimide-modified EG_6COOH SAMs demonstrated similar reaction efficiencies with cycRGDfC (Supplementary Fig. S4.2); however, unlike on labile cycRGDfC-presenting substrates, cells on maleimide-modified cycRGDfC substrates failed to undergo self-assembly to form 3D aggregates (Fig. 4.2B-C). These results supported our hypothesis that lability of the linkage between RGD peptides and SAMs is necessary and sufficient for aggregate self-assembly, suggesting that the approach described here can be translated broadly to chemical schemes that create linkages susceptible to cleavage in biological media[29].

4.4.3 Cell aggregate self-assembly depends on integrin-mediated adhesion and cytoskeletal contractility.

Dynamic assembly of cell collectives is regulated by a combination of mechanical forces originating from cell-matrix adhesions and cell cytoskeleton-mediated contractility[32,33]. Thus, we investigated whether manipulating cell-substrate adhesion or cytoskeletal contractility could serve as a means to control the process of cell aggregate self-assembly, specifically tracking decreases in cell population area over time as an indicator of aggregation kinetics[31]. In the absence of any external manipulation, aggregation kinetics depended on the density of reactive groups in the SAM (i.e., $\%EG_6COOH$). However, actively interfering with cell-substrate interactions provided an additional means to modulate aggregation kinetics. Addition of soluble cyclic RGDfC peptide – capable of competing for integrin binding sites – could accelerate the rate of aggregation in a dose-dependent manner, while mutant peptides with no integrin-binding activity (cycRADfC) had no significant effect on aggregation (Fig. 4.3A and 4.3B). However, we did not observe instances in

which patterned cell populations lifted off labile substrates as intact cell sheets, suggesting that loss of cell-substrate adhesion was not the sole governing factor for cell aggregate self-assembly. Notably, a recent study from Takebe et al. probed *in vitro* cell "condensation" mechanisms and implicated cytoskeletal contractility as essential for self-driven assembly of cell collectives, since perturbing myosin II regulatory light chain or Rho kinase activities significantly interfered with the formation of cell condensates[33]. Similarly, we found that antagonizing Rho kinase activity with Y-27632 decreased the rate of aggregate self-assembly on labile substrates in a dose-dependent manner (Fig. 4.3A and 4.3C). Together, these findings suggest that aggregation kinetics on labile substrates can be regulated via chemical manipulation of specific cell adhesion and contractility pathways, affording an additional degree of control over the aggregation process on labile substrates.

4.4.4 Labile substrates enable simple, scalable self-assembly of aggregates from diverse cell types.

Patterning of labile substrate arrays enabled the generation of >400 aggregates within the area of a standard 1" x 3" glass slide (Fig. 4.4A). Of note, the formation of cell aggregates via self-assembly required only two processing steps: i) seeding of a singularized cell suspension and ii) rinse and media exchange 1-3 hours after seeding. Thereafter, cells underwent self-assembly to form aggregates within 3-4 days, without the need for any additional physical manipulation, mechanical forces, or use of enzymes (Fig. 4.4B). Aggregate size and shape were controlled by modifying the geometry of patterned substrates (Supplementary Fig. S4.4, Supplementary Videos 4.1 and 4.2). We demonstrated that a wide array of cell types including pluripotent and adult stem cells (ESCs, iPSCs, MSCs), iPSC-derived differentiated cell types (neural progenitor cells), and

primary cells (fibroblasts, hepatocytes) were amenable to self-assembled aggregation on labile substrates, suggesting the broad applicability of this approach to cells from diverse lineages and tissue sources (Fig. 4.4C, Supplementary Videos 4.3-4.6). Aggregates either released into suspension or remained weakly adherent to patterned SAMs without reattaching and could be collected in bulk by pipetting at the substrate with a gentle stream of media (Fig. 4.4D). Thus, this approach is not only generalizable across cell types but also decreases the amount of labor required for large-scale generation of aggregates, since it involves few pipetting steps and minimal intervention from the end user between cell seeding and aggregate collection steps. Furthermore, this technology may be easily amenable to automation, as it eliminates the need for consistent and repetitive pipetting that poses a major obstacle to automated spheroid generation with existing technologies[34].

4.4.5 Labile substrates promote consistent formation of viable aggregates from hPSCs and primary hepatocytes.

In addition to simplifying the processing steps required for cell aggregation, labile substrates also improved the consistency of forming viable aggregates for cell types known to be sensitive to aggregation conditions. For example, we and others[4] have observed inconsistencies in the aggregation efficiency of hPSCs subjected to forced aggregation in polymeric microwells under seemingly equivalent conditions (seeding density, microwell material and geometry). In addition, primary cells such as pancreatic β-cells and hepatocytes isolated from tissue have been reported to aggregate poorly or inconsistently depending on the preparation[3]. This observation may be attributed to enzymatic destruction of cell surface molecules, such as cadherins, during the isolation procedure[25]. Thus, we were interested in whether cell aggregation on labile substrates, a

process that relies initially on integrin-mediated cell adhesion to RGD followed by gradual 3D aggregation over the course of days, would have additional advantages for generating viable and reproducible aggregates from cell types that are adhesion-dependent and rely on immediate formation of cell-matrix and/or cell-cell contacts[35] to avoid death by anoikis.

To investigate whether a cell-substrate adhesion-mediated process influenced the robustness and consistency of aggregate formation, we compared aggregates generated on labile substrates to those formed by FC in microwell arrays, using two cell types known to be susceptible to anoikis upon single-cell dissociation – hPSCs[36–38] and primary hepatocytes[39–41]. In our hands, formation of hPSC aggregates by FC was inconsistent between experimental replicates, with equivalent cell seeding densities resulting in varying degrees of cell incorporation into aggregates (Supplementary Fig. S4.5). Poor hPSC aggregation was typically characterized by extensive cell debris and dead cells surrounding intact aggregates with well-defined borders (Supplementary Fig. S4.5A, outlined in cyan); however, in some cases, the FC approach failed to produce intact aggregates at all (not shown). Similarly, when we attempted to recapitulate processing conditions that would lead to poor aggregation by subjecting hPSCs to extensive trypsinization, FC resulted in low cell viability and poor aggregate compaction while labile substrates facilitated consistent cell attachment and formation of uniformly-sized, viable hPSC aggregates (Supplementary Fig. S4.5B). We observed similar improvements in viability with primary hepatocytes seeded on labile substrates. For example, primary hepatocytes that plated poorly on Matrigel demonstrated robust adhesion and typical hepatocyte morphology on labile substrates and went on to form viable hepatocyte spheroids, as assessed by LIVE/DEAD staining (Supplementary Fig. S4.6). In contrast, FC in microwell arrays resulted in poor hepatocyte viability and failure to form compact spheroids (Supplementary Fig. S4.7A).

4.4.6 Self-assembled hepatocyte aggregates demonstrate improved viability and function compared to 2D Matrigel overlays.

To demonstrate the utility of our approach for generating cell aggregates with comparable or superior function to conventional methods, we compared primary hepatocyte spheroids formed on labile substrates to hepatocytes grown in a Matrigel overlay format, a current standard for long-term hepatocyte culture[42]. We also made comparisons to spheroids formed in 96-well low-attachment round-bottom plates (96w RB) which, in our hands, routinely outperformed FC hepatocytes in terms of consistency and viability (Supplementary Fig. S4.7). Freshly isolated rat hepatocytes attached to labile substrates within 3-4 hours, and displayed polygonal morphology and prominent nucleoli typical of healthy hepatocytes by 12 hours. Hepatocytes began to release from labile substrates around 48 hours and self-assembled into loose clusters that gradually compacted into tight spheroids by 96-120 hours after seeding (Fig. 4.4D). Similarly, hepatocytes in the 96w RB format began as irregular clusters and compacted into spheroids with well-defined edges over the course of 4-5 days in culture (Supplementary Fig. S4.7B).

Hepatocytes seeded on labile substrates with 1.2 mm diameter patterns formed self-assembled spheroids with average diameters of 199 ± 36 μm, and the size distribution of self-assembled spheroids was similar to that of 500-cell spheroids formed in 96w RB plates (200 ± 25 μm) (Fig. 4.5A). Both SA and 96w RB spheroids expressed E-cadherin localized to cell-cell junctions, indicative of maintained epithelial phenotype, and no necrotic core was observed in either SA or 96w RB spheroids through at least 10 days of culture (Fig. 4.5B). We next assessed viability and hepatobiliary transporter function of SA spheroids and 96w RB spheroids, compared to primary hepatocytes grown in a Matrigel overlay format. Matrigel overlay hepatocytes exhibited

normal morphology and formed a confluent monolayer of cells that was maintained through day 3, at which point the cells remained highly viable as assessed by LIVE/DEAD staining. Day 3 Matrigel overlay hepatocytes also demonstrated robust CMFDA uptake and excretion into bile canaliculi, indicative of the functional activity of multi-drug resistance-like protein (MRP2), a biliary efflux transporter[43] (Fig. 4.6A). However, by day 7 we observed substantial loss of hepatocyte monolayer integrity on Matrigel, which coincided with adoption of a spread, fibroblastic cell morphology characteristic of a dedifferentiated phenotype[44], and an apparent decrease in viable cell number as well as the number of bile canaliculi structures formed. In contrast, SA spheroids were highly viable during long-term culture. Compared to cells in Matrigel overlay or 96w RB spheroid formats, day 7 SA spheroids exhibited few dead nuclei stained by ethidium homodimer (Fig. 4.6B). Additionally, day 7 hepatocytes comprising SA and 96w RB spheroids demonstrated the capacity to take up CMFDA and subsequent excretion of the dye into bile canaliculi (Fig. 4.6B).

Quantification of cell viability at day 11 showed that SA spheroids retained 58.7 ± 8.8% and 88.0 ± 23.4 % viable hepatocytes (for untreated and dexamethasone-induced, respectively), which was substantially higher than Matrigel overlay hepatocytes (23.5 ± 4.6% and 27.0 ± 2.1% viable for untreated and dexamethasone-induced cells) (Fig. 4.6C). This result was unsurprising; while Matrigel overlay is known to extend the *ex vivo* longevity of primary hepatocytes, preservation of native hepatocyte functions remains short-lived[42]. In line with their comparatively low viability after long-term culture, Matrigel overlay hepatocytes also expressed genes for Cytochrome P450 family enzymes at lower levels compared to SA spheroids. Notably, basal expression of *Cyp3a2* and *Cyp3a23* by day 9 SA hepatocyte spheroids was orders of magnitude higher than that of Matrigel overlay hepatocytes (1259-fold and 605-fold increase, respectively)

(Fig. 4.6D). As CYP3A subfamily enzymes are responsible for the metabolism of approximately 30% of clinically used drugs[45], these results suggest that SA hepatocyte spheroids may serve as improved *in vitro* models for hepatotoxicity screening, as they maintain high viability even after 7 days of culture and exhibit elevated metabolic functions relative to Matrigel overlay cells. A more comprehensive assessment of metabolism for different CYP enzymes, at basal levels and in response to known inducers, should be conducted in future studies to determine the suitability of SA hepatocyte spheroids for drug hepatotoxicity screening applications. Overall, our results here indicate that self-assembly from labile substrates produces cell aggregates with improved long-term viability and function relative to standard 2D cultures, and offers enhanced throughput and control compared to traditional aggregation methods.

4.5 CONCLUSIONS

In this work, we describe a novel approach leveraging the lability of engineered synthetic substrates to generate cell aggregates with controllable size and shape. The method is scalable and enables consistent formation of viable and uniform aggregates from a variety of adhesion-dependent cell types, with minimal intervention from the end user. Additionally, our data suggest that, compared to conventional methods that rely solely on formation of cell-cell contacts through cadherin engagement, cell aggregation from substrates that present integrin-binding ligands may offer advantages for preserving initial viability of cell types sensitive to anoikis. Finally, we demonstrate that labile substrates support the aggregation of a model cell type – primary hepatocytes – to form spheroids that exhibit extended viability and enhanced metabolic phenotype compared to 2D cultures. Thus, labile substrates should be an accessible and widely applicable technology for generating functional cell aggregates for research and therapeutic applications.

4.6 MATERIALS AND METHODS

4.6.1 Materials and reagents: Carboxylic acid-terminated hexa(ethylene glycol) undecanethiol (HS-C_{11}-(O-CH_2-CH_2)$_6$-O-CH_2-COOH) (‘‘EG_6COOH’’) and 11-tri(ethylene glycol)-undecane-1-thiol (HS-C_{11}-(O-CH_2-CH_2)$_3$-OH) (‘‘EG_3OH’’) were purchased from Prochimia. N-hydroxysuccinimide (NHS), *n*-(3-dimethylaminopropyl)-N’-ethylcarbodiimide hydrochloride (EDC) and sodium dodecyl sulfate (SDS) were from Fisher Scientific. Cyclo(Arg-Gly-Asp-D-Phe-Cys) (cycRGDfC), cyclo(Arg-Gly-Asp-D-Phe-Lys) (cycRGDfK), and cyclo(Arg-Ala-Asp-D-Phe-Lys) (cycRADfK) peptides were purchased from Peptides International. CRGDS (“NH2-CRGDS”) and ac-CRGDS were purchased from GenScript. Gly-Trp-Gly-Gly-Arg-Gly-Asp-Ser-Pro (GWGGRGDSP) was synthesized by standard solid-phase Fmoc peptide synthesis as previously described[46]. Peptides were used at a concentration of 0.3 mM in pH 7.4 PBS unless otherwise indicated.

4.6.2 Fabrication of PDMS stencils: Polydimethylsiloxane (PDMS) stencils containing arrays of wells were fabricated by soft lithography as previously described[31]. Briefly, PDMS was prepared by mixing a 10:1 ratio of base to curing agent, followed by degassing for 1 hr. The degassed mixture was cast over SU-8 masters and cured for 6 hr at 80°C. Following curing, PDMS stencils were removed from molds and cleaned overnight in hexanes by Soxhlet extraction.

4.6.3 Preparation of SAMs: Alkanethiol solutions were prepared by combining 1 mM ethanolic solutions of EG_3OH and EG_6COOH at molar ratios equivalent to the desired surface concentration of EG_6COOH, as previously described[31]. For cell-based experiments, 5% EG_6COOH SAMs were

patterned in 1.2 mm diameter circular spots unless otherwise indicated. 100% EG_6COOH SAMs were used for all XPS surface analysis experiments.

Gold-coated glass slides (100 Å Au ‹111›, 20 Å Ti adhesion layer; Platypus Technologies) were cleaned via sonication in 100% EtOH for 2 minutes, rinsed with EtOH, and dried with N_2 gas. PDMS wells were filled with 1 mM ethanolic alkanethiol solution and incubated for 10 minutes for local SAM formation. Alkanethiol solutions were then aspirated and wells were rinsed with deionized water (diH_2O). PDMS wells were incubated in a solution of 100 mM NHS and 250 mM EDC in diH_2O for 15 minutes to activate carboxylate groups. After an additional rinse with DIUF H_2O, peptides were covalently coupled to patterned SAMs by incubating peptide solutions in PDMS wells for 1 hour. (For fabrication of maleimide crosslinker-modified surfaces, *N*-(2-aminoethyl-maleimide) at 7 mg/mL in pH 7.4 PBS (Sigma-Aldrich) was incubated on SAMs for 1 hr prior to the peptide incubation step.) Following peptide conjugation, PDMS wells were rinsed with diH_2O, and regions surrounding array spots were backfilled by removing the PDMS stencil and incubating the gold substrate with EG_3OH (0.1 mM in diH_2O, pH 2) for 10 min. The array was then rinsed with 0.1% SDS, diH_2O, and EtOH, and dried with N_2 gas. SAM arrays were stored in 100% EtOH and used within 24 hours of fabrication. Prior to cell-based experiments or cell-free incubation experiments, SAM arrays were incubated in 70% EtOH for 20 min and rinsed with sterile deionized water before placing into aqueous media.

4.6.4 XPS analysis of SAMs: X-ray photoelectron spectroscopy of peptide-conjugated SAMs was performed as previously described[31] using a Thermo Scientific Model K-Alpha XPS instrument equipped with a monochromatic Al Kα X-ray source ($h\nu$ = 1486.7 eV). Survey and high-resolution spectra were obtained using analyzer pass energy of 200 eV and 50 eV, respectively, with an X-

ray spot size of 400 μm. High-resolution spectra were obtained for carbon, nitrogen, sulfur, oxygen, and gold. At least three independent sample replicates were scanned per condition. Spectra were analyzed using Thermo Scientific Avantage XPS software package and peak fitting using a Shirley/Smart type baseline. For each sample, calculated atomic percent values for the N1(s) and C1(s) peaks were used to determine the N/C ratio, which was used to calculate reaction efficiency for cycRGDfC-, cycRGDfK-, and crosslinker-modified substrates, based on the theoretical N/C ratio for each surface assuming 100% reaction efficiency with the SAM. For assessment of peptide loss over time in aqueous media, mean values of N/C ratio measured from day 7 pre-incubated surfaces were normalized to day 0 values for each respective peptide, and presented as percentage peptide remaining on the surface. Statistical significance was determined by two-tailed Student's *t*-test ($p < 0.05$).

4.6.5 Cell-free SAM incubations: CycRGDfC and cycRGDfK SAMs were prepared and sterilized as described above and incubated in either phosphate-buffered saline (PBS) or Essential 8 (E8; Thermo Fisher Scientific) media for 7 days prior to cell seeding or analysis by XPS. All cell-free incubations were performed at 37°C, 5% CO_2 to mimic cell culture conditions. Pre-incubated substrates were rinsed with sterile PBS prior to cell seeding as described below.

4.6.6 Cell culture: H1 human embryonic stem cells (WA01-DL-12, WiCell) or WTc11 human induced pluripotent cells (kindly provided by Dr. Bruce Conklin, UCSF/Gladstone) were maintained on Matrigel-coated 6-well plates (8.7 μg/cm^2) in Essential 8 medium with daily media exchange, and passaged by standard protocols[47] using Versene-EDTA every 3 to 4 days. For seeding on SAM substrates, hPSCs were washed with PBS and incubated with TrypLE at 37°C

for 5 minutes to singularize cells. Following singularization, cell suspensions were diluted with 2X volume of E8 supplemented with 5 μM ROCK inhibitor (Y-27632) and pelleted by centrifugation at 200g for 5 minutes. Cell pellets were resuspended in E8 supplemented with 5 μM Y-27632 and seeded at a density of 2.25 x 10^5 cells/cm^2. After 2 hrs incubation in a humidified incubator at 37°C and 5% CO_2 to allow cell adhesion, seeded SAM arrays were immersed in basal medium to remove loosely or non-specifically adhered cells, and then placed into new wells containing fresh E8 medium supplemented with 5 μM Y-27632.

Human mesenchymal stem cells (hMSCs) were purchased from Lonza and maintained in adherent culture in alphaMEM supplemented with 10% fetal bovine serum (FBS; Gibco) and 1x penicillin/streptomycin (Hyclone). hMSCs were passaged at 70% confluence and used for all experiments between passages 4 and 7. For seeding on SAM substrates, hMSCs were singularized with 0.05% trypsin/EDTA following standard methods and seeded at a density of 9 x 10^4 cells/cm^2. After 1 hr incubation to allow cell adhesion, seeded SAM arrays were immersed in basal medium to remove loosely or non-specifically adhered cells, and then placed into new wells containing fresh medium.

Human dermal fibroblasts (hDFs) were purchased from the American Type Culture Collection (ATCC; Cat. #PCS-201-010) and maintained in adherent culture in DMEM supplemented with 5% FBS and 1x penicillin/streptomycin. For seeding on SAM substrates, hDFs were singularized with 0.05% trypsin/EDTA following standard methods and seeded at a density of 9 x 10^4 cells/cm^2. After 1 hr incubation to allow cell adhesion, seeded SAM arrays were immersed in basal medium to remove loosely or non-specifically adhered cells, and then placed into new wells containing fresh medium.

Freshly isolated primary Sprague-Dawley rat hepatocytes (in suspension or in a 96-well Matrigel overlay format) and Animal Hepatocyte Plating Media (PM) and Maintenance Media (MM) were generously provided by Triangle Research Labs and Lonza. Suspension hepatocytes were handled following the vendor's instructions, with cells kept at or below 4°C during all processing steps prior to seeding. Briefly, cells were centrifuged at 60g for 4 min, followed by removal of shipping media. Cells were gently resuspended in PM for seeding on SAMs or Matrigel, or in MM for seeding in 96w RB plates or microwell arrays. Hepatocytes were seeded on SAMs at 1.78 x 10^5 cells/cm^2 and allowed to adhere for 3-5 hrs before immersing SAMs in basal medium to remove loosely adhered cells. SAMs were then placed into new wells containing fresh PM. Following aggregation on labile substrates, spheroids were transferred to low-adhesion flat-bottom plates. 96w RB spheroids were formed by seeding 500 cells per well in low-adhesion round-bottom plates (Corning). MM on 96w RB spheroids was exchanged daily. For Matrigel overlays, hepatocytes were seeded in PM onto Collagen I-coated plates (BD Biocoat) at 1.78 x 10^5 cells/cm^2 and allowed to adhere for 3-5 hrs before adding Matrigel (Corning) at 0.3 mg/mL. At 1 day after seeding, spent medium on SAMs or Matrigel overlays was exchanged with MM, and cells were maintained in MM with daily media changes thereafter.

4.6.7 Generation of FC cell aggregates in agarose microwells: Agarose microwells were fabricated based on previously published methods[48]. A 85 mm bicycle retro-reflector (Grote 4005/4006) or Aggrewell800 inserts (STEMCELL Technologies) were fashioned into 35 mm diameter circular discs to be used as templates for casting silicone molds. Hydrophilic silicone (1:1 mixture of Hydrosil A and B; Siladent) was cast and cured at 40 psi for 180 min to create a reverse mold sized to fit a standard 24-well plate format. Reverse molds were autoclaved prior to each

usage. 1.5% (w/v) agarose in deionized water was sterilized by autoclaving and heated until molten prior to dispensing into silicone molds. Individual agarose molds containing microwells were cooled at room temperature and transferred to 24-well plates. Prior to seeding cells, microwells were covered with media and spun down briefly to remove air trapped underneath the molds.

For single-cell seeding of hPSCs into microwell arrays to form FC aggregates, cells were pre-treated for 4-6 hours with E8 supplemented with 10 μM Y-27632. Cells were then washed with PBS and incubated with TrypLE at 37°C for 5 min (or 0.05% trypsin/EDTA for 10 min, for select experiments) to singularize cells. Cell suspensions were diluted with 2X volume of E8 supplemented with 10 μM Y-27632 and pelleted by centrifugation at 200g for 5 minutes. A small aliquot of cell suspension was used to determine cell count. hPSCs were resuspended and seeded into agarose molds for a final seeding density of 5,000 or 20,000 cells per microwell (Aggrewell800 or Grote Bike Reflector molds, respectively). Plates containing microwell arrays were centrifuged at 300g for 5 min to force aggregation of cells before incubating plates at 37°C, 5% CO_2.

To form FC hepatocyte spheroids, hepatocytes were suspended in MM and 1.5-3.0 x 10^5 cells were dispensed dropwise into agarose molds (24-well, Aggrewell800 format) to create 500- to 1000-cell spheroids, respectively. Microwells were centrifuged at 60g for 4 min to force aggregation of cells prior to incubating at 37°C, 5% CO_2.

4.6.8 Characterization of aggregation process and aggregate size distribution: All timelapse images were acquired using a Nikon Ti Eclipse inverted microscope (10X PhL objective) equipped with NIS Elements software and a TIZ Tokai Hit incubated stage that was humidified and maintained at 37°C and 5% CO_2. Image analysis was performed with NIS Elements analysis

software. Edge detection was used to track the projected cell population area over time on patterned SAMs; this value of projected population area was normalized to initial seeded area for each individual spot as previously described[31]. To quantify hepatocyte spheroid size, day 5 spheroids were collected and imaged. NIS Elements analysis software was used to determine cross-sectional projection areas of individual spheroids. Spheroid diameter was calculated from cross-sectional projection areas by assuming spherical morphology.

4.6.9 Integrin-blocking competition assays: hPSCs were seeded on 5% cycRGDfC or 5% cycRGDfK SAMs as described above, and soluble peptides (0.1 mM cycRGDfC, cycRGDfK, cycRADfK, or linear RGD) were added to the media at 4 hrs (Supplementary Fig. S4.2) or 16 hrs (Fig. 4.3) post-seed to compete with surface-presented RGDs. Patterned hPSC populations on SAMs were monitored hourly by timelapse microscopy and image analysis to determine projected cell population area over time was conducted as described above. “Linear RGD” = GWGGRGDSP. Vehicle (PBS) only conditions were included as controls.

4.6.10 Cytoskeletal contractility inhibition: hPSCs were seeded on 5% cycRGDfC SAMs as described above, in MSC growth media containing a final concentration of 5 µM or 25 µM Y-27632 (EMD Millipore). Y-27632 was washed out with fresh media at 48 hrs post-seed.

4.6.11 Immunohistochemistry of hepatocyte spheroids: Hepatocyte spheroids were collected from labile substrates or 96w RB plates using wide-bore pipette tips, transferred to Eppendorf tubes, and allowed to settle before removing excess media and washing with PBS. Spheroids were then fixed with 10% neutral buffered formalin for 30 min at room temperature, washed twice with

PBS, and incubated in 10% sucrose solution overnight at 4°C before embedding in paraffin. Paraffin-embedded spheroids were sectioned at a thickness of 5 µm, deparaffinized in xylene, and stained with a rabbit anti-E-cadherin primary antibody (3195S, Cell Signaling Technology). Briefly, tissue sections underwent antigen retrieval using 10 mM citrate buffer (pH 6.0) in an 80°C water bath for 2 hours, followed by permeabilization with 0.25% Triton X-100. Sections were blocked with 10% BSA and incubated in primary antibody for 1 hour at room temperature. Endogenous peroxidase activity was quenched and antibody detection was carried out using ImmPRESS anti-rabbit IgG HRP (Vector Labs). Finally, the signal was visualized with ImmPACT DAB (Vector Labs) and sections counterstained with hematoxylin for contrast.

4.6.12 Characterization of hepatocyte spheroid viability: Hepatocytes in Matrigel overlay or 3D aggregates were maintained in hepatocyte MM as described above, or treated with 5 µM dexamethasone (Sigma-Aldrich) in hepatocyte MM for 48 hrs prior to viability assessment. Cell viability was assessed qualitatively using LIVE/DEAD staining kit (Life Technologies) according to manufacturer's instructions and imaged immediately thereafter on a Nikon Ti Eclipse inverted epifluorescence microscope. Quantification of cell viability in hepatocyte spheroids was performed using CellTox Green (Promega) following manufacturer's instructions. Briefly, hepatocyte spheroids were dispensed into 96-well plates and incubated in the working concentration of CellTox Green Reagent (diluted in hepatocyte MM), and an initial read (for signal from viable cells) was taken at 485 nm excitation/528 nm emission on a Biotek Synergy HTX plate reader. Subsequently, CellTox Green Lysis Buffer was added to each well and incubated for 30 min on an orbital shaker, and a second read was taken (for signal from total cells). Blank-

subtracted signal from viable cells was divided by that from total cells to give the percentage of dead cells, which was then converted to % viability.

4.6.13 Imaging of bile canaliculi formation: Matrigel overlay hepatocytes or 3D hepatocyte spheroids were washed with sterile HBSS and incubated in a staining solution of HBSS containing 10 µM CMFDA (Invitrogen) and 10 g/mL Hoechst 33342 (Invitrogen) for 30-35 min at 37°C. Following staining, cells were imaged within 15-60 minutes. Matrigel overlays were imaged by standard epifluorescence microscopy (Nikon Ti Eclipse). 3D hepatocyte spheroids were imaged by confocal microscopy (Leica SP8 3X STED).

4.6.14 Quantitative RT-PCR: For quantitative PCR (qPCR) analyses, cells or spheroids were washed with PBS and total RNA was isolated using the RNeasy mini kit (Qiagen) according to manufacturer's instructions. RNA was reverse transcribed into cDNA using the Quantitect Reverse Transcription Kit (Qiagen). cDNA samples (2.9 ng input RNA/10 µL reaction) were mixed with Quantitect primers and SYBR Green qPCR Master Mix, and run on a LightCycler 4800 system according to the manufacturer's protocol. Data analysis was performed using the ΔCt method, with *Gapd* as a reference gene.

4.6.15 Figure generation and statistics: All schematic graphics were created by the authors using Adobe Illustrator and Microsoft PowerPoint. Graphs were generated in GraphPad Prism or Microsoft Excel. Statistical analyses were performed using GraphPad Prism. The degree of significance for each comparison is denoted in each figure/caption.

4.7 ACKNOWLEDGMENTS

The authors thank Drew Roenneburg (UW-Madison Department of Surgery Histology Core Service) for assistance with preparation of histological samples and Lance Rodenkirch (UW-Madison Optical Imaging Core) for assistance with confocal microscopy. WTc11 human induced pluripotent cells were kindly provided by Dr. Bruce Conklin (UCSF/Gladstone Institutes). Primary hepatocytes and hepatocyte media were generously provided by Triangle Research Labs/Lonza (Research Triangle Park, NC). This work was supported by funding from the National Institutes of Health (R01HL093282 to W.L.M.; Biotechnology Training Program NIGMS 5 T32-GM08349 to A.W.X.), the U.S. Environmental Protection Agency (STAR grant no. 83573701 to W.L.M.), and the National Science Foundation (DGE-1256259 to A.W.X.; DMR-1306482 to W.L.M. and S.K.S.)

4.8 REFERENCES

1. Singh, H., Mok, P., Balakrishnan, T., Rahmat, S. N. B. & Zweigerdt, R. Up-scaling single cell-inoculated suspension culture of human embryonic stem cells. *Stem Cell Res.* **4,** 165–179 (2010).

2. Steiner, D. *et al.* Derivation, propagation and controlled differentiation of human embryonic stem cells in suspension. *Nat. Biotechnol.* **28,** 361–364 (2010).

3. Sengupta, S. *et al.* Aggregate culture of human embryonic stem cell-derived hepatocytes in suspension are an improved in vitro model for drug metabolism and toxicity testing. *Toxicol. Sci.* **140,** 236–45 (2014).

4. Hookway, T. A., Butts, J. C., Lee, E., Tang, H. & McDevitt, T. C. Aggregate formation and suspension culture of human pluripotent stem cells and differentiated progeny. *Methods* (2015). doi:10.1016/j.ymeth.2015.11.027

5. Ungrin, M. D., Joshi, C., Nica, A., Bauwens, C. & Zandstra, P. W. Reproducible, ultra high-throughput formation of multicellular organization from single cell suspension-derived human embryonic stem cell aggregates. *PLoS One* **3,** e1565 (2008).

6. Baker, B. M. & Chen, C. S. Deconstructing the third dimension: how 3D culture microenvironments alter cellular cues. *J. Cell Sci.* **125,** 3015–24 (2012).

7. Edmondson, R., Broglie, J. J., Adcock, A. F. & Yang, L. Three-Dimensional Cell Culture Systems and Their Applications in Drug Discovery and Cell-Based Biosensors. *Assay Drug Dev. Technol.* **12,** 207–218 (2014).

8. Chitcholtan, K., Sykes, P. H. & Evans, J. J. The resistance of intracellular mediators to doxorubicin and cisplatin are distinct in 3D and 2D endometrial cancer. *J. Transl. Med.* **10,** 38 (2012).

9. Bell, C. C. *et al.* Comparison of Hepatic 2D Sandwich Cultures and 3D Spheroids for Long-term Toxicity Applications: A Multicenter Study. *Toxicol. Sci.* **162,** 655–666 (2018).

10. Bratt-leal, M., Carpenedo, R. L. & Mcdevitt, T. C. Engineering the embryoid body microenvironment to direct embryonic stem cell differentiation. 43–51 (2009). doi:10.1021/bp.139

11. Sart, S., Tsai, A.-C., Li, Y. & Ma, T. Three-dimensional aggregates of mesenchymal stem cells: cellular mechanisms, biological properties, and applications. *Tissue Eng. Part B, Rev.* **20,** 365–80 (2014).

12. Kinney, M. A., Hookway, T. A., Wang, Y. & McDevitt, T. C. Engineering three-dimensional stem cell morphogenesis for the development of tissue models and scalable regenerative therapeutics. *Ann. Biomed. Eng.* **42,** 352–367 (2014).

13. Serra, M., Brito, C., Correia, C. & Alves, P. M. Process engineering of human pluripotent stem cells for clinical application. *Trends Biotechnol.* **30,** 350–359 (2012).

14. Rowley, J., Abraham, E., Campbell, A., Brandwein, H. & Oh, S. Meeting lot-size challenges of manufacturing adherent cells for therapy. *Bioprocess Int.* **10,** 16–22 (2012).

15. Want, A. J., Nienow, A. W., Hewitt, C. J. & Coopman, K. Large-scale expansion and exploitation of pluripotent stem cells for regenerative medicine purposes: beyond the T flask. *Regen. Med.* **7,** 71–84 (2012).

16. Schnitzler, A. C. *et al.* Bioprocessing of human mesenchymal stem/stromal cells for therapeutic use: Current technologies and challenges. *Biochem. Eng. J.* **108,** 3–13 (2016).

17. Kehoe, D. E., Jing, D., Lock, L. T., Tzanakakis, E. S. & Ph, D. Scalable Stirred-Suspension Bioreactor Culture. **16,** (2010).

18. Zimmermann, J. A. & McDevitt, T. C. Pre-conditioning mesenchymal stromal cell spheroids for immunomodulatory paracrine factor secretion. *Cytotherapy* **16,** 331–45 (2014).

19. Zimmermann, J. A., Hettiaratchi, M. H. & McDevitt, T. C. Enhanced Immunosuppression of T Cells by Sustained Presentation of Bioactive Interferon-γ Within Three-Dimensional Mesenchymal Stem Cell Constructs. *Stem Cells Transl. Med.* (2016). doi:10.5966/sctm.2016-0044

20. Pettinato, G., Wen, X. & Zhang, N. Formation of well-defined embryoid bodies from dissociated human induced pluripotent stem cells using microfabricated cell-repellent microwell arrays. *Sci. Rep.* **4,** 7402 (2014).

21. Hookway, T. A., Butts, J. C., Lee, E., Tang, H. & McDevitt, T. C. Aggregate formation and suspension culture of human pluripotent stem cells and differentiated progeny. *Methods* (2015). doi:10.1016/j.ymeth.2015.11.027

22. Zhang, Y., Sivasankar, S., Nelson, W. J. & Chu, S. Resolving cadherin interactions and binding cooperativity at the single-molecule level. *Proc. Natl. Acad. Sci.* **106,** 109–114 (2009).

23. Xu, Y. *et al.* Revealing a core signaling regulatory mechanism for pluripotent stem cell survival and self-renewal by small molecules. *Proc. Natl. Acad. Sci.* **107,** 8129–8134 (2010).

24. Chen, Z., Casiano, C. A. & Fletcher, H. M. Protease-active extracellular protein preparations from porphyromonas gingivalis W83 induce N-cadherin proteolysis, loss of cell adhesion, and apoptosis in human epithelial cells. *J.Periodontol.* **72,** 641–650 (2001).

25. Parnaud, G. *et al.* Cadherin engagement protects human β-cells from apoptosis. *Endocrinology* **152,** 4601–4609 (2011).

26. Vachon, P. H. Integrin Signaling, Cell Survival, and Anoikis: Distinctions, Differences, and Differentiation. *J. Signal Transduct.* **2011,** 1–18 (2011).

27. Love, J. C., Estroff, L. a, Kriebel, J. K., Nuzzo, R. G. & Whitesides, G. M. *Self-assembled monolayers of thiolates on metals as a form of nanotechnology. Chemical reviews* **105,** (2005).

28. Koepsel, J. T. & Murphy, W. L. Patterned Self-Assembled Monolayers: Efficient, Chemically Defined Tools for Cell Biology. *ChemBioChem* **13,** 1717–1724 (2012).

29. Schmitt, S. K. *et al.* Polyethylene Glycol Coatings on Plastic Substrates for Chemically Defined Stem Cell Culture. *Adv. Healthc. Mater.* **4,** 1555–1564 (2015).

30. Schmitt, S. K. *et al.* Peptide Conjugation to a Polymer Coating via Native Chemical Ligation of Azlactones for Cell Culture. *Biomacromolecules* **17,** 1040–1047 (2016).

31. Xie, A. W. *et al.* Controlled Self-assembly of Stem Cell Aggregates Instructs Pluripotency and Lineage Bias. *Sci. Rep.* **7,** 1–15 (2017).

32. Wrighton, P. J. & Kiessling, L. L. Forces of change: Mechanics underlying formation of functional 3D organ buds. *Cell Stem Cell* **16,** 453–454 (2015).

33. Takebe, T. *et al.* Vascularized and complex organ buds from diverse tissues via mesenchymal cell-driven condensation. *Cell Stem Cell* **16,** 556–565 (2015).

34. Drewitz, M. *et al.* Towards automated production and drug sensitivity testing using scaffold-free spherical tumor microtissues. *Biotechnol. J.* **6,** 1488–1496 (2011).

35. Hofmann, C. *et al.* Cell-Cell Contacts Prevent Anoikis in Primary Human Colonic Epithelial Cells. *Gastroenterology* **132,** 587–600 (2007).

36. Ohgushi, M. *et al.* Molecular pathway and cell state responsible for dissociation-induced apoptosis in human pluripotent stem cells. *Cell Stem Cell* **7,** 225–239 (2010).

37. Vitillo, L., Baxter, M., Iskender, B., Whiting, P. & Kimber, S. J. Integrin-Associated Focal Adhesion Kinase Protects Human Embryonic Stem Cells from Apoptosis, Detachment, and Differentiation. *Stem Cell Reports* **7,** 167–176 (2016).

38. Vitillo, L. & Kimber, S. J. Integrin and FAK Regulation of Human Pluripotent Stem Cells. *Curr. Stem Cell Reports* **3,** 358–365 (2017).

39. Smets, F. N., Chen, Y., Wang, L.-J. & Soriano, H. E. Loss of cell anchorage triggers apoptosis (anoikis) in primary mouse hepatocytes. *Mol. Genet. Metab.* **75,** 344–352 (2002).

40. Luebke-Wheeler, J. L., Nedredal, G., Yee, L., Amiot, B. P. & Nyberg, S. L. E-cadherin protects primary hepatocyte spheroids from cell death by a caspase-independent mechanism. *Cell Transplant.* **18,** 1281–7 (2009).

41. Vinken, M. *et al.* Primary hepatocytes and their cultures in liver apoptosis research. *Arch. Toxicol.* **88,** 199–212 (2014).

42. LeCluyse, E. L., Witek, R. P., Andersen, M. E. & Powers, M. J. Organotypic liver culture models: meeting current challenges in toxicity testing. *Crit. Rev. Toxicol.* **42,** 501–48 (2012).

43. Roelofsen, H., Soroka, C. J., Keppler, D. & Boyer, J. L. Cyclic AMP stimulates sorting of the canalicular organic anion transporter (Mrp2/cMoat) to the apical domain in hepatocyte couplets. *J. Cell Sci.* **111 (Pt 8,** 1137–45 (1998).

44. Godoy, P. *et al.* Extracellular matrix modulates sensitivity of hepatocytes to fibroblastoid dedifferentiation and transforming growth factor β-induced apoptosis. *Hepatology* **49,** 2031–2043 (2009).

45. Zanger, U. M. & Schwab, M. Cytochrome P450 enzymes in drug metabolism: Regulation of gene expression, enzyme activities, and impact of genetic variation. *Pharmacol. Ther.* **138,** 103–141 (2013).

46. Koepsel, J. T. *et al.* A chemically-defined screening platform reveals behavioral similarities between primary human mesenchymal stem cells and endothelial cells. *Integr. Biol.* **4,** 1508 (2012).

47. Beers, J. *et al.* Passaging and colony expansion of human pluripotent stem cells by enzyme-free dissociation in chemically defined culture conditions. *Nat. Protoc.* **7,** 2029–2040 (2012).

48. Dahlmann, J. *et al.* The use of agarose microwells for scalable embryoid body formation and cardiac differentiation of human and murine pluripotent stem cells. *Biomaterials* **34,** 2463–71 (2013).

4.9 FIGURES

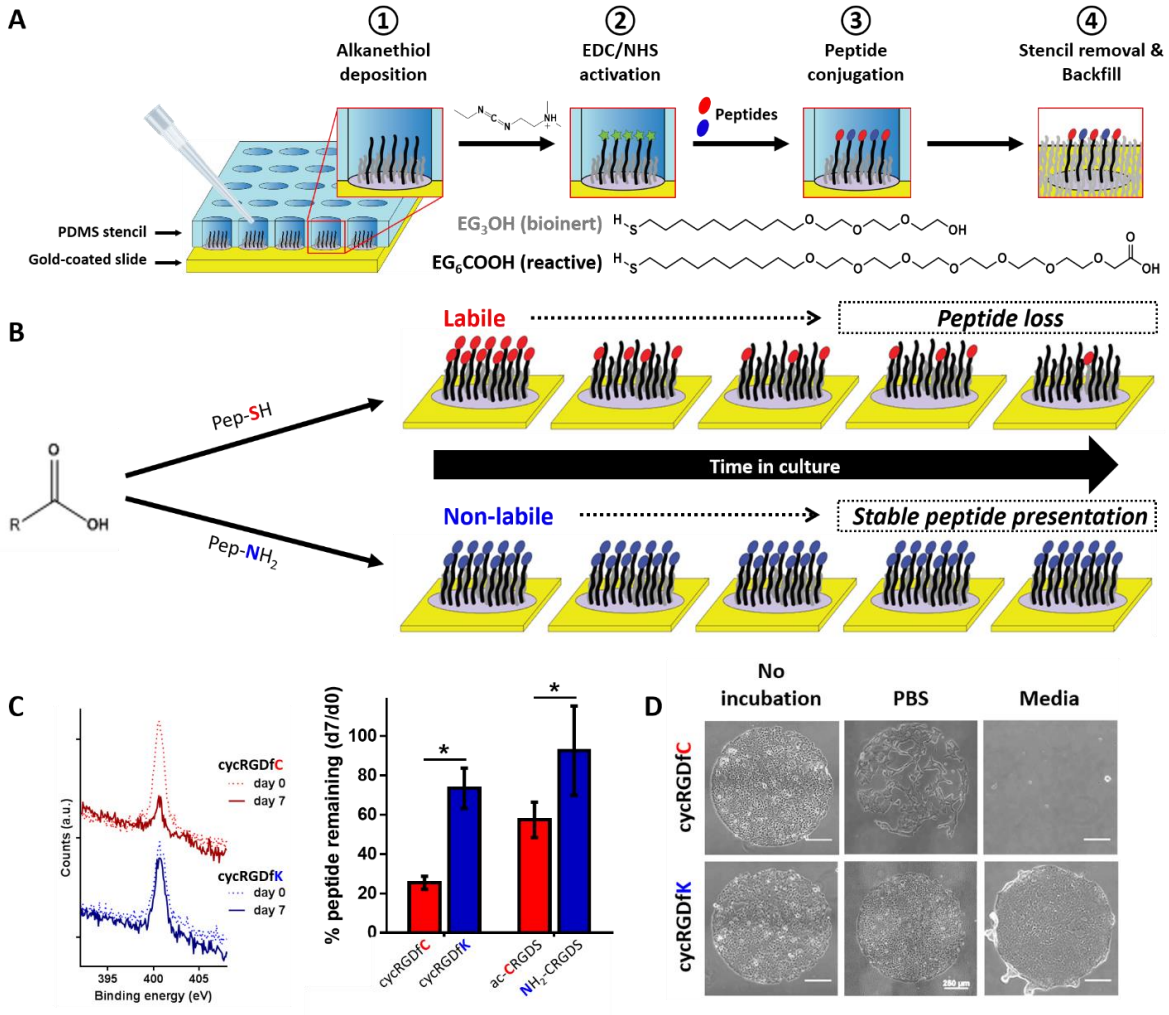

Figure 4.1 Mechanism and characterization of labile SAM-based substrates for cell aggregate generation. (A) Approach for patterning labile substrates. A PDMS stencil is placed in contact with the gold-coated slide to form an array of wells on the substrate, and ethanolic solutions containing a mixture of carboxyl-terminated EG_6COOH ("reactive") and hydroxyl-terminated EG_3OH ("bioinert") alkanethiols are pipetted into wells to form SAMs in localized regions on the gold. EG_6COOH carboxy groups are activated by EDC/NHS, followed by nucleophilic reaction with peptide(s) of interest. The PDMS stencil is then removed and the remaining bare regions of the gold slide are backfilled by immersing in a solution of bioinert EG_3OH alkanethiols. (B) Schematic representation of reaction between EG_6COOH carboxy groups and peptide nucleophiles. EG_6COOH reaction with free thiols (e.g., cycRGDfC) and primary amines (e.g., cycRGDfK) are expected to result in thioester (labile) and amide (non-labile) bonds, respectively. Labile bonds are cleaved in aqueous media, resulting in release of RGD peptide from the SAM over time, while non-labile bonds enable stable presentation of peptide. (C) (left) Representative XPS scans of N(1s) signal on EG_6COOH SAMs reacted with cycRGDfC or cycRGDfK, immediately after functionalization (dashed line) or 7 days after incubation in PBS (solid line). (right) Quantification of percentage of initial peptide remaining on substrates after 7-day PBS

incubation. Values represent the mean ± s.d. of n = 3 replicates; asterisks denote statistical significance (*$p < 0.05$, Student's t-test). (D) Adhesion of human embryonic stem cells (hESCs) on labile cycRGDfC- or non-labile cycRGDfK-presenting SAMs immediately after functionalization or after 7-day pre-incubation of substrates in PBS or cell culture media. Both labile and non-labile substrates mediate strong cell adhesion immediately after functionalization. Labile substrates pre-incubated in PBS or culture media partially or fully lose their capacity to support hESC adhesion, while non-labile substrates support strong hESC adhesion following pre-incubation in aqueous solutions. Scale bars = 250 μm.

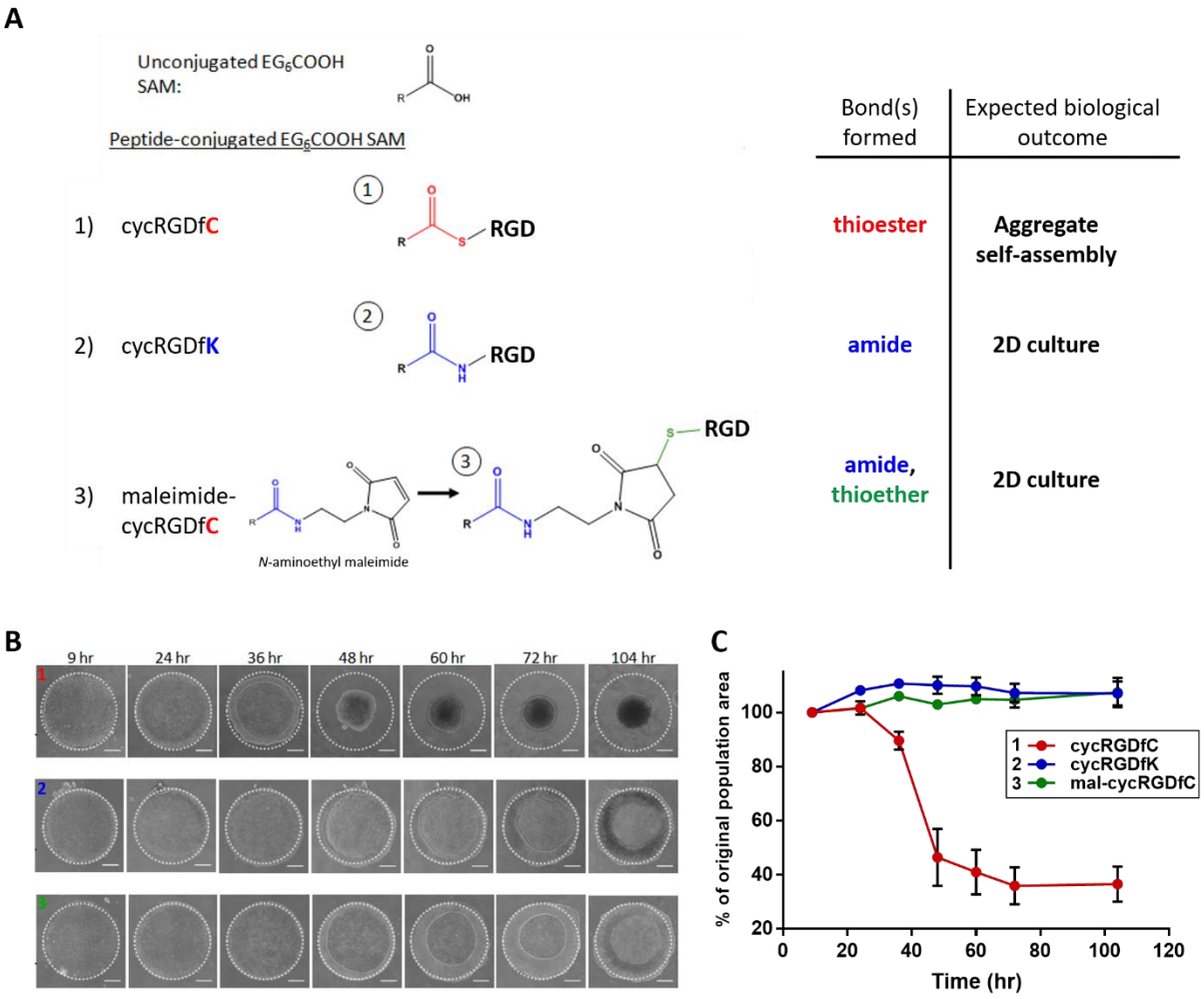

Figure 4.2 Cell aggregate self-assembly depends on bond lability. (A) Experimental scheme used to determine whether labile substrates permit cell aggregate formation and the role of bond lability in this process. In Reactions 1 and 2, cycRGDfC and cycRGDfK peptides are reacted directly with activated EG_6COOH SAMs, resulting in formation of thioester and amide bonds between the SAM and RGD peptide, respectively. In Reaction 3, activated EG_6COOH SAMs are first reacted with *N*-aminoethyl maleimide crosslinker prior to reacting with cycRGDfC peptide, to form amide and thioether linkages between the SAM and RGD. (B) Representative biological outcomes observed with hESC culture on the substrates generated in (A). hESC aggregates formed on labile substrates generated in Reaction 1 but did not form on substrates from Reactions 2 and 3. Representative images shown. Scale bars = 250 µm. (C) Quantification of cell population area over time, as a percentage of original population area at t = 9 hrs after seeding (areas bounded by white dashed lines in (B)). hESCs reproducibly self-assembled to form 3D aggregates only on labile cycRGDfC substrates (Reaction 1), as indicated by a decrease in % population area at t ~ 36 hrs. Reaction of the same cycRGDfC peptide with maleimide-modified SAMs (Reaction 3) resulted in sustained 2D hESC culture similar to that on non-labile cycRGDfK substrates (Reaction 2).

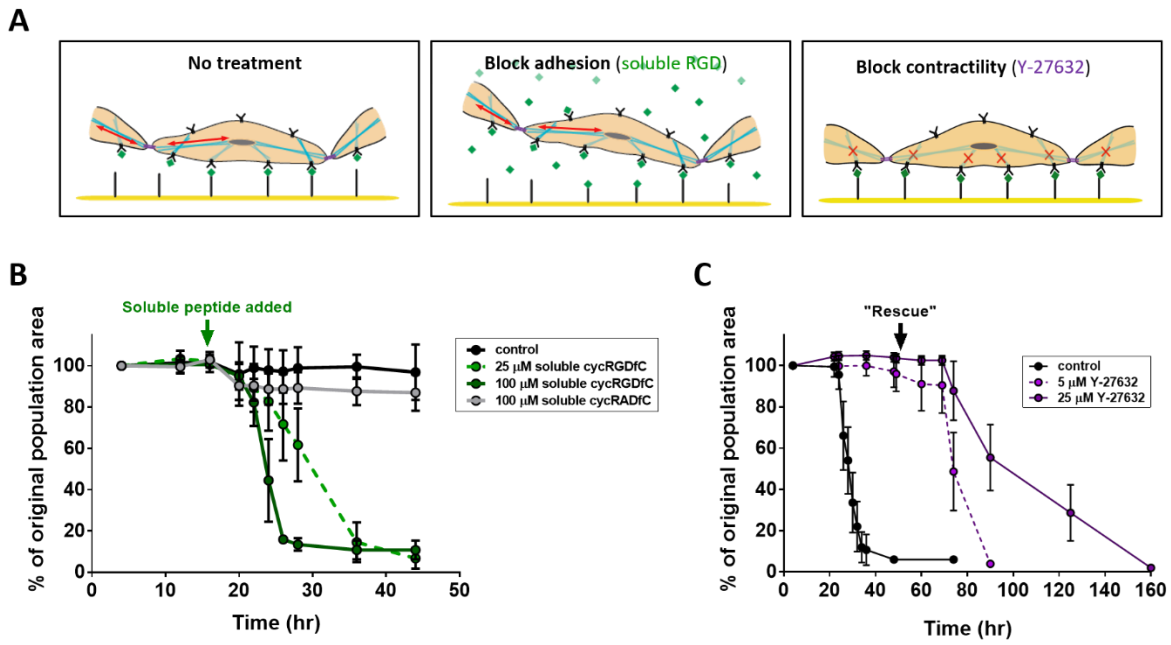

Figure 4.3 Cell aggregate self-assembly is dependent on integrin-mediated adhesion and cytoskeletal contractility. (A) Schematic of proposed treatments to test adhesion- and contractility-dependent mechanisms of cell aggregate self-assembly from labile substrates. (B) Influence of soluble cyclic RGDs on aggregate self-assembly kinetics. hPSCs were seeded on 5% cycRGDfC SAMs and cyclic RGD peptides with varying degrees of integrin-blocking activity were added to the media at 16 hrs post-seed. (C) Influence of cytoskeletal contractility inhibition on aggregate self-assembly kinetics. MSCs were seeded on 5% cycRGDfC SAMs in media containing varying concentrations of ROCK inhibitor Y-27632. Y-27632 was washed out ("rescue") with fresh media at 48 hrs post-seed.

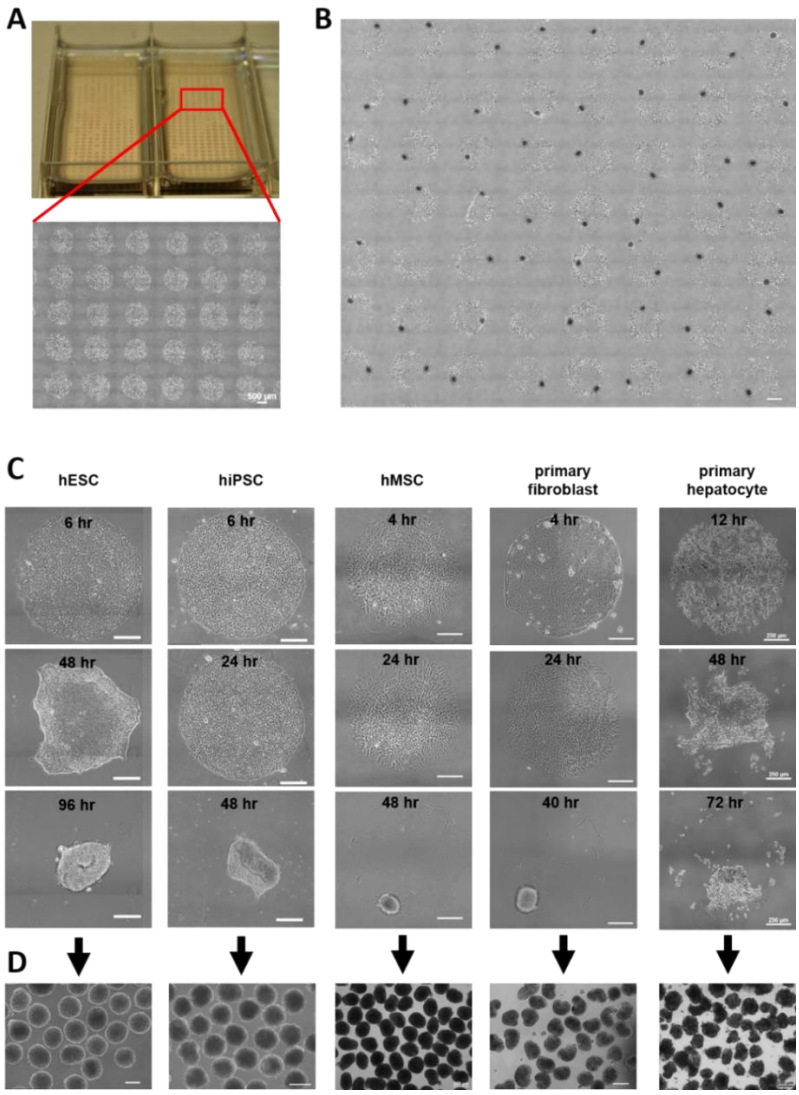

Figure 4.4 Labile substrates enable simple, scalable self-assembly of aggregates from diverse cell types. (A) Arrays of patterned cell "islands" generated on labile substrates undergo a 2D-to-3D transition, resulting in (B) Cell aggregates formed without additional external manipulation (example shown for 1.2 mm diameter circular patterns). (C) Self-assembly behavior is generalizable to many cell types, enabling formation of aggregates of hESCs, hiPSCs, hMSCs, primary fibroblasts, and primary hepatocytes from labile substrates. (D) Self-assembled aggregates generated from the cell types in (C), collected in bulk at day 3-4 after initial seeding. Scale bar = 250 μm.

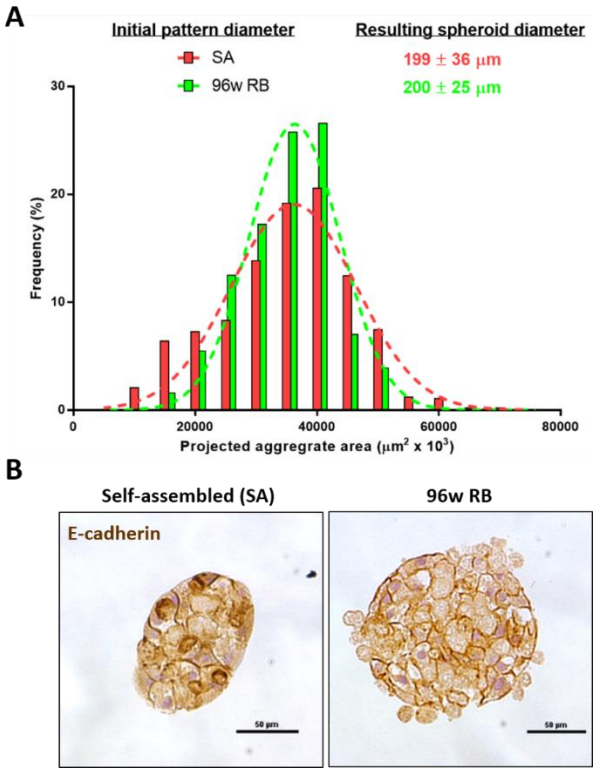

Figure 4.5 Morphometric and histological characterization of self-assembled hepatocyte spheroids. (A) Size distribution of hepatocyte aggregates generated by self-assembly from 1.2 mm diameter patterned labile substrates (SA, red) or in 96-well round-bottom plates (96w RB, green). (B) Immunohistochemistry showing E-cadherin expression at cell-cell junctions and no necrotic core formation in day 10 SA and 96w RB hepatocyte spheroids. Scale bars = 50 µm.

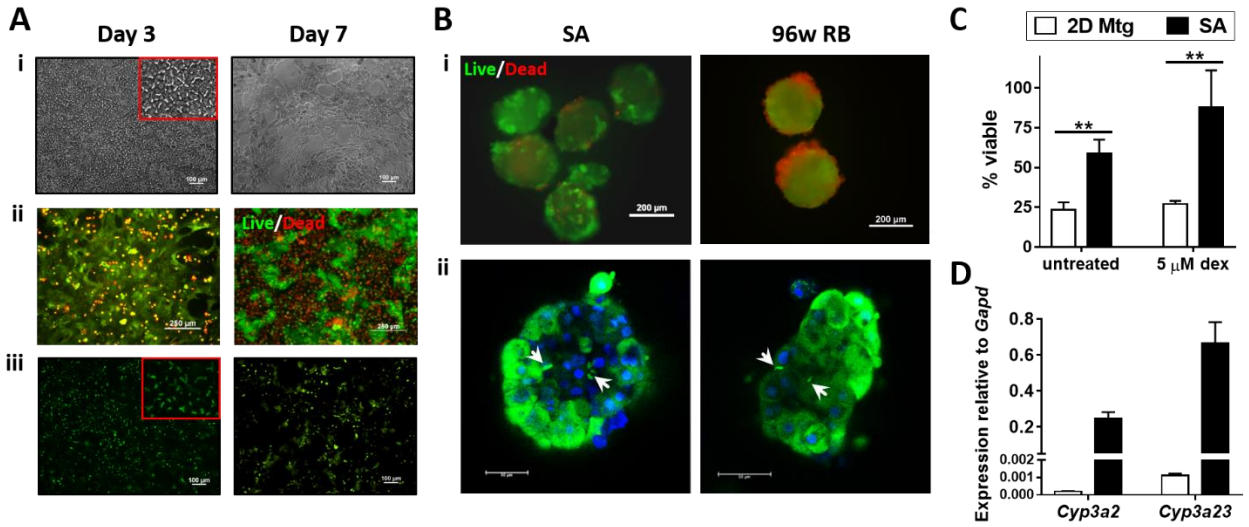

Figure 4.6 Self-assembled hepatocyte spheroids form bile canaliculi and are viable during extended *in vitro* culture. (A) Characterization of 2D primary hepatocyte monolayer controls. (i) Representative phase images of primary hepatocyte monolayers maintained on Collagen I with Matrigel overlay ("2D Mtg") at day 3 (left) and day 7 (right) of culture. (ii) Viability of primary hepatocyte monolayers at day 3 and day 7. (iii) Formation of bile canaliculi (green) in primary hepatocyte monolayers at day 3 (left) and day 7 (right). Scale bars = 100 µm (i and iii), 250 µm (ii). (B) Characterization of SA primary hepatocyte spheroids from labile substrates and comparison to spheroids formed by conventional approach (96-well round-bottom plate; "96w RB"). (i) Viability of day 7 spheroids, as visualized by LIVE/DEAD Viability/Cytotoxicity assay. Scale bars = 200 µm. (ii) Confocal images of bile canaliculi formation (white arrows) in day 7 spheroids. Scale bars = 50 µm. (C) Quantification of percent viable hepatocytes in SA spheroids, conventional spheroids, and 2D controls (untreated and dexamethasone-treated). Asterisks denote statistically significant difference (*$p < 0.01$, two-way ANOVA). (D) Expression of *Cyp3a2* and *Cyp3a23* by day 9 hepatocytes in SA spheroids or 2D Mtg culture (untreated).

4.10 SUPPLEMENTARY FIGURES

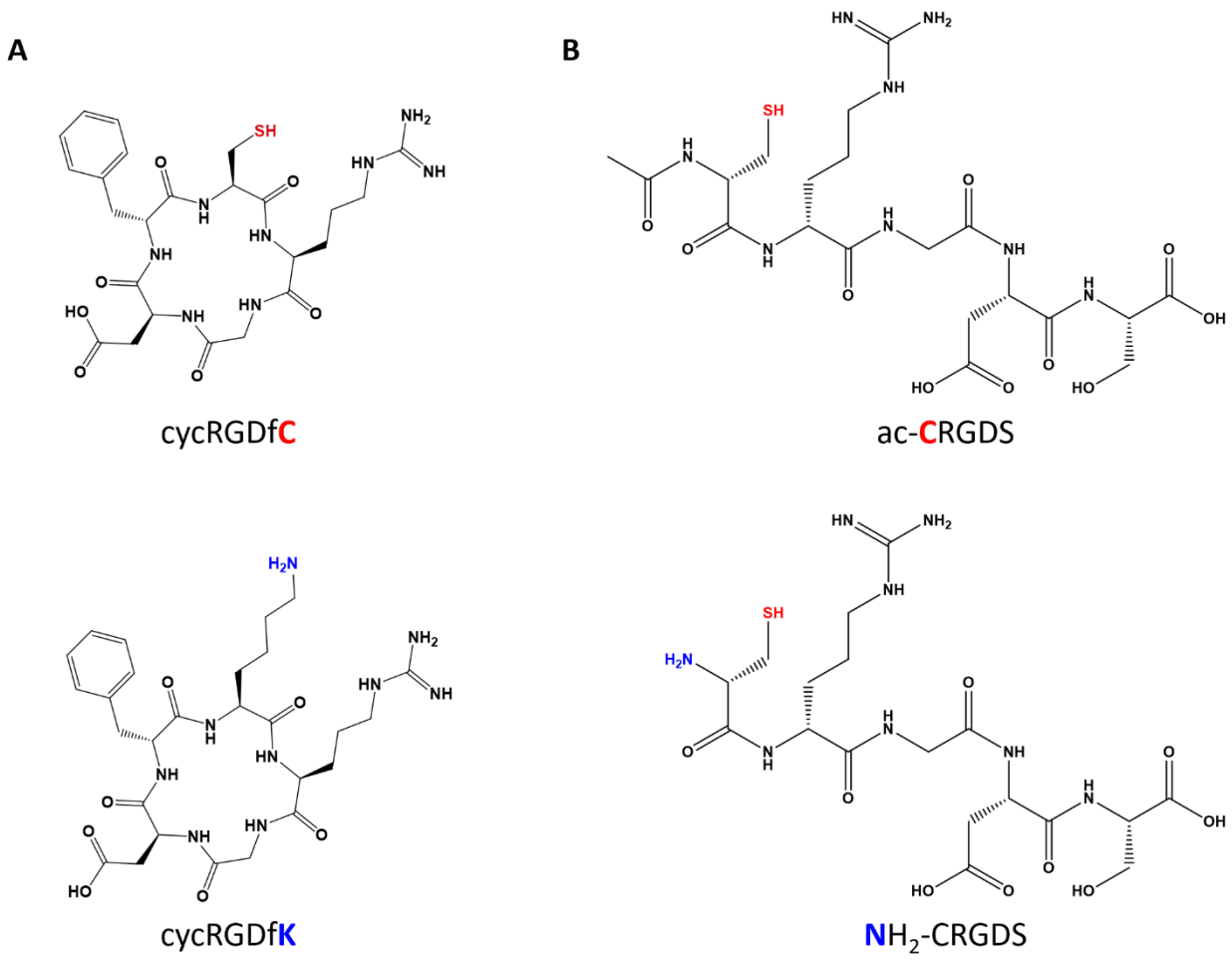

Supplementary Fig. S4.1 Chemical structures for (A) cyclic and (B) linear RGD peptides referred to in Figure 4.1C. Red and blue colors denote nucleophilic functional groups expected to react with EG6COOH SAMs to generate labile and non-labile linkages, respectively.

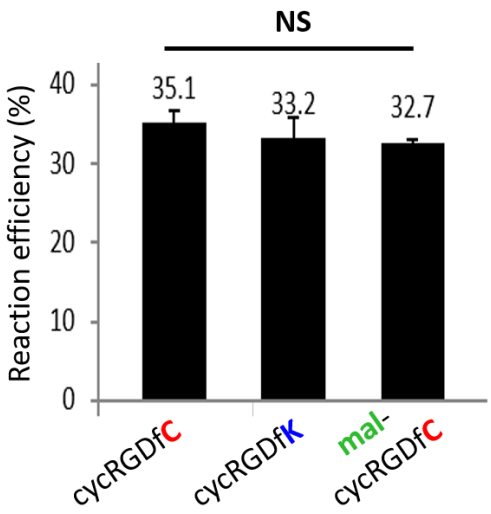

Supplementary Fig. S4.2 Efficiency of EG_6COOH reaction with peptide and/or crosslinkers to form labile or non-labile substrates. EG_6COOH SAMs were functionalized with cycRGDfC, cycRGDfK, or *N*-(2-aminoethyl-maleimide) followed by cycRGDfC. Reaction efficiency was assessed by using XPS to measure the N1(s):C1(s) ratio as an indication of peptide content on the SAMs.

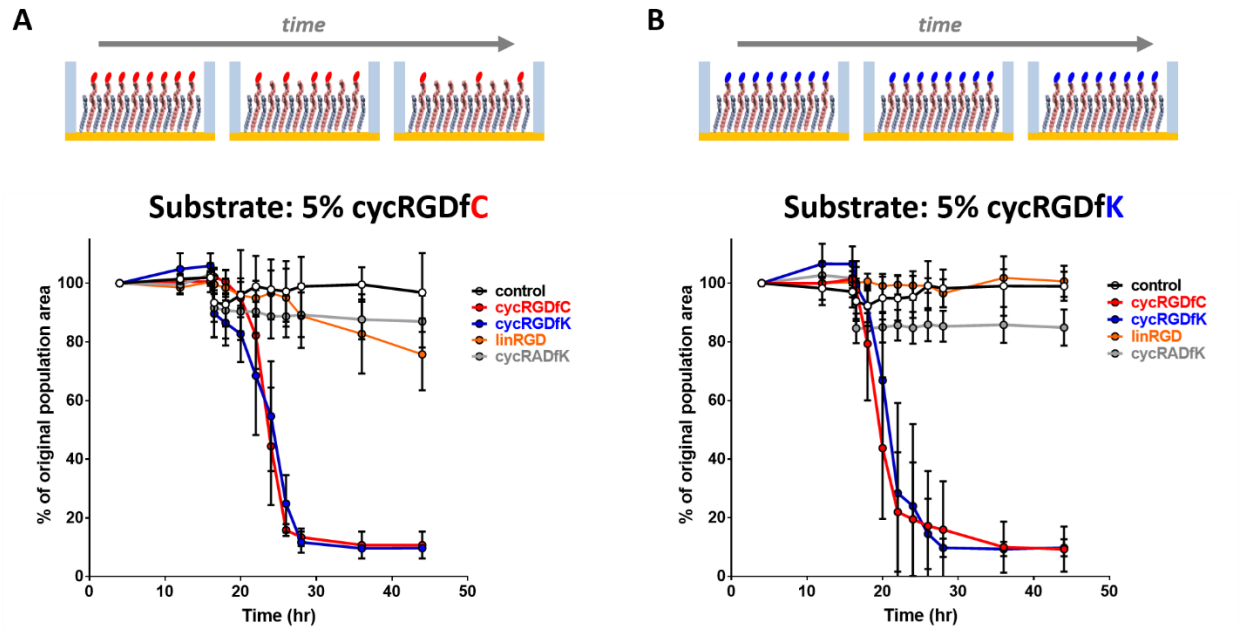

Supplementary Fig. S4.3 Cyclic RGDfC and cycRGDfK demonstrate similar activity in integrin-blocking competition assay. hPSCs were seeded on (A) 5% cycRGDfC or (B) 5% cycRGDfK SAMs and peptides with varying degrees of integrin-blocking activity ("soluble competitors") were added to the media at 4 hrs post-seed. Integrin-blocking activity of each peptide was assessed by its capacity to compete with RGD peptides presented on the substrate (i.e., capacity to promote cell release from the substrate), as measured by a decrease in % of original population area.

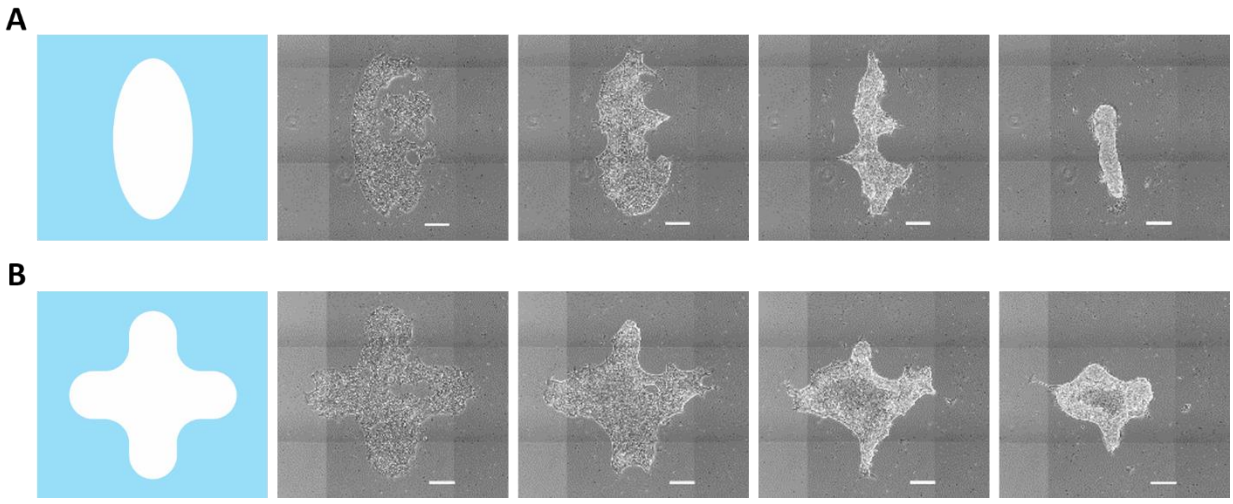

Supplementary Fig. S4.4 Patterning of labile substrates enables control over size and shape of self-assembled cell aggregates. (A) Oval and (B) quatrefoil patterns constrain cell adhesion in 2D and influence 3D cell aggregate shape. Scale bars = 250 µm.

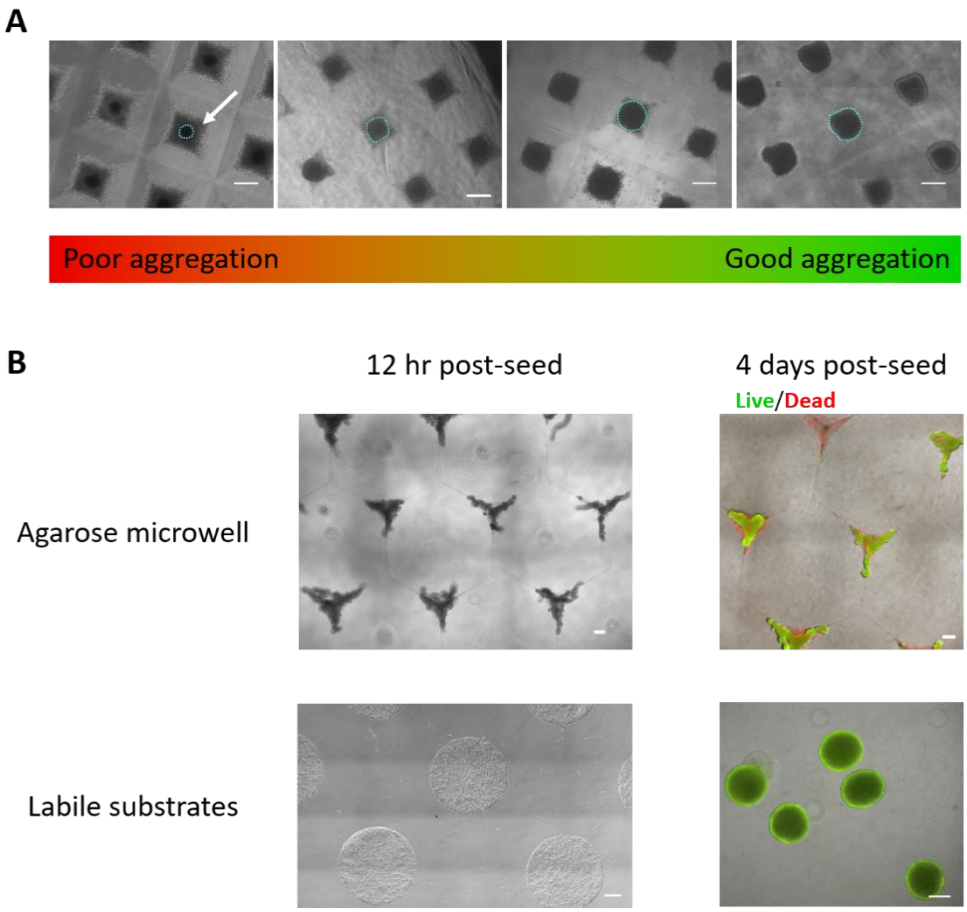

Supplementary Fig. S4.5 Labile substrates improve efficiency of aggregate formation and enable reproducible aggregation of hPSCs, compared to conventional aggregation approaches. (A) Demonstration of inconsistent hPSC aggregation in pyramidal agarose microwells. Individual panels are representative brightfield images from four independent experiments. hPSCs in each experiment were processed similarly and seeded at 5000 cells per microwell, yet vastly different quality of aggregation was observed between experiments, with the efficiency of cell incorporation into aggregates ranging from <50% (poor aggregation) to nearly 100% (good aggregation). Cyan dashed lines in each image indicate the outline of a representative hPSC aggregate, where good aggregation was indicated by intact aggregates with well-defined edges and few unincorporated cells (rightmost image). In conditions with poor aggregation, small aggregates (or no aggregates) formed and were surrounded by cell debris and/or dead cells (leftmost image, white arrow). (B) Labile substrates improve viability and aggregation of cells subjected to extensive trypsinization. hPSCs treated with 0.05% trypsin/EDTA for 10 minutes exhibited poor viability and failed to form compact aggregates in agarose microwells (top). The same cells demonstrated robust adhesion to labile substrates and consistently formed viable aggregates via self-assembly (bottom). Scale bars = 250 μm.

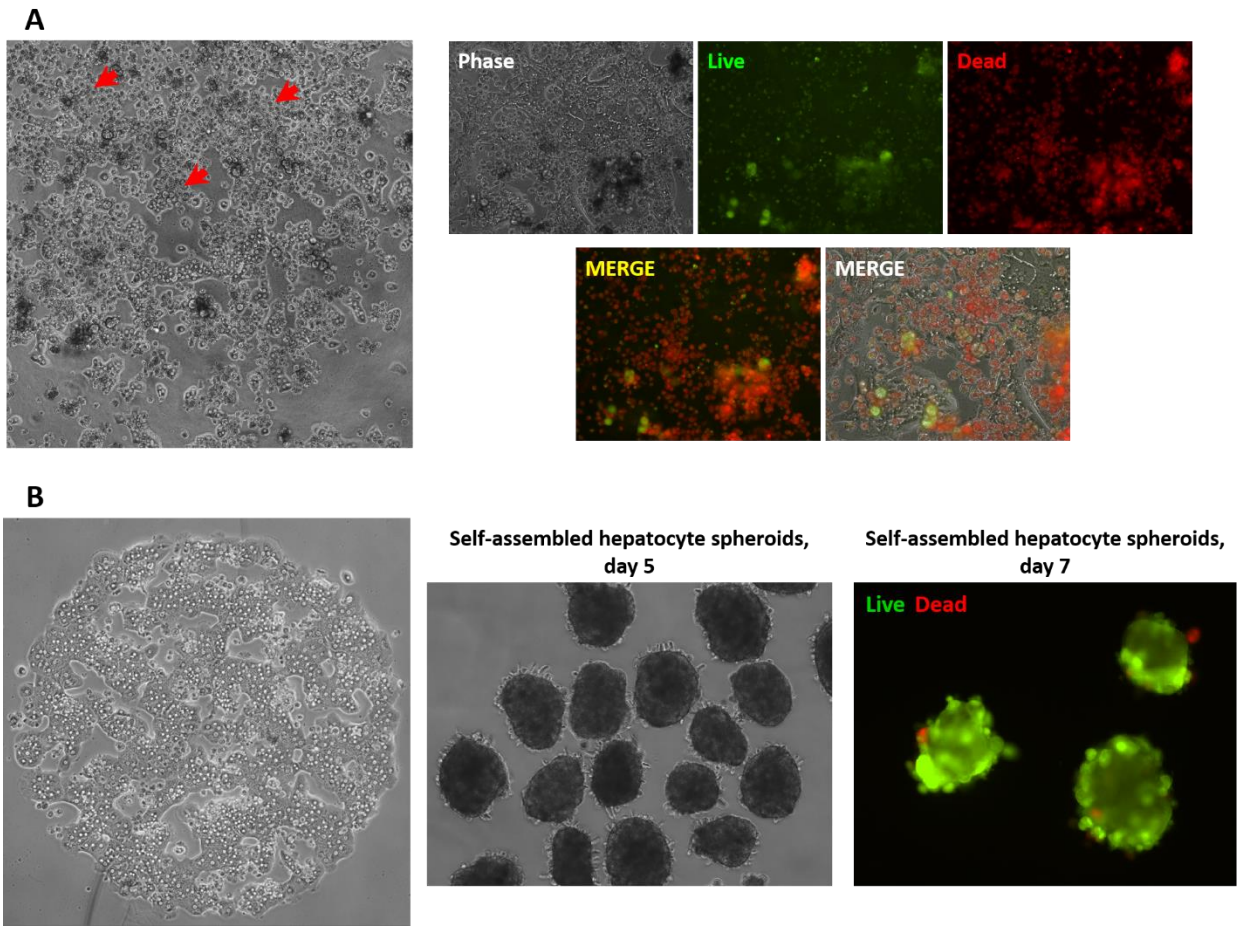

Supplementary Fig. S4.6 Labile substrates select for viable hepatocytes and enable consistent formation of hepatocyte spheroids. (A) Occasional batches of primary hepatocytes plated poorly on Matrigel, as evidenced by low confluence, poor monolayer formation, substantial cell debris (red arrows) and low viability by LIVE/DEAD staining at day 1 after plating. (B) The same batch of cells demonstrated improved adhesion and monolayer formation and typical hepatocyte morphology on labile substrates at day 1 (left) and formed viable aggregates via self-assembly (middle, right).

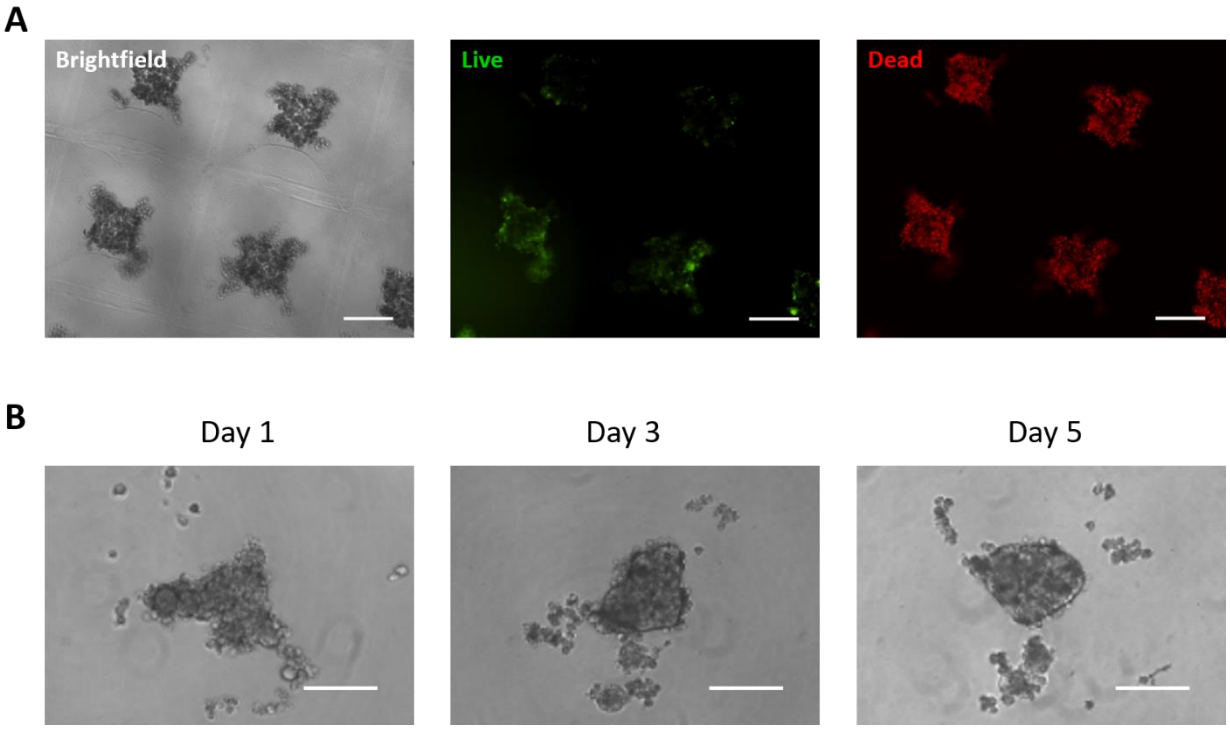

Supplementary Fig. S4.7 Formation of 3D primary hepatocyte aggregates by conventional aggregation methods. (A) Primary hepatocytes fail to form viable aggregates via forced centrifugation into microwell arrays, as evidenced by failure of cells to compact into aggregates with well-defined borders. Cells were stained with LIVE/DEAD Viability/Cytotoxicity dyes on day 3 after seeding. Scale bars = 250 µm. (B) Brightfield microscopy showing the time course of aggregation of hepatocytes into spheroids in a 96w round-bottom (RB) plate format. Scale bars = 200 µm.

CHAPTER 5. CONTROLLED SELF-ASSEMBLY OF STEM CELL AGGREGATES INSTRUCTS PLURIPOTENCY AND LINEAGE BIAS

Elements of this chapter have been published as:

Angela W. Xie, Bernard Y.K. Binder, Andrew S. Khalil, Samantha K. Schmitt, Hunter J. Johnson, Nicholas A. Zacharias, and William L. Murphy (2017). Controlled self-assembly of stem cell aggregates instructs pluripotency and lineage bias. *Scientific Reports* **7**, 14070.

5.1 PREFACE

In Chapter 4, we developed a technique to control cell aggregation by engineering patterned substrates presenting adhesion peptides via labile thioester linkages to enable spatially regulated cellular self-assembly (SA) with controllable kinetics. The purpose of studies in this chapter was to apply this platform to investigate the implications of aggregation parameters for cell phenotype in an embryoid body (EB) model of human pluripotent stem cell (hPSC) differentiation. We viewed EBs as an ideal initial testbed for our technology, due to the phenotypic plasticity of hPSCs and the need to control 3D stem cell phenotype during expansion and differentiation steps in hPSC biomanufacturing. Here, we compared EBs generated via our self-assembly platform to size-matched EBs formed via a common approach – forced centrifugation into microwells. Our results indicated that the method used to generate stem cell aggregates had a marked effect on their lineage bias during differentiation, which depended in part on the mechanism and kinetics of aggregation employed. Importantly, despite controlling for EB size, structural features of EBs were markedly affected by aggregation kinetics and corresponded to distinct spatial patterns of growth factor signaling within EBs. Thus, commonly reported metrics

such as aggregate diameter are likely poor indicators of eventual cell phenotype and function without additional consideration of cell processing parameters before and during aggregation.

5.2 ABSTRACT

Stem cell-derived organoids and other 3D microtissues offer enormous potential as models for drug screening, disease modeling, and regenerative medicine. Formation of stem/progenitor cell aggregates is common in biomanufacturing processes and critical to many organoid approaches. However, reproducibility of current protocols is limited by reliance on poorly controlled processes (e.g., spontaneous aggregation). Little is known about the effects of aggregation parameters on cell behavior, which may have implications for the production of cell aggregates and organoids. Here we introduce a bioengineered platform of labile substrate arrays that enable simple, scalable generation of cell aggregates via a controllable 2D-to-3D "self-assembly". As a proof-of-concept, we show that labile substrates generate size- and shape-controlled embryoid bodies (EBs) and can be easily modified to control EB self-assembly kinetics. We show that aggregation method instructs EB lineage bias, with faster aggregation promoting pluripotency loss and ectoderm, and slower aggregation favoring mesoderm and endoderm. We also find that aggregation kinetics of EBs markedly influence EB structure, with slower kinetics resulting in increased EB porosity and growth factor signaling. Our findings suggest that controlling internal structure of cell aggregates by modifying aggregation kinetics is a potential strategy for improving 3D microtissue models for research and translational applications.

5.3 INTRODUCTION

Human pluripotent stem cells (hPSCs) offer considerable promise as a cell source for regenerative medicine. Traditional 2-dimensional (2D) stem cell culture is suitable for basic research applications but lacks the scalability required for biomanufacturing and the biological complexity required to generate organoids for drug/toxin screening[1,2]. Alternatively, three-dimensional (3D) cell aggregates are an attractive cell culture format for such applications. Stem cell aggregates offer increased surface area for cell growth per media volume, which enables stem cell expansion at the scale required for cell therapies[3]. In addition, cell aggregates applied as implantable "scaffold-free" constructs show enhanced survival and function *in vivo*[4–7]. Stem cell aggregates also serve as starting materials for generating organoids, complex multicellular constructs that recapitulate structural and functional aspects of human organs and are useful as *in vitro* tissue models for predicting responses to drugs and toxins[8,9]. The process of cell aggregate formation, typically via reaggregation of singularized cells, is a critical initial step for the generation of many organoids. While several types of stem/progenitor cells have demonstrated an intrinsic capacity to "self-organize" into 3D tissue-specific organoids[10,11], current approaches offer little control over parameters associated with the aggregation process (e.g., aggregate size shape, formation kinetics), which limits optimization of stem cell expansion/differentiation and impedes identification of requisite conditions for organoid formation.

Conventional methods for generating stem cell aggregates, such as hanging drops and spontaneous aggregation (reviewed in [12,13]), are typically low throughput or offer minimal control over properties of resulting aggregates. To address these shortcomings, recent approaches have relied on "forced aggregation," wherein defined numbers of singularized cells are centrifuged into microwell arrays to form size-controlled aggregates[14,15]. While this strategy has been applied toward scalable production of aggregates of hPSCs and other cell types, functional equivalence to

other methods of aggregation has not been well demonstrated, and the centrifugation force applied in these approaches may have unintended effects on stem cell viability and differentiation[16,17]. Despite the importance of stem cell aggregates in bioprocessing applications, few studies have investigated the influence of aggregation parameters on early lineage bias in pluripotent stem cell differentiation. For example, aggregation kinetics may instruct the development of aggregate structural characteristics, thereby altering the microenvironment created within aggregates and the resulting cell phenotype. Since the process of aggregation depends on expression and affinities of cell-cell adhesion molecules such as cadherins, aggregation kinetics are often difficult to systematically modulate without changing the cells' adhesive properties, e.g., via engineered cell surface modifications[18,19]. Bioengineering strategies have achieved improved control over aggregation kinetics by modulating variables such as rotary speed applied to aggregates maintained in dynamic suspension culture; however, these approaches rely on external manipulations that change hydrodynamic forces[20] applied to cells, which may have inherent effects on pluripotency maintenance and differentiation. Consequently, there is a need for methods that control cell aggregation kinetics in the absence of external manipulation.

In this study, we developed a bioengineered platform for highly controllable self-assembly of 3D stem cell aggregates from labile synthetic substrates. The tunability of labile substrates enabled control over resulting aggregate parameters, including the size, shape, and aggregation kinetics. Using an embryoid body (EB) model, we evaluated the influence of aggregation parameters on hPSC lineage bias, and identified aggregation method and kinetics as parameters that may influence EB structure and indirectly instruct stem cell fate.

5.4 RESULTS

5.4.1 Labile substrates promoted cell aggregate self-assembly.

A bioengineered platform based on alkanethiol self-assembled monolayers (SAMs) enabled self-assembly of 3D cell aggregates from substrates presenting the common cell adhesion peptide RGD via a labile bond (Fig. 5.1A). Carboxyl-terminated alkanethiols (EG_6COOH) reacted with nucleophilic functional groups on peptides to covalently link them to the SAM, while substrate peptide density was controlled by changing % EG_6COOH - the ratio of reactive EG_6COOH-terminated to bioinert EG_3OH-terminated alkanethiol groups. Cell adhesion was spatially restricted to patterned islands by reacting EG_6COOH with cell adhesion peptides in regions designated by a silicone stencil (Fig. 5.1B). We seeded hPSCs onto patterned 5% EG_6COOH SAMs reacted with a cysteine-containing cyclic RGD peptide ("5% cycRGDfC"), referred to hereafter as "labile substrates" based on the labile thioester linkage[21–24] formed via the reaction between cysteine free thiols and EG_6COOH (molecule 1, Fig. 5.1B inset). On labile substrates, confluent monolayers of hPSCs detached at the edges of patterned colonies and involuted to form three-dimensional cell aggregates in a process we termed "cell aggregate self-assembly" (Fig. 5.1C, Supplemental Video 5.1). To determine whether self-assembly was dependent on bond lability, we also tested a lysine-substituted variant of cycRGD (cycRGDfK, molecule 2, Fig. 5.1B inset) to generate non-labile substrates presenting an equivalent surface density of RGD via a stable amide linkage between the SAM and the peptide. As expected, although cycRGDfC and cycRGDfK peptides incorporated into SAMs with similar efficiencies (Fig. 5.1E), significant peptide loss occurred on labile substrates, while incubation in cell culture media had negligible effect on the peptide content of non-labile substrates (Fig. 5.1F). Furthermore, hPSCs seeded on non-labile substrates failed to form aggregates and instead remained confined to patterned regions (Fig. 5.1D).

5.4.2 Patterning of labile substrates formed size- and shape-controlled EBs.

Patterning of labile substrates in various geometries (e.g., circles, ovals, quatrefoils of varying dimensions) supported the formation of size- and shape-controlled hPSC colonies in 2-dimensional culture and led to the self-assembly of viable 3-dimensional EBs (Fig. 5.2A-C, Supplementary Fig. S5.1). Day 0 self-assembled EBs (SA-EBs) formed from 1.2 mm circles (mean diameter = 500 ± 72 μm) were smaller than those formed from 1.8 mm circles (mean diameter = 709 ± 59 μm), and mean SA-EB diameter correlated with size of the initial 2-dimensional pattern. We compared SA-EBs from circular patterns to EBs formed by forced centrifugation into agarose microwells (FC-EBs), a commonly used method for generating size-controlled aggregates (Fig. 5.2A)[14,25–27]. hPSCs seeded and centrifuged into microwells started as amorphous clusters and compacted into tight, viable aggregates within 24 hours (Fig. 5.2D). Similar to what has been observed in other studies employing FC-EBs, not all cells within the microwells incorporated into EBs[26] and those that did not incorporate were nonviable; nevertheless, resulting FC-EB size was directly correlated to the initial cell number seeded per microwell (Supplementary Fig. S5.1). A seeding density of 25,000 cells per microwell generated FC-EBs of similar size distribution (mean diameter = 480 ± 71 μm) to SA-EBs from 1.2 mm circular patterns (Fig. 5.2E). Therefore, to mitigate potential confounding effects of EB size on differentiation, we chose to use SA-EBs from 1.2 mm patterns and FC-EBs seeded at 25,000 cells per microwell for further comparisons.

5.4.3 EB formation method instructed pluripotency and lineage bias.

hPSCs retained pluripotency marker expression during cell aggregate self-assembly, with 95.4 ± 3.4% Oct4+ and 87.3 ± 15.8% Nanog+ cells in day 0 SA-EBs, as determined by flow

cytometry (Fig. 5.3A, Supplementary Fig. S5.2). Accordingly, we observed robust expression of Oct4, Nanog, Sox2, and E-cadherin in immunostained aggregate sections, which showed minimal expression of early differentiation markers at day 0 (Fig. 5.3B, Supplementary Fig. S5.3). In contrast, both Oct4 and Nanog were rapidly lost in FC-EBs, which were only 71.6 ± 14.7% Oct4+ and 40.6 ± 26.7% Nanog+ at day 0. We next subjected SA-EBs and FC-EBs to spontaneous differentiation to determine whether EB formation method biases differentiation trajectory (Supplementary Fig. S5.4). Consistent with assessment of EBs by flow cytometry, levels of the pluripotency genes *POU5F1* and *NANOG* were markedly reduced in day 0 FC-EBs (0.24-fold and 0.03-fold change relative to undifferentiated hPSCs, respectively) and decreased further in day 4 and day 14 FC-EBs. In contrast, day 0 SA-EBs exhibited comparable expression of *POU5F1* and increased expression of *NANOG* (2.88-fold change) relative to undifferentiated hPSCs (Fig. 5.3C-D). Expression of both *POU5F1* and *NANOG* remained significantly higher compared to that of FC-EBs at all equivalent time points. *CDH1* (E-cadherin), a gene associated with pluripotency, was significantly upregulated in both day 0 SA-EBs and FC-EBs compared to undifferentiated hPSCs in 2-dimensional culture. *CDH1* expression in SA-EBs was further upregulated at day 4 before decreasing by day 14, while expression in day 4 and day 14 FC-EBs was not significantly different from that of undifferentiated hPSCs (Fig. 5.3E, Supplementary Fig. S5.5).

The method of aggregate formation significantly influenced lineage bias of the resulting EBs during spontaneous differentiation. Several genes associated with germ layer differentiation were upregulated in FC-EBs relative to SA-EBs at day 0, including genes representative of ectoderm (*CDH2*, *PAX6*), primitive streak (*BRACHYURY/T*), and mesoderm (*RUNX1*, *GATA2*) (Fig. 5.4A-H). During early differentiation, FC-EBs demonstrated a bias toward ectoderm differentiation, with 8 of 9 ectoderm-associated genes upregulated relative to SA-EBs at day 0,

including *PAX6*, which was increased >40-fold in FC-EBs. By day 14, a clear distinction was evident between SA-EBs and FC-EBs; FC-EBs demonstrated a greater preference for ectoderm differentiation while SA-EBs upregulated genes associated with primitive streak, mesoderm, and endoderm differentiation (Fig. 5.4I). In support of these results, we observed neural rosettes in >50% of plated FC-EBs and the emergence of cells of neuronal morphology at the perimeter of FC-EB outgrowths within 2-3 days following the first appearance of rosettes (Supplementary Fig. S5.4). We did not observe any neuronal cells in SA-EB outgrowths throughout the course of spontaneous EB differentiation.

Differences in lineage bias in SA-EBs versus FC-EBs were associated with signaling downstream of the transforming growth factor-beta (TGF-β)/Activin/Nodal signaling axis. Histology revealed that phosphorylation of Smad2/3 was homogeneous throughout day 0 SA-EBs, whereas phosphoSmad2/3 was strongly expressed near the periphery but diminished in the interior of FC-EBs. Similarly, western blot analysis of day 0 EBs showed higher levels of phosphoSmad2/3 in SA-EBs compared to FC-EBs (Supplementary Fig. S5.6). To determine whether differential levels of Smad2/3 signaling in SA-EBs and FC-EBs correlated with the efficiency of their directed differentiation, we next induced cells dissociated from day 0 EBs toward lineages known to be specified (definitive endoderm)[28,29] or inhibited (neuroectoderm)[30,31] by the TGF-β/Activin/Nodal signaling axis. Cells from SA-EBs differentiated with higher efficiency toward definitive endoderm compared to those from FC-EBs (63.7% vs. 35.4% FoxA2/Sox17+). In contrast, differentiation toward neuroectoderm was less efficient in cells from SA-EBs (29.9% Pax6+, vs. 78.3% Pax6+ from FC-EBs).

5.4.4 Fast vs. slow aggregation kinetics correlated with lineage-specific gene expression in spontaneously differentiating EBs.

We next modulated cycRGDfC peptide density on labile substrates to control the kinetics of cell aggregate self-assembly from labile substrates. Specifically, we tracked the projected area of individual patterned cell populations over time and determined a t_{50} value for each (defined as the time required for the cell monolayer to assemble into 3D and decrease its surface coverage to 50% of the original 2D monolayer population area) as a metric by which to quantify aggregation kinetics (Supplementary Fig. S5.7). The rate of aggregate self-assembly was dependent on initial peptide density, with hPSCs on 0.01% cycRGDfC SAMs reaching t_{50} by 14 hours while hPSCs on 0.5% and 5% cycRGDfC exhibited mean t_{50} values of 21 hours and 46 hours, respectively (Fig. 5.5A-B). In line with our previous observations, hPSCs on SAMs presenting a similar range of cycRGDfK densities (non-labile substrates) did not undergo self-assembly to form aggregates.

Importantly, fast vs. slow aggregation kinetics resulted in distinct profiles of lineage-specific gene expression in differentiating EBs. We assessed EBs formed from 0.5% cycRGDfC substrates ("fast SA-EB"), which self-assemble with accelerated kinetics compared to those formed from 5% cycRGDfC substrates ("slow SA-EB"). We considered FC-EBs as representing the extreme end of the spectrum associated with fastest aggregation kinetics, as our observations corroborated previous reports of FC-EB formation within 12-24 hours[26]. By day 14, fast SA-EBs exhibited increases in ectoderm gene expression (e.g., *OTX2*, *CDH2*, *and PAX6*) and decreases in expression of pluripotency (*POU5F1*, *NANOG*), mesoderm and endoderm genes (e.g., *RUNX1*, *GATA2*, *SOX17*, and *HNF4A*), relative to slow SA-EBs (Fig. 5.5C). For 18 of the 25 pluripotency and differentiation genes assessed, fast SA-EBs represented an intermediate expression profile between slow SA-EBs and FC-EBs (Fig. 5.5D), and non-supervised hierarchical clustering

resulted in the grouping of fast SA-EBs with FC-EBs. These data suggested that the observed bias in EB differentiation trajectory may be a function of aggregation kinetics.

The timing and kinetics of morphogenesis events have been associated with changes to tissue structure and function in developmental contexts (e.g., neural tube closure, palate development, mesenchymal condensation) as well as in 3D spheroid models *in vitro*[32–34]. To determine whether differences in aggregation kinetics affected subsequent aggregate structure, we assessed slow SA-EBs, fast SA-EBs, and FC-EBs by histology. FC-EBs exhibited a compacted morphology with densely packed cells and minimal internal porosity. In contrast, SA-EBs displayed extensive porosity, with large pores distributed throughout the interior of slow SA and fast SA-EBs (Fig. 5.6A). Image analysis of H&E-stained histological sections showed that slow SA-EBs were more porous than fast SA-EBs (Fig. 5.6B), as measured by the fraction of EB area occupied by pores (0.20 ± 0.03 vs. 0.12 ± 0.03 for slow vs. fast SA-EBs, respectively; $p < 0.01$). Day 0 SA-EBs were also less cell-dense compared to FC-EBs, with fewer DAPI+ puncta per EB area (Fig. 5.6C). These initial results suggested that the observed bias in EB differentiation trajectory may be a function of changes to EB structure, aspects of which may also be influenced by aggregation kinetics.

5.5 DISCUSSION

In this study, we patterned chemically defined labile substrates to generate size/shape-controlled EBs that self-assemble in the absence of physical manipulation or enzymatic treatment. We demonstrated that substrates formed via the reaction of free thiol-containing RGD cell adhesion peptides with carboxylate-presenting surfaces (“labile substrates”) would promote the

collective assembly of 2-dimensional cell cultures into 3-dimensional cell aggregates ("cell aggregate self-assembly") through a controllable, lability-dependent process (Fig. 5.1A).

Several seminal studies have reported that EB size[35–38] is a major determinant of lineage bias during spontaneous differentiation. In light of these considerations, we attempted to limit EB size-dependent effects on differentiation by optimizing seeding conditions for each aggregation method, resulting in size-matched EBs between the SA and FC methods (Fig. 5.2). While the resulting FC-EBs resembled SA-EBs in size and shape, FC-EBs exhibited a rapid and drastic loss of pluripotency marker expression and demonstrated a bias toward ectoderm lineages that was apparent as early as day 0 and persisted in later stages of spontaneous differentiation (Figs. 5.3 and 5.4). In contrast, EBs formed via self-assembly from labile substrates exhibited an initial delay in the loss of pluripotency marker expression and had a higher propensity to generate mesoderm and endoderm derivatives. These results indicate formation method in size-matched EBs has a substantial effect on early lineage bias. Importantly, our findings may partly explain the disparities between numerous reports that have investigated lineage bias solely as a function of EB size. Indeed, it is common practice to stratify initial EB populations based on morphometric traits such as EB diameter[14,15,35,36,39]; however, such metrics give little indication of the processing parameters that affect cell fate prior to and during EB formation. Based on the results of this study, aggregation method and kinetics should be considered as critical parameters when developing bioprocessing workflows for the expansion of hPSC aggregates and in the development of stem cell-derived organoids.

Strategies to prevent differentiation of stem cell aggregates while retaining the scale-up and bioprocessing advantages of 3D culture are of particular interest for cell therapy applications[1,40]. Compared to 2D monolayer culture, suspension culture of hPSCs as aggregates

enables more efficient use of nutrients and growth factors in the media during scale-up cell expansion. However, restricted transport of oxygen and media components into the interior of hPSC aggregates can lead to stem cell population heterogeneity and the onset of spontaneous differentiation, which reduces downstream differentiation efficiency and yield. Pluripotency markers such as Oct4 and Nanog are often downregulated rapidly in EBs of comparable size (~400-500 μm diameter) to those used in this study, an effect that has been partially attributed to limited diffusion of pluripotency-promoting cytokines into the interior of large, cell-dense aggregates[41–43]. Notably, we found that aggregation method alone influences pluripotency marker loss in EBs, with SA-EBs exhibiting sustained expression of Oct4 and Nanog compared to stage-matched FC-EBs. One possible explanation for this result is that the aggregate self-assembly process results in a more porous EB structure with improved mass transport characteristics, which may promote access of nutrients and signaling molecules from culture media into the EB interior. In particular, early SA-EBs exhibited a highly porous structure, low cell density, and minimal necrosis despite EB diameters exceeding 200 μm, in stark contrast to the dense cell packing, interior cell death, and necrotic core formation we observed in FC-EBs (Fig. 5.6, Supplementary Fig. S5.8).

Importantly, we also found that in early EBs cultured in Essential 8 medium, in which TGF-β is a critical component for pluripotency maintenance[44], TGF-β-dependent Smad2/3 phosphorylation was homogeneous throughout the aggregate interior in SA-EBs but decreased as a function of distance from the aggregate perimeter in FC-EBs. This expression pattern was not only consistent with the spatial distribution of Oct4 and Nanog but also corresponded to higher overall TGF-β signaling activity in SA-EBs compared to FC-EBs (Supplementary Fig. S5.6). The TGF-β signaling pathway has a well-established role in hPSCs, where activation of downstream

Smad2/3 transcriptional regulators has been shown to be essential for pluripotency maintenance and mesendoderm specification whereas inhibition of TGF-β signaling is required for efficient neural differentiation[31]. Our observation that highly porous SA-EBs showed high TGF-β activity and mesoderm/endoderm differentiation, while decreased porosity in FC-EBs correlated with low TGF-β activity and ectoderm differentiation, further supports the possibility that differences in soluble factor transport are responsible for the distinct lineage biases observed between EBs formed via different aggregation methods and kinetics. In light of these findings, we speculate that the process of self-assembly from labile substrates promotes the emergence of unique structural and functional properties not previously exhibited in stem cell aggregates, which may in turn affect the transport and signaling of soluble factors that instruct cell fate within the aggregate. Future studies will aim to better understand the implications of these properties for downstream applications of cell aggregates in stem cell biomanufacturing and the generation of organoids.

In addition to the effects of aggregation method on the timing of pluripotency marker loss in EBs, we found that aggregation method also has a significant impact on EB lineage bias during spontaneous differentiation. The propensity for SA-EBs to preferentially generate mesendoderm derivatives during later stages of differentiation may be related to their high levels of *POU5F1* (Oct3/4) and *NANOG* expression at the start of differentiation, as both were upregulated in day 0 SA-EBs compared to undifferentiated hPSCs (Fig. 5.3). Although Oct4 and Nanog are known to cooperate in a self-regulating pluripotency network with Sox2, they fulfill distinct roles as both pluripotency-promoting factors and lineage specifiers[45–47]. Multiple studies suggest that high Nanog levels reinforce the pluripotent state; Nanog overexpression permits pluripotency maintenance in the absence of leukemia inhibitory factor in mouse embryonic stem cell culture[48] and enables the robust growth of undifferentiated hPSCs in feeder-free cultures[49]. On the other

hand, elevated levels of Oct4 expression have been linked to lineage priming toward mesendoderm fates[47,50,51]. Ramanathan and coworkers previously reported that Oct4 and Sox2 levels can serve as continuous temporal markers of hPSC progression toward lineage selection prior to the activation of lineage-specific markers; Oct4 was found to specifically repress only the neural ectoderm fate, while Sox2 repressed only the mesendoderm fate[52]. In the present study, we observed ~2-fold lower *SOX2* and ~5.5-fold higher *POU5F1* expression in day 0 SA-EBs compared to FC-EBs (Fig. 5.4), which in combination may push cells toward mesendoderm bias. Of note, the population-level changes in gene expression reported here likely do not capture the full extent of gene expression differences and lineage bias exhibited by cells as a function of their spatial location within SA-EBs or FC-EBs. Single cell analyses, particularly in combination with emerging technologies that allow for spatial resolution of gene expression[53,54], will be crucial for understanding how cell aggregation parameters influence spatiotemporal patterning within stem cell-derived microtissues and its consequences for organoid culture.

An increasing interest in dictating the structural and functional properties of developing 3D human organoids has led to improved control over various aspects of 3D cell aggregation. Aggregation parameters that may be controlled include the composition of the initial (stem) cell population, the mechanism of aggregation, the size and shape of resulting aggregates, and the presence of exogenous or cell-secreted factors. Aggregation kinetics constitute an additional parameter that has previously been suggested to influence stem cell differentiation trajectory[20,33,55], but could not be evaluated without introducing variables such as hydrodynamic forces[20] that may have inherent effects on differentiation[1]. In this study, we demonstrated that labile substrates could be “pre-programmed” to control aggregation kinetics without the requirement for physical or enzymatic perturbations, and found that changing aggregation kinetics resulted in differences in

EB lineage bias, with faster aggregation promoting ectoderm and inhibiting mesendoderm fates during EB differentiation.

One mechanism by which altered aggregation kinetics may influence stem cell fate is through signaling downstream of E-cadherin adherens junctions. It is well established that E-cadherin junctional complex formation is dependent on the extent of cell-cell contacts, which increases when cells are grown as 3D aggregates versus 2-dimensional culture[20,56]. In our study, while *CDH1* was upregulated in all day 0 EBs relative to monolayer hPSCs, the temporal profile of *CDH1* expression varied depending on EB aggregation kinetics (Supplementary Fig. S5.5). In FC-EBs, which formed compact aggregates within 12 hours after seeding, *CDH1* levels peaked at day 0 and decreased thereafter, whereas slow SA-EBs exhibited an increase in *CDH1* between days 0 and 4 of differentiation before gradual loss of expression. Similarly, Kinney et al. reported that when rotary speed was modulated to change aggregation kinetics of mouse EBs, rapidly aggregating EBs had monotonically decreasing E-cadherin expression over 7 days of differentiation while slower aggregating EBs exhibited biphasic expression levels that peaked at mid-differentiation[55]. The kinetics of E-cadherin expression was further linked to Wnt/β-catenin signaling activity, which was subsequently found to affect the efficiency of cardiogenic differentiation. Interestingly, we found that expression kinetics of the Wnt target gene *FZD7* matched the trajectory of *CDH1* expression in both SA-EBs and FC-EBs (Supplementary Fig. S5.5). Further studies are needed to establish a mechanistic link between the temporal regulation of E-cadherin expression and differentiation outcomes downstream of Wnt and other signaling pathways.

It is important to note that, even though we controlled EB size and aggregation kinetics while limiting potential effects on differentiation due to external forces during EB formation, there

remain several potentially confounding variables in the comparison of EBs generated via different aggregation methods and kinetics. One inherent difference between EBs formed by different methods is the subsequent culture conditions under which the cells are maintained. In this study, we observed stark differences in the structure of EBs from different formation methods, which results in disparities in effective cell density (Fig. 5.6) and likely in other properties (e.g., levels of paracrine factors or oxygen gradients within the EBs) known to influence stem cell phenotype[43,57,58]. We suspect that many such properties of the microenvironment *within* the EB interior are intrinsic to the method of EB formation and would be difficult to control for without modifying the EB formation method or affecting other parameters (e.g., EB size). As such, the development of aggregation approaches that allow variables such as cell packing density, aggregate size, and oxygen levels to be systematically covaried will be valuable to our understanding of the factors that influence cell fate and phenotype within stem cell aggregates.

The culture environment *external* to EBs is another variable affecting stem cell fate, that may be changed (whether it be intentionally or unintentionally) between different aggregation methods. It is often difficult to control for all differences in the external environment, particularly when the mechanism for EB formation places restrictions on the culture conditions. One obvious example of this is with EBs formed in conventional hanging drops, where the media volume per EB is limited by surface tension, often resulting in depletion of nutrients from the media and changes in EB gene expression within days[16]. In probing the effects of initial culture conditions on EBs, we found that incremental changes in the media volume per cell directly correlated with changes in day 0 *NANOG* expression, independently of the aggregation method used (Supplementary Fig. S5.9). However, *NANOG* expression in day 0 FC-EBs did not reach levels equivalent to that in SA-EBs when media volume per cell was matched between conditions or even

when FC-EBs were provided with >2.5-fold excess media per cell, suggesting that differences in external media conditions alone do not account for the dramatic changes in gene expression between aggregation methods (Supplementary Fig. S5.9). In addition, we compared FC-EBs to "settled EBs" that were formed in the same agarose microwell format by gravity-based settling (i.e., without centrifugation) and therefore experienced the same culture conditions as FC-EBs. We found that in comparison to FC-EBs, settled EBs display a similar yet distinct expression profile of lineage-specific genes. At day 14 of differentiation, both FC-EBs and settled EBs showed low levels of the pluripotency genes *POU5F1* and *NANOG* and upregulated expression of several ectoderm-associated genes (e.g., *CDH2*, *SOX1*, *ZIC1*). However, settled EBs also expressed several mesoderm- (*PDGFRA*, *RUNX1*) and endoderm-specific genes (*HNF4A*, *AFP*) at similar levels compared to SA-EBs (Supplementary Fig. S5.9), providing further evidence that changes to the aggregation method are sufficient to shift EB differentiation under equivalent culture conditions.

Finally, by developing labile substrates that promote cell aggregation via mechanisms fundamentally distinct from existing approaches, we identified porosity within EBs as a variable that likely influences gene expression during their differentiation. EBs formed by conventional methods (gravity-based settling or forced aggregation into microwells) demonstrated minimal porosity while cell aggregate self-assembly from labile substrates supported the extensive development of pores, typically tens of microns in diameter, throughout the interior of EBs (Fig. 5.6). The origin of pore formation in SA-EBs is currently unknown but appears distinct from what has been previously described for cystic EBs[59,60], as we have observed the early stages of pore development even prior to the completion of EB self-assembly (not shown) whereas cyst formation is typically observed in later stages of EB differentiation. Interestingly, changing aggregation

kinetics by varying the amount of RGD ligand presented on labile substrates had a significant effect on SA-EB porosity, with faster assembling SA-EBs exhibiting decreased porosity compared to slower assembling SA-EBs. Aggregation kinetics also influenced the expression of lineage-specific genes in differentiating SA-EBs, where faster self-assembly favored an ectoderm differentiation program at the expense of mesendoderm fates. Whether these changes in EB differentiation fate are due primarily to differences in aggregation kinetics or porosity, or a combination of both factors, remains to be seen. Nevertheless, our findings suggest that aggregation method and kinetics are critical determinants of EB lineage bias, and open new avenues for studying the relationship between aggregation conditions, structure, and function in stem cell aggregates.

5.6 CONCLUSIONS

In the current study, we developed patterns of RGD-presenting labile substrates for self-assembly of human embryoid bodies. Cell aggregate self-assembly from 2D to 3D was dependent on substrate lability, and patterning of labile substrates enabled control over the size and shape of EBs formed. Comparison of EBs generated by self-assembly to those generated by forced centrifugation revealed that the method of aggregation had potent effects on pluripotency maintenance and lineage bias toward neuroectoderm versus mesendoderm during spontaneous and directed differentiation. While there exist numerous methods for generating size-controlled EBs, cell aggregation driven by substrate lability constitutes a novel mechanism for EB formation, in which parameters such as aggregation kinetics can be finely controlled. We modulated aggregation kinetics of self-assembled EBs by varying initial RGD density on labile substrates and found that the rate of aggregation influences lineage-specific gene expression during differentiation. Of note,

the self-assembly mechanism allows for control over aggregation kinetics independently of confounding external factors such as physical force, enabling a clearer mechanistic understanding of the effects of aggregation kinetics on cell fate. While the present study provides a proof of concept in EBs generated from uniform hPSC populations, we speculate that the method and rate of aggregation will affect phenotypic outcomes in other cell types, likely in part by altering aggregate structure. Thus, we anticipate that the technological advances and insights described in this study will inform strategies for the biomanufacturing of homotypic and heterotypic cell aggregates for multiple applications, including clinical-scale stem cell expansion and organoid generation.

5.7 MATERIALS AND METHODS

5.7.1 Materials and reagents: Carboxylic acid-terminated hexa(ethylene glycol) undecanethiol (HS-C_{11}-(O-CH_2-CH_2)$_6$-O-CH_2-COOH) (referred to herein as ‘‘EG_6COOH’’) and 11-tri(ethylene glycol)-undecane-1-thiol (HS-C_{11}-(O-CH_2-CH_2)$_3$-OH) (referred to herein as ‘‘EG_3OH’’) were purchased from Prochimia. N-hydroxysuccinimide (NHS), *n*-(3-dimethylaminopropyl)-N’-ethylcarbodiimide hydrochloride (EDC) and sodium dodecyl sulfate (SDS) were purchased from Fisher Scientific. Cyclo(Arg-Gly-Asp-D-Phe-Cys) (cycRGDfC) and cyclo(Arg-Gly-Asp-D-Phe-Lys) (cycRGDfK) peptides were purchased from Peptides International and used in SAM experiments at a concentration of 0.3 mM in pH 7.4 PBS unless otherwise indicated.

5.7.2 Fabrication of PDMS stencils: Polydimethylsiloxane (PDMS) stencils containing arrays of wells were fabricated by soft lithography[61]. Briefly, master molds containing arrays of cylindrical posts were fabricated from SU-8 spin-coated silicon wafers using conventional photolithography

techniques. PDMS was prepared by mixing a 10:1 ratio of base to curing agent, followed by degassing for >45 minutes. The degassed mixture was cast over the master and cured for 6 hr at 80°C. Following curing, PDMS stencils were removed from molds and cleaned in hexanes using an overnight Soxhlet extraction. Stencils were allowed to dry in a fume hood for at least 2 hours prior to use.

5.7.3 Preparation of SAMs: We used a mixed self-assembled monolayer (SAM) system previously established in our laboratory for generating patterned arrays of alkanethiols on gold with defined and controllable peptide density in each array spot[62]. Hydroxyl-terminated alkanethiols ("EG_3OH") served as a bioinert background preventing non-specific protein adsorption, while carboxyl-terminated alkanethiols ("EG_6COOH") allowed for conjugation of cyclized RGD ("cycRGD") cell adhesion peptides via carbodiimide chemistry. Individual conditions within the array were isolated by patterning alkanethiols within an elastomeric stencil, and total peptide density in each array spot was varied by changing the percentage of reactive EG_6COOH available for peptide coupling among background non-reactive EG_3OH molecules. Alkanethiol solutions were prepared by combining 1 mM ethanolic solutions of EG_3OH and EG_6COOH at molar ratios equivalent to the desired surface concentration of EG_6COOH (e.g., alkanethiol solutions for 5% EG_6COOH SAMs were composed of 5 EG_6COOH:95 EG_3OH volume ratios). For cell-based experiments, SAMs were patterned into 1.2 mm diameter circular spots unless otherwise indicated. 100% EG_6COOH SAMs were used for all XPS surface analysis experiments.

Gold-coated glass slides (100 Å Au ‹111›, 20 Å Ti adhesion layer; Platypus Technologies) were cleaned via sonication in 100% EtOH for 2 minutes, rinsed with EtOH, and dried with N_2

gas. SAM arrays were patterned using PDMS stencils as follows: Briefly, PDMS wells were filled with 1 mM ethanolic alkanethiol solution and incubated for 10 minutes for local SAM formation. Alkanethiol solutions were then aspirated and wells were rinsed with deionized water (diH_2O). Carboxylate groups were converted to active ester groups by incubating PDMS wells in a solution of 100 mM NHS and 250 mM EDC in diH_2O for 15 minutes. After an additional rinse with DIUF H_2O, peptides were covalently coupled to patterned SAMs by incubating peptide solutions in PDMS wells for 1 hour. After peptide conjugation, PDMS wells were rinsed with diH_2O, and regions surrounding array spots were backfilled by removing the PDMS stencil and incubating the gold substrate with EG_3OH (0.1 mM in diH_2O, pH 2) for 10 min. The array was then rinsed with 0.1% SDS, diH_2O, and EtOH, and dried with N_2 gas. SAM arrays were stored in 100% EtOH and used within 24 hours of fabrication. Prior to cell-based experiments or cell-free incubation experiments, SAM arrays were incubated in 70% EtOH for 20 min and rinsed with sterile deionized water before placing into cell culture media.

5.7.4 hPSC maintenance: H1 human embryonic stem cells (WA01-DL-12, WiCell) were maintained on Matrigel-coated 6-well plates (8.7 μg/cm^2) in Essential 8 medium with daily media exchange, and passaged by standard protocols[63] using Versene-EDTA every 3 to 4 days. Initial hPSC populations for both EB formation methods were >95% Oct4+ and Nanog+ by flow cytometry. Initial karyotypic analysis and mycoplasma testing of the WA01 line were provided by WiCell and Bionique, respectively, and demonstrated normal karyotype and no contamination. Authentication of the WA01 line by STR was performed by the UW Molecular Diagnostics Laboratory and demonstrated positive identity.

5.7.5 Generation of self-assembled embryoid bodies (SA-EBs): For single-cell seeding of hPSCs onto SAM arrays, cells were washed with PBS and incubated with TrypLE at 37°C for 5 minutes to singularize cells. Following singularization, cell suspensions were diluted with 2X volume of E8 supplemented with 5 μM ROCK inhibitor (Y-27632) and pelleted by centrifugation at 200g for 5 minutes. Cell pellets were resuspended in E8 supplemented with 5 μM Y-27632 before seeding at desired densities. After 2 hrs incubation in a humidified incubator at 37°C and 5% CO_2 to allow cell adhesion, seeded SAM arrays were immersed in basal medium to remove loosely or non-specifically adhered cells. SAM arrays were then placed into new wells containing fresh E8 medium supplemented with 5 μM Y-27632 and maintained in this medium unless otherwise indicated. High seeding densities were used to ensure confluence shortly after seeding and to minimize defects in the initial cell monolayer. Unless otherwise stated, hPSCs were seeded onto SAMs at a density of 225,000 cells/cm^2. As the formation of compact and morphologically defined SA-EBs from 5% cycRGDfC substrates occurred within 72 hours after seeding, we denoted this time point "day 0" (Supplementary Fig. S5.4).

5.7.6 Generation of forced centrifugation embryoid bodies (FC-EBs) and settled EBs: Agarose microwells were fabricated based on previously published methods[25]. A 85 mm bicycle retro-reflector (Grote 4005/4006) was fashioned into 35 mm diameter circular portions, each of which was used as a template upon which hydrophilic silicone (1:1 mixture of Hydrosil A and B, Siladent) was cast and cured at 40 psi for 180 min to create a reverse mold sized to fit a standard 24-well plate format. Molds were autoclaved prior to each usage. 1.5% agarose in deionized water was sterilized by autoclaving and heated until molten prior to dispensing into silicone reverse molds. Individual agarose molds containing microwells were allowed to solidify at room

temperature, transferred to 24-well plates using a sterile spatula, submerged under 1.0 mL/well of E8 supplemented with 10 μM Y-27632, and spun down at 2,000g for 3 min to remove air trapped underneath the molds.

For single-cell seeding of hPSCs into microwell arrays to form FC-EBs, cells were pre-treated for 4-6 hours with E8 supplemented with 10 μM Y-27632 based on previous results demonstrating extensive cell death and poor formation of FC-EBs without pre-treatment. Cells were then washed with PBS and incubated with TrypLE at 37°C for 5 minutes to singularize cells. Cell suspensions were diluted with 2X volume of E8 supplemented with 10 μM Y-27632 and pelleted by centrifugation at 200g for 5 minutes. A small aliquot of cell suspension was used to determine cell count. Cells used to form FC-EBs were resuspended and seeded into agarose molds for a final seeding density of 25,000 cells per EB unless stated otherwise (note that not all cells incorporated into FC-EBs; Supplementary Fig. S5.1). Plates were centrifuged at 300g for 5 min (FC-EB only) and incubated at 37°C, 5% CO_2. Settled EBs were formed in the same manner, without centrifugation. A half-volume medium exchange with E8 was performed at 24 hrs post-seed ("day -2", Supplementary Fig. S5.4).

For media volume:cell number matching control experiments, FC-EBs were formed by seeding hESCs for one EB per well into 96-well polyHEMA-coated roundbottom plates, where media volume per cell could be varied over the range described in Supplementary Fig. S5.9. Plates were centrifuged at 300g for 5 min and incubated at 37°C, 5% CO_2, and EBs were collected at day 0 for assessment of *NANOG* expression by qPCR.

5.7.7 Spontaneous differentiation of EBs: EBs were subjected to spontaneous differentiation following a protocol adapted from existing methods.[64–67] EBs were collected at day 0, transferred

to suspension culture dishes, and transitioned from E8 to differentiation medium (DM) from day 0 to day 3 (Supplemental Fig. S5.4); EBs were placed in 75:25 E8:DM at day 0, 50:50 E8:DM at day 1, 25:75 E8:DM at day 2, and 100% DM at day 3, and maintained in DM thereafter. DM consisted of 20% Knockout Serum Replacement in Knockout-DMEM with 0.1 mM β-mercaptoethanol, 1% non-essential amino acids, and 1% L-glutamine. At day 4, EBs were transferred to Matrigel-coated plates and allowed to form adherent outgrowths. Media was changed on adherent EBs every 2 days.

5.7.8 XPS analysis of SAMs: X-ray photoelectron spectroscopy of peptide-conjugated SAMs was performed using a Thermo Scientific Model K-Alpha XPS instrument equipped with a monochromatic Al Kα X-ray source ($h\nu$ = 1486.7 eV). Survey and high-resolution spectra were obtained using analyzer pass energy of 200 eV and 50 eV, respectively, with an X-ray spot size of 400 μm. High-resolution spectra were obtained for carbon, nitrogen, sulfur, oxygen, and gold. At least three independent sample replicates were scanned per condition. Spectra were analyzed using Thermo Scientific Avantage XPS software package and peak fitting using a Shirley/Smart type baseline. For each sample, measured atomic percent values for the N1(s) and C1(s) peaks were used to determine the N/C ratio, which was used to calculate percentage peptide incorporation at day 0 for cycRGDfC and cycRGDfK surfaces, based on the theoretical N/C ratio for each surface assuming 100% reaction efficiency with the SAM. Mean values of N/C ratio measured from day 7 surfaces were normalized to day 0 values for each respective peptide, and presented as percentage peptide remaining on the surface. Statistical significance was determined by two-tailed Student's *t*-test ($p < 0.05$).

5.7.9 Cell-free SAM incubations: All cell-free incubations were performed at 37°C, 5% CO_2 to mimic cell culture conditions. SAMs were prepared and sterilized as described above, and incubated in E8 media for 7 days prior to analysis by XPS. Extra SAMs were prepared and immediately used for baseline (day 0) XPS measurements. For each peptide, percentage of peptide remaining (d7/d0) was calculated by dividing the mean N1s peak area from day 7 (post-incubation) samples by the mean N1s peak area from day 0 (pre-incubation) samples.

5.7.10 Quantification of hPSC aggregation kinetics, EB size distribution, and EB porosity:

hPSC aggregation kinetics during EB self-assembly: All timelapse images were acquired using a Nikon Ti Eclipse inverted microscope (10X PhL objective) equipped with NIS Elements software, Perfect Focus System, and a TIZ Tokai Hit incubated stage that was humidified and maintained at 37°C and 5% CO_2. All image analysis was performed with NIS Elements analysis software. To aid in exploration of cellular and material parameters influencing cell aggregate self-assembly, timelapse images of self-assembling aggregates were subjected to edge detection analysis to track the projected population area over time. The "Autodetect ROIs" feature was used to draw ROIs representing projected population area for each timelapse frame. At each time point, projected population area for each individual spot was normalized to the initial seeded area of the spot to standardize this metric for different starting pattern sizes. For each individual spot, normalized projected population area over time was plotted in MATLAB, fitted to a sigmoid curve using MATLAB's Curve Fitting Toolbox, and t_{50} values were calculated as the time to reach 50% of initial population area (defined as population area at 4 hrs after seeding). Individual spots for which the projected population area at 4 hrs after seeding was < 50% of the theoretical pattern area occurred in only a small fraction of all samples; these samples were omitted from analysis based

on our pre-established findings that < 50% cell coverage of patterns impeded controllable aggregate self-assembly. Statistical significance between conditions was determined by two-tailed Student's *t*-test ($p < 0.05$).

EB size distribution: SA-EBs and FC-EBs were collected at day 0 and counted from brightfield images. NIS Elements analysis software was used to determine cross-sectional projection areas of individual EBs. EB diameter was calculated from cross-sectional projection areas by assuming spherical EB morphology.

EB porosity: EBs were processed for histology (see below), stained with hematoxylin and eosin, and slides imaged on a Nikon Ti Eclipse microscope equipped with DS-U3 color camera and analyzed in Nikon NIS Elements software. Briefly, an ROI was defined for the area of each EB and binary thresholding was applied to highlight the stained area within each EB ("interior ROI"). The total pore area (total ROI area minus thresholded interior ROI area) was normalized to EB area and expressed as fractional pore area.

5.7.11 Directed differentiation of EBs: Day 0 SA-EBs and FC-EBs were collected, washed with PBS, and incubated in Accutase for 10 min at 37°C to dissociate. Accutase was quenched by adding 2X volume of E8 medium supplemented with 10 μM Y-27632, and cells were centrifuged at 200g for 5 min. EB-dissociated cells were plated onto Matrigel-coated plates at a density of 65,000 cells/cm^2 in E8 medium supplemented with 10 μM Y-27632 and allowed to attach overnight before beginning differentiation toward neuroectoderm or definitive endoderm. For neuroectoderm differentiation, cells were maintained in Essential 6 medium (Life Technologies) for 6 days. For definitive endoderm differentiation, cells were maintained in E8 medium for an

additional 24 hrs prior to induction for 5 days (daily media change) with RPMI/B27 containing 100 ng/mL Activin A (R&D Systems).

5.7.12 Flow cytometry: Briefly, hPSCs or EBs were collected, washed with PBS, and incubated with 0.25% trypsin/EDTA for 8-10 min at 37°C followed by pipetting to dissociate. Trypsin activity was quenched by adding 2X volume of 20% FBS in RPMI supplemented with 5 μM Y-27632. Samples were centrifuged at 200g for 5 min and pelleted samples were fixed with 1% paraformaldehyde for 20 min at room temperature, permeabilized with ice-cold 90% methanol for 15 min at 4°C, and stored at -20°C until processing. Samples were washed twice with Flow Buffer 1 (PBS containing 0.5% BSA) to remove residual methanol, incubated for 1 hr at room temperature with primary antibodies in Flow Buffer 2 (PBS containing 0.5% BSA and 0.1% Triton X-100), washed with Flow Buffer 2, and incubated in the dark for 30 min at room temperature with secondary antibodies in Flow Buffer 2. Samples were washed twice with FlowBuffer 2, resuspended in Flow Buffer 1, and stored on ice prior to data collection. Data were collected on a FACSCalibur flow cytometer and analyzed using FlowJo software. Positive expression was gated by <1% of the isotype control (Oct4 and Nanog) or against undifferentiated hPSCs (Pax6, Sox17, and FoxA2). Primary antibodies and dilutions used: mouse anti-human Oct3/4 (Santa Cruz Biotechnology, sc-5279, 1:60), rabbit anti-human Nanog (Cell Signaling Technology, 4903S, 1:100), mouse anti-human Pax6 (Developmental Studies Hybridoma Bank, 1 ug/mL), mouse anti-human Sox17-AlexaFluor647 (BD Biosciences, 562594, 1:20), mouse anti-human FoxA2-PE (BD Biosciences, 561589, 1:20), normal mouse IgG_{2b} (Santa Cruz Biotechnology, sc-3879), and normal rabbit IgG (Santa Cruz Biotechnology, sc-3888). In assessments of Oct4 and Nanog

expression in SA-EBs and FC-EBs, statistical significance between conditions was determined by two-tailed Student's *t*-test ($p < 0.05$).

5.7.13 Immunostaining of hPSCs on SAMs and EB sections: For immunostaining of hPSCs on SAMs, samples were fixed with 10% neutral buffered formalin for 15 min, permeabilized with 0.1% Triton X-100 in PBS for 5 min, blocked with 1% BSA in PBS for 30 min, and stained with primary antibodies (dilutions made in 1% BSA in PBS) for 1 hr at room temperature. Samples were washed three times with 0.05% Tween-20 in PBS and stained with secondary antibodies (dilutions made in PBS) for 1 hr at room temperature or overnight at 4°C. Nuclei were counterstained with DAPI. For histology and immunostaining of EB sections, EBs were collected from SAMs or agarose molds using wide-bore pipette tips, transferred to Eppendorf tubes, and allowed to settle before removing excess media and washing with PBS. EBs were then fixed with 10% neutral buffered formalin for 30 min at room temperature, washed twice with PBS, and incubated in 10% sucrose solution overnight at 4°C before embedding in either Histogel for processing into paraffin blocks or O.C.T. compound at -80°C for cryosectioning.

Paraffin-embedded EBs were sectioned at a thickness of 5 μm, deparaffinized in xylene, and stained with hematoxylin and eosin. Additional sections were assessed by immunohistochemistry for phosphorylated Smad3 (rabbit anti-human phosphoSMAD3 primary antibody; Thermo Scientific PA5-12693, 1:400). Briefly, tissue sections underwent antigen retrieval using 10 mM citrate buffer (pH 6.0) in an 80°C water bath for 2 hours, followed by permeabilization with 0.25% Triton X-100. Sections were blocked with 10% BSA, and incubated in primary antibody for 1 hour at room temperature. Endogenous peroxidase activity was quenched and antibody detection was carried out using ImmPRESS anti-rabbit IgG HRP (Vector Labs).

Finally, the signal visualized with ImmPACT DAB (Vector Labs) and sections counterstained with hematoxylin for contrast. Frozen samples were sectioned into 5-7 μm slices onto SuperFrost slides using a Leica CM1900 cryostat, and slides with cryosections were stored at -80°C until further processing. For immunostaining of cryosectioned EBs, slides were equilibrated to room temperature for 15 min, fixed/permeabilized in ice-cold acetone for 10 min, and washed 3x with PBS before blocking with 10% BSA for 1 hr at RT. Slides were washed 3x with PBS before incubating overnight at 4°C in mouse anti-human Oct3/4 (Santa Cruz Biotechnology, sc-5279, 1:100) and rabbit anti-human Nanog (Cell Signaling Technology, 4903S, 1:100) primary antibodies, then washed 3x with PBS and incubated for 1 hr at room temperature in secondary antibody solution (goat anti-mouse Alexa Fluor488, goat anti-rabbit Alexa Fluor 568) containing DAPI. After overnight washes in PBS, stained sections were mounted in ProLong Gold Antifade Reagent, allowed to set overnight, and sealed with nail polish. Fluorescence was imaged with a Nikon Ti Eclipse microscope equipped with filters for FITC, Texas Red, and DAPI.

5.7.14 Quantitative RT-PCR: For quantitative PCR (qPCR) analyses, EBs were washed with PBS and total RNA was isolated using the RNeasy mini kit (Qiagen) according to manufacturer's instructions. RNA quality for all samples was assessed using the Agilent Bioanalyzer 3100. Only samples with RIN > 7.0 were used for further analyses. RNA was reverse transcribed into cDNA using the RT^2 First Strand Synthesis Kit (Qiagen). cDNA samples (4.5 ng input RNA/25 μL reaction for 96-well format RT^2 Housekeeping Array, or 2.8 ng input RNA/10 μL reaction for 384-well format RT^2 Custom Profiler Array) were mixed with RT^2 Master Mix, loaded onto RT^2 PCR Arrays (SABiosciences, Tables S1 and S2), and run on a LightCycler 4800 system according to the manufacturer's protocol. Data analysis was performed using the ΔΔCt method, with *HSP90AB*

as an internal control based on analysis of samples run on the RT^2 Housekeeping Array (Supplementary Fig. S5.10). Ct values from the RT^2 Housekeeping Array were analyzed using NormFinder software[68] to identify a stable reference gene for the tested set of genes and samples. For the RT^2 Custom Profiler Array, experimental conditions were run with at least three technical replicates per sample, with $n = 3$ independent biological replicates per condition.

5.7.15 EB viability assessment: Day 0 EBs were collected in Eppendorf tubes and allowed to settle, and excess media was removed and replaced with staining solution. Cell viability was assessed using LIVE/DEAD staining kit (Life Technologies) according to manufacturer's instructions and imaged immediately thereafter on a Nikon Ti Eclipse inverted epifluorescence microscope. For staining of intact EBs, CellTox Green (Promega) was used to visualize nuclei of EBs subjected to lysis following manufacturer's instructions using 2X concentrated lysis buffer.

5.7.16 Western blotting: Day 0 EBs were collected, washed with PBS, and resuspended in ice-cold RIPA buffer containing 1X Halt Protease/Phosphatase Inhibitor Cocktail. Samples were agitated for 15 min at 4°C and spun at 12,000g for 15 min at 4°C. The supernatants from samples were collected and stored at -20°C until use. Total protein was quantified by microBCA assay. Equal amounts of protein per sample were combined with Laemmli buffer, denatured for 5 min at 100°C, loaded in 10% polyacrylamide gels and separated by SDS-PAGE. Proteins were transferred to PVDF membranes and incubated in blocking buffer (5% nonfat dry milk in TBST for 1 hr at RT). Membranes were incubated in primary antibodies in blocking buffer overnight at 4°C, washed with TBST, and incubated in horseradish peroxidase (HRP)-conjugated goat anti-mouse or anti-rabbit IgG secondary antibodies in blocking buffer (Abcam, 1:10,000) for 1 hr at RT. Membranes

were washed with TBST and incubated with ECL Western Blotting substrate (Pierce) for 1 min. Chemiluminescence was detected using a LAS4000 Mini imager and analyzed by densitometry using ImageJ's gel plug-in. β-actin was used as a load control. Raw data were normalized such that SA-EB expression levels were adjusted to unity. Statistical significance between conditions was determined by two-tailed Student's *t*-test ($p < 0.05$). Primary antibodies and dilutions used: rabbit anti-human phosphoSmad2/3 (Cell Signaling Technology, 3101S, 1:1000), rabbit anti-human phosphoSmad1/5 (Cell Signaling Technology, 9516S, 1:1000), and mouse anti-human β-actin (Abcam, ab8224, 1:1000).

5.7.17 Statistical analysis: Unless otherwise stated, one-way analysis of variance (ANOVA) with Tukey's method for multiple comparisons was performed to determine statistical significance ($p < 0.05$) between experimental groups.

5.8 ACKNOWLEDGMENTS

The authors thank Drew Roenneburg and Connie Chamberlain for assistance with preparation of histological samples, and acknowledge support from staff and the use of equipment at the Materials Science Center (NSF DMR-1121288) and UW Carbone Cancer Center Flow Cytometry Laboratory (Support Grant P30 CA014520) at UW-Madison. This work was supported by funding from the National Institutes of Health (R01HL093282 to W.L.M.; Biotechnology Training Program NIGMS 5 T32-GM08349 to A.W.X. and A.S.K.), the U.S. Environmental Protection Agency (STAR grant no. 83573701 to W.L.M.), and the National Science Foundation (DGE-1256259 to A.W.X. and A.S.K.; DMR-1306482 to W.L.M. and S.K.S.)

5.9 REFERENCES

1. Serra, M., Brito, C., Correia, C. & Alves, P. M. Process engineering of human pluripotent stem cells for clinical application. *Trends Biotechnol.* **30,** 350–359 (2012).

2. Want, A. J., Nienow, A. W., Hewitt, C. J. & Coopman, K. Large-scale expansion and exploitation of pluripotent stem cells for regenerative medicine purposes: beyond the T flask. *Regen. Med.* **7,** 71–84 (2012).

3. Rowley, J., Abraham, E., Campbell, A., Brandwein, H. & Oh, S. Meeting lot-size challenges of manufacturing adherent cells for therapy. *Bioprocess Int.* **10,** 16–22 (2012).

4. Bauer, M. *et al.* Adult Cardiac Progenitor Cell Aggregates Exhibit Survival Benefit Both In Vitro and In Vivo. *PLoS One* **7,** 1–10 (2012).

5. Bhang, S. H. *et al.* Angiogenesis in ischemic tissue produced by spheroid grafting of human adipose-derived stromal cells. *Biomaterials* **32,** 2734–2747 (2011).

6. Zhao, S. *et al.* Bioengineering of injectable encapsulated aggregates of pluripotent stem cells for therapy of myocardial infarction. *Nat. Commun.* **7,** 13306 (2016).

7. Xu, Y., Shi, T., Xu, A. & Zhang, L. 3D spheroid culture enhances survival and therapeutic capacities of MSCs injected into ischemic kidney. *J. Cell. Mol. Med.* **20,** 1203–1213 (2016).

8. Lancaster, M. a *et al.* Cerebral organoids model human brain development and microcephaly. *Nature* **501,** 373–9 (2013).

9. Shamir, E. R. & Ewald, A. J. Three-dimensional organotypic culture : experimental models of mammalian biology and disease. *Nat. Publ. Gr.* **15,** 647–664 (2014).

10. Takebe, T. *et al.* Self-organization of human hepatic organoid by recapitulating organogenesis in vitro. *Transplant. Proc.* **44,** 1018–20 (2012).

11. Takebe, T. *et al.* Vascularized and complex organ buds from diverse tissues via mesenchymal cell-driven condensation. *Cell Stem Cell* **16,** 556–565 (2015).

12. Kurosawa, H. Methods for inducing embryoid body formation: in vitro differentiation system of embryonic stem cells. *J. Biosci. Bioeng.* **103,** 389–98 (2007).

13. Sheridan, S. D., Surampudi, V. & Rao, R. R. Analysis of embryoid bodies derived from human induced pluripotent stem cells as a means to assess pluripotency. *Stem Cells Int.* **2012,** (2012).

14. Ungrin, M. D., Joshi, C., Nica, A., Bauwens, C. & Zandstra, P. W. Reproducible, ultra high-throughput formation of multicellular organization from single cell suspension-derived human embryonic stem cell aggregates. *PLoS One* **3,** e1565 (2008).

15. Pettinato, G., Wen, X. & Zhang, N. Formation of well-defined embryoid bodies from dissociated human induced pluripotent stem cells using microfabricated cell-repellent microwell arrays. *Sci. Rep.* **4,** 7402 (2014).

16. Lee, W. G., Ortmann, D., Hancock, M. J., Bae, H. & Khademhosseini, A. A hollow sphere soft lithography approach for long-term hanging drop methods. *Tissue Eng. Part C.*

Methods **16,** 249–259 (2010).

17. Sart, S., Tsai, A.-C., Li, Y. & Ma, T. Three-dimensional aggregates of mesenchymal stem cells: cellular mechanisms, biological properties, and applications. *Tissue Eng. Part B. Rev.* **20,** 365–380 (2014).

18. Gothard, D., Roberts, S. J., Shakesheff, K. M. & Buttery, L. D. Controlled embryoid body formation via surface modification and avidin-biotin cross-linking. *Cytotechnology* **61,** 135–44 (2009).

19. Gartner, Z. J. & Bertozzi, C. R. Programmed assembly of 3-dimensional microtissues. **106,** (2009).

20. Sargent, C. Y. *et al.* Hydrodynamic modulation of embryonic stem cell differentiation by rotary orbital suspension culture. *Biotechnol. Bioeng.* **105,** 611–626 (2010).

21. Hermanson, G. T. *Bioconjugate Techniques Ch.3-Zero-Length Crosslinkers*. *Bioconjugate Techniques* (2008). doi:10.1016/B978-0-12-370501-3.00003-5

22. Schmitt, S. K. *et al.* Peptide Conjugation to a Polymer Coating via Native Chemical Ligation of Azlactones for Cell Culture. *Biomacromolecules* **17,** 1040–1047 (2016).

23. Thapa, P., Zhang, R. Y., Menon, V. & Bingham, J. P. Native chemical ligation: A boon to peptide chemistry. *Molecules* **19,** 14461–14483 (2014).

24. Bracher, P. J., Snyder, P. W., Bohall, B. R. & Whitesides, G. M. The Relative Rates of Thiol-Thioester Exchange and Hydrolysis for Alkyl and Aryl Thioalkanoates in Water. *Orig. Life Evol. Biosph.* **41,** 399–412 (2011).

25. Dahlmann, J. *et al.* The use of agarose microwells for scalable embryoid body formation and cardiac differentiation of human and murine pluripotent stem cells. *Biomaterials* **34,** 2463–71 (2013).

26. Hookway, T. A., Butts, J. C., Lee, E., Tang, H. & McDevitt, T. C. Aggregate formation and suspension culture of human pluripotent stem cells and differentiated progeny. *Methods* (2015). doi:10.1016/j.ymeth.2015.11.027

27. Gevaert, E. *et al.* High Throughput Micro-Well Generation of Hepatocyte Micro-Aggregates for Tissue Engineering. *PLoS One* **9,** e105171 (2014).

28. Kubo, A. *et al.* Development of definitive endoderm from embryonic stem cells in culture. *Development* **131,** 1651 LP-1662 (2004).

29. Tremblay, K. D., Hoodless, P. A., Bikoff, E. K. & Robertson, E. J. Formation of the definitive endoderm in mouse is a Smad2-dependent process. *Development* **127,** 3079 LP-3090 (2000).

30. Hemmati-brivanlou, A. & Melton, D. Will Become Nerve Cells Unless Told Otherwise. *Cell* **88,** 13–17 (1997).

31. Chambers, S. M. *et al.* Highly efficient neural conversion of human ES and iPS cells by dual inhibition of SMAD signaling. *Nat. Biotechnol.* **27,** 275–280 (2009).

32. Lin, R.-Z., Chou, L.-F., Chien, C.-C. M. & Chang, H.-Y. Dynamic analysis of hepatoma spheroid formation: roles of E-cadherin and beta1-integrin. *Cell Tissue Res.* **324,** 411–422 (2006).

33. Carpenedo, R. L., Sargent, C. Y. & McDevitt, T. C. Rotary suspension culture enhances the efficiency, yield, and homogeneity of embryoid body differentiation. *Stem Cells* **25,** 2224–2234 (2007).

34. Tsai, A.-C., Liu, Y., Yuan, X. & Ma, T. Compaction, fusion, and functional activation of three-dimensional human mesenchymal stem cell aggregate. *Tissue Eng. Part A* **21,** 1705–1719 (2015).

35. Ng, E. S., Davis, R. P., Azzola, L., Stanley, E. G. & Elefanty, A. G. Forced aggregation of defined numbers of human embryonic stem cells into embryoid bodies fosters robust, reproducible hematopoietic differentiation. *Blood* **106,** 1601–3 (2005).

36. Mohr, J. C. *et al.* The microwell control of embryoid body size in order to regulate cardiac differentiation of human embryonic stem cells. *Biomaterials* **31,** 1885–93 (2010).

37. Park, J. *et al.* Microfabrication-based modulation of embryonic stem cell differentiation. *Lab Chip* **7,** 1018–28 (2007).

38. Choi, Y. Y. *et al.* Controlled-size embryoid body formation in concave microwell arrays. *Biomaterials* **31,** 4296–303 (2010).

39. Valamehr, B. *et al.* Hydrophobic surfaces for enhanced differentiation of embryonic stem cell-derived embryoid bodies Results. *Pnas* **105,** 14459–14464 (2008).

40. zur Nieden, N. I., Cormier, J. T., Rancourt, D. E. & Kallos, M. S. Embryonic stem cells remain highly pluripotent following long term expansion as aggregates in suspension bioreactors. *J. Biotechnol.* **129,** 421–432 (2007).

41. Van Winkle, A. P., Gates, I. D. & Kallos, M. S. Mass transfer limitations in embryoid bodies during human embryonic stem cell differentiation. *Cells Tissues Organs* **196,** 34–47 (2012).

42. Kinney, M. a, Sargent, C. Y. & McDevitt, T. C. The multiparametric effects of hydrodynamic environments on stem cell culture. *Tissue Eng. Part B. Rev.* **17,** 249–262 (2011).

43. Sachlos, E. & Auguste, D. T. Embryoid body morphology influences diffusive transport of inductive biochemicals: A strategy for stem cell differentiation. *Biomaterials* **29,** 4471–4480 (2008).

44. Chen, G. *et al.* Chemically defined conditions for human iPS cell derivation and culture. *Nat. Methods* **8,** 424–429 (2011).

45. Wang, Z., Oron, E., Nelson, B., Razis, S. & Ivanova, N. Distinct lineage specification roles for NANOG, OCT4, and SOX2 in human embryonic stem cells. *Cell Stem Cell* **10,** 440–454 (2012).

46. Yu, J. & Thomson, J. A. Pluripotent stem cell lines. *Genes Dev.* **22,** 1987–1997 (2008).

47. Loh, K. M. & Lim, B. A precarious balance: pluripotency factors as lineage specifiers. *Cell*

Stem Cell **8,** 363–369 (2011).

48. Chambers, I. *et al.* Functional Expression Cloning of Nanog, a Pluripotency Sustaining Factor in Embryonic Stem Cells. *Cell* **113,** 643–655 (2003).

49. Darr, H., Mayshar, Y. & Benvenisty, N. Overexpression of NANOG in human ES cells enables feeder-free growth while inducing primitive ectoderm features . *Development* **133,** 1193 LP-1201 (2006).

50. Niwa, H., Miyazaki, J. & Smith, A. G. Quantitative expression of Oct-3/4 defines differentiation, dedifferentiation or self-renewal of ES cells. *Nat. Genet.* **24,** 372–376 (2000).

51. Zeineddine, D. *et al.* Oct-3 / 4 Dose Dependently Regulates Specification of Embryonic Stem Cells toward a Cardiac Lineage and Early Heart Development. 535–546 (2006). doi:10.1016/j.devcel.2006.07.013

52. Thomson, M. *et al.* Pluripotency factors in embryonic stem cells regulate differentiation into germ layers. *Cell* **145,** 875–889 (2011).

53. Lee, J. H. Quantitative approaches for investigating the spatial context of gene expression. *Wiley Interdiscip. Rev. Syst. Biol. Med.* **9,** 17–19 (2016).

54. Crosetto, N., Bienko, M. & van Oudenaarden, A. Spatially resolved transcriptomics and beyond. *Nat. Rev. Genet.* **16,** 57–66 (2015).

55. Kinney, M. a, Sargent, C. Y. & McDevitt, T. C. Temporal modulation of β-catenin signaling by multicellular aggregation kinetics impacts embryonic stem cell cardiomyogenesis. *Stem Cells Dev.* **22,** 2665–77 (2013).

56. Azarin, S. M. *et al.* Modulation of Wnt/β-catenin signaling in human embryonic stem cells using a 3-D microwell array. *Biomaterials* **33,** 2041–9 (2012).

57. Hong, S.-H., Werbowetski-Ogilvie, T., Ramos-Mejia, V., Lee, J. B. & Bhatia, M. Multiparameter comparisons of embryoid body differentiation toward human stem cell applications. *Stem Cell Res.* **5,** 120–30 (2010).

58. Wu, J., Rostami, M. R., Cadavid Olaya, D. P. & Tzanakakis, E. S. Oxygen transport and stem cell aggregation in stirred-suspension bioreactor cultures. *PLoS One* **9,** 1–12 (2014).

59. Goh, S.-K., Olsen, P. & Banerjee, I. Extracellular Matrix Aggregates from Differentiating Embryoid Bodies as a Scaffold to Support ESC Proliferation and Differentiation. *PLoS One* **8,** e61856 (2013).

60. Tomov, M. L., Olmsted, Z. T. & Paluh, J. L. The Human Embryoid Body Cystic Core Exhibits Architectural Complexity Revealed by use of High Throughput Polymer Microarrays. *Macromol. Biosci.* **15,** 892–900 (2015).

61. Jo, B. H., Van Lerberghe, L. M., Motsegood, K. M. & Beebe, D. J. Three-dimensional micro-channel fabrication in polydimethylsiloxane (PDMS) elastomer. *J. Microelectromechanical Syst.* **9,** 76–81 (2000).

62. Koepsel, J. T., Brown, P. T., Loveland, S. G., Li, W.-J. & Murphy, W. L. Combinatorial

screening of chemically defined human mesenchymal stem cell culture substrates. *J. Mater. Chem.* **22,** 19474–19481 (2012).

63. Beers, J. *et al.* Passaging and colony expansion of human pluripotent stem cells by enzyme-free dissociation in chemically defined culture conditions. *Nat. Protoc.* **7,** 2029–2040 (2012).

64. Cai, J. *et al.* Assessing self-renewal and differentiation in human embryonic stem cell lines. *Stem Cells* **24,** 516–530 (2006).

65. Huangfu, D. *et al.* Induction of pluripotent stem cells from primary human fibroblasts with only Oct4 and Sox2. *Nat Biotech* **26,** 1269–1275 (2008).

66. Osafune, K. *et al.* Marked differences in differentiation propensity among human embryonic stem cell lines. *Nat. Biotechnol.* **26,** 313–315 (2008).

67. Pal, R., Totey, S., Mamidi, M. K., Bhat, V. S. & Totey, S. Propensity of human embryonic stem cell lines during early stage of lineage specification controls their terminal differentiation into mature cell types. *Exp. Biol. Med. (Maywood).* **234,** 1230–1243 (2009).

68. Andersen, C. L., Jensen, J. L. & Ørntoft, T. F. Normalization of Real-Time Quantitative Reverse Transcription-PCR Data: A Model-Based Variance Estimation Approach to Identify Genes Suited for Normalization, Applied to Bladder and Colon Cancer Data Sets. *Cancer Res.* **64,** 5245 LP-5250 (2004).

5.10 FIGURES

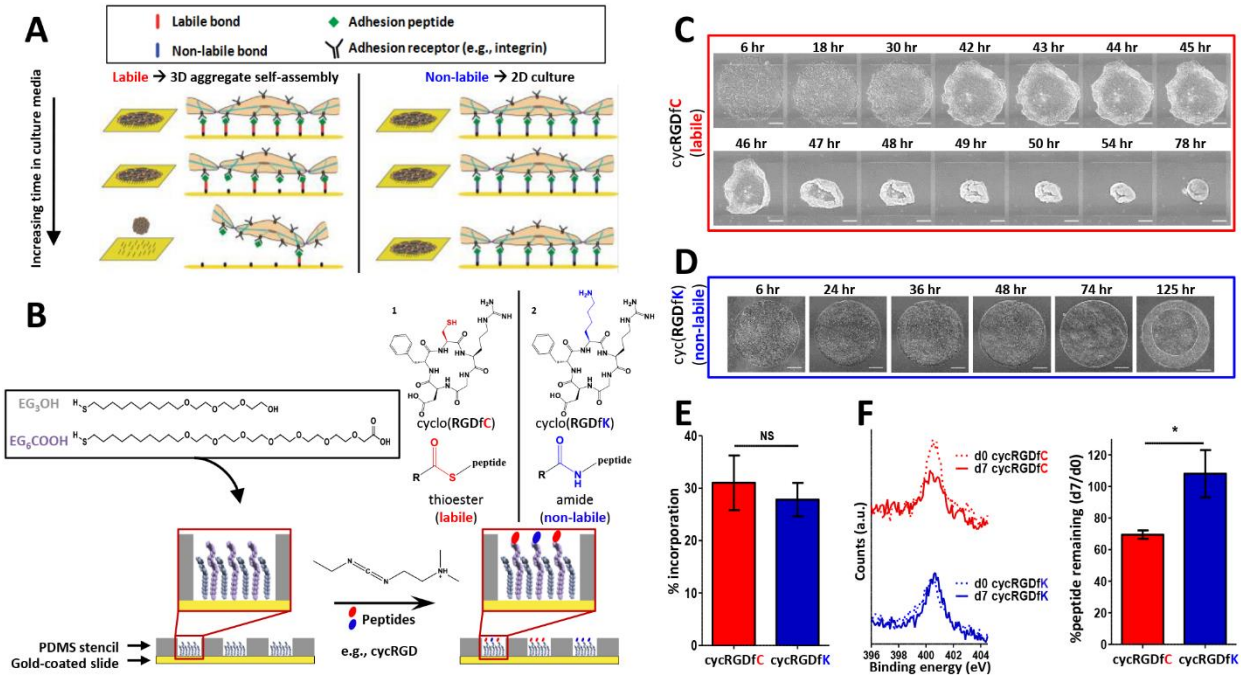

Figure 5.1 Self-assembly mechanism of stem cell aggregates is dependent on substrate lability. (A) Proposed mechanism of substrate-mediated cell aggregate self-assembly on substrates presenting labile chemical bonds. Loss of adhesion peptide over time on labile surfaces promotes 3D cell aggregate self-assembly (left) that is not observed on substrates that present non-labile bonds tethering adhesion peptides stably to the surface (right). (B) Schematic representation of procedure for forming patterned SAM arrays. (inset) Model peptide adhesion ligands that covalently couple to carboxyl-terminated alkanethiol SAMs to form 1) "labile" thioester or 2) "non-labile" amide linkages between the peptide and the SAM. "R" denotes the EG_6COOH alkanethiol, excluding the terminal carboxyl group. (C) Phase images from timelapse microscopy of hPSC aggregate self-assembly from 2-dimensional monolayers, as shown on 5% cycRGDfC patterned SAMs. (D) Phase images from timelapse microscopy of hPSCs grown on 5% cycRGDfK (non-labile) patterned SAMs, which prohibit aggregate self-assembly. Scale bars in (C) and (D) represent 250 μm. (E) Efficiency of peptide incorporation on cycRGDfC and cycRGDfK SAMs. (F) (left) Representative XPS scans of N(1s) signal on cycRGDfC and cycRGDfK SAMs immediately after SAM functionalization (dashed lines) and after 7-day incubation in media (solid lines). (right) Quantification of percentage of initial peptide remaining on surface after 7-day incubation in media. Values in (E) and (F) represent the mean ± s.d. of $n = 3$ replicates, $* p < 0.05$. "NS" denotes no statistical significance.

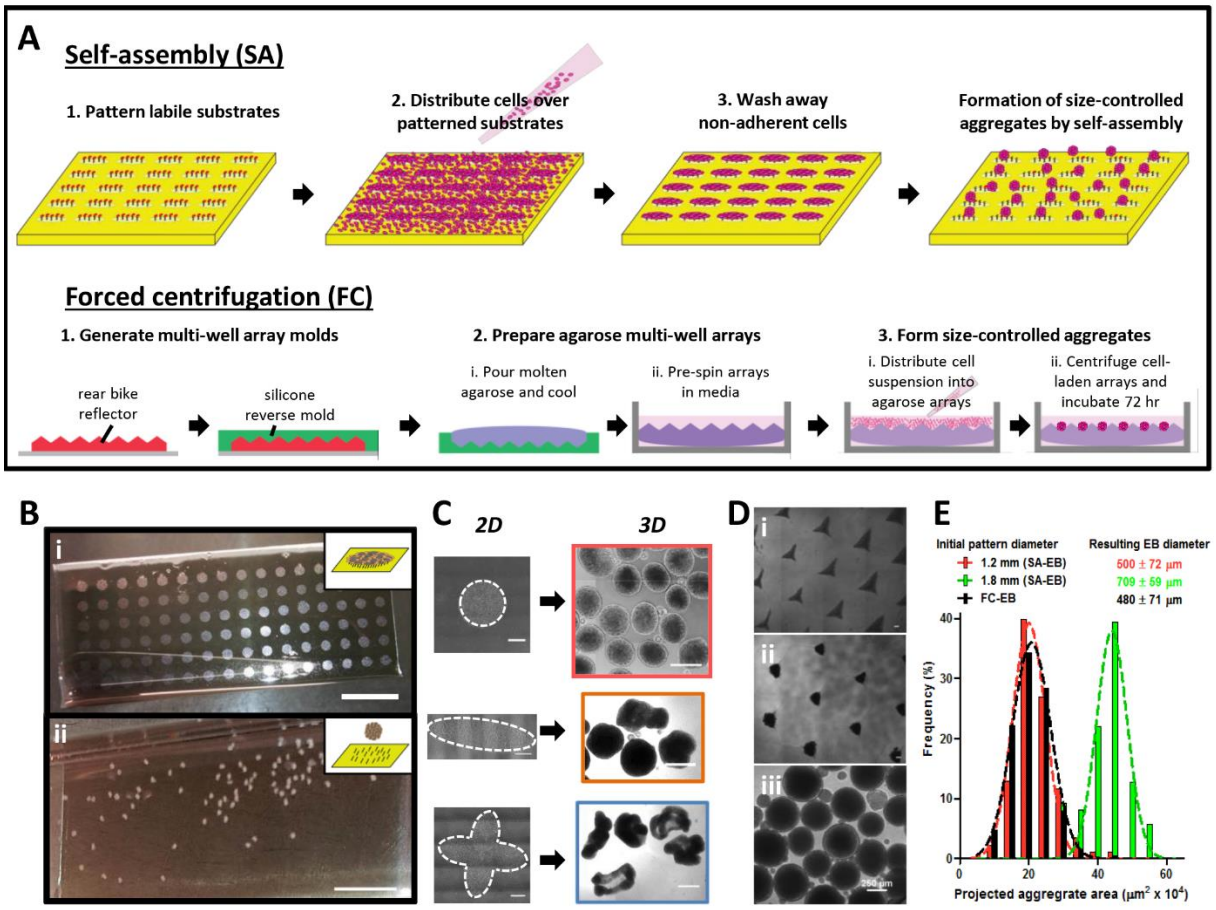

Figure 5.2 Efficient generation of EBs via self-assembly (SA) and forced centrifugation (FC). (A) Schematics demonstrating the process of SA-EB formation on labile substrates (top) and FC-EB formation in agarose microwells (bottom). (B) (i) hPSCs seeded on patterned labile substrates remain in 2D at 4 hrs and (ii) self-assemble into 3D aggregates within 72 hrs. (C) Patterning of labile substrates enables control over the geometry of hPSC colonies in 2-dimensional culture and leads to the self-assembly of size- and shape-controlled 3-dimensional EBs. (D) FC-EBs at (i) 4 hrs and (ii) 72 hrs after seeding and (iii) following collection. (E) Histogram of cross-sectional area for SA-EBs generated from 2-dimensional patterns of varying size. Size distribution of FC-EBs generated by forced centrifugation into microwells is overlaid for comparison (black histogram). Resulting EB diameter is represented as the mean ± s.d. Scale bars represent (B) 500 μm, (C) 10 mm (i-ii) or 250 μm (iii), (D) 250 μm (i-iii).

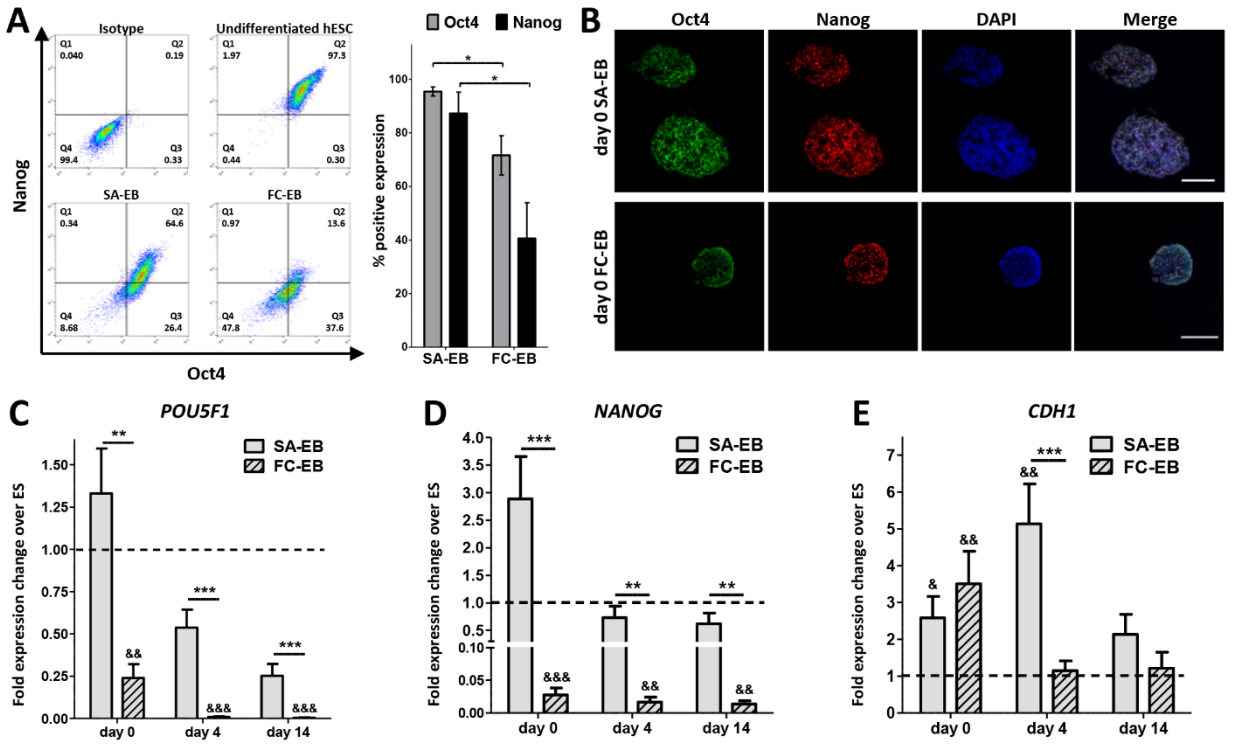

Figure 5.3 Assessment of pluripotency loss in SA-EBs and FC-EBs during spontaneous embryoid body differentiation. (A) Representative flow cytometry plots (left) and quantification (right) showing Oct4 and Nanog expression in day 0 SA-EBs and FC-EBs. Error bars represent s.e.m. from n = 4 independent biological replicates. (B) Immunofluorescence staining for pluripotency markers Oct4 and Nanog in sectioned day 0 SA-EBs (i) and FC-EBs (ii). Scale bar represents 250 μm. (C,D,E) *POU5F1*, *NANOG*, and *CDH1* expression in SA-EBs and FC-EBs at days 0, 4, and 14 during spontaneous EB differentiation. Fold-changes in expression are relative to undifferentiated hPSCs. Values represent the mean ± s.e.m. of n = 3 independent biological replicates. Dashed line represents expression level of undifferentiated hPSCs. Asterisks represent statistical significance between indicated conditions (* $p < 0.05$, ** $p < 0.005$, *** $p < 0.0005$); &s represent statistical significance relative to undifferentiated hPSCs.

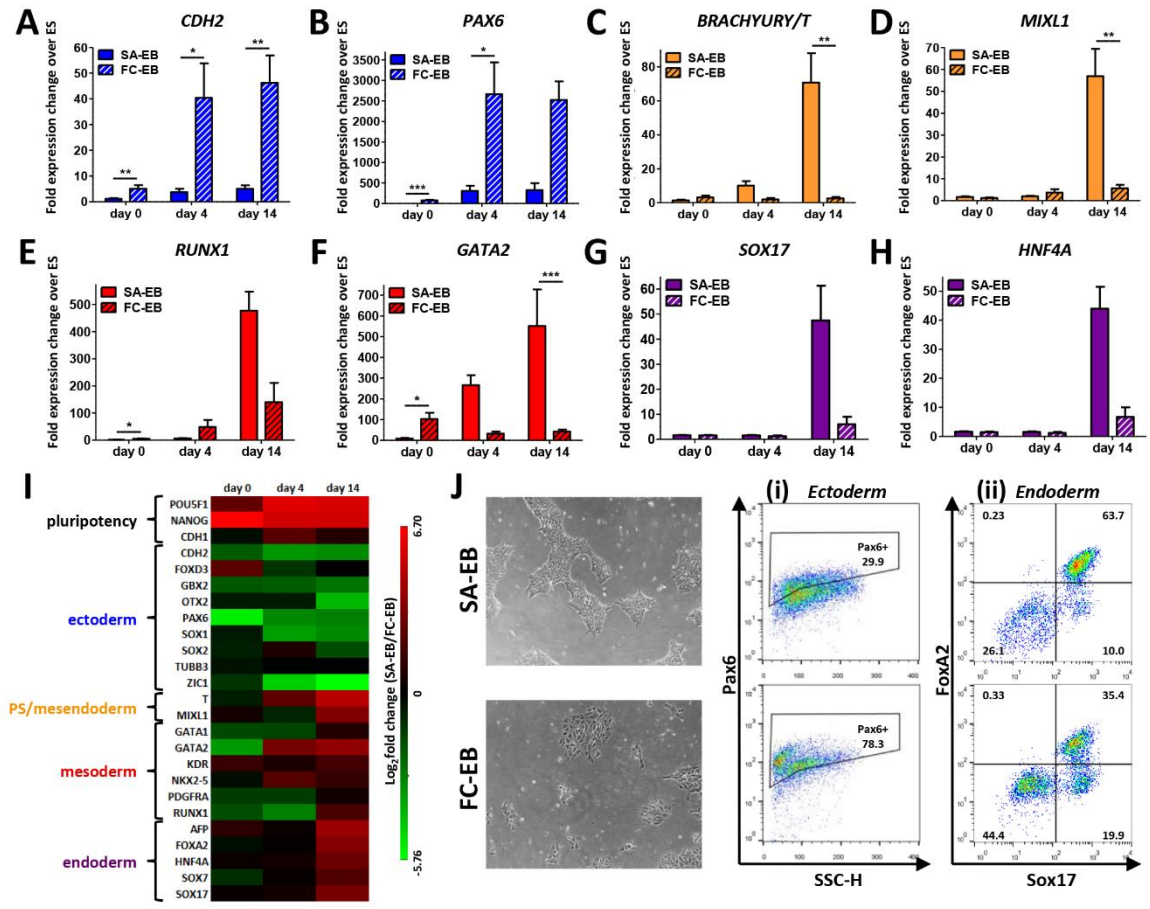

Figure 5.4 Analysis of the propensity of SA-EBs and FC-EBs to differentiate toward the primary germ lineages. Expression of genes related to ectoderm (A,B), primitive streak (C,D), mesoderm (E,F), and endoderm (G,H) in SA and FC aggregates at days 0, 4, and 14 during spontaneous EB differentiation. Fold-changes in expression are relative to undifferentiated hPSCs. Values represent the mean ± s.e.m. of $n = 3$ independent biological replicates. Asterisks represent statistical significance between indicated conditions (* $p < 0.05$, ** $p < 0.005$, *** $p < 0.0005$). (I) Summary of gene expression related to pluripotency and differentiation toward ectoderm, mesoderm, and endoderm in SA-EBs vs. FC-EBs on days 0, 4, and 14 of spontaneous differentiation, expressed as $\log_2$(fold expression change of SA over FC). Values represent the mean of $n = 3$ independent biological replicates. (J) Directed differentiation of SA-EB- and FC-EB-derived cells. (left) Phase contrast images of cells derived from day 0 SA-EBs and FC-EBs prior to directed differentiation. Arrows indicate differentiated colonies with flattened morphology. (right) Flow cytometry plots showing expression of (i) neuroectoderm marker Pax6 and (ii) definitive endoderm markers FoxA2 and Sox17 in cells differentiated from day 0 SA-EBs (top) and FC-EBs (bottom).

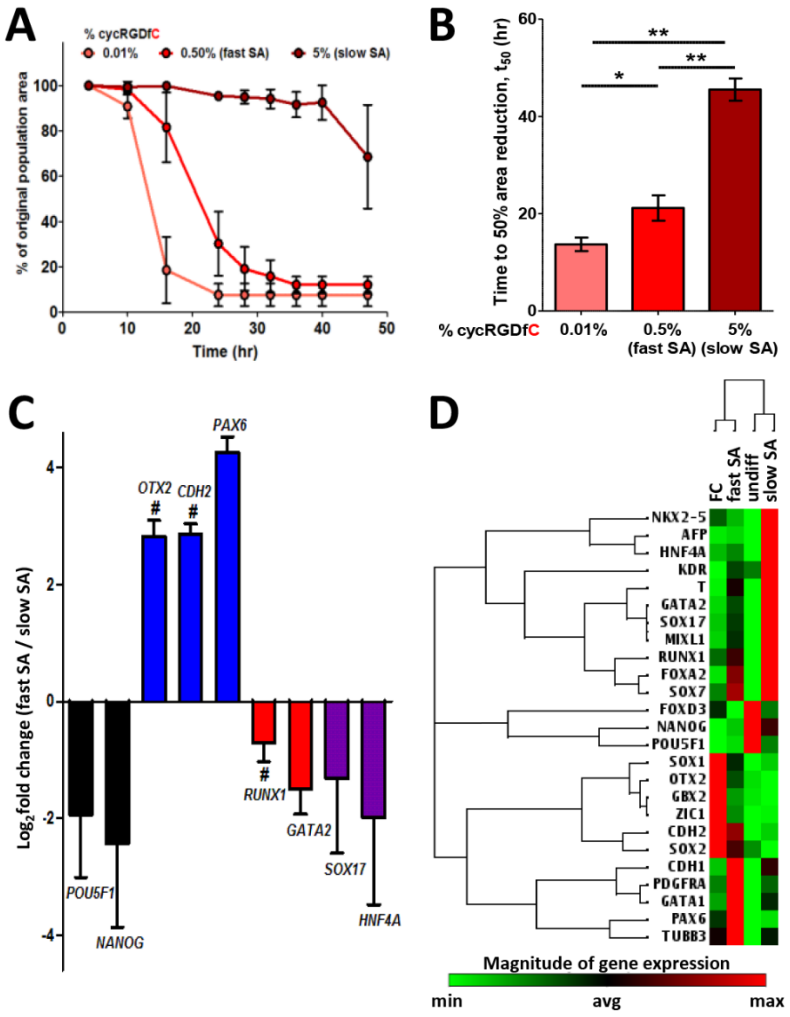

Figure 5.5 Labile substrate ligand density controls self-assembly kinetics and modulates lineage-specific gene expression during spontaneous EB differentiation. (A) hPSC aggregate self-assembly kinetics as a function of initial peptide density on labile substrates. Values represent the mean of n = 10, 12, and 6 replicates for 0.01%, 0.5%, and 5% cycRGDfC, respectively. Error bars represent 95% c.i. (B) Mean t_{50} values of self-assembly kinetics for EBs generated from labile substrates of varying cycRGDfC density. Error bars represent 95% c.i. * $p < 0.001$, ** $p < 0.0001$ (C) Fold-change expression of pluripotency and differentiation genes at day 14 in 0.5% SA-EBs (fast SA) vs. 5% SA-EBs (slow SA). # represents statistically significant difference between "slow SA" and "fast SA" ($p < 0.05$). Values represent the mean ± s.e.m. of n = 3 independent biological replicates. (D) Non-supervised hierarchical clustering of day 14 pluripotency and differentiation gene expression for slow and fast SA-EBs, FC-EBs, and undifferentiated hPSCs. Values represent the mean of n = 3 independent biological replicates.

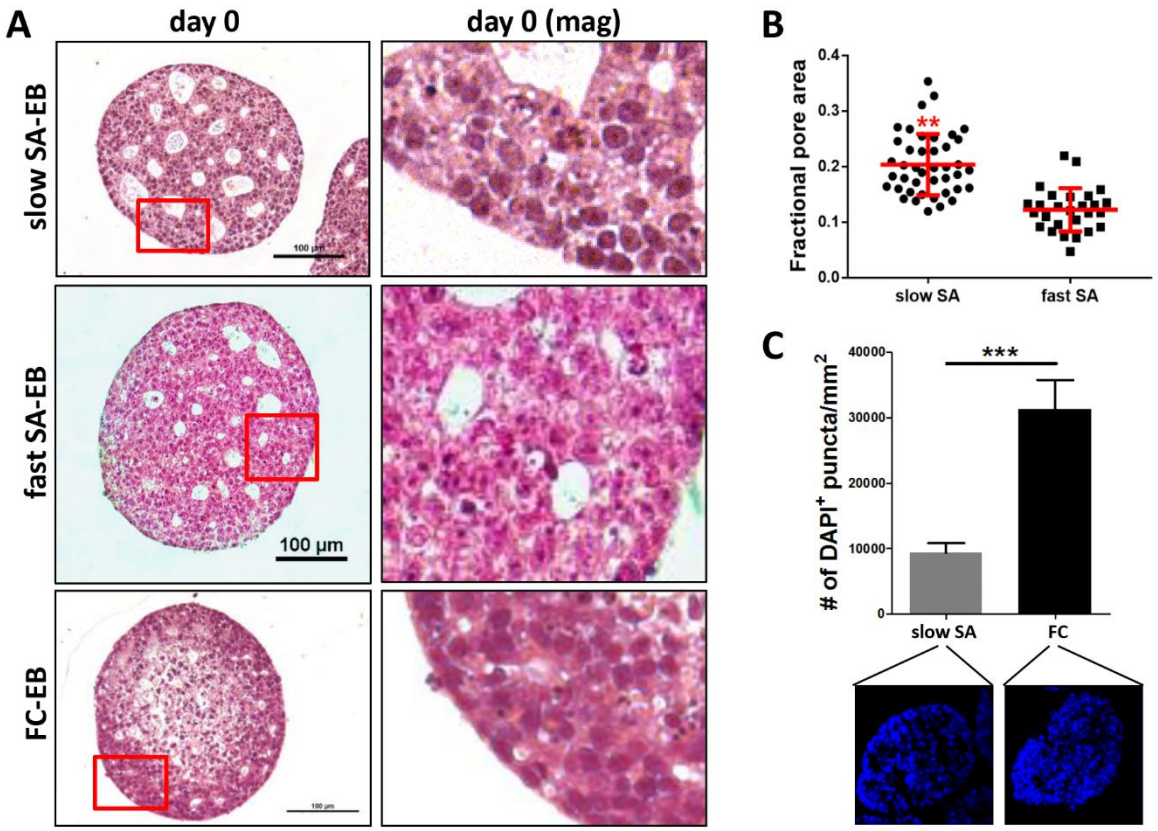

Figure 5.6 Aggregation method and kinetics affect EB structure. (A) H&E staining of histological sections from day 0 slow SA-EBs, fast SA-EBs, and FC-EBs. (right) Higher magnification micrographs of representative areas from EB sections (red boxes, left). (B) Quantification of porosity in slow and fast SA-EBs. Individual points represent values analyzed from histological sections of $n = 6$ distinct EBs per condition. Red bars represent the mean ± s.d. (** $p < 0.01$, two-tailed Student's t-test) (C) Quantification of cell density in cryosectioned day 0 SA-EBs and FC-EBs, as represented by number of DAPI-positive puncta per area. Values represent the mean ± s.d. (*** $p < 0.0005$, two-tailed Student's t-test)

5.11 SUPPLEMENTARY FIGURES & TABLES

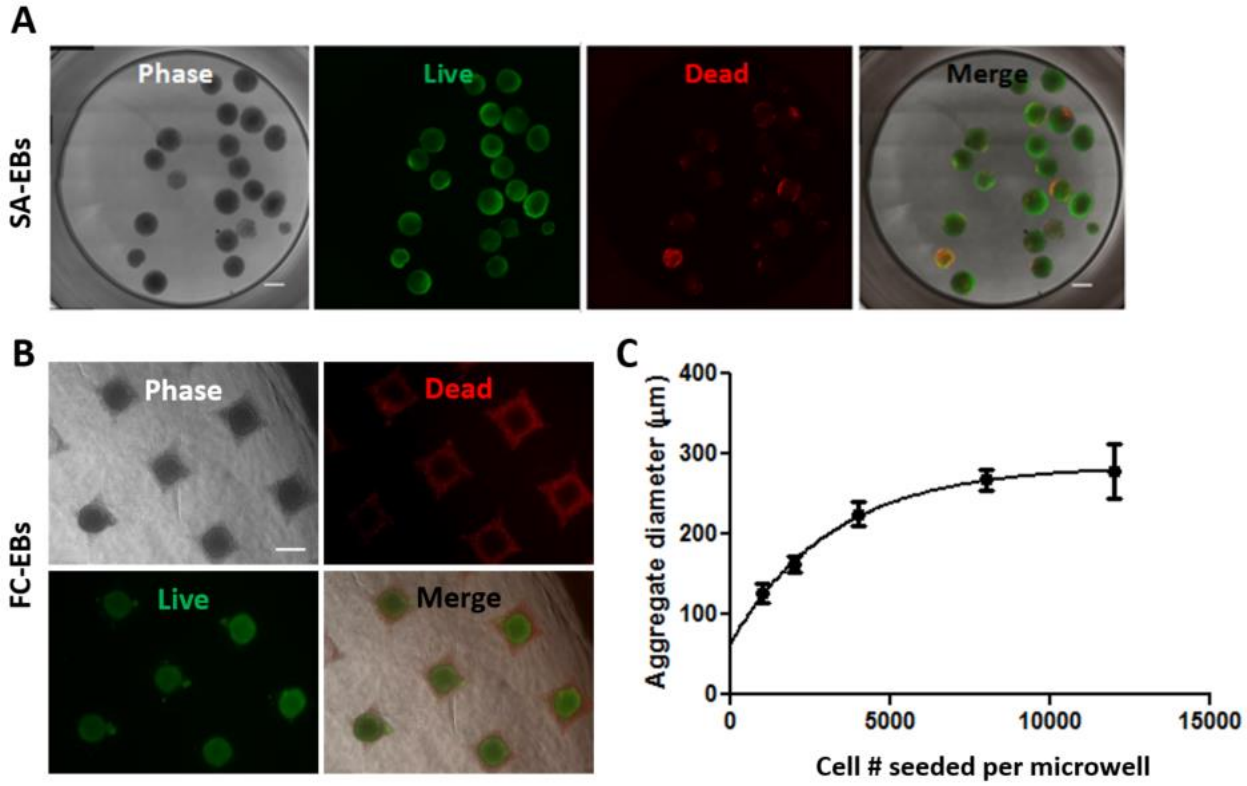

Supplementary Fig. S5.1 Characterization of viability and EB size in SA-EBs and FC-EBs. A) Viability of 5% cycRGDfC SA-EBs at day 0, assessed by LIVE/DEAD staining. Scale bar represents 500 μm. (B) LIVE/DEAD staining of FC-EBs at 24 hours after seeding. Not all cells within the microwells incorporated into EBs and those that did not incorporate were nonviable. (C) Control over FC-EB size. Varying initial cell numbers were centrifuged into agarose microwells and allowed to form EBs. EB diameter was assessed by microscopy at day 0.

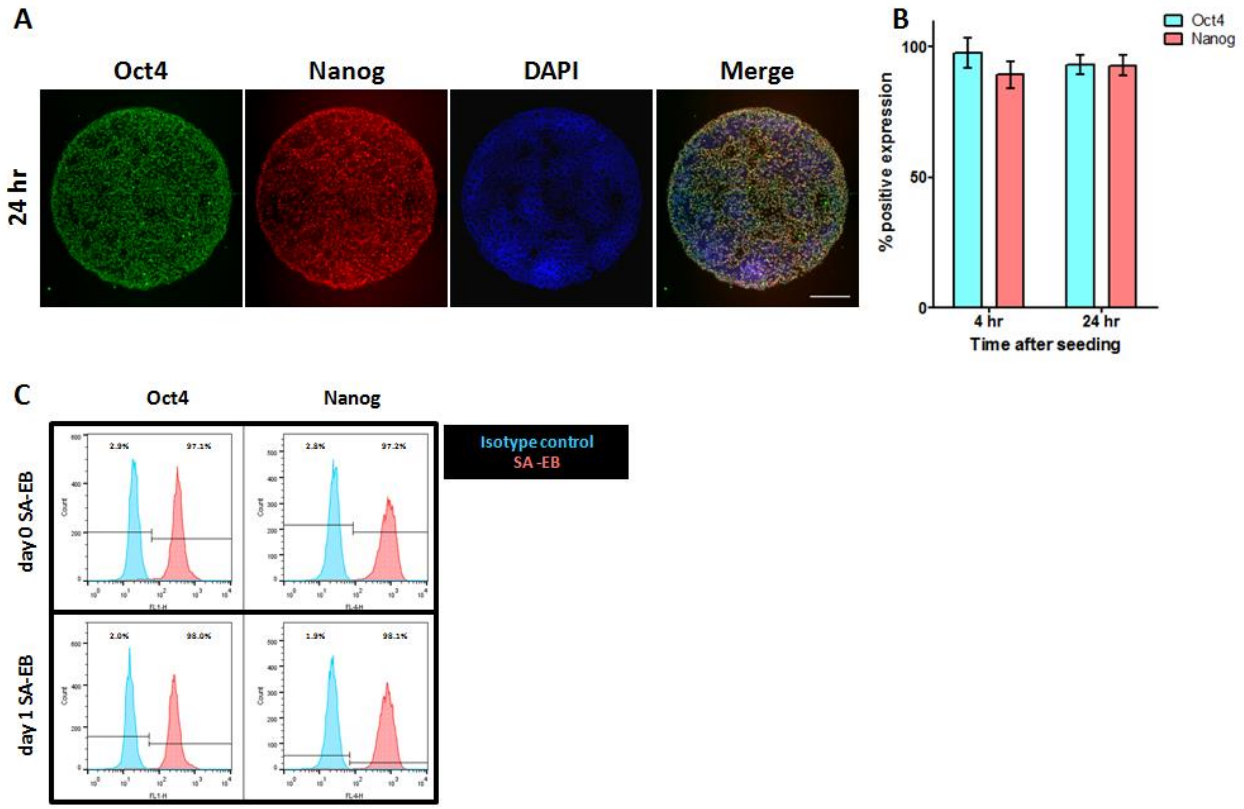

Supplementary Fig. S5.2 Assessment of Oct4 and Nanog expression in SA-EBs. (A) Immunofluorescence staining of hPSCs cultured on 5% cycRGDfC SAMs prior to self-assembly, at 24 hr after seeding. Cells were immunostained for Oct4 (green) and Nanog (red). DAPI was used to stain cell nuclei. Scale bar represents 250 μm. (B) Quantification of Oct4 and Nanog expression by hPSCs cultured on patterned 5% cycRGDfC SAMs at 4 hr and 24 hr after seeding. Immunofluorescence images at each time point were used to quantify percentage of positive cells per patterned spot. Error bars represent s.d. (C) Representative flow cytometry histograms quantifying expression of Oct4 and Nanog in day 0 and day 1 5% cycRGDfC SA-EBs. SA-EBs were formed and maintained in Essential 8 media, then collected and dissociated prior to staining with Oct4 and Nanog and evaluation by flow cytometry.

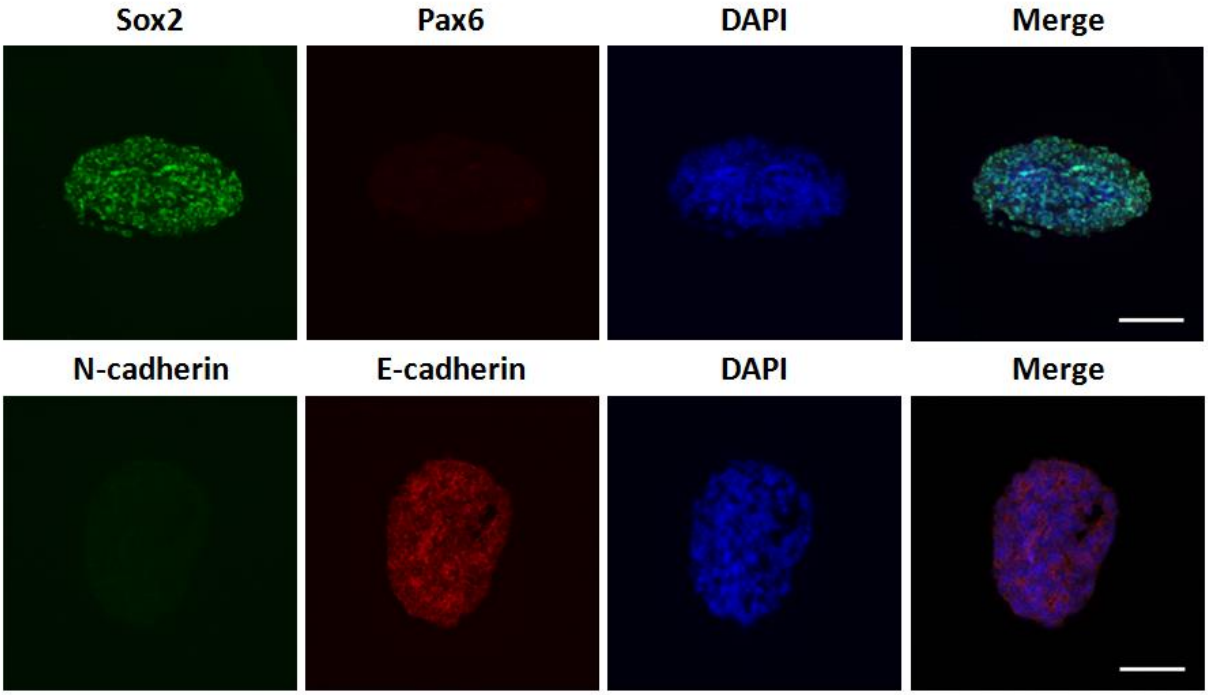

Supplementary Fig. S5.3 Immunofluorescence staining of day 0 SA-EBs for pluripotency and early differentiation markers. Cryosectioned EBs were stained for markers associated with pluripotency (Sox2, E-cadherin) or early differentiation (Pax6, N-cadherin). DAPI was used to stain nuclei. Scale bars represent 250 μm.

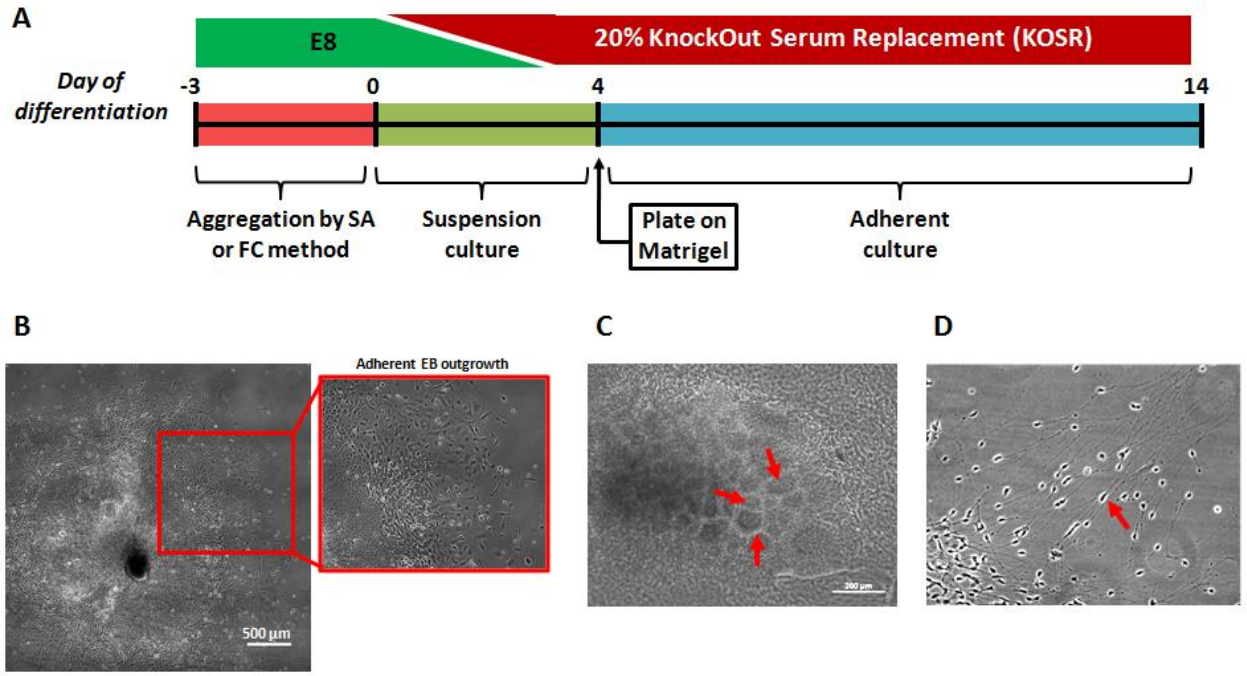

Supplementary Fig. S5.4 Spontaneous differentiation of EBs. (A) Schematic of protocol for spontaneous differentiation of SA-EBs and FC-EBs. EBs were transitioned from Essential 8 to differentiation medium ("DM" = 20% KOSR) between days 0 and 3 and maintained in DM until day 14. EBs were maintained in suspension culture (days 0-3) and plated on Matrigel at day 4 for further differentiation. (B) Plated EBs formed outgrowths containing differentiated cells. (C) Representative image of neural rosettes formed from plated FC-EBs at day 6. Rosettes were observed in >50% of FC-EB outgrowths. (D) Cells of neuronal morphology were found in day 9 FC-EB outgrowths.

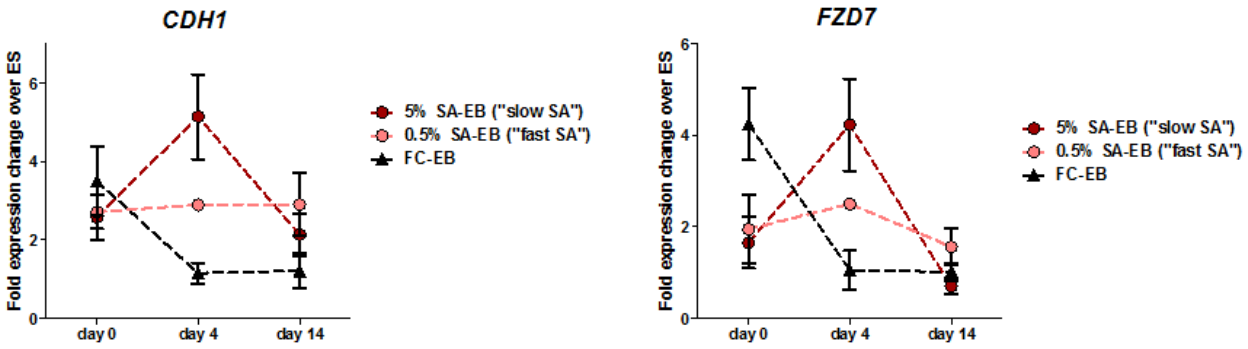

Supplementary Fig. S5.5 Self-assembly kinetics affects temporal expression of genes related to cell adhesion and Wnt signaling. *CDH1* (left) and *FZD7* (right) expression in slow and fast SA-EBs and FC-EBs at days 0, 4, and 14 during spontaneous EB differentiation. Fold-changes in expression are relative to undifferentiated hPSCs.

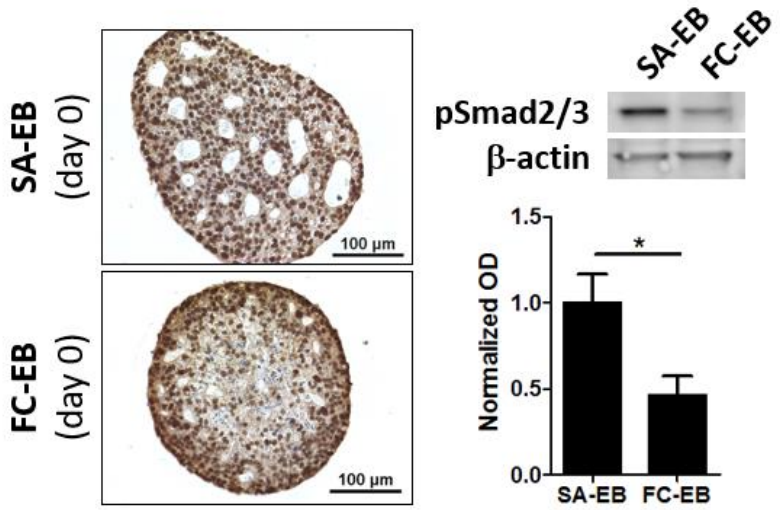

Supplementary Fig. S5.6 Aggregation method influences TGFβ signaling in EBs. (A) Cryosections of day 0 SA-EBs and FC-EBs stained for phosphoSmad2/3. Scale bar represents 50 µm. (B) Western blot analysis of phosphoSmad2/3 and phosphoSmad1/5 expression in whole cell lysates from day 0 SA-EBs and FC-EBs. β-actin was used as a load control. Representative blots shown (top), with quantification by densitometry (bottom). Error bars represent s.e.m. from $n = 4$ independent biological replicates. * $p < 0.05$

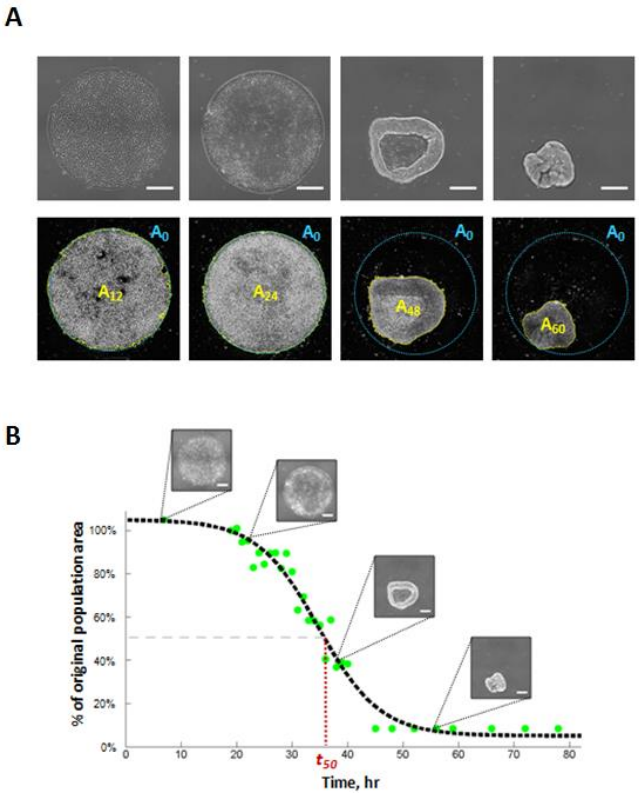

Supplementary Fig. S5.7 Method for quantification of SA-EB aggregation kinetics. (A) hPSCs were seeded onto patterned labile substrates and time lapse images of each patterned spot were acquired. Projected population area at each time point (A_n) was defined by edge detection and automated ROI drawing in NIS Elements analysis software. "Percent of original population area" was calculated as A_n normalized to initial area A_0 (defined as projected population area at 4 hrs after seeding), plotted as a function of time, and fit to a sigmoid curve. (B) Representative trace of EB self-assembly over time, with sigmoid fit showing determination of t_{50}.

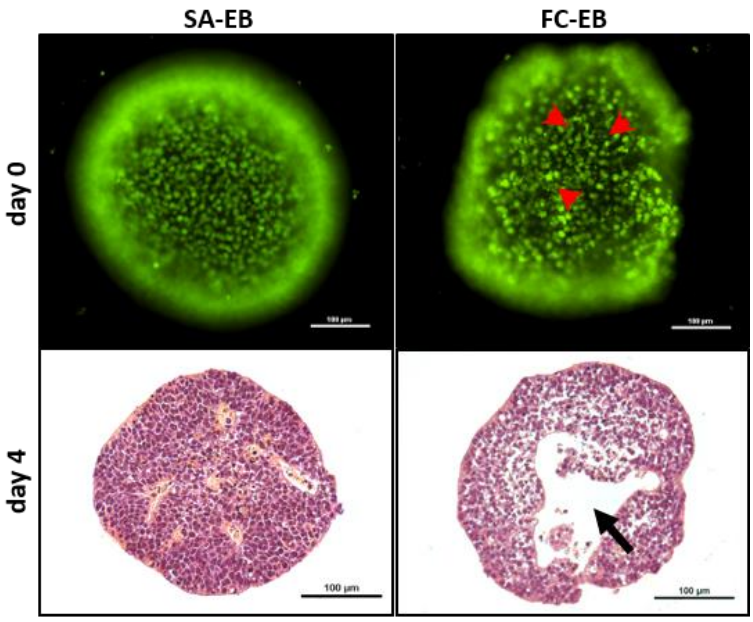

Supplementary Fig. S5.8 Aggregation method affects EB viability and necrotic core formation. (A) Optical sections of day 0 SA-EBs and FC-EBs, stained with CellTox Green DNA-binding dye. Red arrowheads denote fragmented nuclei indicative of poor cell viability. (B) H&E staining of paraffin-embedded day 4 (slow) SA-EBs and FC-EBs. EBs were maintained in suspension culture in Essential 8 media. Black arrow indicates presence of a necrotic core.

A

96w RB "FC-EB" condition	Calculated media volume:cell number ratio (μL/cell)
SA-matched	2.9×10^{-3}
FC-matched	1.5×10^{-3}
excess media	7.5×10^{-3}

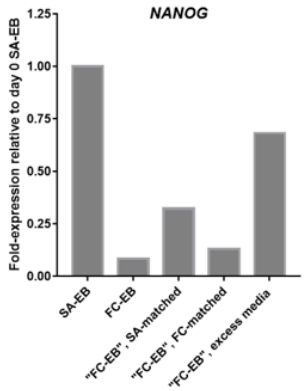

B

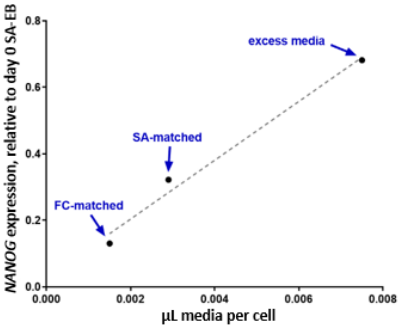

C

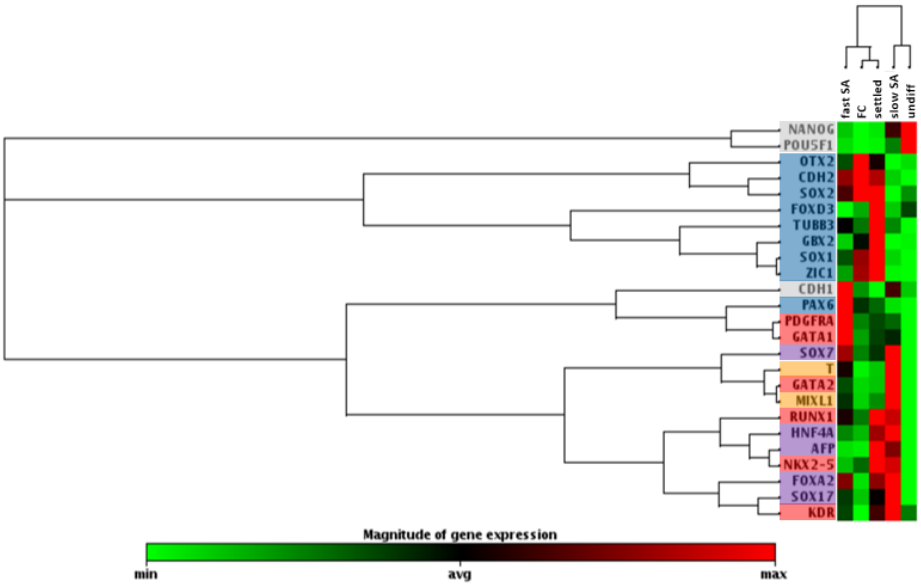

Supplementary Fig. S5.9 Aggregation method influences EB gene expression under equivalent culture conditions. (A) (left) Conditions for forming "FC-EBs" in 96-well low-adhesion roundbottom plates with media volume:cell number ratio matched to SA-EBs and FC-EBs. (right) *NANOG* expression in SA-EBs, FC-EBs, 96-well "FC-EBs" formed under SA- and FC-matched conditions and with a media volume:cell number ratio in excess of matched conditions. (B) *NANOG* expression in 96-well "FC-EBs" as a function of media volume per cell. (C) Non-supervised hierarchical clustering of day 14 pluripotency and differentiation gene expression for slow and fast SA-EBs, FC-EBs, settled EBs, and undifferentiated hPSCs. Colors denote association of genes with pluripotency (gray), ectoderm (blue), mesendoderm/primitive streak (orange), mesoderm (red), or endoderm (purple). Values represent the mean of $n = 3$ independent biological replicates. Settled EBs were formed under identical culture conditions as FC-EBs in agarose microwells, except without centrifugation.

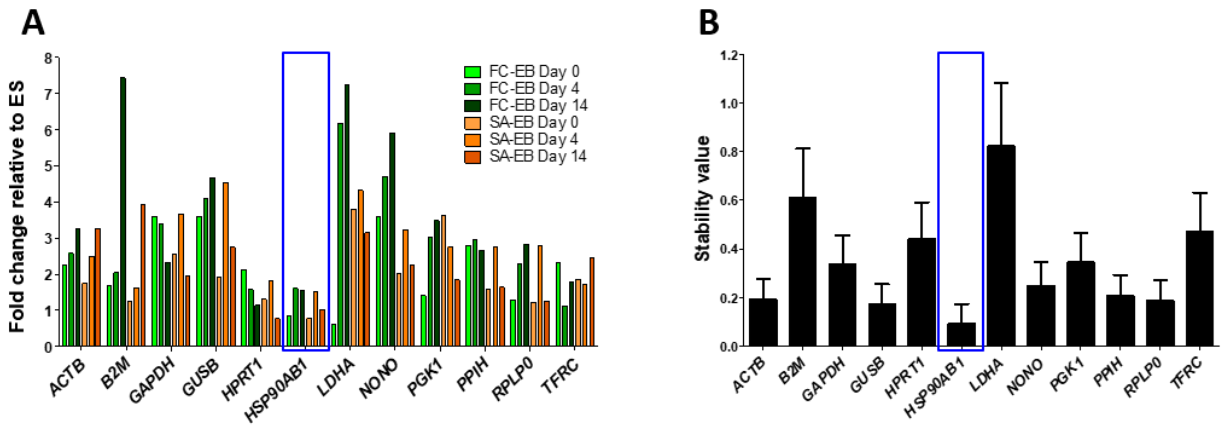

Supplementary Fig. S5.10 Identification of a stable reference gene in SA-EBs and FC-EBs throughout 14 days of spontaneous EB differentiation. (A) Fold-change expression of 12 reference genes in day 0, 4, and 14 SA and FC aggregates. qPCR data were analyzed by the ΔCt method. Fold-changes are expressed relative to undifferentiated hPSCs. Criteria for ideal reference genes included stable expression across both types of EBs as well as undifferentiated hPSC controls (i.e., fold-change ~ 1) and across time points. (B) Alternatively, Ct values from the same set of genes shown in (A) were analyzed using NormFinder software to identify a stable reference gene for the tested set of genes and samples. In this analysis, stable expression is indicated by a "stability value" closer to 0. *HSP90A* was identified as an appropriate reference gene via both approaches.

Supplementary Table S5.1 List of pluripotency and differentiation genes for RT^2 Custom Profiler PCR Array.

Gene Symbol	Refseq #	Description
AFP	NM_001134	Alpha-fetoprotein
CDH1	NM_004360	Cadherin 1, type 1, E-cadherin (epithelial)
CDH2	NM_001792	Cadherin 2, type 1, N-cadherin (neuronal)
FOXA2	NM_021784	Forkhead box A2
FOXD3	NM_012183	Forkhead box D3
FZD7	NM_003507	Frizzled family receptor 7
GATA1	NM_002049	GATA binding protein 1 (globin transcription factor 1)
GATA2	NM_032638	GATA binding protein 2
GBX2	NM_001485	Gastrulation brain homeobox 2
HNF4A	NM_178849	Hepatocyte nuclear factor 4, alpha
HSP90AB1	NM_007355	Heat shock protein 90kDa alpha (cytosolic), class B member 1
KDR	NM_002253	Kinase insert domain receptor (a type III receptor tyrosine kinase)
MIXL1	NM_031944	Mix paired-like homeobox
NANOG	NM_024865	Nanog homeobox
NKX2-5	NM_004387	NK2 homeobox 5
OTX2	NM_021728	Orthodenticle homeobox 2
PAX6	NM_000280	Paired box 6
PDGFRA	NM_006206	Platelet-derived growth factor receptor, alpha polypeptide
POU5F1	NM_002701	POU class 5 homeobox 1
RUNX1	NM_001754	Runt-related transcription factor 1
SOX1	NM_005986	SRY (sex determining region Y)-box 1
SOX2	NM_003106	SRY (sex determining region Y)-box 2
SOX7	NM_031439	SRY (sex determining region Y)-box 7
SOX17	NM_022454	SRY (sex determining region Y)-box 17
T	NM_003181	T, brachyury homolog (mouse)
TUBB3	NM_006086	Tubulin, beta 3
ZIC1	NM_003412	Zic family member 1

Supplementary Table S5.2 List of genes for RT^2 Housekeeping Array.

UniGene	Refseq #	Gene Symbol	Description
Hs.520640	NM_001101	*ACTB*	Actin, beta
Hs.534255	NM_004048	*B2M*	Beta-2-microglobulin
Hs.544577	NM_002046	*GAPDH*	Glyceraldehyde-3-phosphate dehydrogenase
Hs.255230	NM_000181	*GUSB*	Glucuronidase, beta
Hs.412707	NM_000194	*HPRT1*	Hypoxanthine phosphoribosyltransferase 1 (Lesch-Nyhan syndrome)
Hs.509736	NM_007355	*HSP90AB1*	Heat shock protein 90kDa alpha (cytosolic), class B member 1
Hs.2795	NM_005566	*LDHA*	Lactate dehydrogenase A
Hs.533282	NM_007363	*NONO*	Non-POU domain containing, octamer-binding
Hs.78771	NM_000291	*PGK1*	Phosphoglycerate kinase 1
Hs.256639	NM_006347	*PPIH*	Peptidylprolyl isomerase H (cyclophilin H)
Hs.546285	NM_001002	*RPLP0*	Ribosomal protein, large, P0
Hs.529618	NM_003234	*TFRC*	Transferrin receptor (p90, CD71)

CHAPTER 6. CONTROLLED AGGREGATION FOR OPTIMIZING THE IMMUNOMODULATORY POTENTIAL OF MESENCHYMAL STROMAL CELL AGGREGATES

Angela W. Xie, Nicholas A. Zacharias, and William L. Murphy. Controlled aggregation for optimizing the immunomodulatory potential of MSC aggregates. *In Preparation*.

6.1 PREFACE

In Chapter 2, we discussed the transition from planar to three-dimensional (3D) culture formats for scalable biomanufacturing of adhesion-dependent cells, and emphasized the utility of biomaterial technologies to study and ultimately control features of the 3D cell microenvironment. Advancing this concept, we described the development of a biomaterial platform to control the assembly of 3D cell aggregates (Chapter 4). We then demonstrated the utility of this platform in unraveling mechanistic effects of aggregation kinetics on growth factor signaling and lineage bias in embryoid bodies (Chapter 5). This study underscored the effect of aggregation kinetics on long-term structure and phenotype within stem cell aggregates, which has implications for the design of aggregation strategies in biomanufacturing processes.

In the current chapter, we use the technology from Chapters 4 and 5 to understand effects of culture geometry, aggregation method and kinetics on MSC aggregate structure and secretion of key paracrine immune mediators. We then combine the ability of our platform to control aggregate size and formation kinetics with a Design of Experiments approach to identify optimal aggregation parameters for MSC function in immunomodulatory potency assays.

6.2 ABSTRACT

Human mesenchymal stromal cells (MSCs) offer clinical promise as cell therapies due to their relative ease of isolation and expansion and their ability to secrete a variety of anti-apoptotic, pro-angiogenic, and immunomodulatory factors. 3D aggregation "self-activates" MSCs to augment their pro-angiogenic and immunomodulatory potential, but the microenvironmental features and culture parameters that promote optimal MSC immunomodulatory function in 3D aggregates are poorly understood. Here, we generated MSC aggregates via three published methods – self-assembly (SA), hanging drop (HD), and forced centrifugation (FC) – and compared them with regard to their i) aggregate structure and ii) immunomodulatory phenotype under resting conditions and in response to inflammatory stimulus. We observed that methods associated with fast aggregation kinetics (FC and HD) formed aggregates with higher cell packing density and reduced ECM synthesis compared to those with slow aggregation kinetics (SA). While all three methods of 3D aggregation enhanced MSC expression of key immunomodulatory factors compared to 2D culture, different aggregation methods differed in cells' temporal expression of these factors. Specifically, FC and HD aggregates initially expressed prostaglandin E2 (PGE2) at high levels that dropped dramatically over time in culture, whereas SA aggregates exhibited low but sustained expression of PGE2. A Design of Experiments approach, in which aggregate size and aggregation kinetics were systematically co-varied, identified that both parameters had a significant effect on MSCs' ability to regulate immune cell phenotypes. Compared to small aggregates formed with fast kinetics, large aggregates with slow assembly kinetics were more effective at suppressing T cell proliferation and polarizing macrophages toward an anti-inflammatory phenotype. Based on these results, we posit that culture parameters including aggregation method, kinetics, and

aggregate size influence both the structural properties of aggregates and their paracrine immunomodulatory function. These findings underscore the utility of engineering strategies to control the properties of 3D MSC aggregates, which may identify new avenues for optimizing the immunomodulatory function of MSC-based cell therapies.

6.3 INTRODUCTION

Human mesenchymal stromal cells are a cell type of particular interest in regenerative medicine, as evidenced by their use in >600 clinical trials for indications including stroke, osteoarthritis, diabetes, graft-versus-host disease (GvHD), and myocardial infarction[1,2]. A subset of therapeutic indications harness MSCs' multilineage differentiation potential for tissue engineering applications, where MSC differentiation and physical contribution to tissue repair are thought to be the primary mechanism of action. However, following *in vitro* and *in vivo* studies showing their unique capacity to suppress inflammation[3,4], MSCs have been widely explored for their ability to enhance functional outcomes in a variety of immune- and inflammatory-related diseases by regulating excessive responses from innate and adaptive immune cells and by stimulating resident cells involved in tissue repair[5–9]. In these contexts, the pro-regenerative mechanism-of-action of MSCs has been largely attributed to their secretion of trophic and immunomodulatory factors such as vascular endothelial growth factor (VEGF), prostaglandin E2 (PGE2), tumor necrosis factor-stimulated gene 6 (TSG-6), and indoleamine dioxygenase (IDO)[10,11]. For example, MSC-secreted PGE2 has established effects on multiple immune cells; it inhibits NK cell cytotoxicity and cytokine production[12], pushes resident pro-inflammatory (M1-like phenotype) macrophages toward an anti-inflammatory (M2-like) phenotype[13,8], and inhibits T cell activation and proliferation[14], among many other proposed

effects. Similarly, TSG-6 has multiple anti-inflammatory actions including inhibiting macrophage intracellular signaling to limit their secretion of inflammatory mediators[15], whereas IDO has been implicated as a primary soluble mediator of MSC suppression of T cell proliferation[16].

While a multitude of animal studies have established the benefits of MSC paracrine activity in models of inflammation- and immune-related diseases, clinical outcomes of MSC administration have been less unambiguously positive. The safety of MSC administration in humans is well-established, yet clear demonstrations of clinical efficacy in well-designed trials have been limited. Some reports posit that these discrepancies in treatment efficacy between animal and clinical trials may be ascribed to differences in dosing, as MSC dosing per weight is more than an order of magnitude higher in mouse models (typically 50 x 10^6 cells/kg) compared to what has been delivered intravenously in human trials (typically 2 x 10^6 cells/kg)[17]. Irrespective of the exact dose dependency for a specific application, clinical experience to date indicates that the required MSC doses for beneficial effect in humans are considerable. In recent Phase III clinical trials that met their primary endpoints, Remestemcel-L (GvHD, Mesoblast) dosed MSCs at 2 million cells/kg twice a week for four weeks (NCT02336230), while Alofisel (Crohn's disease-associated treatment-refractory complex perianal fistulas, TiGenix) delivered 120 million cells in a single treatment (NCT01541579). However, the cost of a cell therapy product is proportional to the number of cells per dose, and thus from the standpoint of biomanufacturing feasibility and accessibility of the therapy to patients, there is a strong case to be made for minimizing the number of cells per dose by increasing the effective potency of the cells delivered[18].

The goal to provide more functionally potent MSCs for clinical use has led to the investigation of various *in vitro* conditioning or "activation" regimens to enhance MSC paracrine function immediately before delivery. For instance, stimulation of MSCs with interferon-gamma (IFN-γ), an inflammatory cytokine that is produced by neutrophils and T cells and is abundant in injury sites, increases MSC immunosuppressive function *in vitro*[19–22] and appears to be required for maximal MSC effect in some animal models[23]. Interestingly, three-dimensional (3D) aggregation of MSCs has recently been proposed to independently "self-activate" MSCs' paracrine function, leading to enhanced secretion of molecules associated with immune cell regulation and tissue regeneration compared to 2D monolayer MSCs[24–26] – even in the absence of inflammatory cytokine activation. Complementary advantages of MSC aggregates have been proposed as well. These include the potential for 3D aggregates to survive and persist longer *in vivo* compared to dissociated cells[27–30] and the possibility that aggregation results in more sustained enhancements to MSC function compared to cytokine activation[31], for which the effects of activation are transient.

Early reports attributed MSC "self-activation" to the formation of a hypoxic core[32] or increased apoptosis-, cytokine-, and juxtacrine-related signaling[33] within 3D aggregates, although the exact contributions of some of these signaling mechanisms have since been questioned[26,34,35]. Thus, it is clear that assembly into 3D aggregates can generally prime MSCs to upregulate their secretion of specific paracrine factors, but a limited understanding of how the aggregate microenvironment influences the MSC secretome – and to what degree it can be manipulated – hinders efforts to optimize MSC aggregates for enhanced immunomodulatory functions. Recent efforts have demonstrated the utility of biomaterials to "engineer" the MSC aggregate microenvironment by incorporating loaded microparticles that sustain release of MSC-

activating cytokines within the aggregate interior[36]. Such strategies show promise for controlling the soluble environment of MSCs but have yet to be matched with approaches to systematically control the aggregation process (e.g., aggregation kinetics), which has been shown to influence aggregate structural characteristics and resulting cell phenotype[37,38]. In particular, hanging drops and forced aggregation via centrifugation – two commonly published methods for generating size-controlled cell aggregates – promote 3D aggregation of MSCs with relatively rapid kinetics (<12 hours) based on gravity-driven sedimentation and centrifugation force, which are not readily tunable. Novel approaches that enable spatiotemporal aspects of MSC aggregation to be systematically controlled may broaden the experimental space for identifying aggregation parameters that maximize MSC immunomodulatory function.

We previously described the development of a bioengineered platform encompassing patterned labile cell culture substrates that enable control over the size and aggregation kinetics of self-assembled (SA) pluripotent stem cell aggregates. Using this platform, we showed that aggregation method and kinetics impact 3D aggregate structure and lineage bias during differentiation of human embryoid bodies[39]. In the current study, we used a similar approach to evaluate the effects of aggregation method on MSC immunomodulatory phenotype and function. After verifying that our approach could control MSC aggregation kinetics, we demonstrated that methods associated with different kinetics of aggregation induced distinct temporal profiles of MSC paracrine factor secretion that correlated with changes in aggregate structural features including cell packing density, ECM synthesis, and differential expression of mechanotransduction-related genes related. Finally, we used a multifactorial Design of Experiments approach to identify a combination of culture conditions that significantly enhanced the anti-inflammatory and immunomodulatory potential of MSC aggregates. By tuning aggregate

size and aggregation kinetics, we co-optimized the paracrine immunomodulatory function of MSC aggregates to suppress T cell proliferation and polarize macrophages toward an M2 anti-inflammatory phenotype.

6.4 RESULTS

6.4.1 Labile substrates supported self-assembly of MSC aggregates with tunable size and aggregation kinetics.

We previously demonstrated that engineered substrates presenting patterns of the cyclized cell adhesion peptide RGD ("cycRGDfC") via a labile bond could control pluripotent stem cell aggregation kinetics based on initial substrate cycRGDfC density[39]. Here, we verified that MSC self-assembly (SA) into aggregates on these substrates was controllable in a similar manner, dependent on both lability of the substrate and cycRGDfC density. MSCs seeded on 0.05% cycRGDfC labile substrates rapidly formed aggregates within < 16 hours (t_{50} of self-assembly = 8.3 ± 1.9 hrs) while those on 5% cycRGDfC aggregated significantly more slowly (t_{50} = 41.1 ± 11.3 hrs), and cells failed to aggregate at all on non-labile substrates (Fig. 6.1A-B). The size of SA MSC aggregates depended on 2D pattern geometry, with SA aggregates from 1.2 mm and 2.4 mm diameter patterns generating aggregates of significantly different diameters (217 ± 18 μm and 400 ± 28 μm, respectively) (Fig. 6.1C-D).

We directly compared MSC aggregates generated by our SA approach to those formed by two conventional methodologies – hanging drop (HD) and forced aggregation (FC) – to determine characteristic aggregation kinetics and the degree of control over aggregate size distribution offered by each method. Consistent with prior studies, HD and FC MSCs aggregated on rapid time scales, with loose, clearly three-dimensional structures formed by 6 hours after

seeding, and compact spheroids arising by 24 hours (Supplementary Fig. S6.1). The size of aggregates generated by HD and FC could be varied by controlling cell number per droplet or per microwell, respectively (not shown). HD and FC aggregation methods demonstrated slightly broader distributions of MSC aggregate diameter (424 ± 58 μm and 428 ± 51 μm, respectively) compared to SA aggregates of similar size (Fig. 6.1C-E). We chose SA MSCs formed on 5% cycRGDfC substrates for further characterization, as this slowly-aggregating condition provided the largest disparity in aggregation kinetics, compared to HD and FC methods.

6.4.2 Aggregation method affected structural properties and trilineage differentiation of MSC aggregates.

The method used to generate MSC aggregates had a significant effect on 3D cell packing density. Analysis of DAPI-stained sections of size-matched aggregates revealed that FC and HD aggregates had higher numbers of nuclei per cross-sectional area (11.06 ± 3.35 and 6.99 ± 1.11 x 10^3 nuclei per mm^2, respectively) compared to SA aggregates (4.48 ± 0.78 x 10^3 per mm^2) (Fig. 6.2A). Interestingly, aggregation method also appeared to affect MSC nuclear shape. Cell nuclei in HD and FC aggregates were smaller and more rounded in morphology, compared to nuclei within SA aggregates which were more elongated and associated with a spindle-like cell morphology (Fig. 6.2B). 3D culture and aggregation method also influenced MSC synthesis of ECM- and proliferation-related genes. Day 0 aggregates, particularly those formed by HD and FC methods, exhibited significantly lower expression of *CTGF*, *COL1A1*, and *MKI67* compared to 2D MSCs (Fig. 6.2C). Notably, SA aggregates expressed these genes at higher levels than HD or FC aggregates, although these differences were not statistically significant. In accordance with

the gene expression results, we also observed more collagen deposition in SA aggregates compared to FC aggregates (Fig. 6.2D).

To investigate whether 3D aggregation affected trilineage differentiation potential, we plated aggregates or 2D MSCs on collagen-coated dishes in the presence of appropriate induction media. Aggregates attached within 24 hours of plating and individual cells migrated out to varying degrees depending on the type of outgrowth and the media environment. All three methods of aggregation produced MSCs capable of differentiating toward adipogenic and chondrogenic fates. We observed high densities of Oil Red O-positive cells in HD and FC aggregates, whereas intermediate and low densities were observed in SA aggregates and 2D MSCs, respectively (Supplementary Fig. S6.2A). 3D aggregates in chondrogenic medium stained positively for Alcian Blue, with the strongest staining in regions within or in close proximity to the original aggregate (Supplementary Fig. S6.2B). In contrast, all three aggregation methods exhibited poor osteogenic differentiation. Following three weeks of osteogenic induction, weak Alizarin Red staining was observed in plated SA aggregates, while no areas of positive staining were seen in HD or FC aggregates. 2D MSCs retained osteogenic differentiation potential as evidenced by strong Alizarin Red staining after the three-week differentiation (Supplementary Fig. S6.2C).

6.4.3 Culture format and aggregation method influenced MSC immunomodulatory phenotype and temporal response to pro-inflammatory environments.

Previous work indicated that exposure to pro-inflammatory stimuli[20,40–42] (e.g., interferon-gamma; IFN-γ) and three-dimensional culture of MSCs[24,35,43,44] can independently enhance aspects of MSC immunomodulatory phenotype. To better understand the influence of

3D culture geometry and aggregation method on the sustained immunomodulatory properties of MSCs, we performed gene expression analysis for IFN-γ-stimulated versus unstimulated ("resting") MSCs cultured in 2D monolayers or 3D cell aggregates, over a 7-day time course. Irrespective of the method used to aggregate the cells and the presence of IFN-γ, 3D MSC aggregates demonstrated higher expression of *VEGFA*, a gene associated with angiogenesis and wound healing, as well as increased expression of genes associated with paracrine induction of tolerogenic immune cell phenotypes (*TNFAIP6*, *PTGS2*, and *IDO1*), relative to the corresponding 2D MSC conditions across all time points assessed (Fig. 6.3A). On the other hand, 2D MSCs exhibited elevated expression of genes associated with cell proliferation (*MKI67*) and ECM synthesis (*COL1A1*, *CTGF*), genes that were downregulated in 3D MSC aggregates.

Treatment with IFN-γ had a significant influence on MSC expression of a subset of immunomodulatory genes. Specifically, *IDO1* expression was undetectable in resting MSCs in 2D and 3D culture but was induced at high levels upon IFN-γ stimulation (Fig. 6.3A). Expression of *TNFAIP6* was also significantly affected by IFN-γ treatment; at day 0, IFN-γ induced a 2.4-fold downregulation of *TNFAIP6* in 2D MSCs but upregulated *TNFAIP6* expression >3.1-fold in all three 3D aggregate conditions (Fig. 6.3B, Supplementary Fig. S6.3). This IFN-γ-dependent inducibility of *TNFAIP6* expression in 3D MSC aggregates persisted at days 3 and 7 (3.0- to 7.1-fold upregulation relative to resting MSC), while IFN-γ had only a marginal effect on expression in 2D MSCs (<1.6-fold upregulation; Supplementary Fig. S6.3). Additionally, IFN-γ treatment decreased the expression of *MKI67*, *COL1A1*, and *CTGF* in MSCs across all time points and culture formats, with the exception of *COL1A1* which was marginally upregulated in 2D MSCs in response to IFN-γ (Fig. 6.3B).

Immunomodulatory gene expression profiles were dynamic over the course of 7 days in culture, and MSC secretion of paracrine factors depended on the method of 3D aggregation. HD and FC aggregates expressed high levels of *VEGFA*, *TNFAIP6*, and *PTGS2* at day 0 but significantly downregulated their expression at days 3 and 7, whereas expression of these genes gradually increased over time in SA aggregates (Fig. 6.3C, Supplementary Fig. S6.3). In agreement with trends observed in the gene expression profiles, production of PGE2 by SA aggregates steadily increased over time (0.50 ± 0.49 pg PGE2/ng DNA at day 0, vs. 7.68 ± 2.85 pg PGE2/ng at day 7). This trend of increasing PGE2 secretion over time was in stark contrast to PGE2 production by HD and FC aggregates, which dramatically decreased between day 0 (134.30 ± 83.81 pg PGE2/ng DNA for HD, 30.56 ± 25.26 pg PGE2/ng DNA for FC) and day 7 (3.46 ± 2.00 and 5.20 ± 3.11 pg PGE2/ng DNA, respectively) (Fig. 6.3D). Strikingly, the amount of PGE2 secreted by MSCs in 2D monolayer was 40-fold lower than that of the lowest 3D aggregate condition (Supplementary Fig. S6.4). Taken together, culturing MSCs in 3D aggregates enhanced their secretion of paracrine factors involved in immune cell modulation, under both resting conditions and following inflammatory stimulus. Furthermore, 3D aggregation not only influenced MSC response to pro-inflammatory environmental cues but also affected temporal regulation of MSC immunomodulatory phenotype depending on the method of aggregation used.

6.4.4 Multifactorial Design of Experiments (DOE) identified the size and aggregation kinetics of MSC aggregates as parameters that influence immunomodulatory function.

Prior studies have implicated aggregate size[26,45–49] and kinetics of aggregation[37,39] as factors that independently instructed cell phenotype in 3D. We hypothesized that each of these

factors may have both distinct and interacting effects on MSC capacity to regulate specific immune cell types, and that a combination of these factors could be identified to promote the overall anti-inflammatory and immune-suppressive functions of MSCs. To address this hypothesis, we used a Design of Experiments approach to systematically investigate the influence of aggregate size and aggregation kinetics on the immunomodulatory function of IFN-γ-treated SA MSC aggregates. As before, size of SA aggregates was controlled by varying pattern size of labile substrates (Fig. 6.1C-D), while aggregation kinetics were controlled by varying %cycRGD, where higher %cycRGD corresponded to slower aggregation rates (Fig. 6.1B).

We constructed a two-factor, three-level full factorial design that resulted in nine unique conditions that we tested for their capacity to suppress T cell proliferation (i.e., minimize %Ki67+ CD3+ PBMCs) and polarize macrophages toward an M2-like phenotype (i.e., maximize IL-10 and minimize TNF-α secretion by Mφ) (Fig. 6.4, Supplementary Fig. S6.5-6.6). Multivariate analysis of immune cell responses as a function of MSC aggregation parameters identified independent and interacting effects of aggregate size and aggregation kinetics on MSC immunomodulatory function (Fig. 6.5). Specifically, the model identified a negative linear relationship between %cycRGD and T cell proliferation ($p < 0.0001$, Fig. 6.5A) and a positive linear relationship between %cycRGD and Mφ secretion of IL-10 ($p < 0.05$, Fig. 6.5B), suggesting that slower aggregation kinetics promote both T cell suppression and M2 Mφ polarization by SA MSC aggregates. Aggregate size alone had no significant effect on T cell suppression ($p = 0.14$) or Mφ IL-10 secretion ($p = 0.23$) (Fig. 6.5A-B). In contrast, the model identified a negative linear relationship between aggregate size and Mφ TNF-α secretion ($p < 0.01$), but no significant effect of %cycRGD on TNF-α secretion (Fig. 6.5C).

6.4.5 Validation of DOE-identified conditions to optimize T cell suppression and macrophage polarization by MSC aggregates.

We tested the DOE model by generating SA MSC aggregates from two additional MSC donors (Table 6.1), specifically comparing aggregates that were predicted by the DOE model to perform well (5.0 mm pattern/10% cycRGD, i.e. "large/slow") versus poorly (1.2 mm pattern/0.1% cycRGD, i.e. "small/fast") in assays of immunomodulatory function. To determine whether the effects identified by the model were specific to MSC aggregates generated by the SA approach, we also compared FC MSC aggregates of different sizes ("small" = ~800 cells per aggregate; "large" = ~13,500 cells per aggregate). In T-cell suppression assays, DOE-optimized SA MSC aggregates outperformed all other aggregate conditions tested for both MSC donors. Large/slow-assembling SA aggregates from Donors 2 and 3 reduced the percentage of proliferating T cells to 76.0% and 69.5%, respectively, while small/fast-assembling SA aggregates resulted in 90.2% and 84.7% proliferating T cells following co-culture (Fig. 6.6A(i)). DOE-optimized SA MSC aggregates also exhibited the highest capacity for M2 macrophage polarization. Secreted IL-10:TNF-α ratio was higher for macrophages cultured in conditioned media from large/slow-assembling SA aggregates (2.73 ± 0.10 and 10.31 ± 5.29) compared to those in media conditioned by small/fast-assembling SA aggregates (1.05 ± 0.02 and 2.48 ± 0.70) from Donors 2 and 3, respectively (Fig. 6.6B,D).

Although FC aggregates generally performed worse than SA aggregates in immune cell assays, we nevertheless still observed a positive effect of increasing aggregate size in these conditions. Co-culture with large FC aggregates resulted in 92.7% and 85.5% proliferating cells (Donors 2 and 3), while small FC aggregates had marginal effects on T cell proliferation (97.7%

and 97.6%, vs. 95.8% Ki67+ in controls without MSCs) (Fig. 6.6A(ii)). Similarly, media conditioned by large FC aggregates induced a higher macrophage IL-10:TNF-α ratio compared to that of small aggregates (1.55 ± 0.49 vs. 0.79 ± 0.42, 2.48 ± 0.65 vs. 0.91 ± 0.37 for Donors 2 and 3, respectively) (Fig. 6.6C,D).

6.5 DISCUSSION

In this study, we sought to characterize the influence of different 3D aggregation methods on the structure and function of MSC aggregates. We previously reported that the method and kinetics of aggregation had striking effects on cell density, porosity, and growth factor signaling in human embryoid bodies, which influenced loss of pluripotency and lineage bias during their spontaneous differentiation[39]. Thus, we hypothesized here that the same parameters could affect the structure and immunomodulatory function of MSC aggregates. We first characterized the structure of MSC aggregates generated via three approaches associated with distinct aggregation kinetics, where aggregates were matched in approximate diameter across conditions. While the size of cell aggregates is commonly reported as a basis for comparison across studies, recent reports suggest that this metric alone is a poor indicator of phenotypic equivalence – even within aggregates generated from the same cell line/source – without also accounting for processing parameters such as the method of aggregation[37–39,50]. Indeed, despite having compared size-matched SA, HD, and FC aggregates, we observed differences in cell packing density, nuclear morphology, and ECM synthesis within MSC aggregates based on the aggregation method used. Cells within SA aggregates were present at a significantly lower density (Fig. 6.2A), had more elongated nuclear morphologies (Fig. 6.2B), and deposited greater quantities of collagen (Fig. 6.2D) compared to cells from HD or FC aggregates. These marked differences in cell packing

density and cell morphologies in SA vs. HD and FC aggregates led us to investigate whether genes associated with known cell mechanosensing pathways, specifically YAP/TAZ signaling, were affected by the method of aggregation.

Yes-associated protein (YAP) and its homolog, transcriptional co-activator with PDZ-binding motif (TAZ), have been implicated as key effectors of the Hippo pathway in the mechanotransduction of biophysical cues such as cell shape[51], substrate stiffness[52,53], and cell density[54] in 2D culture *in vitro*, and in organ size control[55] and fibrosis[56] *in vivo*. In MSCs, elevated YAP activity has been associated with low cell density[57], spread cell morphologies[58], production of type I collagen[59], and increased proliferation[57,60]. On the other hand, mechanotransduction of high cell density and rounded cell morphologies is thought to occur through decreases in YAP activity, which are mediated by phosphorylation of YAP that marks it for cytoplasmic retention, ubiquitination and proteosomal degradation[51,61]. We observed that while 3D aggregation markedly downregulated expression of YAP target genes (*CTGF, CYR61*) and genes associated with proliferation (*MKI67*) and ECM synthesis (*COL1A1*) relative to 2D conditions, day 0 SA aggregates still expressed all three of these genes – as well as Collagen I protein – at higher levels compared to HD or FC aggregates (Fig. 6.2C-D, Supplementary Fig. S6.7). Furthermore, Western blots for phosphoYAP revealed higher YAP phosphorylation in FC aggregates compared to SA aggregates, indicative of higher YAP activity in SA conditions (Supplementary Fig. S6.8). These results support the hypothesis that differences in aggregate structure as a function of aggregation method may be interpreted on the cellular level through a YAP-mediated pathway.

Our observations of trilineage differentiation capacity for 3D MSC aggregates further supported the possibility of differential YAP involvement. In prior studies investigating MSCs in

simplified 2D culture models, differential YAP signaling in MSCs instructed trilineage differentiation bias; RhoA-mediated YAP activation was required for osteogenic differentiation while YAP inhibition led to increased adipogenic differentiation at the expense of osteogenic fates. In our study, although aggregates generated by all three methods demonstrated poor osteogenic differentiation, SA aggregates exhibited stronger Alizarin Red staining (Supplementary Fig. S6.2C), a lower density of Oil Red O-positive clusters (Supplementary Fig. S6.2A), and higher *RHOA* expression (Supplementary Fig. S6.7) compared to HD and FC aggregates, mirroring the reported RhoA-mediated effects of YAP activity on lineage bias during MSC differentiation[62]. While it remains unclear to what degree these changes in YAP-associated genes are elicited by differences in aggregation kinetics, our preliminary data indicate that faster rates of SA aggregation further downregulate expression of *CTGF*, *COL1A1*, *MKI67* (Supplementary Fig. S6.9), indicating that the described effects are not simply artefacts of particular aggregation methods. Together, these results support a potential role for YAP signaling in 3D MSC aggregates and suggest that differences in aggregation kinetics may be linked to phenotypic changes via mechanosensitive signaling pathways.

Based on clear structural differences between aggregates generated via SA vs. HD and FC methods, we were interested in whether these differences correlated with distinct changes in MSC production of trophic and immunomodulatory paracrine factors. We chose to additionally compare the effects of treatment with the pro-inflammatory cytokine IFN-γ on 2D vs. 3D MSCs. While IFN-γ treatment has been widely proposed as a means of "activating" ("licensing") MSCs' immunomodulatory functions[63], its effects have not been thoroughly explored in MSC aggregates, partly because 3D aggregation alone was proposed to "self-activate" MSC immunomodulatory potential even in the absence of exogenous inflammatory signals[31,43]. Thus,

we were also interested in whether the method of aggregation influenced responsiveness to IFN-γ, or if 3D "self-activation" alone was an adequate substitute for cytokine-based priming of MSCs.

We looked specifically at paracrine factors previously reported to be strongly induced by 3D aggregation of MSCs (VEGF[64,65], PGE2[66,67], TSG-6[24,33]). VEGF, a potent pro-angiogenic factor, was chosen based on its known roles in tissue repair[68] and suggested involvement in M2 macrophage polarization[69]. PGE2 and the enzyme responsible for its synthesis, COX-2 (*PTGS2*), have been widely implicated in MSCs' capacity to attenuate pro-inflammatory M1 macrophage phenotypes[13] and suppress other inflammatory immune cells during injury[14]. TSG-6 (*TNFAIP6*) has been shown to reproduce many of the benefits of MSC administration in animal models of corneal inflammation[70], peritonitis[71], and myocardial infarction[72]. We also assessed expression of IDO, a molecule proposed to be a major regulator of MSCs' immunosuppressive effects on T cells[73]. Profiling genes associated with these factors revealed stark differences in expression between 2D and 3D MSCs, irrespective of aggregation method (Fig. 6.3A). Under both resting and IFN-γ-treated conditions, expression of *VEGFA*, *PTGS2*, and *TNFAIP6* was markedly upregulated at early time points in SA, HD, and FC aggregates relative to their 2D counterpart (Supplementary Fig. S6.3). These differences were reflected by measurements of secreted factors in the media, where the amount of PGE2 secreted by aggregates was at least 40-fold higher than in 2D MSCs (Supplementary Fig. S6.4).

Notably, day 0 in our studies – 72 hours following initial seeding – corresponds to a time point around which HD and FC aggregates are reported to undergo a "compaction" process. MSC aggregate compaction is associated with changes in expression of integrins and cadherins, alterations in cytoskeletal arrangement, and increased activation of genes for cytokines and

immune mediators[24,32,43,67,74]. Interestingly, Tsai et al. demonstrated that robust compaction was associated with upregulation of caspase 3/7 signaling, and that inhibition via the pan-caspase inhibitor Q-VD-OPh not only reduced compaction but also knocked down functional enhancements (CXCR-4, PGE2 expression) in MSC aggregates. Thus, we surmised that the time of compaction might represent a "burst" in the expression of many genes previously reported to be induced by 3D aggregation of MSCs. This premise would suggest that aggregates forming via different kinetics exhibit distinct temporal profiles of immunomodulatory factor production, depending on the timing and duration of the compaction process. By carrying cultures out to day 7, we identified highly dynamic expression of key genes in HD and FC aggregates. In particular, expression of both *VEGFA* and *PTGS2* – as well as secreted PGE2 – was high at day 0 and decreased dramatically at days 3 and 7 in HD and FC aggregates, but markedly increased over time in SA aggregates (Fig. 6.3C-E, Supplementary Fig. S6.3).

To our knowledge, there have been few reports, if any, that have characterized the duration over which 3D aggregation promotes sustained enhancements in MSC paracrine function. Our findings indicate that – for certain secreted factors like PGE2 – conventional aggregation by HD or FC methods induces a short-lived "burst" of enhanced paracrine function in MSCs, whereas different methods and kinetics of aggregation may change the magnitude and duration of those enhancements. Based on recent reports linking cell-cell contact-mediated signaling pathways to improved MSC immunomodulatory function[75,76], future extensions of the current work should investigate whether structural remodeling and alterations in the cytoskeletal network – which are reported to be extensive in conventional MSC aggregates[32,34,77] – are directly linked to the duration of MSC "self-activation." Such studies may inspire development

of new strategies to tailor MSC aggregate structure for prolonged paracrine functions in clinical applications.

Our comparison of resting and IFN-γ-treated MSCs revealed effects of culture geometry (2D vs. 3D) on MSC response to inflammatory stimulus. *IDO1* – in line with prior studies – was not detectable under resting conditions and, following IFN-γ treatment, was not significantly affected by 3D culture geometry (Supplementary Fig. S6.3). *TNFAIP6*, on the other hand, was not only more highly expressed but also displayed greater induction in response to IFN-γ in 3D aggregates (Fig. 6.3B). This is notable in the context of overwhelming evidence that immunomodulatory functions of MSCs are not constitutive but rather depend on appropriate licensing by the inflammatory microenvironment[42,7]. Indeed, responsiveness to inflammatory cues such as IFN-γ, TNF-α, and danger signals in the disease/injury environment are likely to be an important determinant of MSCs' beneficial effects *in vivo*[23]. It is worth considering that the response of a 3D aggregate to external stimuli is potentially modulated by autocrine signaling from factors produced within the aggregate. For example, multiple studies have found that FC and HD MSC aggregates produce detectable levels of cytokines commonly used to license MSC immunomodulatory function (IFN-γ, TNF-α, IL-1α, IL-1β), and chemical inhibition of endogenous IL-1 and TNF-α signaling in MSC aggregates was shown to abrogate production of PGE2 and other immune mediators[26,33]. Our own preliminary work indicates that production of endogenous IFN-γ and TNF-α depends on aggregation method (not shown); thus, future approaches to engineer the aggregate microenvironment may consider manipulating endogenous cytokine signaling as a means to control MSC phenotype following *in vivo* delivery. Overall, 3D culture geometries appear to enhance specific MSC paracrine responses to inflammation, which could be an attractive feature for therapeutic applications.

Although our results established a correlation between MSC aggregation kinetics and distinct temporal profiles of paracrine factor production, our initial characterizations of MSC immunomodulatory phenotype were conducted using ~400 μm diameter aggregates across SA, HD, and FC methods (Fig. 6.1D), which restricted our observations to a narrow experimental space. Thus, we next sought to explore whether differences in aggregation kinetics and aggregate size ultimately affected MSCs' capacity to regulate immune cell phenotype. Specifically, we used a Design of Experiments (DOE) approach (Fig. 6.4C) that would enable us to identify not only main effects of each parameter on a multivariate output but also interacting effects between parameters. To avoid potential confounding effects specific to particular aggregation methods, we varied both parameters in SA aggregates, for which we could control aggregation kinetics by varying cycRGDfC density (0.1%, 1%, 10%; Fig. 6.1B) and aggregate size by patterning different labile substrate geometries (1.2 mm, 2.4 mm, 5.0 mm circles; Fig. 6.1C).

We chose to focus on MSC effects on T cells and macrophages, based on the key roles and complex cross-talk between these cell types in resolving inflammation and determining clinical outcomes of injury and disease[78–80]. Specifically, we quantified MSC aggregates' performance in T cell suppression and M2 macrophage polarization assays (Fig. 6.4A-B) to build the DOE model. The model identified significant individual effects of aggregation kinetics and aggregate size on MSC function, where slower aggregation kinetics and larger aggregates correlated with improved immune cell suppression/polarization (Fig. 6.5, Supplementary Fig. S6.10). These effects were recapitulated in preliminary studies with MSCs from two additional donors, as large SA aggregates with slow aggregation kinetics were more effective at suppressing T cells and polarizing macrophages toward M2 phenotypes, compared to small SA aggregates that aggregated quickly (Fig. 6.6). Similarly, large FC aggregates outperformed small

FC aggregates, and although we could not tune aggregation kinetics via this method, FC aggregates displayed inferior immunomodulatory function compared to their SA counterparts overall (Fig. 6.6). Taken together, the data from two additional donors and across two different aggregation methods corroborated the model prediction that MSC immunomodulatory function can be enhanced by increasing aggregate size and decreasing the rate of aggregation.

The effect of aggregation kinetics identified by the DOE model was somewhat surprising based on our initial findings that *IDO1* and PGE2 production – implicated heavily in T cell suppression and M2 macrophage polarization, respectively – were either unchanged or significantly lower in SA aggregates compared to FC aggregates (Fig. 6.3D, Supplementary Fig. 6.3). However, it is likely that the overall effect of MSCs on immune cell function is not fully represented by the limited subset of paracrine mediators that we assessed. In addition, the initial characterization studies were conducted using different aggregation parameters (5% cycRGDfC, 2.4 mm SA aggregates) than the DOE-selected conditions and represented measurements that were normalized to cell number. As we only controlled for input MSC number in the DOE studies, it is feasible that the identified effects are due to differences in MSC proliferation or viability/apoptosis between aggregate conditions that performed well vs. poorly. The latter possibility is supported by reports showing increased apoptosis and elevated caspase 3/7 signaling in larger (60,000- to 100,000-cell) aggregates compared to smaller (10,000-cell) aggregates[24,34]. As some of the same pathways proposed to contribute to the paracrine immunomodulatory phenotype of MSCs have been linked to caspase signaling and NFκB, a stress response pathway[33,81–83], activation of these pathways may transiently promote MSCs' functional effects but could also compromise cell viability and function long-term. These

possibilities, as well as the potential role of differences in structure and cytoarchitecture of optimal versus sub-optimal MSC aggregates, should be tested in future experiments.

6.6 CONCLUSIONS

In the current study, we characterized MSC aggregates generated via three distinct methods, specifically assessing their typical aggregation kinetics, structure, and trophic and immunomodulatory phenotype. From this analysis, we identified general enhancements to MSC immunomodulatory phenotype resulting from 3D aggregation as well as a potential link between aggregation kinetics, resulting aggregate structure and cell density-associated mechanotransduction pathways. Exploiting an engineered platform capable of controlling aggregate size and aggregation kinetics, we discovered significant effects of both variables on MSC immunomodulatory function and manipulated these variables to generate large, slow-assembling MSC aggregates with enhanced capacity to suppress T cell proliferation and polarize macrophages toward an anti-inflammatory phenotype. Together, these findings underscore the utility of engineering approaches to control the formation of cell aggregates, and establish aggregation kinetics as a culture parameter that may be manipulated to instruct the structure, phenotype and therapeutic function of 3D MSC aggregates.

6.7 MATERIALS AND METHODS

6.7.1 Cell culture:

MSCs: Human mesenchymal stromal cells (hMSCs) were purchased from Lonza and maintained in adherent culture in MSC growth medium (alphaMEM supplemented with 10% fetal bovine

serum (FBS; Gibco) and 1x penicillin/streptomycin (Hyclone)). hMSCs were passaged at 70% confluence and used for all experiments between passages 4 and 7.

Macrophages: THP-1 monocytes (ATCC® TIB-202™) were thawed and maintained in upright T75 flasks in RPMI1640 supplemented with 10% heat-inactivated FBS and pen/strep. Cells were propagated by centrifugation and resuspension in fresh media every three days, maintained at a density of 10^5-10^6 cells/mL, and used for experiments between passages 6 and 20. A macrophage differentiation protocol was adapted from previously published work[84,85]. Briefly, THP-1 cells were seeded into 24-well plates at a density of 1.5 x 10^5 cells/well and differentiated into macrophages with 500 nM phorbol myristate acetate (PMA) for 72 hr followed by a 24 hr resting period in serum-free RPMI. Macrophages were then polarized toward an M1-like phenotype by treating with THP-1 growth medium containing 20 ng/mL IFN-γ for an additional 24 hr. Following an additional 24 hr rest period in serum-free RPMI, macrophages were treated with MSC-conditioned media (MSC-CM) or control media for 36 hr prior to collecting macrophage-conditioned media (Mφ-CM). Control media treatments included PBMC media alone or containing 2 ng/mL PGE2 (Cayman Chemical, 14010).

PBMCs: Human peripheral blood mononuclear cells were purchased frozen (ZenBio) or isolated fresh by density gradient centrifugation from whole blood (Interstate Blood Bank) using SepMate™-50 (IVD) tubes with Lymphoprep™ (STEMCELL Technologies) following manufacturer's instructions. PBMCs were thawed and maintained in PBMC medium (RPMI1640 supplemented with 10% heat-inactivated FBS, pen/strep, non-essential amino acids (Hyclone), and sodium pyruvate (Gibco)), and used within 96 hours following thaw.

6.7.2 Generation of self-assembled (SA) MSC aggregates: Patterned SAM arrays were fabricated following previously published methods[39]. For single-cell seeding of MSCs onto labile and non-labile substrates, cells were washed with PBS and incubated with 0.05% trypsin/EDTA at 37°C for 5 minutes to singularize cells. Following singularization, trypsin was quenched with an equal volume of FBS-containing medium and cells pelleted by centrifugation at 200g for 5 minutes. Cell pellets were resuspended in MSC growth medium before seeding at desired densities. After 1 hr incubation in a humidified incubator at 37°C and 5% CO_2 to allow cell adhesion, seeded SAM arrays were immersed in basal medium to remove non-specifically adhered cells. SAM arrays were then placed into new wells containing MSC growth medium and maintained in this medium unless otherwise indicated. High seeding densities were used to ensure confluence shortly after seeding. Unless otherwise stated, MSCs were seeded onto SAMs at a density of 9×10^4 cells/cm^2.

As the formation of compact and morphologically defined SA aggregates from 5% cycRGDfC substrates occurred within 72 hours after seeding, we denoted this time point "day 0". This nomenclature is used throughout to describe 2D and 3D MSCs at 72 hours post-seed. Unless otherwise stated, "SA MSC aggregates" referred to throughout Figures 6.1-6.3 were generated from 5% cycRGDfC substrates.

6.7.3 Generation of Hanging Drop (HD) and Forced Centrifugation (FC) aggregates:

HD: MSCs were trypsinized as described above and resuspended at desired densities in MSC growth medium. Aggregates were formed using the hanging drop technique[86] with 20,000 cells per 25 μL droplet (size-matched to 2.4 mm SA aggregates) unless otherwise stated.

FC: Agarose microwells were fabricated based on previously published methods[39]. Aggrewell800 inserts or bicycle retro-reflector (Grote 4005/4006) (machined into 35 mm diameter discs) were used as templates for casting hydrophilic silicone (1:1 mixture of Hydrosil A and B, Siladent). Silicone was cured at 40 psi for 180 min to create a reverse mold sized to fit a standard 24-well plate format. Molds were autoclaved prior to each usage. 1.5% agarose in deionized water was sterilized by autoclaving and heated until molten prior to dispensing into silicone reverse molds. Individual agarose molds containing microwells were allowed to solidify at room temperature, transferred to 24-well plates using a sterile spatula, submerged in MSC growth media, and spun down at 2,000g for 1 min to remove air trapped underneath the molds. MSCs were trypsinized as described above and seeded into agarose molds for a final seeding density of 25,000 cells per aggregate (size-matched to 2.4 mm SA aggregates) unless stated otherwise. Plates were centrifuged at 300g for 5 min and incubated at 37°C, 5% CO_2. Aggregates were collected by gently pipetting at the mold surface with a wide orifice pipette tip to dislodge aggregates and transfer them to collection tubes and/or assay plates.

6.7.4 Quantification of aggregation kinetics and aggregate size distribution: All timelapse images were acquired using a Nikon Ti Eclipse inverted microscope (10X PhL objective) equipped with a TIZ Tokai Hit incubated stage that was humidified and maintained at 37°C and 5% CO_2. Image analysis was performed using NIS Elements as previously described[39].

6.7.5 Maintenance of MSCs for gene expression and immune cell assays: 2D MSCs were maintained in tissue culture-treated polystyrene plates, while 3D MSC aggregates were maintained in ultra-low adhesion plates (Corning) in MSC growth medium unless otherwise

specified. For routine feeding or IFN-γ stimulation of 3D cultures, wide-bore pipette tips or serological pipettes were used to transfer aggregates to sterile Eppendorf tubes, and spent media were replaced with fresh growth or stimulation media. IFN-γ stimulation of MSCs was performed for 24 hrs in alphaMEM containing 0.5% FBS and 20 ng/mL human IFN-γ (R&D Systems, 285-IF-100). For MSC-CM experiments, treatment media were removed and replaced with PBMC media for conditioning for 24 hr. All conditioned media were clarified by centrifugation at 12,000g for 10 min at 4°C. For media conditioning and PBMC co-culture experiments, total MSC number was matched across all SA aggregates conditions based on scaling by the pattern area of labile substrates (e.g., 200 aggregates from 1.2 mm diameter pattern ≈ 50 aggregates from 2.4 mm diameter pattern). In comparisons between SA and FC aggregates, total MSC number was matched based on quantification of DNA per SA aggregate that was converted to cell number per aggregate using a MSC DNA standard curve (see 6.7.10); total cell number in FC conditions was then adjusted to match based on the cell number per aggregate and number of aggregates used in each assay.

6.7.6 Trilineage differentiation: 2D MSCs (7.5×10^3 cells/cm^2) or 3D MSC aggregates formed by SA (2.4 mm diameter circular patterns), HD or FC (20,000 cells/aggregates) were plated on Collagen I-coated plates (Corning) in MSC growth medium. At 72 hours after plating, growth medium was exchanged with differentiation media. Media were changed every 3-4 days, and cells were fixed in 10% neutral buffered formalin for analysis after 21 days of differentiation. As negative controls, cells were grown for 21 days in MSC growth medium.

Adipogenic medium: High-glucose Dulbecco's Modified Eagle's Medium (DMEM) supplemented with 10% FBS, 1 µM dexamethasone, 1 µg/mL insulin, 500 µM

isobutylmethylxanthine, and pen/strep. *Chondrogenic medium:* High-glucose Dulbecco's Modified Eagle's Medium (DMEM) supplemented with 10% FBS, ITS Premix, 0.9 mM sodium pyruvate, 50 µg/mL L-ascorbic acid 2-phosphate, 40 µg/mL L-proline, 0.1 µM dexamethasone, and 10 ng/mL transforming growth factor-β1, and pen/strep. *Osteogenic medium:* alphaMEM supplemented with 10% FBS, 0.1 µM dexamethasone, 10 mM β-glycerophosphate, 50 µM L-ascorbic acid 2-phosphate, and pen/strep.

6.7.7 Histology of MSC aggregates: MSC aggregates were fixed in 10% neutral buffered formalin for 1-2 hr at room temperature, washed with PBS, and incubated in 10% sucrose solution overnight at 4°C before embedding in either Histogel for processing into paraffin blocks or O.C.T. compound at -80°C for cryosectioning.

Frozen samples were sectioned into 5-7 µm slices on SuperFrost slides using a Leica CM1900 cryostat. Slides were equilibrated to room temperature for 15 min, fixed/permeabilized in ice-cold acetone for 10 min, and washed 3x with PBS before blocking with 10% BSA for 1 hr at RT. For quantification of cell density in aggregates, slides were stained with DAPI and washed twice with PBS before mounting in ProLong Gold Antifade Reagent. Stained and mounted slides were allowed to set overnight and sealed with clear nail polish before imaging on a Nikon Ti Eclipse microscope. DAPI-positive nuclei were counted in ImageJ (Cell Counter plug-in) and cell counts for each individual aggregate were normalized to cross-sectional area of the aggregate. Counts were analyzed from histological sections of $n = 10$ distinct aggregates per condition, from two independent experimental replicates.

Paraffin-embedded aggregates were sectioned at a thickness of 5 µm, deparaffinized in xylene, and stained with hematoxylin and eosin.

6.7.8 Quantitative RT-PCR: For quantitative PCR (qPCR) analyses, 2D MSCs or aggregates were washed with PBS and total RNA was isolated using the RNeasy mini kit (Qiagen) according to manufacturer's instructions. RNA was reverse transcribed into cDNA using the QuantiTect Reverse Transcription Kit or RT^2 First Strand Synthesis Kit (Qiagen). For 384-well format RT^2 MSC Profiler Array, cDNA samples (1.84 ng input RNA/10 μL reaction) were mixed with RT^2 Master Mix, loaded onto RT^2 PCR Arrays (Qiagen, Supplementary Table S6.1), and run on a Roche LightCycler 4800 system according to the manufacturer's protocol. Results were analyzed using Qiagen's GeneGlobe Data Analysis Center. For individual primer assays, cDNA was mixed with Qiagen SYBR Green Master Mix and QuantiTect primers (Qiagen) prior to loading and running plates according to the manufacturer's protocol. *TBP* (Qiagen, QT00000721) was used as a reference gene.

6.7.9 ELISAs: ELISAs for measuring PGE2 (R&D Systems, KGE004B), IL-10 (R&D Systems, DY217B-05), and TNF-α (R&D Systems, DY210-05) were performed following the manufacturer's recommended protocols.

6.7.10 Quantification of DNA content in MSC aggregates: Day 0 MSC aggregates were collected, washed with PBS, and a known number of aggregates was dispensed per replicate sample tube. Excess PBS was removed from aggregates prior to resuspension in papain buffer. Cell standards containing known numbers of singularized MSCs were also resuspended papain buffer, and samples and standards were incubated at 65°C for 18-24 hrs to dissociate aggregates. DNA content of papain-dissociated samples was then quantified by Quant-iT PicoGreen dsDNA

Assay Kit (Thermo Fisher Scientific) following manufacturer's instructions, and the average cell number per aggregate was calculated using the cell standard. Composition of papain buffer: 100 mM sodium acetate, 10 mM Na_2EDTA, 5 mM cysteine hydrochloride, 40 µg/mL papain (from papaya latex), dissolved in 0.2 M sodium phosphate buffer at pH 6.4.

6.7.11 T-cell proliferation assay: Unless otherwise stated, T-cell proliferation assays were carried out in 24-well tissue culture plates (2D adherent MSCs) or ultra-low adhesion plates (3D suspension MSC aggregates) with a total media volume of 550 µL PBMC media per well, following protocols adapted from previously published work[87,88]. MSCs, PBMCs, and anti-CD2/CD3/CD28 antibody-functionalized beads (MSC Suppression Inspector; Miltenyi Biotec) were all prepared in PBMC culture media as described above. Indirect MSC and PBMC co-cultures were performed in a Transwell setup (1.0 µm pore size), where PBMCs were cultivated in the top chamber for 96 hrs in the presence of anti-CD2/CD3/CD28 activating beads, separated from MSCs in the bottom chamber.

6.7.12 Flow cytometry: Unless otherwise stated, flow cytometry preparations were carried out in 96-well V-bottom polypropylene plates. Briefly, PBMCs were collected, centrifuged at 300g/5 min, washed with PBS to remove traces of serum, and incubated in suspension with Ghost Dye™ Red 780 viability dye (2 µL dye per mL PBS; Tonbo Biosciences) for 30 min on ice. Samples were centrifuged to pellet, decanted, and incubated with Human TruStain FcX™ (BioLegend; 5 µL/100 µL cell suspension in FACS Buffer) for 10 minutes at room temperature to block FcR-mediated antibody binding. After centrifugation and decanting, cells were stained for CD3 for 30 min at room temperature, fixed with 1% paraformaldehyde for 20 min at room

temperature, permeabilized with ice-cold 90% methanol for 15 min at 4°C, and stored at -20°C until ready for intracellular staining for Ki67. Samples were washed twice with Flow Buffer 1 (PBS containing 0.5% BSA) to remove residual methanol and incubated for 1 hr at room temperature with primary antibody in Flow Buffer 2 (PBS containing 0.5% BSA and 0.1% Triton X-100). Samples were washed with Flow Buffer 2, resuspended in Flow Buffer 1, and stored on ice prior to data collection. Data were collected on a MACSQUANT flow cytometer (Miltenyi Biotec) and analyzed using FlowJo software.

Primary antibodies and dilutions used: AlexaFluor488 mouse IgG1 anti-human Ki67 primary conjugate, Clone B56 (BD Biosciences; 1:80), APC mouse IgG2a anti-human CD3 primary conjugate, Clone HIT3a (BD Biosciences; 1:10).

Compositions of buffers: FACS Buffer - 2% FBS in PBS. Flow Buffer 1 - PBS containing 0.5% BSA. Flow Buffer 2 - PBS containing 0.5% BSA and 0.1% Triton X-100.

6.7.13 Western blotting: Day 0 MSC aggregates were collected, washed with PBS, and resuspended in ice-cold RIPA buffer containing 1X Halt Protease/Phosphatase Inhibitor Cocktail. Aggregates were homogenized in buffer using a polypropylene pestle (Bel-Art), followed by agitation of samples for 15 min at 4°C and centrifugation at 12,000g for 15 min at 4°C. The supernatants from samples were collected and stored at -20°C until use. Total protein was quantified by microBCA assay. Equal amounts of protein per sample were combined with Laemmli buffer containing beta-mercaptoethanol, denatured for 5 min at 100°C, loaded in 10% polyacrylamide gels and separated by SDS-PAGE. Proteins were transferred to PVDF membranes and incubated in blocking buffer (5% nonfat dry milk in TBST for 1 hr at room temp). Membranes were incubated in rabbit anti-human phosphoYAP Ser127 primary antibody

(Cell Signaling Technology, 4911S, 1:1000) in Antibody Diluent (Thermo Fisher, 00-3118) overnight at 4°C, washed with TBST, and incubated in HRP-conjugated goat anti-rabbit IgG secondary antibodies in blocking buffer (Abcam, 1:10,000) for 1 hr at RT. Membranes were washed with TBST and incubated with ECL Western Blotting substrate (Pierce) for 1 min. Chemiluminescence was detected using a LAS4000 Mini imager and analyzed by densitometry using ImageJ's gel plug-in. β-actin was used as a load control.

6.7.14 DOE design and modeling: JMP software (SAS) was used to create a full-factorial DOE design encompassing two factors (aggregate size and %cycRGD) at three levels. The DOE was carried out in triplicate and quadruplicate for T cell and macrophage assays, respectively. Based on the considerable variability in Mφ IL-10 and TNF-α secretion that we observed between experimental replicates, normalized "scores" for immune cell assays were used as the response variables in the DOE analysis. Within a given experiment, scores from 0 to 1 were assigned to each experimental condition, corresponding to its performance in each immune cell assay. The lowest and highest conditions within each assay were assigned scores of 0 and 1, respectively, and the scores of the remaining conditions were calculated based on their distribution within this range. The DOE model was generated with least squares fitting of linear dependences for aggregate size and %cycRGD and included a first-order interaction term (aggregate size*%cycRGD). The Factor Profiler in JMP was used to maximize desirability, which was defined as minimization of T cell proliferation (%Ki67+ CD3+ PBMCs) and maximization of macrophage polarization toward an M2-like phenotype (maximize IL-10, minimize TNF-α secretion; equally weighted).

6.7.15 Figure generation and statistics: All schematics and graphics were created using Adobe Illustrator and Microsoft PowerPoint. The DOE graphs, models, and statistics were generated in JMP. Graphs were generated in GraphPad Prism or Microsoft Excel and statistical analyses were performed using GraphPad Prism. The degree of significance for each comparison is denoted in each figure/caption.

6.8 ACKNOWLEDGMENTS

The authors thank Sierra Raglin (UW Dept of Surgery Histology Core) for assistance with preparation of histological samples and acknowledge support from staff and the use of equipment at the UW Carbone Cancer Center Flow Cytometry Laboratory (Support Grant P30 CA014520) at UW-Madison. Chondrogenic induction media and MSCs (Donor 2) were kindly provided by Dr. Wan-Ju Li and his laboratory (UW-Madison, Department of Biomedical Engineering). This work was supported by funding from the National Institutes of Health (R01HL093282 to W.L.M.; Biotechnology Training Program NIGMS 5 T32-GM08349 to A.W.X.), the U.S. Environmental Protection Agency (STAR grant no. 83573701 to W.L.M.), and the National Science Foundation (DGE-1256259 to A.W.X.; DMR-1306482 to W.L.M.).

6.9 REFERENCES

1. Kim, N. & Cho, S.-G. Clinical applications of mesenchymal stem cells. *Korean J. Intern. Med.* **28,** 387–402 (2013).

2. Squillaro, T., Peluso, G. & Galderisi, U. Clinical Trials With Mesenchymal Stem Cells: An Update. *Cell Transplant.* **25,** 829–48 (2016).

3. Klyushnenkova, E. *et al.* T cell responses to allogeneic human mesenchymal stem cells: Immunogenicity, tolerance, and suppression. *J. Biomed. Sci.* **12,** 47–57 (2005).

4. Aggarwal, S. Human mesenchymal stem cells modulate allogeneic immune cell responses. *Blood* **105,** 1815–1822 (2005).

5. English, K. Mechanisms of mesenchymal stromal cell immunomodulation. *Immunol. Cell Biol.* **91,** 19–26 (2013).

6. Shi, M., Liu, Z.-W. & Wang, F.-S. Immunomodulatory properties and therapeutic application of mesenchymal stem cells. *Clin. Exp. Immunol.* **164,** 1–8 (2011).

7. Bernardo, M. E. & Fibbe, W. E. Mesenchymal stromal cells: Sensors and switchers of inflammation. *Cell Stem Cell* **13,** 392–402 (2013).

8. Zheng, G., Ge, M., Qiu, G., Shu, Q. & Xu, J. Mesenchymal Stromal Cells Affect Disease Outcomes via Macrophage Polarization. *Stem Cells Int.* **2015,** 1–11 (2015).

9. Qi, K., Li, N., Zhang, Z. & Melino, G. Tissue regeneration: The crosstalk between mesenchymal stem cells and immune response. *Cell. Immunol.* **326,** 86–93 (2018).

10. Uccelli, A. & de Rosbo, N. K. The immunomodulatory function of mesenchymal stem cells: Mode of action and pathways. *Ann. N. Y. Acad. Sci.* **1351,** 114–126 (2015).

11. Madrigal, M., Rao, K. S. & Riordan, N. H. A review of therapeutic effects of mesenchymal stem cell secretions and induction of secretory modification by different culture methods. *J. Transl. Med.* **12,** 260 (2014).

12. Spaggiari, G. M. *et al.* Mesenchymal stem cells inhibit natural killer-cell proliferation, cytotoxicity, and cytokine production: role of indoleamine 2,3-dioxygenase and prostaglandin E2. *Blood* **111,** 1327–1333 (2007).

13. Vasandan, A. B. *et al.* Human Mesenchymal stem cells program macrophage plasticity by altering their metabolic status via a PGE2-dependent mechanism. *Sci. Rep.* **6,** 38308 (2016).

14. Najar, M. *et al.* Mesenchymal stromal cells use PGE2 to modulate activation and proliferation of lymphocyte subsets: Combined comparison of adipose tissue, Wharton's Jelly and bone marrow sources. *Cell. Immunol.* **264,** 171–179 (2010).

15. Prockop, D. J. Concise review: two negative feedback loops place mesenchymal stem/stromal cells at the center of early regulators of inflammation. *Stem Cells* **31,** 2042–6 (2013).

16. Meisel, R. *et al.* Human bone marrow stromal cells inhibit allogeneic T-cell responses by

indoleamine 2,3-dioxygenase-mediated tryptophan degradation. *Blood* **103,** 4619–4621 (2004).

17. Galipeau, J. & Sensébé, L. Mesenchymal Stromal Cells: Clinical Challenges and Therapeutic Opportunities. *Cell Stem Cell* **22,** 824–833 (2018).

18. Carmen, J., Brindley, D. A., Davie, N. L. & Smith, D. in *Stem Cells in Regenerative Medicine* 49–68 (John Wiley & Sons, Ltd, 2016). doi:10.1002/9781118846193.ch4

19. Valencic, E., Piscianz, E., Andolina, M., Ventura, A. & Tommasini, A. The immunosuppressive effect of Wharton's jelly stromal cells depends on the timing of their licensing and on lymphocyte activation. *Cytotherapy* **12,** 154–160 (2010).

20. Prasanna, S. J., Gopalakrishnan, D., Shankar, S. R. & Vasandan, A. B. Pro-inflammatory cytokines, IFNγ and TNFα, influence immune properties of human bone marrow and Wharton jelly mesenchymal stem cells differentially. *PLoS One* **5,** (2010).

21. Salem, B. *et al.* Quantitative activation suppression assay to evaluate human bone marrow-derived mesenchymal stromal cell potency. *Cytotherapy* **17,** 1675–1686 (2015).

22. Klinker, M. W., Marklein, R. A., Lo Surdo, J. L., Wei, C.-H. & Bauer, S. R. Morphological features of IFN-γ–stimulated mesenchymal stromal cells predict overall immunosuppressive capacity. *Proc. Natl. Acad. Sci.* **114,** E2598–E2607 (2017).

23. Polchert, D. *et al.* IFN-γ activation of mesenchymal stem cells for treatment and prevention of graft versus host disease. *Eur. J. Immunol.* **38,** 1745–1755 (2008).

24. Bartosh, T. J. *et al.* Aggregation of human mesenchymal stromal cells (MSCs) into 3D spheroids enhances their antiin fl ammatory properties. *Proc. Natl. Acad. Sci. U. S. A.* **107,** 13724–13729 (2010).

25. Ylostalo, J. H., Bartosh, T. J., Tiblow, A. & Prockop, D. J. Unique characteristics of human mesenchymal stromal/progenitor cells pre-activated in 3-dimensional cultures under different conditions. *Cytotherapy* **16,** 1486–1500 (2014).

26. Murphy, K. C. *et al.* Multifactorial Experimental Design to Optimize the Anti-Inflammatory and Proangiogenic Potential of Mesenchymal Stem Cell Spheroids. *Stem Cells* **35,** 1493–1504 (2017).

27. Cheng, N. C., Wang, S. & Young, T. H. The influence of spheroid formation of human adipose-derived stem cells on chitosan films on stemness and differentiation capabilities. *Biomaterials* **33,** 1748–1758 (2012).

28. Ho, S. S., Murphy, K. C., Binder, B. Y. K., Vissers, C. B. & Leach, J. K. Increased Survival and Function of Mesenchymal Stem Cell Spheroids Entrapped in Instructive Alginate Hydrogels. *Stem Cells Transl. Med.* (2016). doi:10.5966/sctm.2015-0211

29. Kim, J. & Ma, T. Endogenous extracellular matrices enhance human mesenchymal stem cell aggregate formation and survival. *Biotechnol. Prog.* **29,** 441–451 (2013).

30. Xu, Y., Shi, T., Xu, A. & Zhang, L. 3D spheroid culture enhances survival and therapeutic capacities of MSCs injected into ischemic kidney. *J. Cell. Mol. Med.* **20,** 1203–1213

(2016).

31. Ylostalo, J. H., Bazhanov, N., Mohammadipoor, A. & Bartosh, T. J. Production and Administration of Therapeutic Mesenchymal Stem/Stromal Cell (MSC) Spheroids Primed in 3-D Cultures Under Xeno-free Conditions. *J. Vis. Exp.* 1–13 (2017). doi:10.3791/55126

32. Sart, S., Tsai, A.-C., Li, Y. & Ma, T. Three-dimensional aggregates of mesenchymal stem cells: cellular mechanisms, biological properties, and applications. *Tissue Eng. Part B, Rev.* **20,** 365–80 (2014).

33. Bartosh, T. J., Ylöstalo, J. H., Bazhanov, N., Kuhlman, J. & Prockop, D. J. Dynamic compaction of human mesenchymal stem/precursor cells into spheres self-activates caspase-dependent il1 signaling to enhance secretion of modulators of inflammation and immunity (PGE2, TSG6, and STC1). *Stem Cells* **31,** 2443–2456 (2013).

34. Murphy, K. C. *et al.* Measurement of oxygen tension within mesenchymal stem cell spheroids. *J. R. Soc. Interface* **14,** 20160851 (2017).

35. Costa, M. H. G., McDevitt, T. C., Cabral, J. M. S., da Silva, C. L. & Ferreira, F. C. Tridimensional configurations of human mesenchymal stem/stromal cells to enhance cell paracrine potential towards wound healing processes. *J. Biotechnol.* **262,** 28–39 (2017).

36. Zimmermann, J. A., Hettiaratchi, M. H. & McDevitt, T. C. Enhanced Immunosuppression of T Cells by Sustained Presentation of Bioactive Interferon-γ Within Three-Dimensional Mesenchymal Stem Cell Constructs. *Stem Cells Transl. Med.* **6,** 223–237 (2017).

37. Sargent, C. Y. *et al.* Hydrodynamic modulation of embryonic stem cell differentiation by rotary orbital suspension culture. *Biotechnol. Bioeng.* **105,** 611–626 (2010).

38. Raghavan, S. *et al.* Comparative analysis of tumor spheroid generation techniques for differential *in vitro* drug toxicity. *Oncotarget* **7,** (2016).

39. Xie, A. W. *et al.* Controlled Self-assembly of Stem Cell Aggregates Instructs Pluripotency and Lineage Bias. *Sci. Rep.* **7,** 1–15 (2017).

40. Crop, M. J. *et al.* Inflammatory conditions affect gene expression and function of human adipose tissue-derived mesenchymal stem cells. *Clin. Exp. Immunol.* **162,** 474–486 (2010).

41. Pourgholaminejad, A., Aghdami, N., Baharvand, H. & Moazzeni, S. M. The effect of pro-inflammatory cytokines on immunophenotype, differentiation capacity and immunomodulatory functions of human mesenchymal stem cells. *Cytokine* **85,** 51–60 (2016).

42. Krampera, M. Mesenchymal stromal cell 'licensing': a multistep process. *Leukemia* **25,** 1408–1414 (2011).

43. Bartosh, T. J., Ylöstalo, J. H., Bazhanov, N., Kuhlman, J. & Prockop, D. J. Dynamic compaction of human mesenchymal stem/precursor cells into spheres self-activates caspase-dependent IL1 signaling to enhance secretion of modulators of inflammation and immunity (PGE2, TSG6, and STC1). *Stem Cells* **31,** 2443–56 (2013).

44. Ylostalo, J. H., Bartosh, T. J., Tiblow, A. & Prockop, D. J. Unique characteristics of human mesenchymal stromal/progenitor cells pre-activated in 3-dimensional cultures under different conditions. *Cytotherapy* **16,** 1486–1500 (2014).

45. Ng, E. S., Davis, R. P., Azzola, L., Stanley, E. G. & Elefanty, A. G. Forced aggregation of defined numbers of human embryonic stem cells into embryoid bodies fosters robust, reproducible hematopoietic differentiation. *Blood* **106,** 1601–3 (2005).

46. Mohr, J. C. *et al.* The microwell control of embryoid body size in order to regulate cardiac differentiation of human embryonic stem cells. *Biomaterials* **31,** 1885–1893 (2010).

47. Park, J. *et al.* Microfabrication-based modulation of embryonic stem cell differentiation. *Lab Chip* **7,** 1018–28 (2007).

48. Choi, Y. Y. *et al.* Controlled-size embryoid body formation in concave microwell arrays. *Biomaterials* **31,** 4296–303 (2010).

49. Xie, L., Mao, M., Zhou, L., Zhang, L. & Jiang, B. Signal Factors Secreted by 2D and Spheroid Mesenchymal Stem Cells and by Cocultures of Mesenchymal Stem Cells Derived Microvesicles and Retinal Photoreceptor Neurons. *Stem Cells Int.* **2017,** 1–13 (2017).

50. Kinney, M. A., Sargent, C. Y. & McDevitt, T. C. Temporal modulation of β-catenin signaling by multicellular aggregation kinetics impacts embryonic stem cell cardiomyogenesis. *Stem Cells Dev.* **22,** 2665–77 (2013).

51. Dupont, S. *et al.* Role of YAP/TAZ in mechanotransduction. *Nature* **474,** 179–183 (2011).

52. Musah, S. *et al.* Substratum-induced differentiation of human pluripotent stem cells reveals the coactivator YAP is a potent regulator of neuronal specification. *Proc. Natl. Acad. Sci. U. S. A.* **111,** 13805–10 (2014).

53. Yang, C., Tibbitt, M. W., Basta, L. & Anseth, K. S. Mechanical memory and dosing influence stem cell fate. *Nat. Mater.* **13,** 645–52 (2014).

54. Hsiao, C. *et al.* Human pluripotent stem cell culture density modulates YAP signaling. *Biotechnol. J.* 662–675 (2016). doi:10.1002/biot.201500374

55. Low, B. C. *et al.* YAP/TAZ as mechanosensors and mechanotransducers in regulating organ size and tumor growth. *FEBS Lett.* **588,** 2663–2670 (2014).

56. Liu, F. *et al.* Mechanosignaling through YAP and TAZ drives fibroblast activation and fibrosis. *Am. J. Physiol. - Lung Cell. Mol. Physiol.* **308,** L344–L357 (2015).

57. Karystinou, A. *et al.* Yes-associated protein (YAP) is a negative regulator of chondrogenesis in mesenchymal stem cells. *Arthritis Res. Ther.* **17,** (2015).

58. Caliari, S. R., Vega, S. L., Kwon, M., Soulas, E. M. & Burdick, J. A. Dimensionality and spreading influence MSC YAP/TAZ signaling in hydrogel environments. *Biomaterials* **103,** 314–323 (2016).

59. Komatsu, N. *et al.* Type I collagen deposition via osteoinduction ameliorates YAP / TAZ activity in 3D floating culture clumps of mesenchymal stem cell / extracellular matrix

complexes. *Stem Cell Res. Ther.* **9,** 1–15 (2018).

60. Zhong, W. *et al.* Mesenchymal Stem Cell and Chondrocyte Fates in a Multishear Microdevice Are Regulated by Yes-Associated Protein. *Stem Cells Dev.* **22,** 2083–2093 (2013).

61. Pan, D. The hippo signaling pathway in development and cancer. *Dev. Cell* **19,** 491–505 (2010).

62. Nardone, G. *et al.* YAP regulates cell mechanics by controlling focal adhesion assembly. *Nat. Commun.* **8,** (2017).

63. Galipeau, J. *et al.* International Society for Cellular Therapy prespective on immune functional assays for mesenchymal stromal cells as potency release criterion for advanced phase clinical trials. *Cytotherapy* **18,** 151–159 (2016).

64. Murphy, K. C., Fang, S. Y. & Leach, J. K. Human mesenchymal stem cell spheroids in fibrin hydrogels exhibit improved cell survival and potential for bone healing. *Cell Tissue Res.* **357,** 91–99 (2014).

65. Ho, S. S., Murphy, K. C., Binder, B. Y. K., Vissers, C. B. & Leach, J. K. Increased Survival and Function of Mesenchymal Stem Cell Spheroids Entrapped in Instructive Alginate Hydrogels. *Stem Cells Transl. Med.* **5,** 773–781 (2016).

66. YlÖstalo, J. H., Bartosh, T. J., Coble, K. & Prockop, D. J. Human Mesenchymal Stem/Stromal Cells Cultured as Spheroids are Self-activated to Produce Prostaglandin E2 that Directs Stimulated Macrophages into an Anti-inflammatory Phenotype. *Stem Cells* **30,** 2283–2296 (2012).

67. Tsai, A.-C., Liu, Y., Yuan, X. & Ma, T. Compaction, fusion, and functional activation of three-dimensional human mesenchymal stem cell aggregate. *Tissue Eng. Part A* **21,** 1705–1719 (2015).

68. Bao, P. *et al.* The Role of Vascular Endothelial Growth Factor in Wound Healing. *J. Surg. Res.* **153,** 347–358 (2009).

69. Wheeler, K. C. *et al.* VEGF may contribute to macrophage recruitment and M2 polarization in the decidua. *PLoS One* **13,** 1–18 (2018).

70. Oh, J. Y. *et al.* Anti-inflammatory protein TSG-6 reduces inflammatory damage to the cornea following chemical and mechanical injury. *Proc. Natl. Acad. Sci.* **107,** 16875–16880 (2010).

71. Choi, H., Lee, R. H., Bazhanov, N., Oh, J. Y. & Prockop, D. J. Anti-inflammatory protein TSG-6 secreted by activated MSCs attenuates zymosan-induced mouse peritonitis by decreasing TLR2/NF- B signaling in resident macrophages. *Blood* **118,** 330–338 (2011).

72. Lee, R. H. *et al.* Intravenous hMSCs Improve Myocardial Infarction in Mice because Cells Embolized in Lung Are Activated to Secrete the Anti-inflammatory Protein TSG-6. *Cell Stem Cell* **5,** 54–63 (2009).

73. Tipnis, S., Viswanathan, C. & Majumdar, A. S. Immunosuppressive properties of human

umbilical cord-derived mesenchymal stem cells: Role of B7-H1 and IDO. *Immunol. Cell Biol.* **88,** 795–806 (2010).

74. Egger, D., Tripisciano, C., Weber, V., Dominici, M. & Kasper, C. Dynamic Cultivation of Mesenchymal Stem Cell Aggregates. *Bioengineering* **5,** 48 (2018).

75. Lee, B.-C. *et al.* PGE2 maintains self-renewal of human adult stem cells via EP2-mediated autocrine signaling and its production is regulated by cell-to-cell contact. *Sci. Rep.* **6,** 26298 (2016).

76. Qazi, T. H., Mooney, D. J., Duda, G. N. & Geissler, S. Biomaterials that promote cell-cell interactions enhance the paracrine function of MSCs. *Biomaterials* **140,** 103–114 (2017).

77. Kinney, M. A., Hookway, T. A., Wang, Y. & McDevitt, T. C. Engineering three-dimensional stem cell morphogenesis for the development of tissue models and scalable regenerative therapeutics. *Ann. Biomed. Eng.* **42,** 352–367 (2014).

78. Kulkarni, O. P., Lichtnekert, J., Anders, H. J. & Mulay, S. R. The Immune System in Tissue Environments Regaining Homeostasis after Injury: Is 'Inflammation' Always Inflammation? *Mediators Inflamm.* **2016,** (2016).

79. Sugimoto, M. A., Sousa, L. P., Pinho, V., Perretti, M. & Teixeira, M. M. Resolution of inflammation: What controls its onset? *Front. Immunol.* **7,** (2016).

80. Wynn, T. A. & Vannella, K. M. Macrophages in Tissue Repair, Regeneration, and Fibrosis. *Immunity* **44,** 450–462 (2016).

81. Mercurio, F. & Manning, A. M. NF-κB as a primary regulator of the stress response. *Oncogene* **18,** 6163–6171 (1999).

82. Lawrence, T. The nuclear factor NF-kappaB pathway in inflammation. *Cold Spring Harb. Perspect. Biol.* **1,** 1–10 (2009).

83. Spees, J. L., Lee, R. H. & Gregory, C. A. Mechanisms of mesenchymal stem/stromal cell function. *Stem Cell Res. Ther.* **7,** 125 (2016).

84. Lund, M. E., To, J., O'Brien, B. A. & Donnelly, S. The choice of phorbol 12-myristate 13-acetate differentiation protocol influences the response of THP-1 macrophages to a pro-inflammatory stimulus. *J. Immunol. Methods* **430,** 64–70 (2016).

85. Genin, M., Clement, F., Fattaccioli, A., Raes, M. & Michiels, C. M1 and M2 macrophages derived from THP-1 cells differentially modulate the response of cancer cells to etoposide. *BMC Cancer* **15,** 1–14 (2015).

86. Del Duca, D., Werbowetski, T. & Del Maestro, R. F. Spheroid preparation from hanging drops: characterization of a model of brain tumor invasion. *J. Neurooncol.* **67,** 295–303 (2004).

87. Bloom, D. D. *et al.* A reproducible immunopotency assay to measure mesenchymal stromal cell-mediated T-cell suppression. *Cytotherapy* **17,** 140–151 (2015).

88. Zimmermann, J. A., Hettiaratchi, M. H. & McDevitt, T. C. Enhanced Immunosuppression of T Cells by Sustained Presentation of Bioactive Interferon-γ Within Three-Dimensional

Mesenchymal Stem Cell Constructs. *Stem Cells Transl. Med.* (2016). doi:10.5966/sctm.2016-0044

6.10 FIGURES

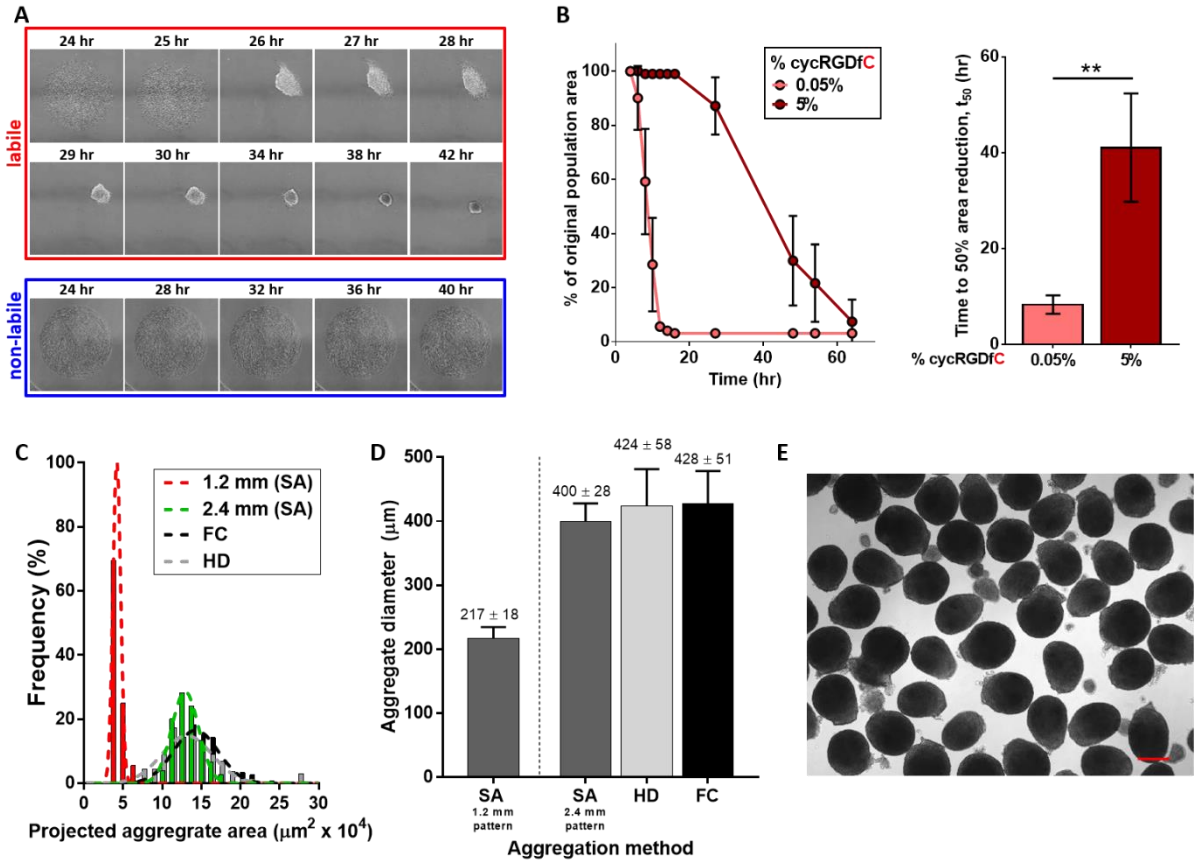

Figure 6.1 Generation of self-assembled (SA) MSC aggregates with controllable size and kinetics from labile substrates. (A) Timelapse images of MSCs on substrates presenting cyclic RGD (cycRGD) via a labile (top) or non-labile (bottom) linkage. Labile substrates promote MSC self-assembly into 3D cell aggregates, while non-labile substrates promote continued MSC culture in 2D. (B) (left) MSC aggregate self-assembly kinetics (measured as % of original population area over time) as a function of initial peptide density on labile substrates. Error bars represent 95% c.i. (right) Mean t_{50} values of self-assembly for MSC aggregates generated from labile substrates of varying cycRGDfC density. "t_{50}" refers to the time required for the cell population to reach 50% of the original population area, previously established as a metric of aggregation kinetics[39]. Error bars represent 95% c.i., $^{**}p < 0.01$. (C) Histogram of projected aggregate area for SA MSC aggregates generated from labile substrates (1.2 mm or 2.4 mm diameter circular patterns). Size distributions of HD and FC aggregates are overlaid for comparison (black and gray bars, respectively). (D) Measurement of average size for day 0 MSC aggregates generated by SA from 1.2 mm and 2.4 mm diameter circular patterns, versus size-matched HD and FC aggregates. (E) Representative brightfield image of day 0 SA MSC aggregates generated from 2.4 mm diameter circular patterns. Scale bar = 250 μm.

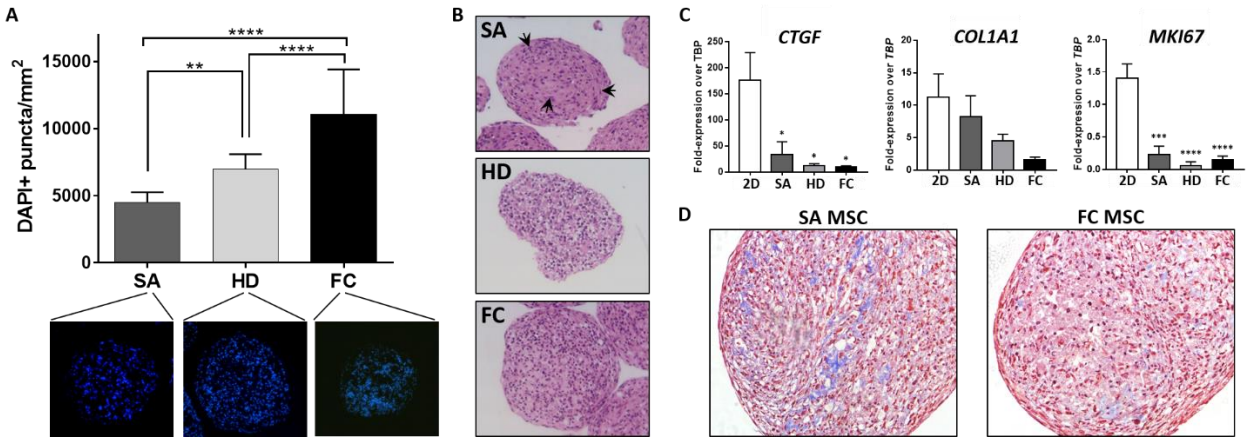

Figure 6.2 Method of cell aggregation influences initial cell density and ECM synthesis in MSC aggregates. (A) Quantification of cell density in cryosectioned day 0 MSC aggregates formed by SA, HD, or FC. Size-matched aggregates between all three methods (see Fig. 6.1D) were used for analysis. Values represent the mean ± s.d. (**$p < 0.01$, ****$p < 0.0001$, one-way ANOVA with Tukey's post-hoc test). (B) Representative H&E stains of day 0 SA, HD, and FC aggregates showing differences in aggregate structure and nuclear shape based on aggregation method. Cell nuclei within SA aggregates demonstrated elongated morphology (black arrows), whereas nuclei in HD and FC aggregates were rounded and compact. (C) Expression of ECM- and proliferation-associated genes in day 0 MSC aggregates compared to 2D MSCs. Asterisks denote a significant difference relative to 2D MSCs (*$p < 0.05$, ***$p < 0.001$, ****$p < 0.0001$; one-way ANOVA with Tukey's post-hoc test). (D) Histological sections of day 10 SA and FC MSC aggregates, stained with Masson's Trichrome, showing differences in aggregate structure and collagen deposition between aggregation methods.

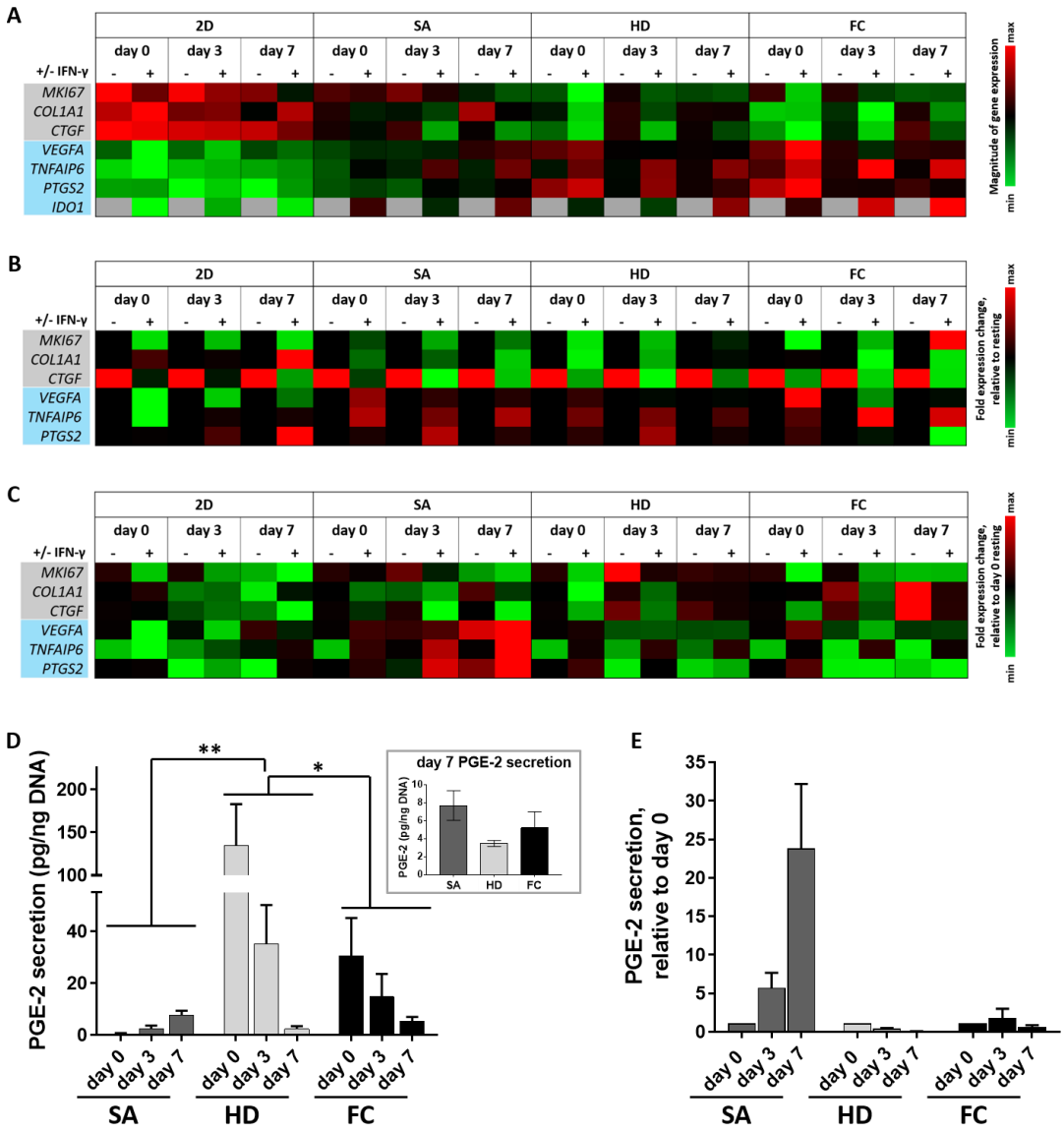

Figure 6.3 Culture format and aggregation method influences MSC immunomodulatory phenotype and temporal response to pro-inflammatory environments. Gene expression profiles for MSCs cultured in 2D monolayer (2D) or in 3D aggregates (SA, HD, or FC aggregation methods), in the presence (+) or absence (−) of IFN-γ. The assessed genes were associated with cell proliferation and ECM synthesis (gray), or pro-angiogenic and immunomodulatory paracrine factors (blue). Gene expression heatmaps are displayed as (A) Expression relative to *TBP*, (B) Fold expression relative to resting (i.e., without IFN-γ), and (C) Fold expression relative to day 0 resting conditions. (D) Time course of PGE2 production by IFN-γ-primed MSC aggregates formed via SA, HD, and FC approaches. PGE2 was measured from media conditioned for 24 hrs following IFN-γ priming. Asterisks indicate statistically significant difference between denoted aggregation methods (*$p < 0.05$, **$p < 0.01$; two-way ANOVA with Tukey's post-hoc test). (inset) Comparison of PGE2 secretion by day 7 aggregates. (E) Fold change in PGE2 production by IFN-γ-primed MSC aggregates over 7 days, relative to day 0.

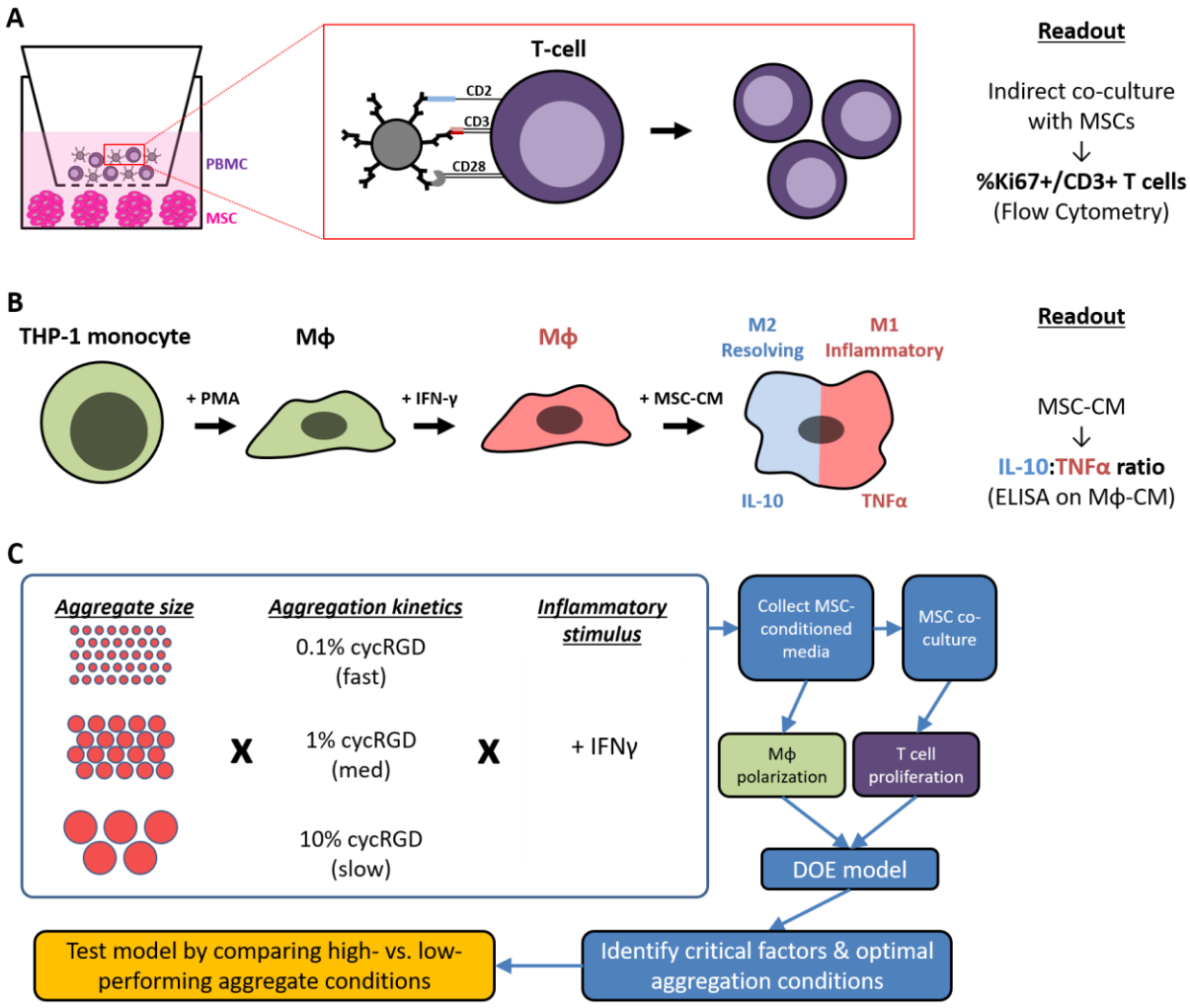

Figure 6.4 Experimental approach to assessing the role of aggregate size and aggregation kinetics on MSC immunomodulatory function. (A) Schematic representation of T cell proliferation assay. MSC aggregates are cultured on a low-adhesion surface in the bottom chamber of a Transwell setup. PBMCs are added to the top chamber, separated by a porous membrane (1.0 μm pore size), and co-cultured with MSC aggregates for 96 hrs in the presence of anti-CD2/CD3/CD28 activating beads. MSCs are cultured in the lower chamber and produce paracrine factors that suppress T cell proliferation. (B) Schematic representation of macrophage polarization. THP-1 monocytes are differentiated into macrophages (Mφ) by PMA treatment and further polarized toward M1 Mφ phenotype with IFN-γ treatment. MSC immunomodulatory function in this assay is determined by the ability of MSC-CM to polarize Mφ toward M2 (high IL-10-, low TNF-α-secreting) phenotype. "MSC-CM" = MSC-conditioned media, "Mφ-CM" = macrophage-conditioned media. (C) Schematic of Design of Experiments (DOE) approach and tested conditions. Varying SA aggregate sizes (1.2, 2.4, and 5.0 mm patterns) and aggregation kinetics (0.1%, 1%, and 10% cycRGDfC) were tested in a two-factor, three-level full factorial design in which all conditions included IFN-γ stimulation of MSCs. A subset of additional experiments included a comparison of resting and IFN-γ-treated MSC aggregates.

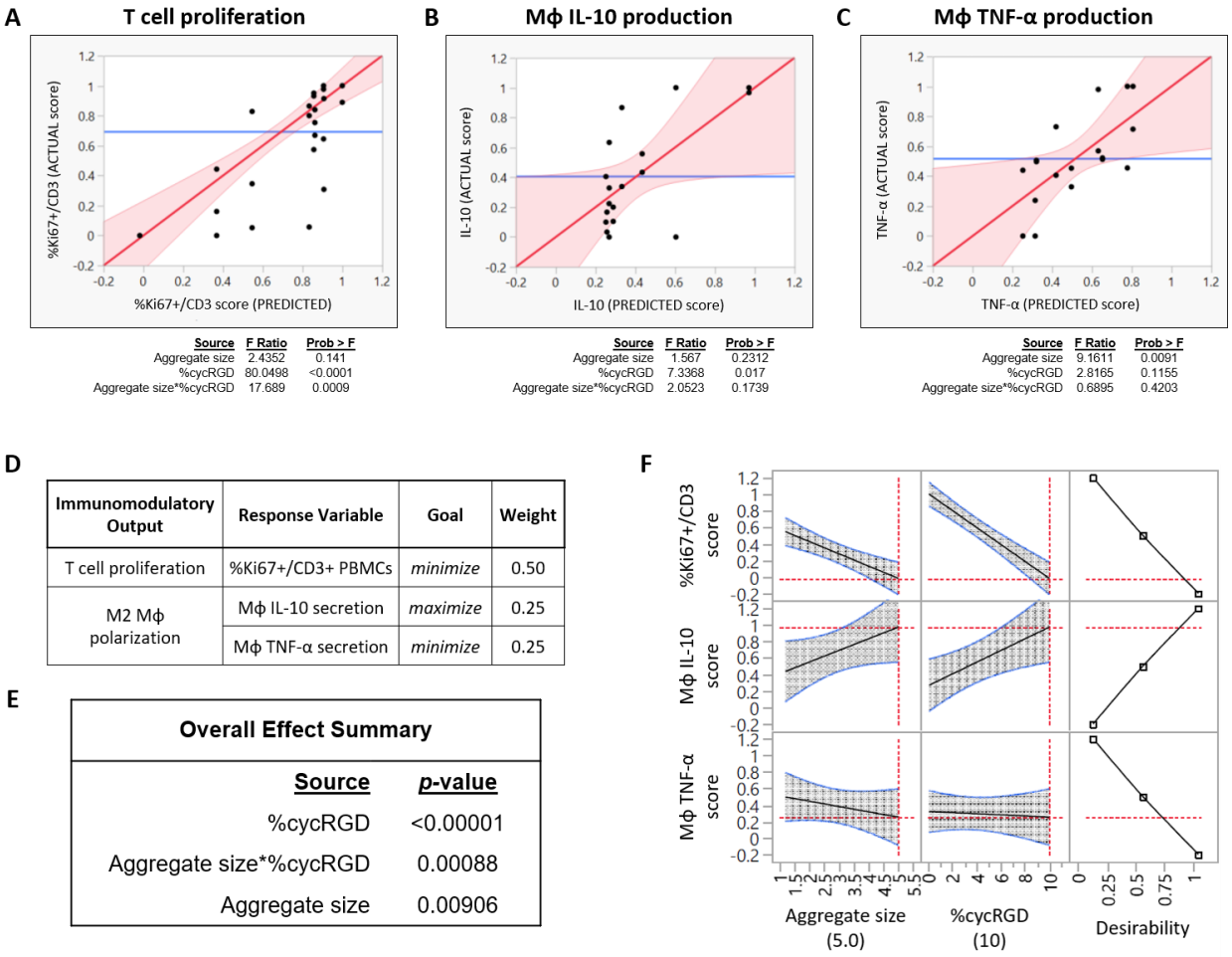

Figure 6.5 Results of DOE-generated models to optimize MSC aggregate immunomodulatory function. Model predictions for (A) T cell suppression, (B) Mφ IL-10 production, and (C) Mφ TNF-α production. The fits of the models were visualized by plotting predicted versus actual scores in immune cell assays upon quantifying (i) %Ki67+ fraction of CD3+ PBMCs following indirect co-culture with MSC aggregates and (ii) Mφ secretion of IL-10 and TNF-α (ELISA) following culture in media conditioned by MSC aggregates. Results of effect tests for each response variable are shown below the model fit. (D) Overall desirability in the DOE model was defined as minimization of T cell proliferation (%Ki67+ CD3+ PBMCs) and maximization of macrophage polarization toward an M2-like phenotype (maximize IL-10, minimize TNF-α secretion). (E) Overall effect summary for factors influencing desirability in the model. (F) Maximizing desirability within the experimental space identifies optimal aggregate size (5.0 mm) and aggregation kinetics (10% cycRGD) for T cell suppression and macrophage polarization.

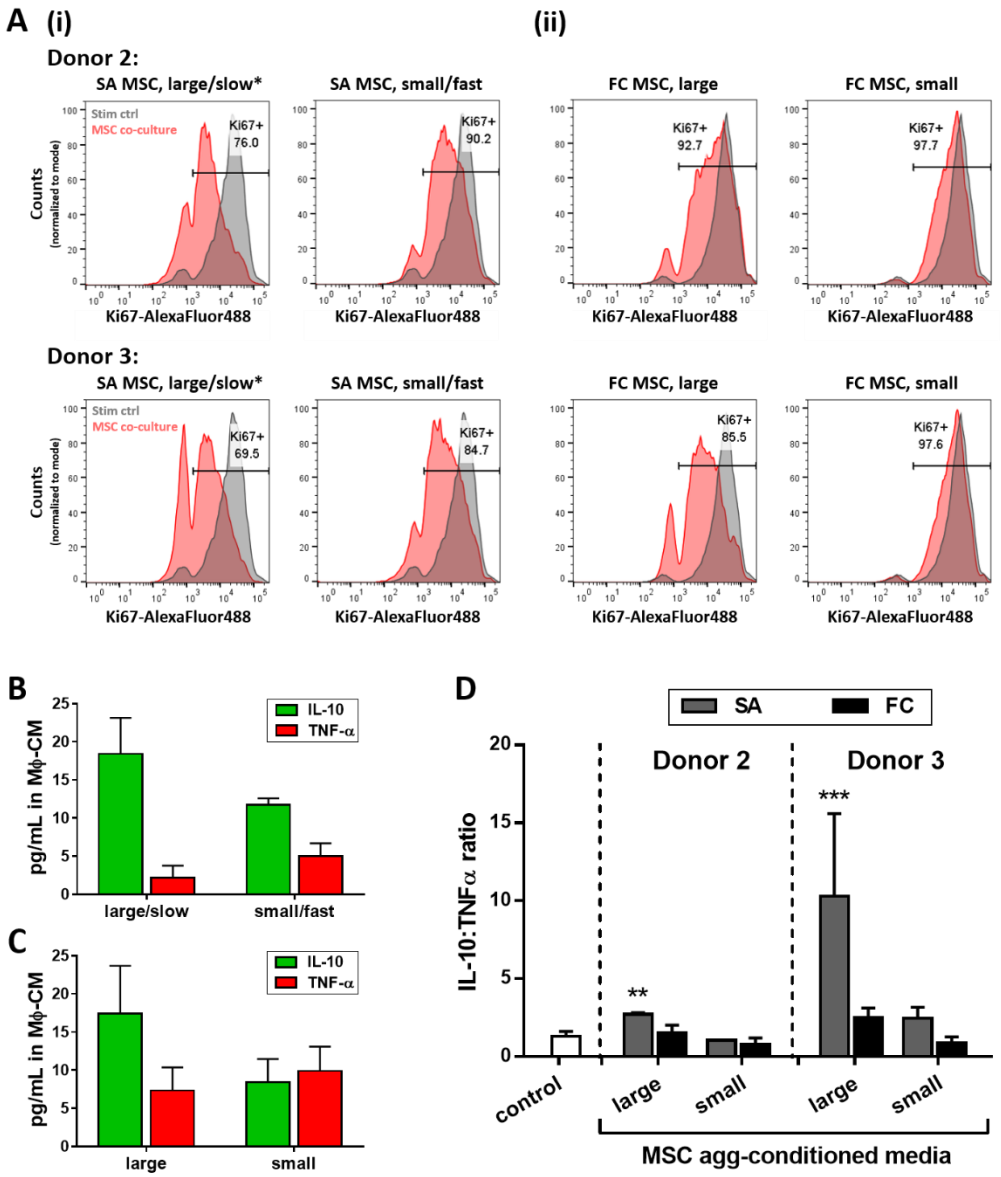

Figure 6.6 Validation of DOE model in two different MSC donors. Immunomodulatory function of DOE-optimized SA MSC aggregates was tested in 2 additional MSC donors. (A) T cell suppression: Flow cytometry histograms of %Ki67+ CD3 T cells following indirect co-culture with (i) SA MSC aggregates predicted by DOE to perform well (large/slow*) or poorly (small/fast), and (ii) large or small FC MSC aggregates, from two additional MSC donors. Gray histogram corresponding to stimulated PBMC control is shown in all plots for comparison. Y-axis displays cell counts, normalized to mode. At least 8,000 CD3+ cells were counted per experimental condition. (B-C) Macrophage polarization: Representative IL-10 and TNF-α concentrations measured in Mϕ-CM from macrophages treated with MSC-CM from (B) SA MSC and (C) FC MSC aggregates. Data shown for MSC Donor 3. (D) IL-10:TNF-α ratio in Mϕ-CM from macrophages treated with media conditioned by MSC aggregates described in (A). Asterisks denote statistically significant differences relative to control (no treatment). $^{**}p < 0.01$, $^{***}p < 0.001$

ID	Source	Supplier	Sex	Donor age	Passage # at use
Donor 1	bone marrow	Lonza (commercial)	F	26	5-7
Donor 2	bone marrow	Wan-Ju Li lab (UW-Madison)	F	25	5-7
Donor 3	bone marrow	Lonza (commercial)	F	21	5-7

Table 6.1 Donor information for MSCs used in the study. Donor 1 MSCs were used for all experiments characterizing differences between 2D monolayer and 3D MSC aggregates, as well as for experiments informing the DOE model. Validation of the DOE model was performed using MSCs from Donors 2 and 3.

6.11 SUPPLEMENTARY FIGURES

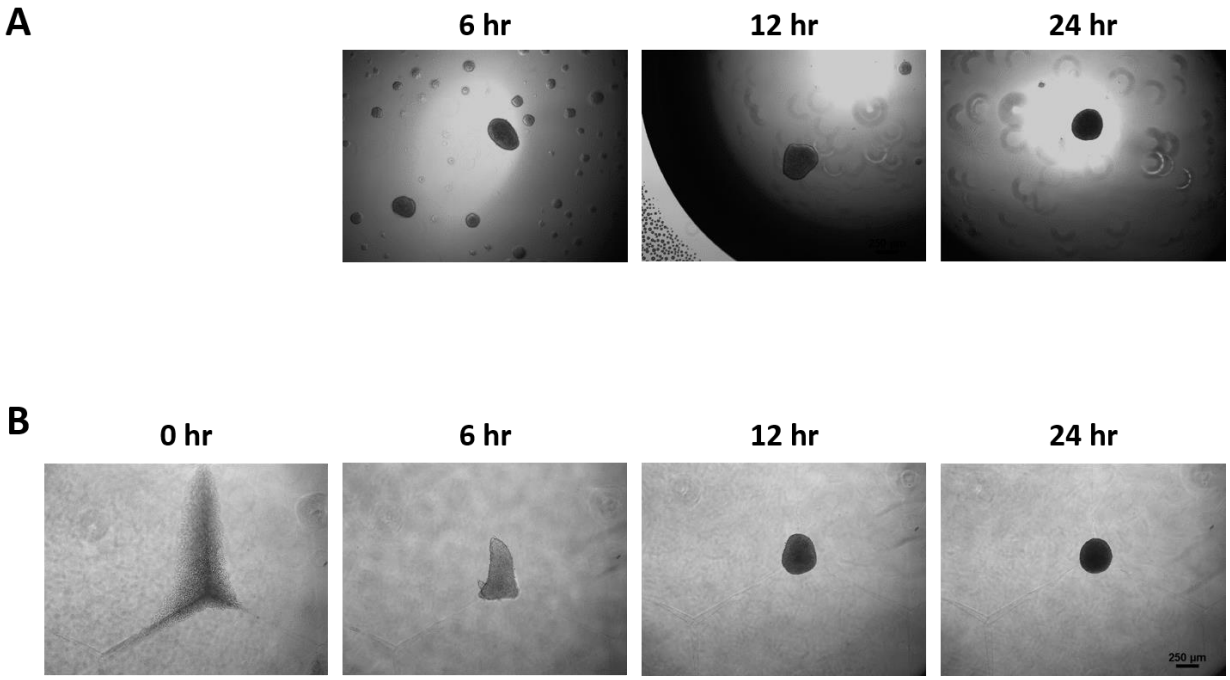

Supplementary Fig. S6.1 Time course of MSC aggregation by conventional methods. Brightfield images of MSCs in (A) HD and (B) FC formats from the time of seeding (0 hr) to 24 hr post-seed. Both methods generated three-dimensional structures by 6 hr post-seed, and formed compact aggregates by 24 hr. Compaction of HD and FC aggregates over time can be seen as changes in shape (oblong to spherical) and increased opacity from 6 hr to 24 hr.

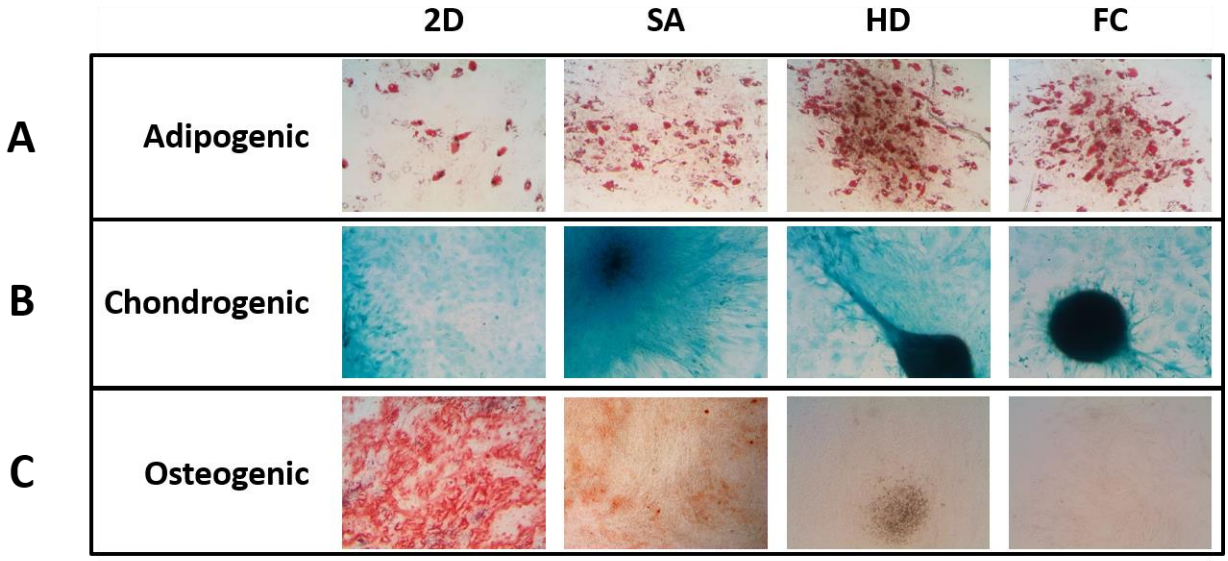

Supplementary Fig. S6.2 Trilineage differentiation capacity of 2D monolayer and 3D aggregate MSCs. 2D MSCs or 3D MSC aggregates (SA, HD, and FC) were plated on Collagen I-coated plates and maintained in adipogenic, chondrogenic, or osteogenic differentiation media for 21 days before staining for Oil Red O, Alcian Blue, and Alizarin Red, respectively.

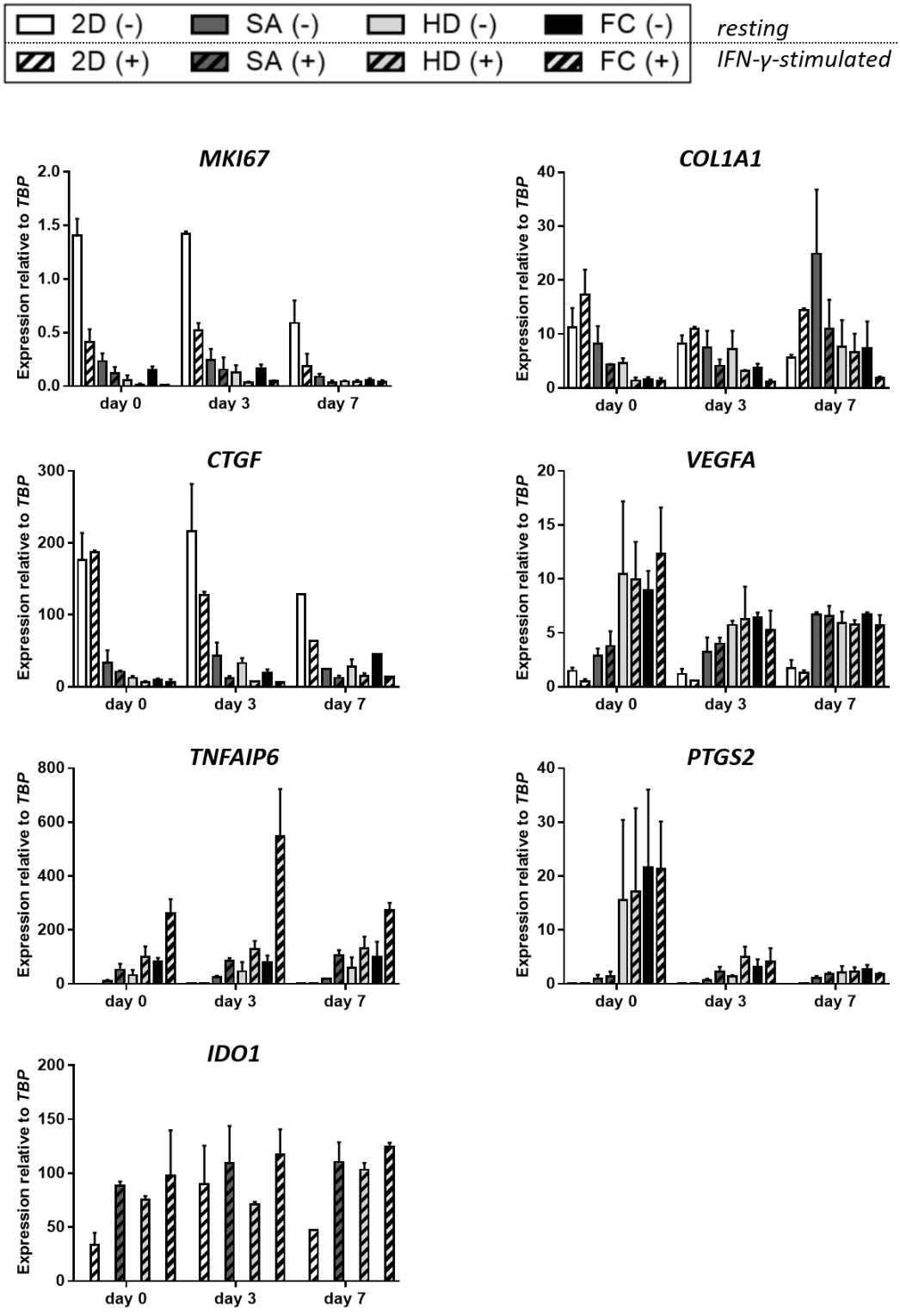

Supplementary Fig. S6.3 Relative gene expression over time in resting or IFN-γ-stimulated MSCs cultured in 2D vs. 3D. Time course of expression for proliferation-, ECM-, pro-angiogenic, and immunomodulatory genes in 2D monolayer MSCs vs. SA, HD, and FC MSC aggregates.

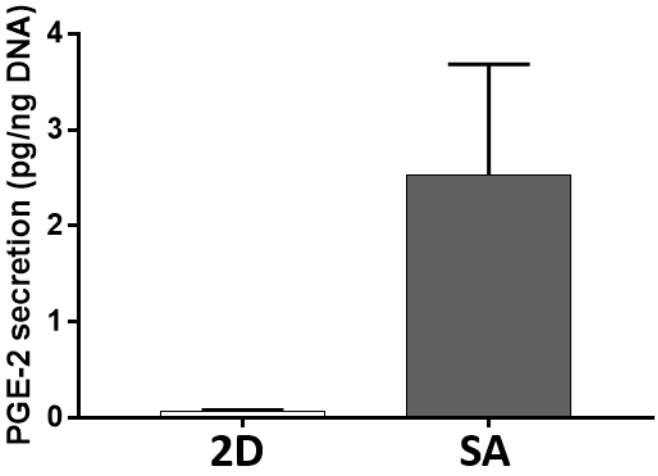

Supplementary Fig. S6.4 PGE2 production in 2D vs. 3D MSCs. MSCs in 3D aggregates (SA) produce >40-fold higher levels of PGE2 compared to 2D monolayer MSCs. PGE2 was measured in conditioned media from IFN-γ-stimulated MSCs.

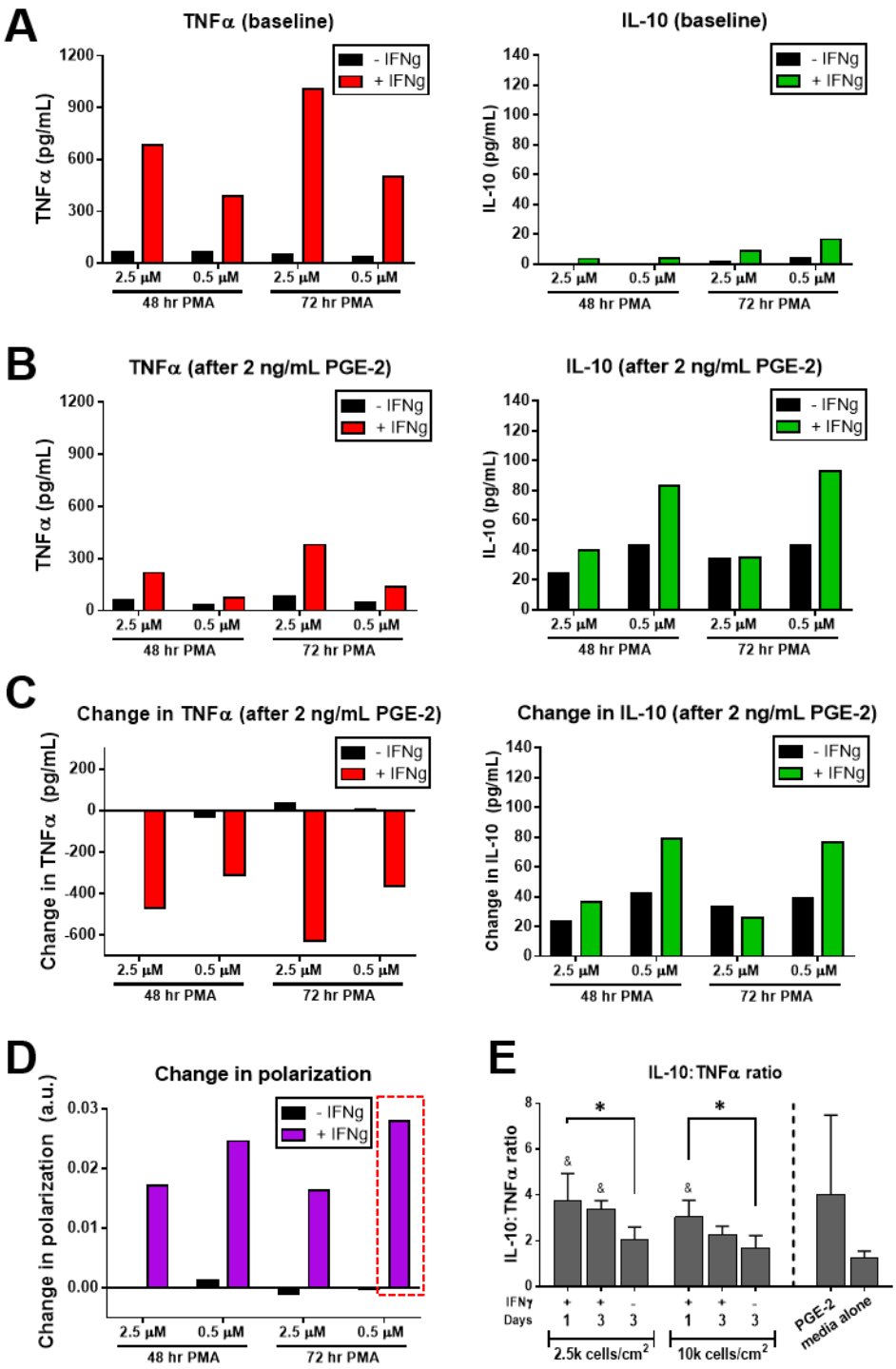

Supplementary Fig. S6.5 Development of macrophage polarization assay. (A) Baseline cytokine profile in Mφ-CM following treatment (± IFNg) of PMA-treated THP-1s. (B) Cytokine profile in Mφ-CM following additional treatment with 2 ng/mL PGE-2. (C) Change in cytokine profile in Mφ-CM between baseline and PGE-2-treated Mφ. (D) "Change in Mφ polarization", defined as a composite metric taking into account the differences in both TNFα and IL-10 production after PGE-2 treatment of Mφ. Absolute changes in pg/mL secretion of each cytokine were weighted equally; decreases in TNFα production and increases in IL-10 production

contributed positively to “change in polarization” metric. Red box denotes the treatment condition that was used for macrophage polarization assays. (E) Determination of cell number per media volume and duration (days) of MSC media conditioning for macrophage polarization assays. MSC media conditioning was performed with 2D MSCs in 12-well plate format (2.5k/cm^2 = 4,500 cells/mL; 10k/cm^2 = 18,000 cells/mL). Graph shows IL-10:TNFα ratio in Mφ-CM following treatment of macrophages with PGE-2 or media conditioned by IFNγ-stimulated or resting MSCs for 1 or 3 days. * indicates significant difference between denoted conditions. & denotes significant difference relative to negative control (“media alone”). $p < 0.05$

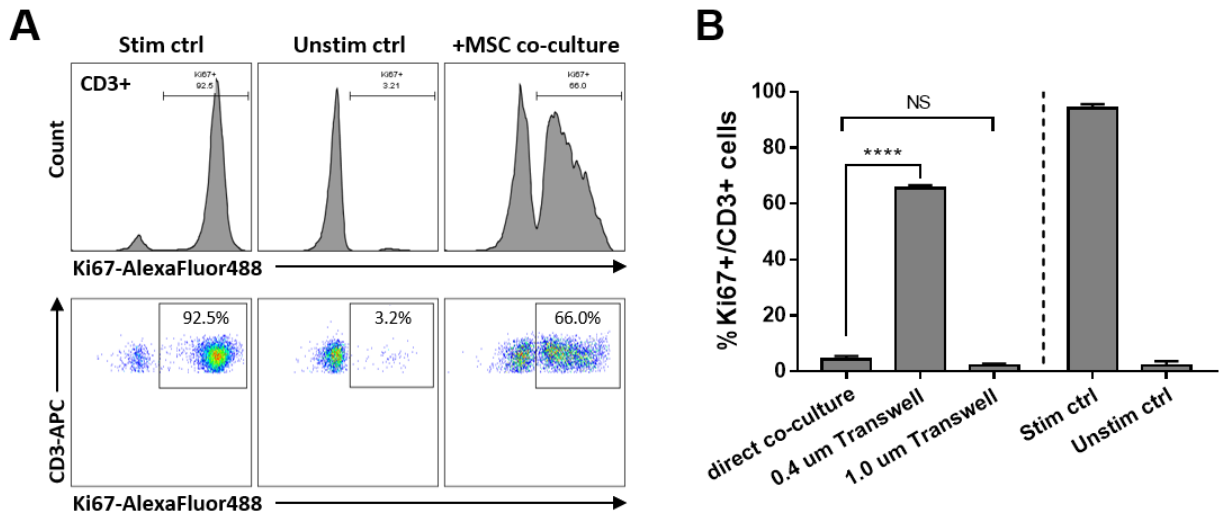

Supplementary Fig. S6.6 Refinement of T cell suppression assay. (A) Histogram representation of MSC-mediated suppression of T cell proliferation. (B) Effect of Transwell pore size on MSC suppression of T cell proliferation. 0.4 µm Transwell significantly reduces the capacity of 2D monolayer MSCs to suppress T cell proliferation, while 1.0 µm pore Transwell rescues the full suppressive effect of MSCs seen in direct co-culture. "Stim ctrl": PBMCs activated by Suppression Inspector beads, no MSCs. "Unstim ctrl": PBMCs without beads, no MSCs.

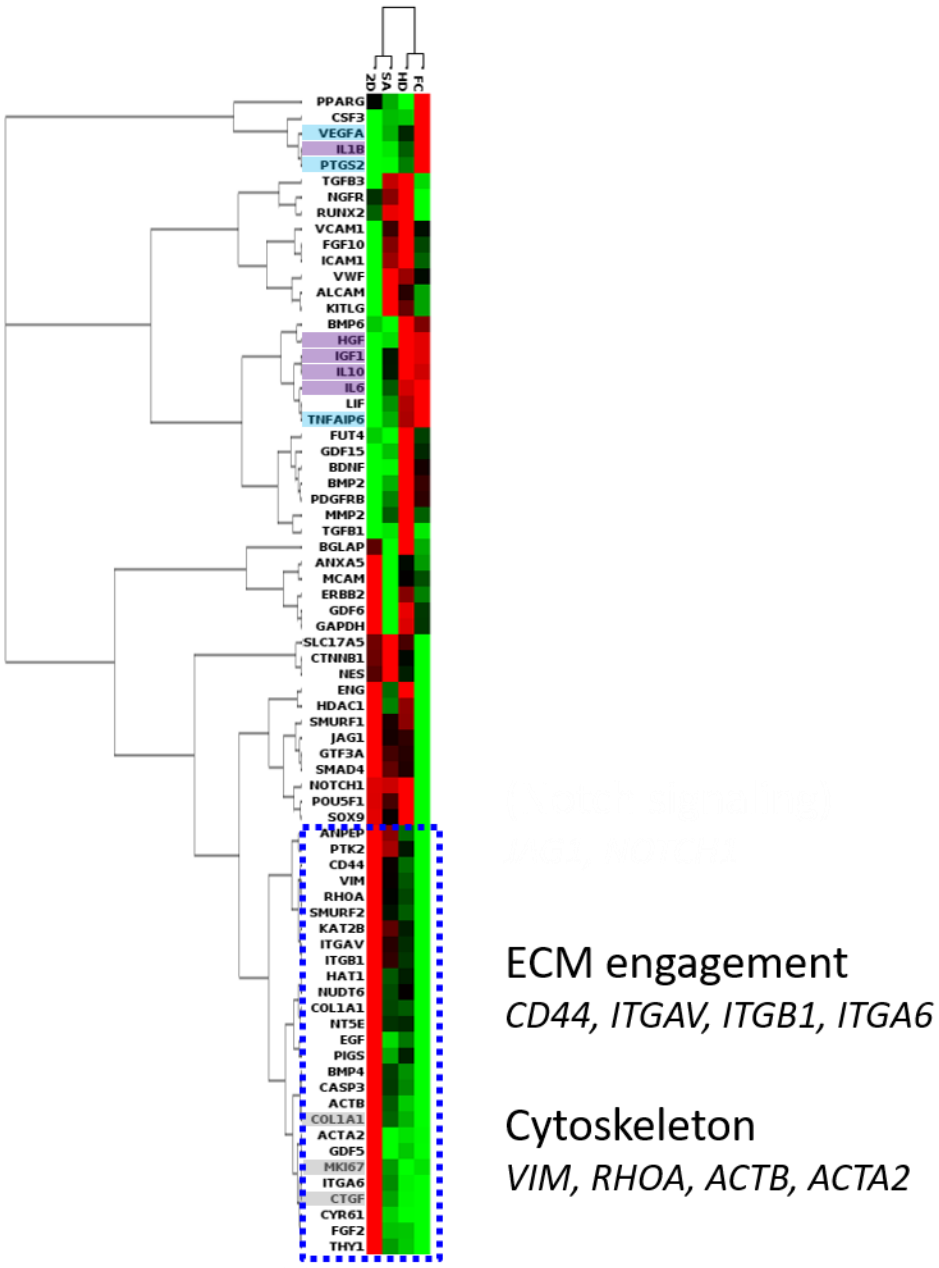

Supplementary Fig. S6.7 Unsupervised hierarchical clustering of MSC genes vs. culture format. Genes related to trophic/immunomodulatory factor production, cell-cell and cell-matrix interactions, cytoskeleton, and stemness/differentiation for 2D monolayer MSCs and 3D MSC aggregates generated by SA, HD, and FC methods were assessed by qPCR array at day 0 (resting conditions). Gene names highlighted in light blue and gray denote those that were assessed in time course studies in Fig. 3. Gene names in purple denote other common cytokines involved in immune regulation.

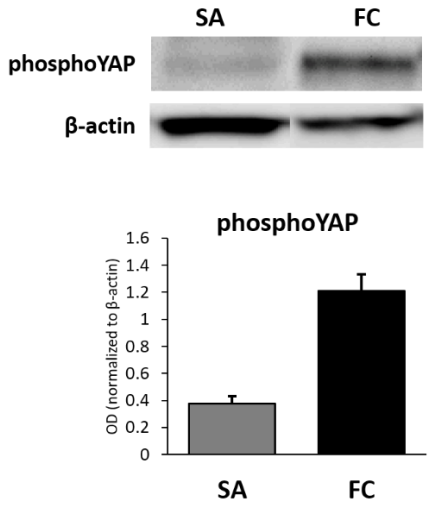

Supplementary Fig. S6.8 MSC aggregation method influences YAP phosphorylation. SA and FC MSC aggregates were formed by SA or FC methods and harvested for Western blot analysis at day 0 (72 hours after initial seeding). Western blots confirmed higher phosphoYAP levels in FC aggregates, indicative of decreasing YAP activity.

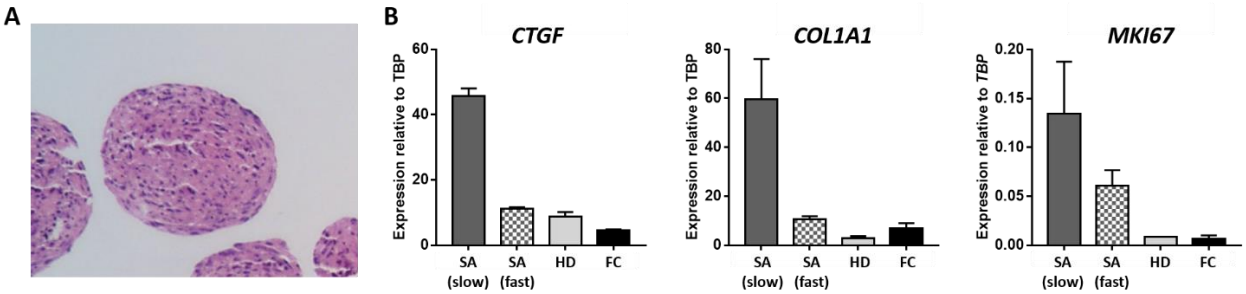

Supplementary Fig. S6.9 Faster aggregation kinetics downregulates expression of ECM- and proliferation-associated genes in SA aggregates. SA aggregates formed via "fast" self-assembly were generated from 0.5% cycRGDfC labile SAMs. (A) Representative H&E stain of day 0 "fast SA" MSC aggregates. (B) Expression of ECM- and proliferation-associated genes in day 0 "fast SA" MSC aggregates, compared to other conditions tested in this study. Data shown are from experiments independent from those used to generate the data in Supplementary Fig. S6.2.

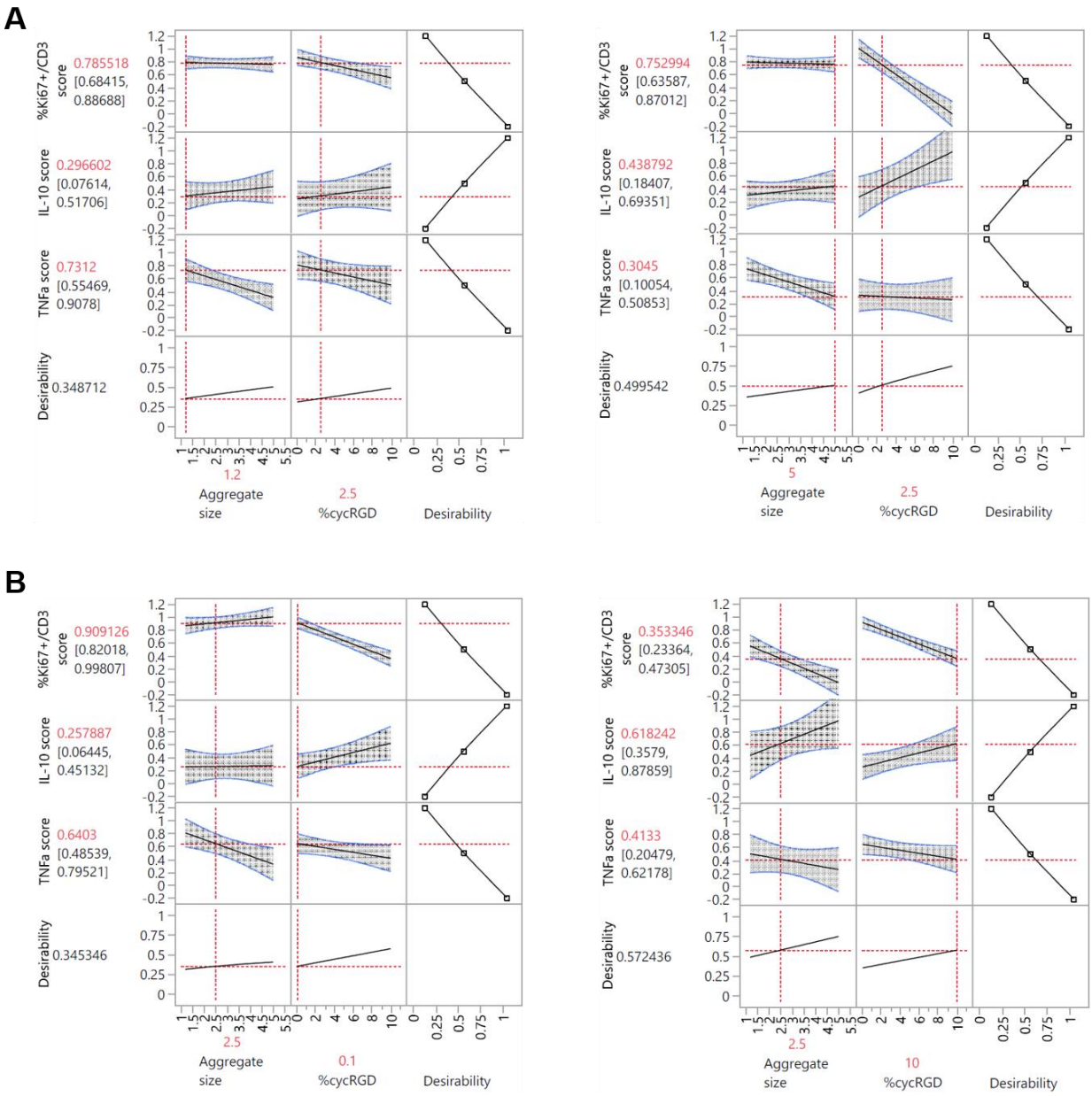

Supplementary Fig. S6.10 Extended model predictions from DOE model exemplify the interaction effect between aggregate size and aggregation kinetics. Prediction profiles showing effects of (A) Changing aggregate size while holding %cycRGD constant and (B) Changing aggregation kinetics (%cycRGD) while holding aggregate size constant. The DOE model identified an interaction effect between aggregate size and kinetics in their influence on %Ki67+/CD3 score.

Supplementary Table S6.1 List of genes for RT2 Profiler qPCR Array – Human Mesenchymal Stem Cells.

UniGene	GenBank	Gene Symbol	Description
Hs.489033	NM_000927	ABCB1	ATP-binding cassette, sub-family B (MDR/TAP), member 1
Hs.500483	NM_001613	ACTA2	Actin, alpha 2, smooth muscle, aorta
Hs.591293	NM_001627	ALCAM	Activated leukocyte cell adhesion molecule
Hs.1239	NM_001150	ANPEP	Alanyl (membrane) aminopeptidase
Hs.480653	NM_001154	ANXA5	Annexin A5
Hs.502182	NM_001709	BDNF	Brain-derived neurotrophic factor
Hs.654541	NM_199173	BGLAP	Bone gamma-carboxyglutamate (gla) protein
Hs.73853	NM_001200	BMP2	Bone morphogenetic protein 2
Hs.68879	NM_130851	BMP4	Bone morphogenetic protein 4
Hs.285671	NM_001718	BMP6	Bone morphogenetic protein 6
Hs.473163	NM_001719	BMP7	Bone morphogenetic protein 7
Hs.141125	NM_004346	CASP3	Caspase 3, apoptosis-related cysteine peptidase
Hs.502328	NM_000610	CD44	CD44 molecule (Indian blood group)
Hs.172928	NM_000088	COL1A1	Collagen, type I, alpha 1
Hs.1349	NM_000758	CSF2	Colony stimulating factor 2 (granulocyte-macrophage)
Hs.2233	NM_000759	CSF3	Colony stimulating factor 3 (granulocyte)
Hs.476018	NM_001904	CTNNB1	Catenin (cadherin-associated protein), beta 1, 88kDa
Hs.419815	NM_001963	EGF	Epidermal growth factor
Hs.76753	NM_000118	ENG	Endoglin
Hs.446352	NM_004448	ERBB2	V-erb-b2 erythroblastic leukemia viral oncogene homolog 2, neuro/glioblastoma derived oncogene homolog (avian)
Hs.664499	NM_004465	FGF10	Fibroblast growth factor 10
Hs.284244	NM_002006	FGF2	Fibroblast growth factor 2 (basic)
Hs.69747	NM_000148	FUT1	Fucosyltransferase 1 (galactoside 2-alpha-L-fucosyltransferase, H blood group)
Hs.390420	NM_002033	FUT4	Fucosyltransferase 4 (alpha (1,3) fucosyltransferase, myeloid-specific)
Hs.647029	NM_003508	FZD9	Frizzled family receptor 9
Hs.616962	NM_004864	GDF15	Growth differentiation factor 15
Hs.1573	NM_000557	GDF5	Growth differentiation factor 5
Hs.492277	NM_001001557	GDF6	Growth differentiation factor 6
Hs.447688	NM_182828	GDF7	Growth differentiation factor 7
Hs.445977	NM_002097	GTF3A	General transcription factor IIIA
Hs.632532	NM_003642	HAT1	Histone acetyltransferase 1
Hs.88556	NM_004964	HDAC1	Histone deacetylase 1
Hs.396530	NM_000601	HGF	Hepatocyte growth factor (hepapoietin A; scatter factor)
Hs.654455	NM_000545	HNF1A	HNF1 homeobox A

Hs.643447	NM_000201	ICAM1	Intercellular adhesion molecule 1
Hs.856	NM_000619	IFNG	Interferon, gamma
Hs.160562	NM_000618	IGF1	Insulin-like growth factor 1 (somatomedin C)
Hs.193717	NM_000572	IL10	Interleukin 10
Hs.126256	NM_000576	IL1B	Interleukin 1, beta
Hs.654458	NM_000600	IL6	Interleukin 6 (interferon, beta 2)
Hs.654579	NM_000207	INS	Insulin
Hs.133397	NM_000210	ITGA6	Integrin, alpha 6
Hs.436873	NM_002210	ITGAV	Integrin, alpha V (vitronectin receptor, alpha polypeptide, antigen CD51)
Hs.248472	NM_000887	ITGAX	Integrin, alpha X (complement component 3 receptor 4 subunit)
Hs.643813	NM_002211	ITGB1	Integrin, beta 1 (fibronectin receptor, beta polypeptide, antigen CD29 includes MDF2, MSK12)
Hs.728907	NM_000214	JAG1	Jagged 1
Hs.533055	NM_003884	KAT2B	K(lysine) acetyltransferase 2B
Hs.479756	NM_002253	KDR	Kinase insert domain receptor (a type III receptor tyrosine kinase)
Hs.1048	NM_003994	KITLG	KIT ligand
Hs.2250	NM_002309	LIF	Leukemia inhibitory factor (cholinergic differentiation factor)
Hs.599039	NM_006500	MCAM	Melanoma cell adhesion molecule
Hs.513617	NM_004530	MMP2	Matrix metallopeptidase 2 (gelatinase A, 72kDa gelatinase, 72kDa type IV collagenase)
Hs.527971	NM_006617	NES	Nestin
Hs.415768	NM_002507	NGFR	Nerve growth factor receptor
Hs.495473	NM_017617	NOTCH1	Notch 1
Hs.153952	NM_002526	NT5E	5'-nucleotidase, ecto (CD73)
Hs.558459	NM_007083	NUDT6	Nudix (nucleoside diphosphate linked moiety X)-type motif 6
Hs.509067	NM_002609	PDGFRB	Platelet-derived growth factor receptor, beta polypeptide
Hs.462550	NM_033198	PIGS	Phosphatidylinositol glycan anchor biosynthesis, class S
Hs.249184	NM_002701	POU5F1	POU class 5 homeobox 1
Hs.162646	NM_015869	PPARG	Peroxisome proliferator-activated receptor gamma
Hs.614734	NM_006017	PROM1	Prominin 1
Hs.395482	NM_005607	PTK2	PTK2 protein tyrosine kinase 2
Hs.654514	NM_002838	PTPRC	Protein tyrosine phosphatase, receptor type, C
Hs.247077	NM_001664	RHOA	Ras homolog gene family, member A
Hs.535845	NM_004348	RUNX2	Runt-related transcription factor 2
Hs.597422	NM_012434	SLC17A5	Solute carrier family 17 (anion/sugar transporter), member 5
Hs.75862	NM_005359	SMAD4	SMAD family member 4

Hs.189329	NM_020429	SMURF1	SMAD specific E3 ubiquitin protein ligase 1
Hs.705442	NM_022739	SMURF2	SMAD specific E3 ubiquitin protein ligase 2
Hs.518438	NM_003106	SOX2	SRY (sex determining region Y)-box 2
Hs.647409	NM_000346	SOX9	SRY (sex determining region Y)-box 9
Hs.381715	NM_181486	TBX5	T-box 5
Hs.492203	NM_198253	TERT	Telomerase reverse transcriptase
Hs.645227	NM_000660	TGFB1	Transforming growth factor, beta 1
Hs.592317	NM_003239	TGFB3	Transforming growth factor, beta 3
Hs.644697	NM_006288	THY1	Thy-1 cell surface antigen
Hs.241570	NM_000594	TNF	Tumor necrosis factor
Hs.109225	NM_001078	VCAM1	Vascular cell adhesion molecule 1
Hs.73793	NM_003376	VEGFA	Vascular endothelial growth factor A
Hs.642813	NM_003380	VIM	Vimentin
Hs.440848	NM_000552	VWF	Von Willebrand factor
Hs.336930	NM_033131	WNT3A	Wingless-type MMTV integration site family, member 3A
Hs.335787	NM_174900	ZFP42	Zinc finger protein 42 homolog (mouse)
Hs.520640	NM_001101	ACTB	Actin, beta
Hs.534255	NM_004048	B2M	Beta-2-microglobulin
Hs.592355	NM_002046	GAPDH	Glyceraldehyde-3-phosphate dehydrogenase
Hs.412707	NM_000194	HPRT1	Hypoxanthine phosphoribosyltransferase 1
Hs.546285	NM_001002	RPLP0	Ribosomal protein, large, P0

CHAPTER 7. CONCLUSIONS AND RECOMMENDATIONS FOR FUTURE WORK

7.1 CONCLUSIONS

The past 20 years has seen the rapid expansion of stem cells into diverse areas of regenerative medicine and cell therapy, disease modeling, and drug discovery. Continued success in these areas – particularly in the therapeutic use of stem cells – will depend on an improved understanding of environmental factors and the specific ways in which they instruct stem cell fate and function *in vitro* and *in vivo*. Importantly, such insights will need to be combined with innovative technologies that enable sustainable, reproducible, and cost-effective manufacturing of therapeutically potent cells. In this dissertation, we established novel approaches for the use of synthetic biomaterial technologies to engineer the local biochemical (Chapters 3 and 5) and biophysical (Chapters 5 and 6) stem cell microenvironment in two- (2D) and three-dimensional (3D) culture configurations.

In Chapter 3, we used mineral-coated microparticles (MCMs) to stabilize and provide local sustained release of basic fibroblast growth factor (bFGF) to human pluripotent stem cells (hPSC), providing active regulation of the biochemical microenvironment of hPSCs. Application of bFGF-releasing MCMs substantially reduced the dosage of growth factor required for long-term hPSC expansion in conventional 2D culture and overcame barriers to soluble bFGF diffusion to improve pluripotency maintenance in 3D aggregates. While this study identified novel protein-stabilizing functions for a scalable synthetic biomaterial, it also provided a proof of concept for the broader utility of biomaterial-mediated controlled protein release as a tool for economizing cell biomanufacturing.

Extending the concept of material-mediated control over the stem cell microenvironment in 3D culture geometries, Chapter 4 described the development and characterization of a novel platform utilizing labile chemistries in combination with substrate micropatterning to control the process of cell aggregation. We designed these labile substrates to employ an aggregation mechanism distinct from that of existing methods, which led to the enhanced-throughput generation of cell aggregates with controllable size, shape, and formation kinetics that furthermore exhibited improved viability and reproducibility compared to existing approaches. In Chapters 5 and 6, we exploited these labile substrates to understand the influence of aggregate size, aggregation method, and formation kinetics on the fate and function of two prominent candidates for cell therapy – hPSCs and human mesenchymal stromal cells (MSCs). Through these studies, we established a novel role for aggregation kinetics as a culture parameter that can be tuned to control the internal structure of cell aggregates, which ultimately had significant implications for growth factor signaling and pluripotency in hPSC aggregates and immunomodulatory phenotype/function in MSC aggregates.

Altogether, our findings underscore the utility of synthetic biomaterials for manipulating spatiotemporal features of the *in vitro* stem cell microenvironment, via controlled release of soluble cell-instructive components and controlled 3D assembly of cellular components. These studies serve as examples for how biomaterial strategies can address current challenges in stem cell biomanufacturing. Based on the large parameter space for material characteristics, biological complexity, reproducibility, and scalability of existing biomaterials, there is substantial opportunity for such strategies to usher cell therapies into the clinic.

7.2 RECOMMENDATIONS FOR FUTURE WORK

7.2.1 Controlled growth factor delivery for efficient 2D and 3D expansion of stem cell therapies

The approach described in Chapter 3 built upon the hypothesis that sustained delivery of a growth factor critical to pluripotency maintenance would reduce the growth factor dosage needed to expand hPSCs. In this chapter, we used microparticles functionalized with mineral coatings (MCMs) that our lab has previously shown can efficiently bind and release a wide array of proteins over extended timeframes (weeks to months). Previous reports published by our group have shown the versatility of this material – the concentrations of specific dopants (e.g., fluoride, carbonate) in the modified simulated body fluid solution during mineralization can be adjusted to modulate the rate of coating dissolution thereby controlling protein release kinetics[1–4], and coatings can be formed on a variety of core materials (hydroxyapatite[5–7], polystyrene[7], PLGA[8–10]) and geometries (microspheres[4,6,9], scaffolds[2,11], tissue culture dishes[8], surgical sutures[12,13] and screws[14]). In the current work, we largely limited our investigation of these growth factor-releasing mineral coatings to one specific coating formulation for delivery of a single growth factor, bFGF, in hPSC culture. While optimization of the growth factor binding solution and MCM dose were sufficient to reduce the amount of bFGF required for hPSC maintenance by >80%, the versatility of the material and approach provides many additional avenues for further optimization of this strategy in stem cell biomanufacturing applications. For example, the application of novel tools to manipulate and study signaling downstream of growth factor-receptor binding[15–18] should generate detailed insights into how growth factor signaling kinetics influence pluripotency maintenance, and inform the rational design of biomaterial properties and associated release profiles to achieve optimal growth factor use in hPSC culture. Alternatively, screening of biomaterial libraries[8,19] may

elucidate important material properties that support efficient growth factor delivery in stem cell culture.

Building upon previous work in which our group demonstrated the capacity for mineral coatings to preserve protein activity against exposure to organic solvents and proteases[20], in the current work we demonstrated the ability of MCMs to preserve bFGF activity in the absence of natural stabilizers (e.g., heparin) that are typically required to combat its thermal instability at physiological temperatures. Interestingly, the stabilization of sensitive proteins by mineralized materials is reminiscent of the remarkable preservation of biomacromolecules in the bone matrix of fossilized samples[21–23]. Understanding the mechanisms by which the structure and composition of mineral coatings preserve bFGF activity, and the extent to which these mechanisms extend to stabilization of other proteins in cell culture, should be a major aim of future studies. Insights gleaned from such studies will inform the further development of these mineral coatings toward protein delivery in *ex vivo* cell biomanufacturing and *in vivo* delivery applications.

In addition to a greater mechanistic understanding of the material itself, further emphasis should be placed on understanding the functions of bFGF-MCMs at the cellular level. Material-mediated stabilization is just one of several mechanisms that may have contributed to the improved efficiency of hPSC expansion in the presence of MCMs. For example, we also showed that the ability to deliver growth factors in close proximity to hPSC colonies was a crucial advantage afforded by bFGF-MCMs; optimal MCM doses that maintained short-term pluripotency in direct culture were not effective in doing so in Transwell culture. Our analysis of pluripotency maintenance, however, was largely based on flow cytometry, which did not address spatial heterogeneities created by localized sources of bFGF within the cultures. Thus, there are opportunities for future work to interrogate local growth factor gradients established in direct

culture with bFGF-MCMs, and the application of mineral coatings to core materials that can be spatially patterned (e.g., magnetic polystyrene beads) should enable systematic studies of these gradients and their effects on pluripotency signaling at the single cell level.

Finally, future studies should aim to translate bFGF-MCMs to formats compatible with scalable suspension culture, such as microcarriers and 3D cell aggregates. As discussed in Chapter 2, there have already been intense efforts in expanding hPSCs, MSCs, and their derivatives to suspension bioreactors, and the translation of technologies that have been optimized for 2D culture is not trivial. For the studies conducted in Chapter 3, we carried out a simple optimization scheme co-varying bFGF and MCM concentrations in the MCM binding solution to arrive at an ideal binding formulation that was tested empirically to determine dose-dependence in maintaining hPSC pluripotency in 2D. We have shown in preliminary studies that the optimized bFGF-MCMs, when incorporated into 3D embryoid bodies formed by forced centrifugation, maintain *NANOG* expression at levels three-fold higher than control EBs without MCMs. We also observed a detrimental effect of the material alone on *NANOG* expression at high doses, a phenomenon that was not observed in the 2D studies (Supplementary Fig. S3.13). Our findings in Chapter 5 indicated that rapid loss of pluripotency in large EBs can be partially attributed to poor diffusion of bFGF and TGFβ from Essential 8 media into the center of EBs (Fig. 5.6). Thus, these data together suggest that growth factor delivery from MCMs embedded within the EB interior can overcome growth factor diffusion limitations in stem cell aggregates, but further optimization of the material is needed to optimize the its utility for the expansion of 3D hPSC aggregates.

The results detailed in Chapters 2 and 3 introduce biomaterials as intriguing tools for mitigating growth factor cost in stem cell biomanufacturing. Ultimately, comprehensive studies to understand the relative contributions of sustained growth factor signaling, local growth factor

gradients, and biomaterial-mediated growth factor stabilization and release should begin to elucidate critical parameters for efficient growth factor delivery in the production of cell therapies.

7.2.2 Unbiased statistical approaches to identify critical culture parameters that mediate MSC immunomodulatory function

Several reports now support the finding that 3D culture results in increased paracrine activity of MSCs. However, the majority of these studies have focused on characterizing the expression of a small subset of genes and proteins that were published in early reports. While many of these factors have since been confirmed by mechanistic studies and animal models to play a role in MSC therapeutic efficacy, the collective studies on MSC-immune cell interplay suggest that MSC mechanisms in cell therapy are complex and cannot be recapitulated by any single soluble factor. Thus, designating these paracrine targets *a priori* fails to account for the complexity of the MSC secretome, and is perhaps a limited approach at a time when MSCs' clinical mechanisms of action are poorly understood. The Design of Experiments approach we employed in Chapter 6 builds on strategies employing *in vitro* functional assays with human immune cells as metrics for defining MSC immunomodulatory potency[24,25]. While such assays come with their own set of challenges[26], future use of statistical approaches to dissect data from both phenotypic and functional assays may enable scientists, cell therapy manufacturers, and regulatory agencies to converge on a set of robust and reproducible indicators of MSC potency.

Statistically driven approaches have gained broad interest across cell therapy based on the need to understand how *in vitro* culture parameters affect critical quality attributes of a living cell product. MSCs may be a particularly appropriate cell therapy testbed for DOE and other statistically driven methods; although combinatorial assay matrix approaches that collectively

inform on MSC immune potency have been reported on recently[27], specific culture parameters that optimize MSC therapeutic potency are still in the process of being identified. Notably, MSCs elaborate a wide array of secreted factors that direct the activities of multiple immune cell types, and the holistic MSC paracrine effect on these cell types is likely defined by a complex combination of secretome components not limited to freely soluble molecules[28–31]. Furthermore, the MSC secretome varies widely based on patient[32–36] and tissue source[37–39] as well as the methods used to isolate, expand, and condition the cells[40–44]; hence, the composition of "active ingredients" that determines MSC effects on immune cells may vary between preparations. Thus, we posit that critical insights about the biology of MSC immunomodulation can be derived from unbiased approaches centered around MSC potency in *in vitro* functional assays, combined with comprehensive secretome analysis and methods for assessing large datasets (e.g., dimensionality reduction techniques like Principal Component Analysis). The knowledge gained from such studies should be useful in identifying ways to best harness MSC properties for therapeutic benefit.

7.2.3 Advancing cell aggregates for therapeutic delivery

Recent studies have identified a wide array of culture parameters and pre-conditioning regimens that enhance MSCs' capacity to regulate T cell, macrophage, dendritic cell, and NK cell phenotypes and functions *in vitro*. However, it remains unclear whether these enhancements result in long-term benefits *in vivo*, particularly as dissociated MSCs exhibit poor localization to sites of injury and transient dwell times (hours to days) following intravenous delivery[45,46]. In addition, it has been proposed that dissociated MSCs transplanted into areas of inflammation and ischemia *in vivo* may die of anoikis prior to substantial cytokine release[47], thus mitigating their therapeutic benefits. Although improved therapeutic outcomes are observed after MSC transplantation even

in the absence of apparent long-term engraftment[48,49], effective strategies to enhance MSC survival and persistence *in vivo* is likely required to maximize their paracrine functions in treatments for local inflammatory diseases. In this respect, the idea of delivering cells as 3D aggregates has been gaining increasing traction, as numerous studies have now demonstrated substantial increases in long-term survival and retention in the transplant site for aggregates of MSCs[50], hepatocytes, cardiomyocytes, and other cell types, compared to their dissociated counterparts. For example, Xu et al. observed significantly improved survival of 3D MSC aggregates in a rat model of acute kidney ischemia, a result that was concordant with enhanced *in vivo* production of VEGF, HGF, and TSG-6 compared to dissociated cells[51].

Although the work performed in Chapter 6 did not include an extensive comparison of immunomodulatory function between dissociated (2D) MSCs vs. 3D aggregates, we chose to proceed with comparisons among aggregates primarily based on their substantially higher production of PGE2, VEGF, and TSG-6. However, we also rationalized that a head-to-head comparison of 2D and 3D MSCs under conventional *in vitro* culture conditions (for dissociated MSCs: 21% O_2 in serum-containing media, adherent on tissue culture plastic) would be unlikely to reflect their respective *in vivo* performances. Indeed, following trypsinization and reseeding on tissue culture plastic, 2D MSCs exhibit nearly 100% viability (data not shown) whereas unequivocal evidence from pre-clinical models shows that dissociated MSCs undergo massive cell death or are otherwise largely displaced from the intended site of action shortly following administration. Notably, a growing body of evidence indicated increased resilience of 3D cell aggregates in environments of low GF/nutrient concentrations[50,52], hypoxia[52], and oxidative stress[47,53]. Thus, future studies directly comparing the immunomodulatory function of 2D vs. 3D

MSCs should benefit from *in vitro* models that recapitulate major features of ischemic and inflammatory *in vivo* environments.

Finally, additional consideration should be given to ways in which 3D cell aggregates may be advantageous at the point of care. The work in Chapter 2 highlighted potential advantages of strategies that preserve cell-cell and/or cell-matrix adhesions during the formation of cell aggregates, but these advantages are likely to be just as important at the point of delivery. For example, maintenance of tissue-like structure[54,55] and preservation of cell-ECM interactions[56–58] have been shown to improve cell viability under ambient conditions and during extended hypothermic storage. Thus, cell aggregation may be able to address logistical issues related to the significant decline of viability and function for cell suspensions during their storage prior to therapeutic administration[59–63].

One specific avenue for future investigation is the potential for aggregation to better maintain cell phenotypes following thaw from cryostorage, which we have begun to explore in MSCs. In the current model for MSC-based therapy, cells are isolated and expanded *ex vivo*, cryopreserved, and thawed within hours of administration. However, studies from Galipeau and others indicate functional deficiencies in cryopreserved MSCs that lead to altered biodistribution[64], increased susceptibility to T cell-mediated lysis[65], and vastly accelerated clearance *in vivo*[46]. Notably, François et al. showed that impaired IFN-γ licensing in MSCs administered within 24 hours of thaw – which manifests as poor inducibility of *IDO1*, *CCL2*, and likely other critical genes – is partially responsible for the diminished immunomodulatory efficacy of cryopreserved MSCs[66]. Our initial data indicate that culture in 3D aggregates may mitigate this post-thaw impairment. While inducibility of *IDO1* in response to IFN-γ was diminished ~5-fold in cryopreserved 2D (dissociated) MSCs relative to their fresh counterparts, *IDO1* in cryopreserved

MSC aggregates was induced at levels similar to fresh aggregates and significantly higher than 2D cryopreserved MSCs (Fig. 7.1). While these results are preliminary, they build on the work described in Chapter 6 to highlight the multiplicity of potential benefits offered by 3D aggregation of MSCs. Thus, the potential for cell aggregates as a format for storage and administration of cell therapies should be an avenue for continued exploration.

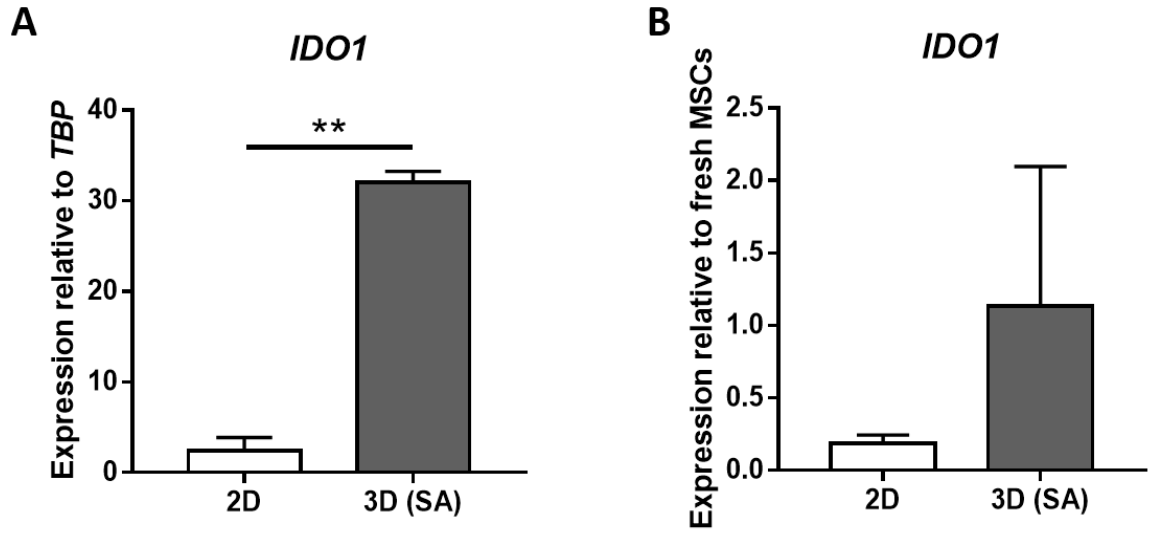

Figure 7.1 Culture geometry influences responsiveness of cryopreserved MSCs to IFN-γ post-thaw. MSCs in 2D or 3D SA aggregates were stimulated for 12 hrs with IFN-γ after continued maintenance in culture ("fresh MSCs") or following post-cryopreservation thaw. Data are from $n = 2$ independent experiments. (A) Post-thaw 3D MSC aggregates express significantly higher levels of *IDO1* compared to post-thaw 2D (dissociated) MSCs. Asterisks indicate statistical significance (**$p < 0.01$, two-tailed Student's t-test). (B) Compared to fresh MSC counterparts, *IDO1* expression in response to IFN-γ priming is dramatically lower in cryopreserved 2D cultured MSCs but is preserved in cryopreserved 3D SA aggregates.

7.3 REFERENCES

1. Choi, S., Yu, X., Jongpaiboonki, L., Hollister, S. J. & Murphy, W. L. Inorganic coatings for optimized non-viral transfection of stem cells. *Sci. Rep.* **3,** 1567–93 (2013).

2. Suárez-González, D. *et al.* Controllable mineral coatings on PCL scaffolds as carriers for growth factor release. *Biomaterials* **33,** 713–721 (2012).

3. Suárez-González, D., Lee, J. S., Lan Levengood, S. K., Vanderby, R. & Murphy, W. L. Mineral coatings modulate β-TCP stability and enable growth factor binding and release. *Acta Biomater.* **8,** 1117–1124 (2012).

4. Yu, X., Khalil, A., Dang, P. N., Alsberg, E. & Murphy, W. L. Multilayered inorganic microparticles for tunable dual growth factor delivery. *Adv. Funct. Mater.* **24,** 3082–3093 (2014).

5. Dang, P. N. *et al.* Controlled Dual Growth Factor Delivery From Microparticles Incorporated Within Human Bone Marrow-Derived Mesenchymal Stem Cell Aggregates for Enhanced Bone Tissue Engineering via Endochondral Ossification. *Stem Cells Transl. Med.* **5,** 206–217 (2016).

6. Yu, X. *et al.* Nanostructured Mineral Coatings Stabilize Proteins for Therapeutic Delivery. *Adv. Mater.* **29,** (2017).

7. Khalil, A. S. *et al.* Functionalization of microparticles with mineral coatings enhances non-viral transfection of primary human cells. *Sci. Rep.* **7,** 1–12 (2017).

8. Choi, S. & Murphy, W. L. A screening approach reveals the influence of mineral coating morphology on human mesenchymal stem cell differentiation. *Biotechnol. J.* **8,** 496–501 (2013).

9. Jongpaiboonkit, L., Franklin-Ford, T. & Murphy, W. L. Mineral-coated polymer microspheres for controlled protein binding and release. *Adv. Mater.* **21,** 1960–1963 (2009).

10. Jongpaiboonkit, L., Franklin-Ford, T. & Murphy, W. L. Growth of Hydroxyapatite Coatings on Biodegradable Polymer Microspheres. *ACS Appl. Mater. Interfaces* **1,** 1504–1511 (2009).

11. Suárez-González, D. *et al.* Controlled nucleation of hydroxyapatite on alginate scaffolds for stem cell-based bone tissue engineering. *J. Biomed. Mater. Res. Part A* **95A,** 222–234 (2010).

12. Lee, J. S., Lu, Y., Baer, G. S., Markel, M. D. & Murphy, W. L. Controllable protein delivery from coated surgical sutures. *J. Mater. Chem.* **20,** 8894–8903 (2010).

13. Lu, Y. *et al.* Histologic evaluation of suture material loaded with basic fibroblast growth factor (bFGF) on acute rotator cuff repair in an ovine model. *Curr. Orthop. Pract.* **22,** 425–431 (2011).

14. Lu, Y. *et al.* Influence of Hydroxyapatite-Coated and Growth Factor-Releasing Interference Screws on Tendon-Bone Healing in an Ovine Model. *Arthrosc. - J. Arthrosc.*

Relat. Surg. **25,** 1–16 (2009).

15. Kim, N. *et al.* Spatiotemporal control of fibroblast growth factor receptor signals by blue light. *Chem. Biol.* **21,** 903–912 (2014).

16. Zhang, K. & Cui, B. Lighting up FGFR signaling. *Chem. Biol.* **21,** 806–808 (2014).

17. Heemskerk, I. *et al.* Morphogen dynamics control patterning in a stem cell model of the human embryo. *bioRxiv* 202366 (2017). doi:10.1101/202366

18. Taniguchi, K., Heemskerk, I. & Gumucio, D. L. Opening the black box: Stem cell–based modeling of human post-implantation development. *J Cell Biol* jcb.201810084 (2018). doi:10.1083/JCB.201810084

19. Patel, A. K. *et al.* High throughput screening for discovery of materials that control stem cell fate. *Curr. Opin. Solid State Mater. Sci.* **20,** 202–211 (2016).

20. Yu, X. *et al.* Nanostructured Mineral Coatings Stabilize Proteins for Therapeutic Delivery. *Adv. Mater.* **29,** 1701255 (2017).

21. Collins, M. J., Gernaey, A. M., Nielsen-Marsh, C. M., Vermeer, C. & Westbroek, P. Slow rates of degradation of osteocalcin: Green light for fossil bone protein? *Geology* **28,** 1139–1142 (2000).

22. Smith, C. I. *et al.* Diagenesis and survival of osteocalcin in archaeological bone. *J. Archaeol. Sci.* **32,** 105–113 (2005).

23. Palmer, L. C., Newcomb, C. J., Kaltz, S. R., Spoerke, E. D. & Stupp, S. I. Biomimetic Systems for Hydroxyapatite Mineralization Inspired By Bone and Enamel. *Chem. Rev.* **108,** 4754–4783 (2008).

24. Bartosh, T. J. & Ylostalo, J. H. Macrophage Inflammatory Assay —BIO-PROTOCOL. **4,** 1–7 (2014).

25. Bloom, D. D. *et al.* A reproducible immunopotency assay to measure mesenchymal stromal cell-mediated T-cell suppression. *Cytotherapy* **17,** 140–151 (2015).

26. Galipeau, J. & Krampera, M. The challenge of defining mesenchymal stromal cell potency assays and their potential use as release criteria. *Cytotherapy* **17,** 125–127 (2015).

27. Chinnadurai, R. *et al.* Potency Analysis of Mesenchymal Stromal Cells Using a Combinatorial Assay Matrix Approach. *Cell Rep.* **22,** 2455–2468 (2018).

28. Konala, V. B. R. *et al.* The current landscape of the mesenchymal stromal cell secretome: A new paradigm for cell-free regeneration. *Cytotherapy* **18,** 13–24 (2016).

29. Spees, J. L., Lee, R. H. & Gregory, C. A. Mechanisms of mesenchymal stem/stromal cell function. *Stem Cell Res. Ther.* **7,** 125 (2016).

30. Vizoso, F. J., Eiro, N., Cid, S., Schneider, J. & Perez-Fernandez, R. Mesenchymal stem cell secretome: Toward cell-free therapeutic strategies in regenerative medicine. *Int. J. Mol. Sci.* **18,** (2017).

31. Di Trapani, M. *et al.* Differential and transferable modulatory effects of mesenchymal

stromal cell-derived extracellular vesicles on T, B and NK cell functions. *Sci. Rep.* **6,** 1–13 (2016).

32. Ribot, J. *et al.* Type 2 diabetes alters mesenchymal stem cell secretome composition and angiogenic properties. *J. Cell. Mol. Med.* **21,** 349–363 (2017).

33. Heathman, T. R. J. *et al.* Characterization of human mesenchymal stem cells from multiple donors and the implications for large scale bioprocess development. *Biochem. Eng. J.* **108,** 14–23 (2016).

34. Patel, R. S. *et al.* Adipose-derived stem cells from lean and obese humans show depot specific differences in their stem cell markers, exosome contents and senescence: role of protein kinase C delta (PKCdelta) in adipose stem cell niche. *Stem Cell Investig* **3,** 2 (2016).

35. Zazzeroni, L., Lanzoni, G., Pasquinelli, G. & Ricordi, C. Considerations on the harvesting site and donor derivation for mesenchymal stem cells-based strategies for diabetes. *CellR4-- repair, Replace. Regen. reprogramming* **5,** 1–13 (2017).

36. Siegel, G. *et al.* Phenotype, donor age and gender affect function of human bone marrow-derived mesenchymal stromal cells. *BMC Med.* **11,** (2013).

37. Deuse, T. *et al.* Immunogenicity and immunomodulatory properties of umbilical cord lining mesenchymal stem cells. *Cell Transplant.* **20,** 655–667 (2011).

38. Yoo, K. H. *et al.* Comparison of immunomodulatory properties of mesenchymal stem cells derived from adult human tissues. *Cell. Immunol.* **259,** 150–156 (2009).

39. Paladino, F. V., Sardinha, L. R., Piccinato, C. A. & Goldberg, A. C. Intrinsic Variability Present in Wharton's Jelly Mesenchymal Stem Cells and T Cell Responses May Impact Cell Therapy. *Stem Cells Int.* **2017,** (2017).

40. Lee, M. J. *et al.* Proteomic Analysis of Tumor Necrosis Factor-α-Induced Secretome of Human Adipose Tissue-Derived Mesenchymal Stem Cells. *J. Proteome Res.* **9,** 1754–1762 (2010).

41. Maffioli, E. *et al.* Proteomic analysis of the secretome of human bone marrow-derived mesenchymal stem cells primed by pro-inflammatory cytokines. *J. Proteomics* **166,** 115–126 (2017).

42. Wobma, H. M. *et al.* The influence of hypoxia and IFN-γ on the proteome and metabolome of therapeutic mesenchymal stem cells. *Biomaterials* **167,** 226–234 (2018).

43. Sarkar, P. *et al.* Reduced neuroprotective potential of the mesenchymal stromal cell secretome with ex vivo expansion, age and progressive multiple sclerosis. *Cytotherapy* **20,** 21–28 (2018).

44. von Bahr, L. *et al.* Long-term complications, immunologic effects, and role of passage for outcome in mesenchymal stromal cell therapy. *Biol. Blood Marrow Transplant.* **18,** 557–564 (2012).

45. Kurtz, A. Mesenchymal Stem Cell Delivery Routes and Fate. *Int. J. Stem Cells* **1,** 1–7

(2008).

46. Braid, L. R., Wood, C. A., Wiese, D. M. & Ford, B. N. Intramuscular administration potentiates extended dwell time of mesenchymal stromal cells compared to other routes. *Cytotherapy* **20,** 232–244 (2017).

47. Xu, Y., Shi, T., Xu, A. & Zhang, L. 3D spheroid culture enhances survival and therapeutic capacities of MSCs injected into ischemic kidney. *J. Cell. Mol. Med.* **20,** 1203–1213 (2016).

48. Iso, Y. *et al.* Multipotent human stromal cells improve cardiac function after myocardial infarction in mice without long-term engraftment. *Biochem. Biophys. Res. Commun.* **354,** 700–706 (2007).

49. Ankrum, J. a, Ong, J. F. & Karp, J. M. Mesenchymal stem cells: immune evasive, not immune privileged. *Nat. Biotechnol.* **32,** 252–60 (2014).

50. Cheng, N. C., Wang, S. & Young, T. H. The influence of spheroid formation of human adipose-derived stem cells on chitosan films on stemness and differentiation capabilities. *Biomaterials* **33,** 1748–1758 (2012).

51. Xu, Y., Shi, T., Xu, A. & Zhang, L. 3D spheroid culture enhances survival and therapeutic capacities of MSCs injected into ischemic kidney. *J. Cell. Mol. Med.* **20,** 1203–1213 (2016).

52. Murphy, K. C., Fang, S. Y. & Leach, J. K. Human mesenchymal stem cell spheroids in fibrin hydrogels exhibit improved cell survival and potential for bone healing. *Cell Tissue Res.* **357,** 91–99 (2014).

53. Costa, M. H. G., McDevitt, T. C., Cabral, J. M. S., da Silva, C. L. & Ferreira, F. C. Tridimensional configurations of human mesenchymal stem/stromal cells to enhance cell paracrine potential towards wound healing processes. *J. Biotechnol.* **262,** 28–39 (2017).

54. Luebke-Wheeler, J. L., Nedredal, G., Yee, L., Amiot, B. P. & Nyberg, S. L. E-cadherin protects primary hepatocyte spheroids from cell death by a caspase-independent mechanism. *Cell Transplant.* **18,** 1281–7 (2009).

55. Jorns, C. *et al.* Strategies for short-term storage of hepatocytes for repeated clinical infusions. *Cell Transplant.* **23,** 1009–1018 (2014).

56. Smets, F. N., Chen, Y., Wang, L.-J. & Soriano, H. E. Loss of cell anchorage triggers apoptosis (anoikis) in primary mouse hepatocytes. *Mol. Genet. Metab.* **75,** 344–352 (2002).

57. He, N. *et al.* Extracellular matrix can recover the downregulation of adhesion molecules after cell detachment and enhance endothelial cell engraftment. *Sci. Rep.* **5,** 1–12 (2015).

58. Kim, J. & Ma, T. Endogenous extracellular matrices enhance human mesenchymal stem cell aggregate formation and survival. *Biotechnol. Prog.* **29,** 441–451 (2013).

59. Muraki, K. *et al.* Technical Report: Assessment of Viability and Osteogenic Ability of Human Mesenchymal Stem Cells After Being Stored in Suspension for Clinical

Transplantation. *Tissue Eng.* **12,** 1711–1719 (2006).

60. Veronesi, E. *et al.* Transportation Conditions for Prompt Use of *Ex Vivo* Expanded and Freshly Harvested Clinical-Grade Bone Marrow Mesenchymal Stromal/Stem Cells for Bone Regeneration. *Tissue Eng. Part C Methods* **20,** 239–251 (2014).

61. Gómez-Lechón, M. J. *et al.* Evaluation of drug-metabolizing and functional competence of human hepatocytes incubated under hypothermia in different media for clinical infusion. *Cell Transplant.* **17,** 887–897 (2008).

62. Fukuoka, K. *et al.* The Optimization of Short-Term Hepatocyte Preservation Before Transplantation. *Transplant. Direct* **3,** e176 (2017).

63. Cui, L. L., Kinnunen, T., Boltze, J., Nystedt, J. & Jolkkonen, J. Clumping and viability of bone marrow derived mesenchymal stromal cells under different preparation procedures: A flow cytometry-based in vitro study. *Stem Cells Int.* **2016,** (2016).

64. Chinnadurai, R. *et al.* Actin cytoskeletal disruption following cryopreservation alters the biodistribution of human mesenchymal stromal cells in vivo. *Stem Cell Reports* **3,** 60–72 (2014).

65. Chinnadurai, R. *et al.* Cryopreserved Mesenchymal Stromal Cells Are Susceptible to T-Cell Mediated Apoptosis Which Is Partly Rescued by IFNγ Licensing. *Stem Cells* **34,** 2429–2442 (2016).

66. François, M. *et al.* Cryopreserved mesenchymal stromal cells display impaired immunosuppressive properties as a result of heat-shock response and impaired interferon-γ licensing. *Cytotherapy* **14,** 147–152 (2012).